RELATIVISTIC NUCLEAR PHYSICS

FROM HUNDREDS OF MeV TO TeV

2009

STARÁ LESNÁ
SLOVAKIA

Объединенный институт ядерных исследований

RELATIVISTIC NUCLEAR PHYSICS: from HUNDREDS of MeV to TeV

Proceedings of the 10th International Workshop

Slovak Republic, Stara Lesna,
5–11 June, 2009

РЕЛЯТИВИСТСКАЯ ЯДЕРНАЯ ФИЗИКА: от СОТЕН МэВ до ТэВ

Труды 10-го международного совещания

Словакия, Стара Лесна,
5–11 июня 2009 г.

Дубна 2010

УДК 539.17(042)
ББК 22.383.5я431
R41

The contributions are reproduced directly from the originals
presented by the Organizing Committee.

Relativistic Nuclear Physics: from Hundreds of MeV to TeV: Proceedings
R41 of the 10th International Workshop (Stara Lesna, Slovakia, June 5–11, 2009). — Dubna: JINR, 2010. — 192 p., photo.

ISBN 978-5-9530-0241-7

The 10th International Workshop from traditional series of «Relativistic Nuclear Physics: from Hundreds of MeV to TeV» workshops was held in Stara Lesna, Slovakia, on 5–11 June 2009. This workshop was organized by the Joint Institute for Nuclear Research (JINR) and Slovak Academy of Sciences and supported by the Russian Foundation for Basic Research (RFBR). During the workshop, the new results from the JINR Nuclotron were reported, and proposals of new experiments were discussed. The project of the new JINR accelerator complex NICA/MPD was also discussed. Other reports at the workshop concerned the status and preparation of the new experiments in other world scientific centres.

Релятивистская ядерная физика: от сотен МэВ до ТэВ: Труды 10-го международного совещания (Стара Лесна, Словакия, 5–11 июня 2009 г.). — Дубна: ОИЯИ, 2010. — 192 с., фото.

ISBN 978-5-9530-0241-7

10-е международное рабочее совещание из традиционной серии «Релятивистская ядерная физика: от сотен МэВ до ТэВ» было проведено с 5 по 11 июня 2009 г. (Стара Лесна, Словакия). Совещание было организовано Объединенным институтом ядерных исследований (ОИЯИ) и Словацкой академией наук и поддержано Российским фондом фундаментальных исследований (РФФИ).

На совещании были представлены новые результаты, полученные на нуклотроне ОИЯИ, и обсуждены предложения новых экспериментов. Был обсужден также проект нового ускорительного комплекса ОИЯИ NICA/MPD. Часть докладов касалась статуса новых экспериментов в других мировых научных центрах.

УДК 539.17 (042)
ББК 22.383.5я431

ISBN 978-5-9530-0241-7

RNP

Stará Lesná - 2009

Hotel ACADEMIA
Stará Lesná
June 5 -- 11, 2009
Slovak Republic

INTERNATIONAL WORKSHOP

"RELATIVISTIC NUCLEAR PHYSICS: FROM HUNDREDS MeV to TeV"

Organizers: *Joint Institute for Nuclear Research, Dubna, Russia*
Institute of Physics, Slovak Academy of Sciences, Bratislava, Slovakia

The workshop continues the series of topical meetings started already in 1996. It will cover all aspects of the relativistic nuclear physics.

Main topics:

- **Recent Relativistic Nuclear Physics Experiments and Current Theoretical Developments**
- **Progress in Understanding of Exotic Phenomena (phase transitions, mixed-phase, etc.)**
- **The JINR Research Programme at the NUCLOTRON Beams, NICA/MPD**
- **Applied Research and Experimentation Using Relativistic Ion Beams**
- **LHC Physics**
- **Physics Programme at FAIR Facility**

International Advisory Committee:

Ts. Baatar, IP MAS, Ulan-Bator
V. V. Burov, JINR, Dubna
S. Dubnicka (co-chairman), IP SAS, Bratislava
M. Gazdzicki, Frankfurt, Germany
T. Hallman, BNL, Upton
V. D. Kekelidze, JINR, Dubna
E. Kistenev, BNL, Upton
J. Kliman, IP SAS, Bratislava
A. D. Kovalenko, JINR, Dubna
A. Kugler, NPI, Prague – Rez
A. I. Malakhov (co-chairman), JINR, Dubna
G. Martinska, Safarik University, Kosice
Y. Miake, KEK, Tsukuba
Yu. A. Panebratsev, JINR, Dubna
Ch. Perdrisat, College. of Wiliam & Mary, Newport News
P. Senger, GSI, Darmstadt
A. N. Sissakian, JINR, Dubna
I. Stamenov, INRNE BAN, Sofia
Yu. V. Zanevski, JINR, Dubna
M. Zamany, Aristotle University, Thessaloniki

Local Organizing Committee:

Yu. S. Anisimov (co-chairman), JINR, Dubna
S. Gmuca (co-chairman), IP SAS, Bratislava
N. M. Dokalenko, JINR, Dubna
S. Hlavac, IP SAS, Bratislava
V. P. Ladygin, JINR, Dubna
V. Matousek, IP SAS, Bratislava
I. I. Migulina, JINR, Dubna
K. Petrik, IP SAS, Bratislava
E. B. Plekhanov, JINR, Dubna
A. S. Sorin, JINR, Dubna
S. Vokal, Safarik University, Kosice
M. Veselsky, IP SAS, Bratislava
P. I. Zarubin, JINR, Dubna

For more information, please contact:

Yu. S. Anisimov: E-mail: anisimov@lhe.jinr.ru
Tel.: +7 (09621) 65113,
Fax: +7 (09621) 65180

Stefan Gmuca: E-mail: gmuca@savba.sk
Tel.: +421 (2) 5941 0532,
Fax.: +421 (2) 5477 6085

Contents

INVESTIGATION OF ASYMPTOTICS IN RELATIVISTIC NUCLEAR PHYSICS AT FAIR AND NICA

A.Malakhov

JINR, 141980, Dubna, Moscow region, Russia

Abstract

The possibility of studying asymptotic properties of a nuclear matter on accelerators FAIR and NICA is discussed. It is shown that for this purpose can serve CBM and MPD setups well.

1. Introduction

The experimentally observable quantities which characterize multi-quark processes are the cross sections of multiple particle production in relativistic nuclear collisions:

$$\mathrm{I} + \mathrm{II} \rightarrow 1 + 2 + 3 + \ldots \tag{1}$$

The problem is to describe the properties of the momentum distributions of secondary particles 1, 2, 3, ... in terms of the quark degrees of freedom starting from the principles and minimum number of hypotheses of a general nature.

In the invariant method of analyzing multiple particle production the processes (1) are considered in a space the points of which are the four-velocities $u_i = P_i/m_i$ or the four-momenta P_i of the particles divided by their masses m_i [1, 2].

The basic quantities which the probability distributions (cross sections) depend upon are dimensionless positive relativistic invariant quantities:

$$b_{ik} = -(u_i - u_k)^2 \tag{2}$$

where $u_i = P_i/m_i$, $u_k = P_k/m_k$, $i, k = \mathrm{I}, \mathrm{II}, 1, 2, 3, \ldots$.

It is possible to suggest the classification of relativistic nuclear collisions on the b_{ik} basis in the following manner (fig.1):

1. The domain $b_{ik} \sim 10^{-2}$ corresponds to the interaction of nuclei as weakly bound systems consisting of nucleons. This is domain of classic nuclear physics.
2. The domain $b_{ik} \sim 5$ is an intermediate one. Here the quark degrees of freedom important in rebuilding of hadron systems. It is so called cumulative domain.
3. The domain $\sim 10 > b_{ik} > 5$ is mixed phase domain. Here the matter exists as f mix quarks and hadrons.
4. In region $b_{ik} >> 1$ hadrons loss their meaning of the quasi-particles of nuclear matter and nuclei should be considered as quark-gluon systems.

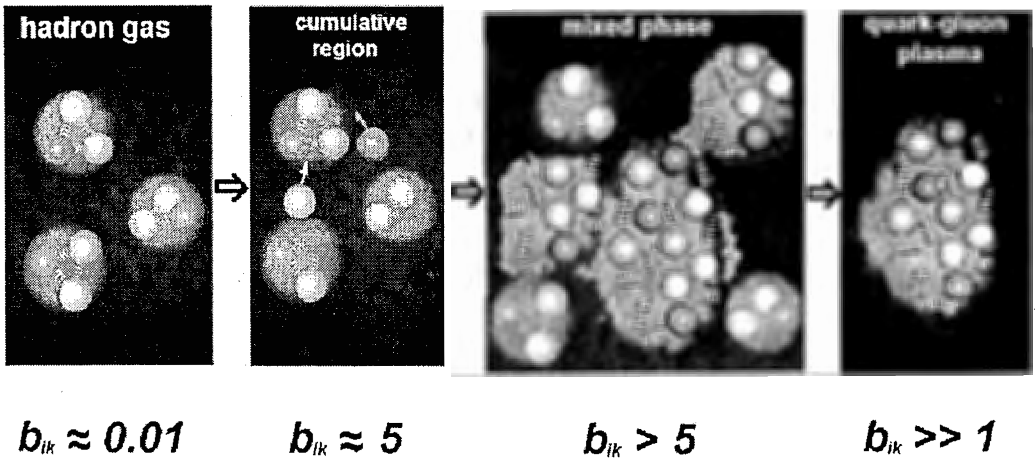

Fig.1. Classification of relativistic nuclear collisions on the b_{ik}.

2. Asymptotics in Relativistic Nuclear Physics

A rigorous statement which makes it possible to describe the asymptotic freedom of quark and gluon fields in terms of observable quantities is the correlation depletion principle (CDP). CDP was offered by N.N.Bogolyubov in statistical physics as universal property of the probability distributions for particle location in ordinary space-time (r, t). The principle is based on the idea that the correlation between largely spaced parts of a macroscopic system practically vanishes and the distribution is factorized. CDP in Relativistic Nuclear Physics was suggested by A.M.Baldin in four-velocity space. Due to complementary of r_{ik} and b_{ik} this principle is quite opposite to the Bogolyubov CDP. The Bogolyubov CDP is valid for $|r_i - r_k|^2 \to \infty$ while the Baldin CDP is fulfilled for $|r_i - r_k|^2 \to 0$ (or $b_{ik} \to \infty$) according to the asymptotic freedom. CDP illustrates the fig.2 [3].

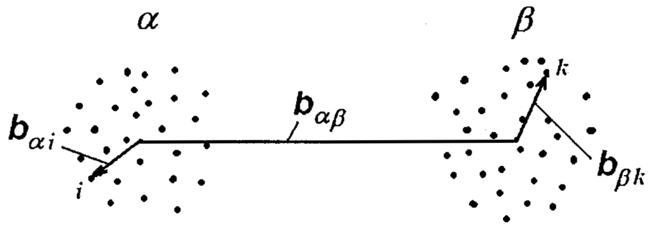

Fig.2. Schematic view of the correlation depletion principle in four-velocity space. Correlations between largely spaced parts α and β of the particle system vanishes when the distance $b_{\alpha\beta}$ in four-velocity space between the centers of systems α and β tends to infinity. The probability distribution which characterized the system is factorized $W \to W_\alpha \cdot W_\beta$ at $b_{\alpha\beta} \to \infty$.

CDP makes it possible to introduce the notion of isolated system. Let V_α be the middle point of a system (group) of strongly interacting particles, u_i - four-velocity of an i-th particle entering the system and u_k - four-velocity of a k–th particle not belonging to the system. The system is isolated if $b_{\alpha i}$ for all the particles entering the system is much smaller than for all the particles not belonging to the system:

$$b_{\alpha i} << b_{\alpha k} \tag{3}$$

$$b_{\alpha i} = - (V_\alpha - u_i)^2 \tag{4}$$

$$b_{\alpha k} = - (V_\alpha - u_k)^2 \qquad (5)$$

The important examples of the isolated system are the hadron jets. In four-velocity space the jet is a claster of hadrons with small relative b_{ik}.

The jet axis (a unit four-vector):

$$V = \Sigma(u_i / \sqrt{(\Sigma u_i)^2} \qquad (6)$$

$$V_o^2 - V^2 = 1. \qquad (7)$$

The summation is performed over all the particles belonging to a selected particle group (claster).

It is possible to determine the squared four-velocity with respect to the axis:

$$b_k = - (V - u_k)^2. \qquad (8)$$

The b_k distributions of π^- mesons in the jets produced in events of different types are presented in fig.3. It is possible to make following conclusions:

1. Distribution of π mesons on b_k in jets of hadron-hadron and hadron-nucleus collisions at high energies are universal. They do not depend either on the collision energy, or on the type of fragmenting system.
2. This universality of properties of four-dimensional hadron jets indicates that the hadronisation of quark systems is defined by the dynamics of interaction of a color charge with QCD vacuum.

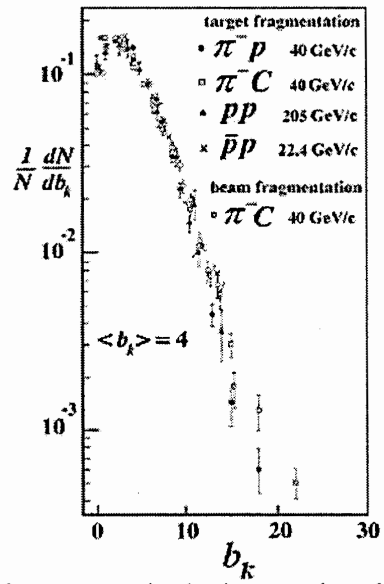

Fig.3. The b_k distributions of π^- mesons in the jets produced in events of different types.

For jets : $<b_k> \sim 1$, for hadrons: $<b_k> \ll 1$.

The important property of relativistic nuclear interactions, which was used in the investigations of the nuclear interactions in four-velocities space, is the automodelity.

The introduction of a self-similarity parameter Π [7]:

$$\Pi = \min[1/2\_(u_I N_I + u_{II} N_{II})^2] \qquad (9)$$

leads to the description of the invariant production cross section for an inclusive particle in the form [8]:

$$E(d^3\sigma/d^3p) = C_1 \cdot A_I^{\,1/3+NI/3} \cdot A_{II}^{\,1/3+NII/3} \cdot \exp(-\Pi/C_2), \qquad (10)$$

where $C_1 = 1.9 \cdot 10^4$ mb·GeV^{-2} c^3·st^{-1}, $C_2 = 0.125 \pm 0.002$.

In formula (9) the N_I and N_{II} are cumulative numbers of the interacting nucleus I and II in reaction (1).

This equation describes a very large amount of experimental data in a wide region of change of the cross sections (by 10 orders of magnitude) and of the energy for different particles and interacting nuclei.

Using the self-similarity parameter Π (9) an analytical expression was obtained for the inclusive invariant cross section of production of particles, nuclear fragments and antinuclei in relativistic nuclear collisions in the central rapidity region [4].

The quantities N_I and N_{II} become measurable if we take into account the law of conservation of four-momentum in the form

$$(N_I m_0 u_I + N_{II} m_0 u_{II} - m_1 u_1)^2 = (N_I m_0 + N_{II} m_0 + \Delta)^2, \qquad (11)$$

neglecting the relative motion of the remaining not detected particles. Here m_0 is the nucleon mass, Δ is the mass of the particles providing conservation of the baryon number, strangeness and other quantum numbers. For antinuclei and K^- mesons (the case of antimatter formation) $\Delta = -m_1$. For particles produced without accompanying antiparticles (π mesons, jets and others) $\Delta = 0$.

Using condition (11) it is possible to find value (9) in the central rapidity region.

The analytical representation for Π enables us to draw the following conclusions:

1. There exists the limiting value of Π.
2. The expression for Π is factorized and proportionality of it to the inclusive particle mass m_1 makes it possible to test in detail the self-similarity laws and the cross section exponentially quickly decreases with increasing m_1. In particular, this implies that the probability of observing even light antinuclei and fragments is insignificantly small.
3. The yield of strange particles in the central rapidity region increases with increasing collision energy.
4. The effective number of nucleons involved in the reaction decreases with increasing collision energy.

In this approach it possible make predictions of the ratios the cross section some particles. The predictions of the ratios of the production cross section for antiparticles to that for particles are presented in Fig. 4. The calculations were carried out for a fixed target and energy of incident nuclei in laboratory system.

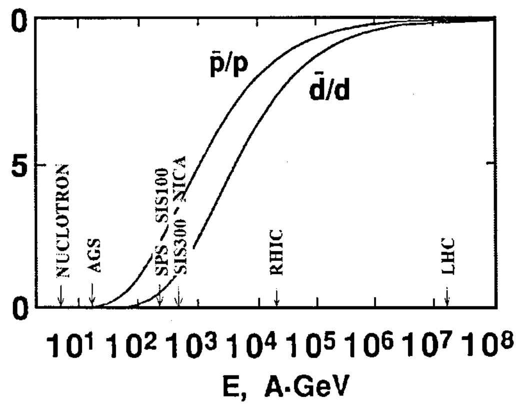

Fig. 4. Predictions of production cross section ratios for antiparticles to particles versus laboratory collision energy.

In intermediate energies where one does not observe a good jet separation it is more convenient to employ for separating out two jet the quantity

$$A_2 = \min\,[-\Sigma(V_\alpha - u_k)^2 - \Sigma(V_\beta - u_i)^2\,], \tag{12}$$

for separating out three jets the quantity

$$A_3 = \min\,[-\Sigma(V_\alpha - u_k)^2 - \Sigma(V_\beta - u_i)2 - \Sigma(V_\gamma - u_j)^2\,], \tag{13}$$

and so on.

Distribution of jet axes is well described QCD as result of the production of quarks and gluons (i.e. color charges). In other words studying of jets is studying of deformation of vacuum by a color charge, studying of the deconfinement.

Now in Germany in Darmstadt the new accelerator complex FAIR [5] is realized and in Dubna the project of the NICA collider [6] is offered. In these centers the heavy ion beams with energy in laboratory system in some tens GeV is planned.

On FAIR setup CBM [7] is created, and on NICA setup MPD [8, 9] is planed. These setups high multiplicity of hadron production will register well.

The Physics Program of CBM is following:

- Deconfinement phase transition at high ρ_B
  - excitation function and flow of strangeness (K, Λ, Σ, Ξ, Ω)
  - excitation function and flow of charm (J/ψ, ψ', D0, D±, Λc)
  - melting of J/ψ and ψ'
- QCD critical endpoint
  - excitation function of event-by-event fluctuations
- The equation-of-state at high ρ_B
  - collective flow of hadrons
  - particle production at threshold energies
- Onset of chiral symmetry restoration at high ρ_B
  - in-medium modifications of hadrons (ρ,ω,ϕ →e+e-(μ+μ-), D).
  -

The physical program of NICA/MPD includes study of in-medium properties of hadrons and nuclear matter equation of state, including a search for possible signs of deconfinement and/or chiral symmetry restoration phase transitions and QCD critical endpoint.

This program includes scanning in beam energy and centrality of excitation functions for obtaining information about:

- Multiplicity and global characteristics of identified hadrons including (multi)strange particles
- Fluctuations in multiplicity and transverse momenta
- Directed and elliptic flows for various identified hadrons
- Particle correlations
- Dileptons and photons.

Thus it is possible detailed studying of a hadron and hadron jets production in asymptotic energy region at CBM and MPD setups.

3. Conclusion

CBM at SIS-100 and MPD at NICA are a unique opportunity for investigation of asymptotic of the nuclear interactions. The parameters of the CBM and MPD and energy region of FAIR and NICA are very well corresponded for investigations of the initial stage of asymptotic regimes and asymptotic regimes of nuclear collisions.

References

1. A.M.Baldin and L.A.Didenko. Fortschr. Phys. 38 (1990) 4, 261-332.
2. A.M.Baldin, A.I.Malakhov, and A.N.Sissakian. Physics of Particles and Nuclei, Vol.32. Suppl. 1, 2001, pp.S4-S30.
3. A.I.Malakhov. ЭЧАЯ, т.31, вып. 7б (2000) сс. 229-236.
4. Baldin A.M., Malakhov A.I. JINR Rapid Communications, No.1(87)-98, 1998, pp.5-12.
5. http://www.gsi.de/fair/index.html
6. http://nica.jinr.ru
7. P.Senger. 24th Winter Workshop on Nuclear Dynamics South Padre, Texas, USA, April 5–12, 2008.
8. A.N.Sissakian, A.S.Sorin. International Conference on Strangness in Quark Matter 2008, Tsinghua University, Beijing, China, October 6-10, 2008.
9. A.N. Sysakian, A.S. Sorin, M.K. Suleymanov, V.D. Toneev and G.M. Zinovjev arXiv:nucl-ex/0601034; Proceedings of the 8th InternationalWorkshop "Relativistic Nuclear Physics: From hundreds MeV to TeV", Dubna, 2006, P.306 [arXiv: nuclex/0511018].

RELATIVISTIC PARTICLES PRODUCED IN ^{208} Pb INDUCED NUCLEAR COLLISIONS AT 158 A GeV/c

S. Vokál[a,1] and J. Vrláková[a]

a) P. J. Šafárik University, Košice, Slovakia

Abstract

The angular structures of relativistic particles produced in $^{208}Pb + Ag(Br)$ collisions in emulsion detector at 158 A GeV/c have been studied. Three different methods of analysis have been used - scaled factorial moments, wavelets and parameter S_2.

An evidence for nonstatistical fluctuations has been shown using the method of scaled factorial moments in pseudorapidity phase space. The comparative study has been done for different beam energies and masses and $Pb + Em$ events with different degree of centrality. No clear minimum has been found in the dependences of intermittency parameter λ_q on q.

The continuous wavelet transform has been applied to the pseudorapidity spectra of produced particles. Some irregularities have been revealed mainly in the scale range $a \leq 0.5$ which can be interpreted as the preferred pseudorapidities of groups of emitted particles.

The nonstatistical ring-like structures of produced particles in azimuthal plane of a collision have been found and their parameters have been determined when the azimuthal structures of produced particles have been investigated using the S_2-method.

1 Introduction

One of the topics intensively investigated in nuclear collisions at high energies is to search for phenomena connected with large densities obtained in such interactions. The existence of quark-gluon plasma (QGP) have been predicted in the frame of the quantum chromodynamics. As an example, the transition from the QGP back to the normal hadronic phase was predicted to give large fluctuations in the number of produced particles in local regions of phase space [1, 2].

The goal of our work was to present our last results obtained when some pecularities in the emission of relativistic particles produced in $^{208}Pb + Ag(Br)$ interactions at 158 A GeV/c have been studied. There are many methods proposed to analyze such effects in relativistic interactions of two nuclei. Three methods have been used in our analysis:

- method of S_2 -parameter [3],
- wavelet method [4],
- scaled factorial moment method [5].

The S_2 -parameter and wavelet methods are described and some selected results are discussed. The main aim of this paper is to present some new results of the search for fluctuations of relativistic particles produced in ^{208}Pb induced interactions with $Ag(Br)$ targets at the CERN SPS energy using the method of scaled factorial moments.

Experimental sample was collected in the EMU12 experiment organized by the EMU01 Collaboration [6, 7]. Comparison of experimental data with model calculations

[1]E-mail: stanislav.vokal@upjs.sk

for events with different degree of centrality and for different beam nuclei have been done using the modified FRITIOF [8, 9] and cascade models [10].

2 Experiment

Nuclear emulsions were irradiated horizontally by 158 A GeV/c ^{208}Pb beam at the CERN SPS - experiment EMU12. Experimental details can be found in [6, 7]. In the measured interactions all charged secondary particles were classified according to the commonly accepted emulsion experiment terminology into following groups:

- b-particles (black) - singly and multi-charged fragments evaporated from the target;
- g-particles (grey) - charged particles with a range $\geq 3mm$, b- and g-particles are target fragments with $\beta < 0.7$;
- s-particles - the relativistic particles with $\beta \geq 0.7$ emitted outside the fragmentation cone, this group includes particles produced in the interactions as well as those knocked-out from the target nucleus;
- f-particles - the projectile fragments with $\beta \sim 0.99$.

The schematic view of our experimental setup is shown in the Fig.1.

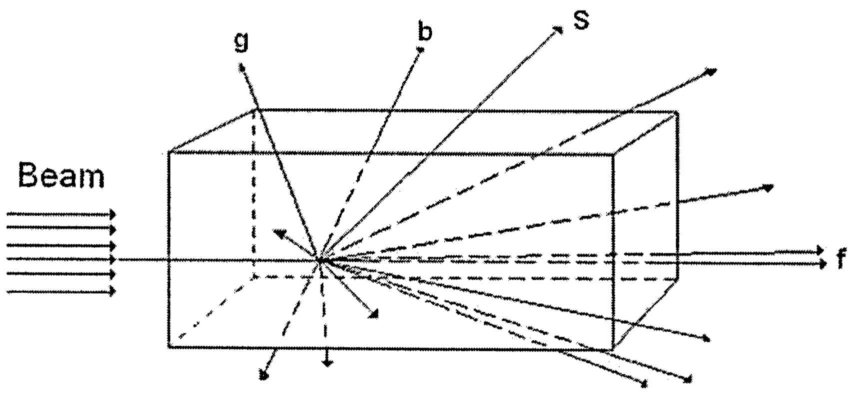

Figure 1: Our experimental setup.

The polar (θ) and azimuthal (Ψ) emission angles of all tracks were measured. The pseudorapidity ($\eta = -ln[\tan \frac{\theta}{2}]$) was calculated for each relativistic particle.

The event of ^{208}Pb nuclear interaction in emulsion detector is presented in the Fig.2. One can see the primary track of Pb nuclei on the left side and the tracks of produced particles, mainly fragments, on the right side.

The dependence of the number of produced relativistic particles (N_s) on the impact parameter b_{imp} calculated by the FRITIOF model for $^{208}Pb + Em$ collisions at 158 A GeV/c is shown in Fig.3 for different emulsion targets [11]. One can see that interactions with $N_s > 350$ are those of lead nuclei with the heavy emulsion targets Ag and

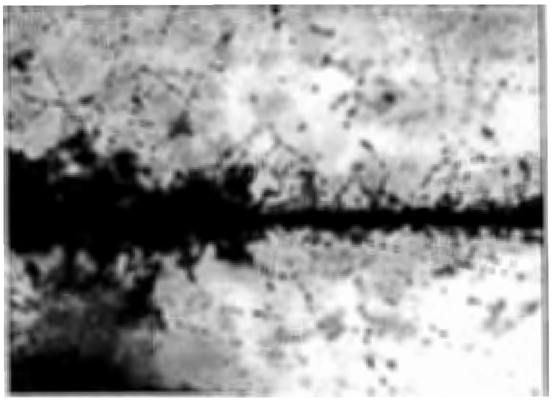

Figure 2: The ^{208}Pb interaction in emulsion detector at 158 A GeV/c.

Br. The group with $N_s \geq 1000$ comprises the central $Pb + Ag(Br)$ interactions with impact parameter $b_{imp} \approx (0-2) fm$.

For the analysis 64 events with the number of relativistic particles $N_s > 350$ have been selected from the total number of 628 minimum bias events of $^{208}Pb + Em$ interactions at 158 A GeV/c.

3 Methods of analysis

In our previous investigations three different methods of analysis (the method of S_2-parameter, wavelet analysis and the method of scaled factorial moments [3-5]) have been used. Two methods (wavelet and S_2-parameter) are described and some selected results are presented here. As was mentioned above in the introduction the main aim of this paper is to present some new results of the search for fluctuations of relativistic particles produced in ^{208}Pb induced interactions with $Ag(Br)$ targets at the CERN SPS energy made by the method of scaled factorial moments.

3.1 Method of the S_2-parameter

The method of S_2-parameter was proposed by E. Stenlund (EMU01 Collaboration) and detailed study of the average values of the parameter S_2 was done in [3].

The azimuthal substructure of particles produced in ultra-relativistic heavy-ion collisions was investigated. It was find out that the observed substructure seems to be of stochastic nature and the features of the experimental data can be understood when effects like gamma-conversion and particle interference (HBT) are taken into account.

How it was find out in [3]? When azimuthal distributions of particles from relativistic heavy-ion collisions, produced within a narrow region of pseudorapidity, are studied, two classes of spectra are seen (Fig.4.). The jet-class consists of cases where several particles seem to form clusters in the azimuthal plane, clusters which are separated with rather large void regions, as sketched in the left figure. The ring-class consists of cases where the particles are distributed almost regularly as the spokes in a wheel (right figure).

In the S_2-method [3] the multiplicity N_d of the analyzed subgroup from an individual event is kept fixed. Each N_d tuple of consecutive particles along the η axis of individual

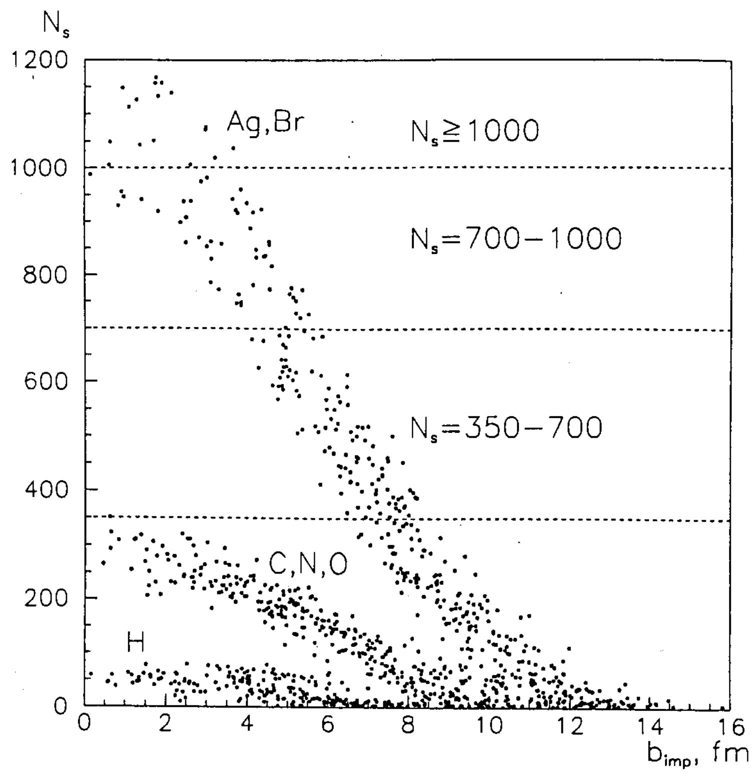

Figure 3: The dependence of multiplicity of produced relativistic particles N_s on the impact parameter b_{imp} for $^{208}Pb + Em$ collisions at 158 A GeV/c for different emulsion targets calculated by the FRITIOF model.

event can then be considered as a subgroup characterized by:

- a size $\Delta\eta_d = \eta_{max} - \eta_{min}$, where η_{min} and η_{max} are the pseudorapidity values of the first and last particles in the subgroup;
- density $\rho_d = N_d/\Delta\eta_d$;
- average pseudorapidity (or subgroup position) $\eta_m = \sum \eta_i / N_d$.

To parametrize the azimuthal structure of the subgroup in a suitable way, a parameter S_2 of the azimuthal structure has been suggested, where $\Delta\phi$ is the difference between azimuthal angles of two neighboring particles in the investigated group (starting from the first and second and ending with the last and first)

$$S_2 = \sum (\Delta\phi_i)^2 \tag{1}$$

For the sake of simplicity, $\Delta\phi$ was counted in units of full revolutions $\Delta\phi_i = 1$. The parameter S_2 is small ($S_2 \to 1/N_d$) for the particle groups with the ring-like structure and is large ($S_2 \to 1$) for the particle groups with the jet-like structure.

The expectation value for the parameter S_2, in the case of a stochastic scenario with independent particles in the investigated group, can be analytically expressed [3] as

$$\langle S_2 \rangle = \frac{2}{(N_d + 1)} \tag{2}$$

This expectation value can be derived from the distribution of gaps between neighbors.

The Fig.5 shows the results of the analysis of the generated FRITIOF+HBT sample, with and without γ -conversion, compared with the results obtained from the data [3].

One can see, that except for some additional jet-structure seen by the S_2 parameter for the dilute groups, the features of the data can be understood as a superposition of stochastic fluctuations, γ - conversion and particle interference. Finally it was conluded in [3] that jet-like and ring-like events do not exhibit significant deviations from what can be expected from stochastic emission. But average value studies do not give a full information about an effect. Next step was performed in 2002 [12] where the systematic study of the S_2 -spectra for subgroups of the particles produced in ^{197}Au induced collisions with heavy targets (Ag, Br) in emulsion detector has started. Nonstatistical ring-like substructures have been found and cone emission angles as well as other parameters have been determined.

What we can expect to see in the experimental $S_2/\langle S_2 \rangle$ distributions in different scenarios was shown in 2004 [13]. It is illustrated shematically in Fig.6 using for example Gauss distributions. In case of a pure stochastic scenario the distribution would have a peak position at 1. The existence of the jet-like structures in collisions results to appearance of additional S_2 distribution from this effect, but shifted to the right side in comparison with stochastic distribution. Analogously, the existence of the ring-like structures results to appearance of additions to S_2 distribution from this effect but shifted to the left side. As a result, the summary S_2 distribution from these three effects may have different form and depends on mutual order and sizes.

After the experimental normalized $S_2/\langle S_2 \rangle$ distributions compared with the distributions calculated by the FRITIOF model have been investigated [14]. One of the results is shown in the Fig.7 ab.

The model spectra were aligned according to the position of the peak with the experimental one. The FRITIOF includes neither the ring-like nor the jet-like effects, so the model spectra are used like the statistical background. Except this, in [3], it was shown that the S_2 distribution for the FRITIOF model coincides with the calculated distribution in the case of the stochastic scenario with independent particles in the investigated group.

One can see that the experimental distributions are broader than the spectra calculated by the FRITIOF model. The experimental distributions have a surplus of events

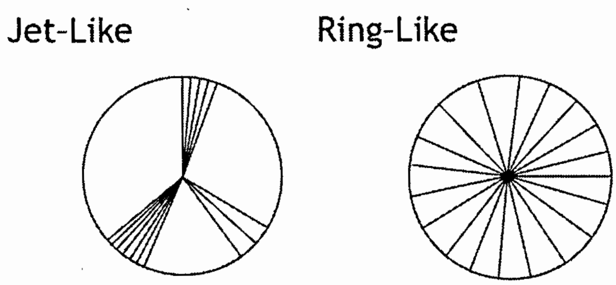

Figure 4: Examples of two extreme azimuthal structures: (a) jet-like, (b) ring-like.

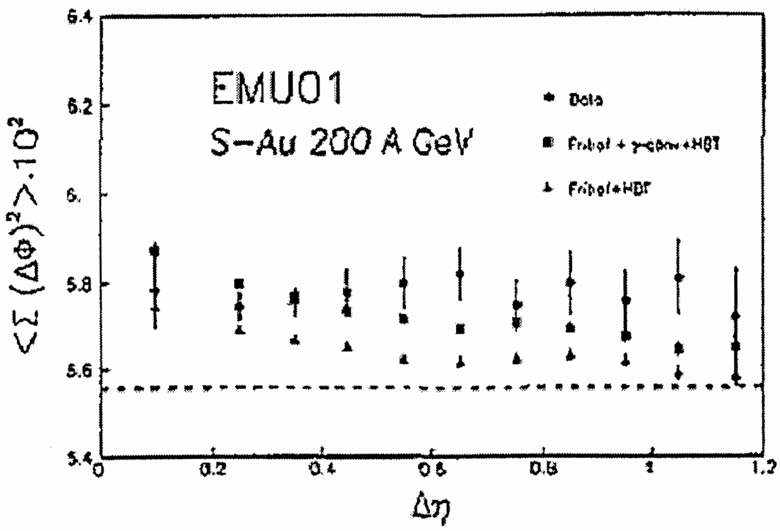

Figure 5: The dependence of the parameter S_2 on group size for central 200 A GeV $S + Au$ interactions, $N_s \geq 300$, $N_d = 35$. The dashed line indicates the expectation values for purely stochastic emission.

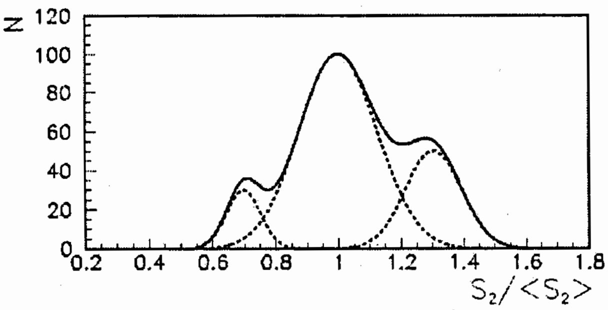

Figure 6: The example of possible summary $S_2/\langle S_2\rangle$ - distribution from three effects: stochastic + ring-like + jet-like effect distribution.

on both sides of the center. Such a situation takes place for all N_s and any N_d groups which were examined.

The results obtained from the experimental data after the subtraction of the statistical background are shown in Fig.7cd. The obtained distributions have two very good distinguishable hills, the first in the region $S_2/\langle S_2\rangle < 1$, where the ring-like effects are expected, and the second in the jet-like region ($S_2/\langle S_2\rangle > 1$).

The preliminary result is that the azimuthal structures of produced particles from collisions induced by the 158 A GeV/c ^{208}Pb beams with $Ag(Br)$ targets in the emulsion detector have been investigated and the additional groups of produced particles in the region of the ring-like structures ($S_2/\langle S_2\rangle < 1$) and the jet-like structures ($S_2/\langle S_2\rangle > 1$) in comparison to the FRITIOF model calculations have been observed [11, 14]. Analogical situation have been observed in the interactions of 11 A GeV/c ^{197}Au beams with heavy targets in the emulsion detector [13].

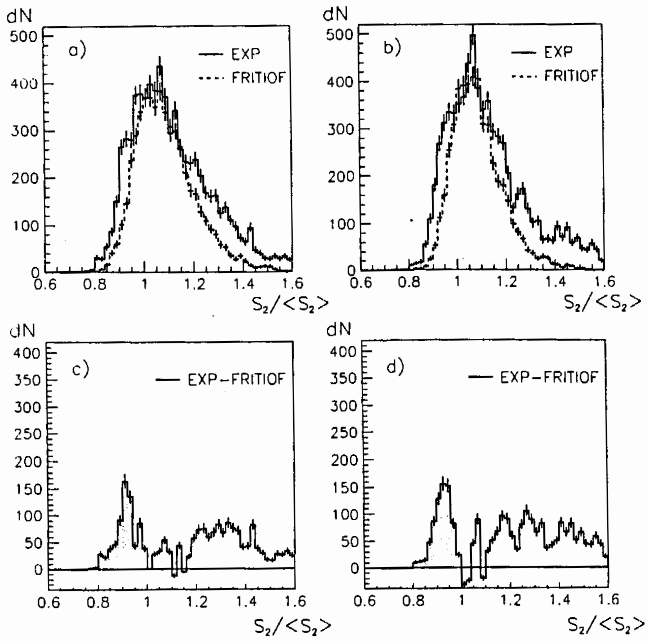

Figure 7: The $S_2/\langle S_2\rangle$ distributions for ${}^{208}Pb+Ag(Br)$ collisions at 158 A GeV/c with $N_s \geq 1000$: the experimental one compared with FRITIOF model calculations for subgroup with (a) $N_d = 60$ and (b) $N_d = 90$. The experimental $S_2/\langle S_2\rangle$ distributions after the subtraction of the FRITIOF ones for (c) $N_d = 60$ and (d) $N_d = 90$.

3.2 Wavelet method

The distributions of both the azimuthal and polar angles of produced particles have been investigared simultaneously to observe irregularities in particle emission. The continuous wavelet approach was applied to the angular spectra of the relativistic particles created in Au and Pb induced nuclear collisions at AGS a SPS energies [15, 16]. The wavelet pseudorapidity spectra have been subsequently surveyed at different scales to look for signs of ring-like structures. The particles contributing to the ring-like structures are expected to give peaks or bumps at certain typical pseudorapidities and to have approximately uniform azimuthal distributions (at certain scales).

Wavelet pseudorapidity spectrum of event is the sum of wavelets representing the individual particles. Wavelet coefficients $W_\psi(a,b)$ reflect the probability to observe particle at some pseudorapidity b and scale a.

$$W_\psi(a,b) = \frac{1}{N}\sum_{i=1}^{N} a^{-1/2}\psi(\frac{\eta_i - b}{a}) \qquad (3)$$

The second derivative g_2 of Gaussian function (also known as Mexican hat) was chosen as a mother wavelet.

Wavelet g_2 pseudorapidity spectra for all s-particles at the three different scales a are presented in the Fig.8 [16].

The b_{max} spectra plotted for the four different scale intervals are presented in Fig.9 [16]. The scale intervals were introduced to investigate how an occurence of maxima $W_\psi(a_{max}, b_{max})$ depends on scale.

One can see that the local maximum reffered to as irregularities were uncovered in the wavelet pseudorapidity distributions mainly in the scale range $a \leq 0.5$. These irregularities indicate the preferred pseudorapidities of groups of emitted particles.

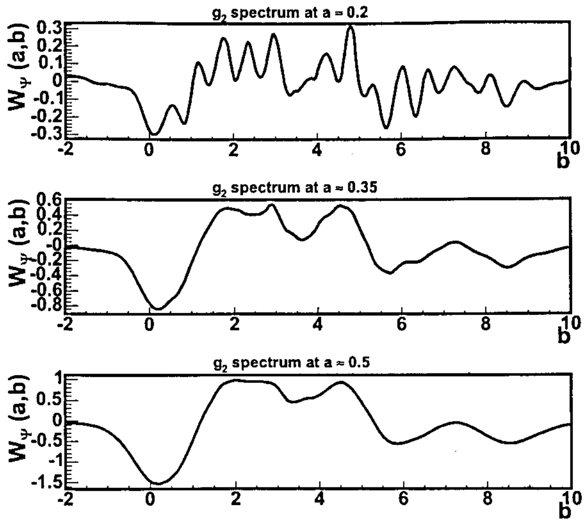

Figure 8: Wavelet g_2 pseudorapidity spectra of all the studied Pb events seen at the three different scales a.

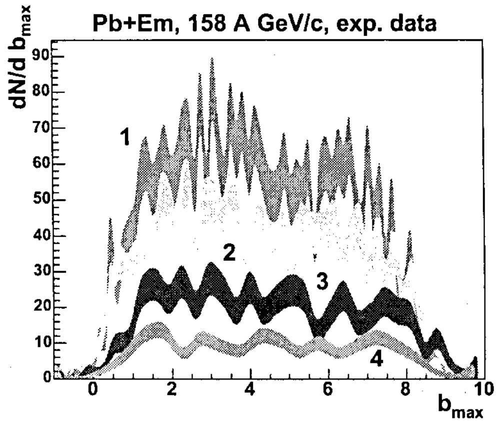

Figure 9: b_{max} spectra of the experimental $Pb + Em$ events seen in the four scale bands: 1.)$-0.05 < a_{max} \leq 0.1$, 2.) $-0.1 < a_{max} \leq 0.2$, 3.) $-0.2 < a_{max} \leq 0.3$, 4.) $-0.3 < a_{max} \leq 0.45$.

3.3 Scaled factorial moments method analysis

Experimental data on particle fluctuations in small space domains have been presented for various high energy multiparticle collisions. Bialas and Peschanski [17, 18] suggested to study the dependence of factorial moments F_q, where q is the order of the moment, as a function of the bin width $\delta\eta$. The intermittent behaviour should lead to a power law dependence of the factorial moments on the bin size $F_q \propto (\frac{\Delta\eta}{\delta\eta})^{\varphi_q}$, $\varphi_q > 0$, where $\Delta\eta$ is the pseudorapidity interval of produced relativistic particles.

Three methods: method of horizontal factorial moments (HFM), vertical factorial moments (VFM) and mixed moments (MFM) have been proposed in [5]. The standard horizontal factorial moments $F_e^{(H)}$ characterizing the eth event are defined by the following formula:

$$F_e^{(H)}(q) = M^{q-1} \sum_{m=1}^{M} \frac{F(n_{me};q)}{[N_e^{(H)}]^q}, \tag{4}$$

where M is the number of equal bins of size $\delta\eta$ into which the pseudorapidity interval $\Delta\eta$ has been divided, n_{me} is the number of shower particles in the mth bin. Non averaging and non normalized factorial moments are given by $F(n;q) = n(n-1)...(n-q+1)$. Vertical averaging of $F_e^{(H)}$ gives the full form

$$F^{(H)}(q) = \frac{1}{E}\sum_{e=1}^{E} F_e^{(H)}(q). \tag{5}$$

Denominator of the horizontal moment (4) is $N_e^{(H)} = \sum_{m=1}^{M} n_{me}$.

Vertical analysis is suggested in case of rare events with sharps peaks. In this case the normalized standard vertical moments characterizing the mth bin are given by

$$F_m^{(V)}(q) = E^{q-1} \sum_{e=1}^{E} \frac{F(n_{me};q)}{[N_m^{(V)}]^q} \tag{6}$$

and the horizontal averaging gives the full form

$$F^{(V)}(q) = \frac{1}{M}\sum_{m=1}^{M} F_m^{(V)}(q), \tag{7}$$

where $N_m^{(V)} = \sum_{e=1}^{E} n_{me}$ is the sum of multiplicities which appear in the mth bin of all events.

Besides the horizontal and vertical factorial moment methods a mixed approach is applied. Mixed factorial moments are defined as

$$F^{(HV)}(q) = \frac{1}{M}\sum_{m=1}^{M} \frac{\frac{1}{E}\sum_{e=1}^{E} F(n_{me};q)}{[\frac{1}{M}\frac{1}{E}\sum_{e=1}^{E} N_e^{(H)}]^q} = M^{q-1}E^{q-1}\frac{\sum_{m=1}^{M}\sum_{e=1}^{E} F(n_{me};q)}{[N^{(HV)}]^q}, \tag{8}$$

where $N^{(HV)} = \sum_{m=1}^{M}\sum_{e=1}^{E} n_{me}$ is the total number of charged particles observed in the sample of E events.

For experimental data of $Si + Ag(Br)$ interactions at 14.6 A GeV/c we used all the three above mentioned methods of analysis - HFM, VFM and MFM. The $ln\langle F_q\rangle$ dependences on lnM have been obtained. The results of this analysis have been published in [19]. The values of slopes are given in Table 1. The values of slopes φ_q obtained by all these methods are similar for $q = 2 - 5$, where q is the order of factorial moment. Because all three methods give similar values of slopes, in next analysis we used the HFM method only.

Table 1: The values of slopes for 14.6 A GeV/c ^{28}Si events in η space for $q = 2 - 5$ using HFM, VFM and MFM methods

	φ_2	φ_3	φ_4	φ_5
HFM	0.037 ± 0.005	0.076 ± 0.012	0.112 ± 0.021	0.145 ± 0.032
VFM	0.030 ± 0.004	0.099 ± 0.018	0.188 ± 0.076	0.228 ± 0.088
MFM	0.034 ± 0.002	0.071 ± 0.005	0.114 ± 0.014	0.171 ± 0.034

From the total number of 628 measured events of $^{208}Pb + Em$ interactions at 158 A GeV/c, 64 collisions with the number of relativistic particles $N_s > 350$ have been selected. The interactions with $N_s > 350$ are those of lead nuclei with heavy emulsion targets (Ag, Br) [13]. The interactions with increasing number of relativistic particles or degree of centrality, respectively, have been studied also (see Table 2).

Table 2: Different groups of ^{208}Pb interactions in emulsion, N_i is number of interactions, $\langle N_s \rangle$ is average number of relativistic particles.

	N_i	$\langle N_s \rangle$
$N_s > 350$	64	635
$N_s > 400$	52	698
$N_s > 500$	40	775
$N_s > 600$	35	809
$N_s > 700$	23	900
$N_s > 800$	14	993
$N_s > 900$	8	1097
$N_s > 1000$	7	1120

The $ln\langle F_q \rangle$ dependences on lnM (for $q = 2 - 6$) have been obtained by horizontal factorial moment method. Some results of this analysis have been published in our previous work [20]. The dependence of $ln\langle F_q \rangle$ on lnM for $Pb + Ag(Br)$ interactions with $N_s > 1000$ obtained by HFM is shown in Fig. 10.

In our next analysis the dependences of parameters α_q and φ_q ($ln\langle F_q \rangle = \alpha_q + \varphi_q.lnM$) on the order of factorial moments q have been studied for $\Delta\eta = 0 - 7.4$ and $M = 7 - 74$. In Fig.11 the increasing dependences of values of slopes (φ_q) on q for two groups ($N_s > 350, N_s > 1000$) of Pb induced interactions in emulsion are shown. The steepest dependence of values of slopes on q has been found for interactions with $N_s > 1000$. These dependences ($\varphi_q > 0$) show an evidence for the presence of intermittent behaviour or non-statistical fluctuations. Fig.12 presents the dependence of intercept parameter α_q on q for the most central Pb interactions, $q = 2 - 6$.

For comparison we used other experimental data obtained by the same standard emulsion method. The characteristics of used experimental data - beam nucleus, momentum (p), number of bins (M) and bin size ($\delta\eta$) of relativistic particles are given in Table 3.

In Fig.13 our new result - the dependences of slope φ_q on q for $Pb + Em$ and $Au + Em$ central interactions is shown. Measurements and calculations have been

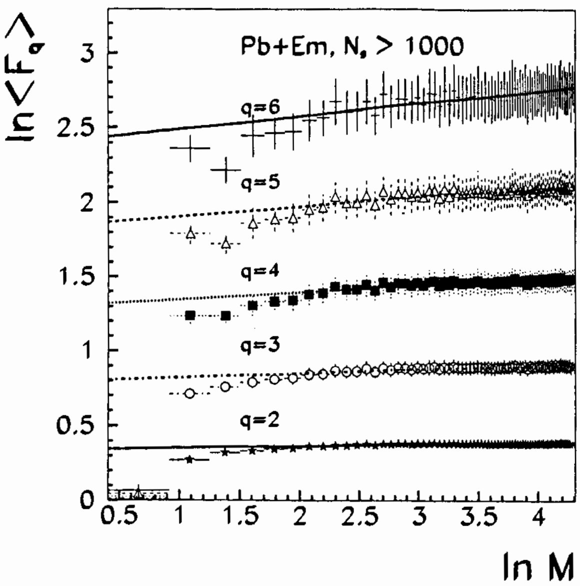

Figure 10: The dependence of $ln\langle F_q\rangle$ on lnM for $Pb+Ag(Br)$ interactions with $N_s >$ 1000, $q = 2-6$, obtained by HFM .

Table 3: Experimental data.

Beam nucleus	^{16}O	^{16}O	^{197}Au	^{208}Pb
p [A GeV/c]	60	200	11.6	158
M	$6-64$	$8-76$	$4-25$	$7-74$
$\delta\eta$	$1.07-0.1$	$0.95-0.1$	$1.25-0.2$	$1.057-0.1$

done in similar conditions: similar masses of projectiles and similar values of bin size ($\delta\eta = 0.1 - 1.057$ for $Pb+Em$ and $\delta\eta = 0.2 - 1.25$ for $Au + Em$). The central events have been selected for this analysis only, i.e. Pb events with $N_s > 350$ and Au events with $N_s > 100$. The similar trend of φ_q dependences on q only for $Pb+Em$ data were published in [21].

The results of analysis using HFM method have been compared with the values obtained from data sample calculated by the modified cascade - evaporation model (CEM). The description of CEM can be found in [10]. The values of slopes obtained by HFM for the experimental data of ^{28}Si interactions at 14.6 AGeV/c and 4.5 A GeV/c are given in the Table 4 [19]. The values in the brackets are from CEM data at the same momenta. The similar comparison for $^{16}O+Em$ experimental and CEM data at 4.5 and 14.6 A GeV/c are given in Table 5. These results have been published in our previous work [22]. One can see that the values of slopes for experimental samples are higher than the values calculated using CEM.

The events of $Pb + Ag(Br)$ with $N_s > 1000$ have been studied also. The φ_q dependences on q for $Pb+Ag(Br)$ experimental and CEM data are presented in Fig.14.

The values of slopes for experimental data are higher than the values from CEM.

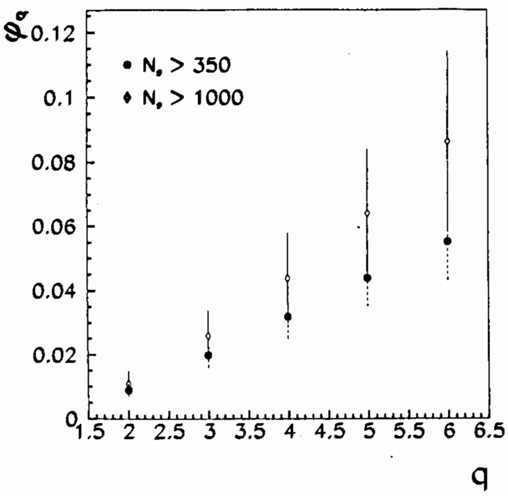

Figure 11: The φ_q dependences on q ($q = 2-6$) for Pb+Em interactions with $N_s > 350$ and $N_s > 1000$, $\Delta\eta = 0 - 7.4$, $M = 7 - 74$.

Table 4: The values of slopes for experimental data from 4.5 A GeV/c and 14.6 A GeV/c ^{28}Si events in η space for q=2-5, the values in the brackets are from CEM data

Energy	φ_2	φ_3	φ_4	φ_5
4.5 A GeV/c	0.044 ± 0.009	0.117 ± 0.025	0.224 ± 0.051	0.336 ± 0.092
	(0.008 ± 0.004)	(0.023 ± 0.012)	(0.032 ± 0.023)	(0.040 ± 0.037)
14.6 A GeV/c	0.037 ± 0.005	0.076 ± 0.012	0.112 ± 0.021	0.145 ± 0.032
	(0.023 ± 0.003)	(0.045 ± 0.008)	(0.063 ± 0.014)	(0.076 ± 0.021)

Similar results have been published by B.Wosiek in [21] for $Pb + Em$ and MC calculations at 158 A GeV/c, where the slopes φ_q increase with increasing value of q and values of slopes are higher than those obtained from MC calculations.

The dependences of intermittency parameter (λ_q) on the order of factorial moment q have been studied. The intermittency parameter is defined as

$$\lambda_q = \frac{\varphi_q + 1}{q} \tag{9}$$

If the function λ_q on q had a minimum at a certain $q = q_c$, there would be possibility of observing a non-thermal phase transition [23,24].

The dependences of intermittency parameter (λ_q) on the order of factorial moment q for two groups of Pb interactions with different degree of centrality ($N_s > 350$ and $N_s > 1000$) are presented in Fig.15. No minimum of λ_q dependence on q has been found. The similar dependences for $\delta\eta = 0.1 - 3.7$ have been published in [20], no minimum of λ_q on q has been found also.

The dependences of intermittency parameter (λ_q) on the order of factorial moment q for different primary nuclei have been studied. In Fig.16 the λ_q dependences on the

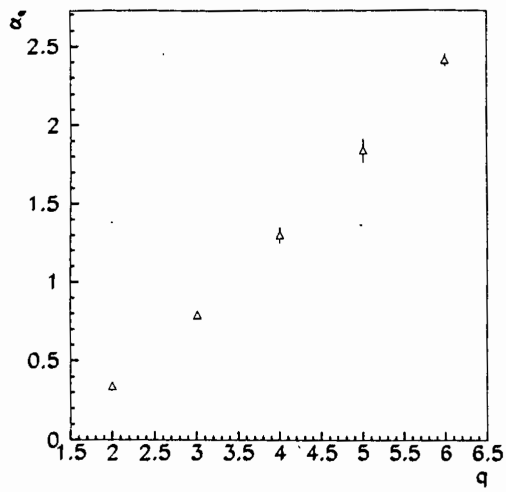

Figure 12: The α_q dependence on q ($q = 2-6$) for $Pb+Em$ interactions with $N_s > 1000$, $\Delta\eta = 0 - 7.4$, $M = 7 - 74$.

Table 5: The values of slopes for experimental data from 4.5 A GeV/c and 14.6 A GeV/c ^{16}O events in η space for q=2-5, the values in the brackets are from CEM data at the same momenta

Energy	φ_2	φ_3	φ_4	φ_5
4.5 A GeV/c	0.041 ± 0.006	0.099 ± 0.015	0.178 ± 0.029	0.270 ± 0.048
	(0.018 ± 0.003)	(0.035 ± 0.004)	(0.050 ± 0.019)	(0.072 ± 0.033)
14.6 A GeV/c	0.040 ± 0.004	0.094 ± 0.017	0.163 ± 0.031	0.236 ± 0.047
	(0.018 ± 0.004)	(0.026 ± 0.009)	(0.021 ± 0.016)	(0.017 ± 0.025)

order of factorial moment q for different experimental data samples (see Tab.3) are presented, but no minimum has been found. There are some hints for existence of minima at $q_c = 4 - 5$ published in [24, 25].

The dependence of values of slopes φ_2 on particle density per unit pseudorapidity ρ has been studied using different primary nuclei. Our preliminary result obtained for interval bin size $\delta\eta \sim 0.1 - 1.25$ (in logarithmic scale) is shown in Fig.17. The similar results for chamber emulsion data in pseudorapidity interval $0.09 < \delta\eta < 2.$ have been published in [26].

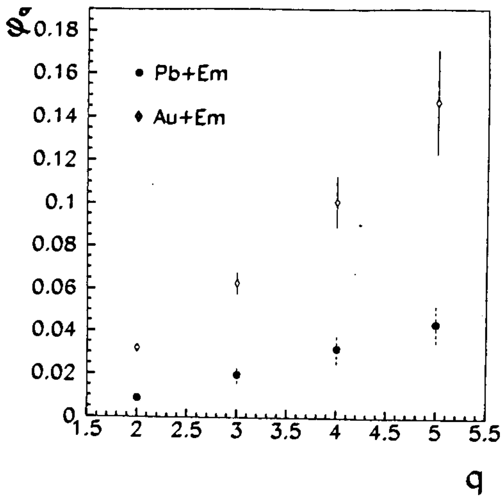

Figure 13: The φ_q dependence on q ($q = 2 - 5$) for $Pb + Em$ and $Au + Em$ central interactions with $N_s > 350$ and $N_s > 100$, respectively.

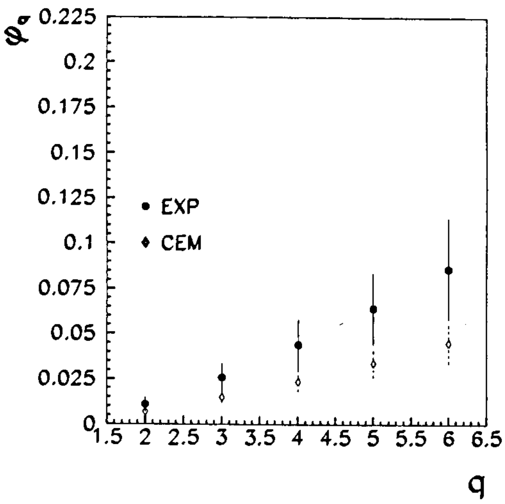

Figure 14: The φ_q on q for Pb experimental and CEM data at 158 A GeV/c $N_s > 1000$.

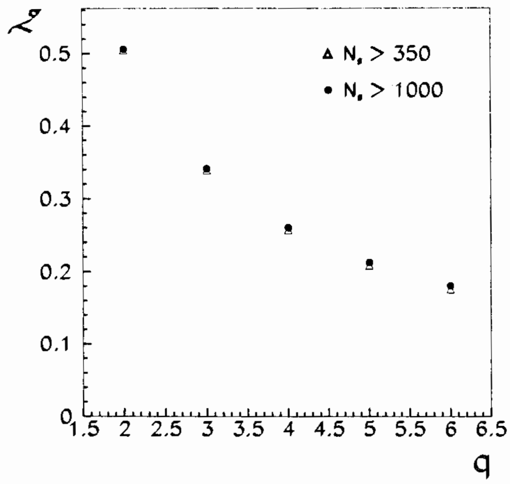

Figure 15: The dependence of intermittency parameter (λ_q) on q ($q = 2 - 6$) for Pb interactions with $N_s > 350$ and $N_s > 1000$.

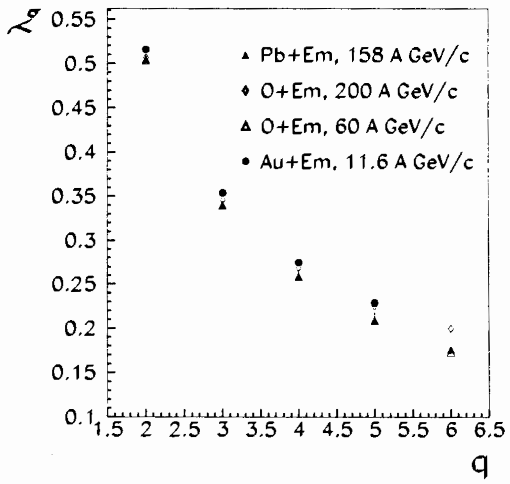

Figure 16: The dependence of intermittency parameter (λ_q) on q ($q = 2{-}6$) for different primary nuclei.

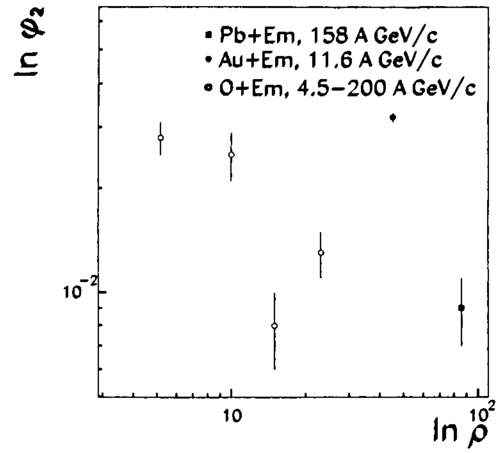

Figure 17: The dependence of $ln\varphi_2$ on $ln\rho$, ρ is particle density per unit pseudorapidity.

Central interactions of ^{208}Pb nuclei at 158 A GeV/ c in emulsion been analysed using the horizontal factorial moment method. The scaled factorial moments F_q of the order q have been studied as a function of the pseudorapidity bin size, parametrized in the form $ln\langle F_q\rangle = \alpha_q + \varphi_q.lnM$. An evidence for the presence of intermittent behaviour has been shown. The dependences of parameters α_q and φ_q on the order of factorial moments q have been studied. The comparison for different primary nuclei (^{16}O at momenta of 4.5 - 200 A GeV/c and ^{197}Au at 11.6 A GeV/c) has been done. The dependences of intermittency parameter λ_q on q for different primary nuclei have been studied, but no clear minimum has been found.

4 Conclusion

Emission of relativistic particles produced in central ^{208}Pb induced nuclear collisions at 158 A GeV/c has been studied using three different approaches - scaled factorial moments, wavelets and parameter S_2.

- An evidence for nonstatistical fluctuations has been shown using horizontal factorial moment method in pseudorapidity phase space. The comparative study has been done for different beam energies and masses and for different centrality selection of Pb events. No clear minimum has been found in the dependences of intermittency parameter λ_q on q.
- In the wavelet analysis some irregularities have been observed mainly in the scale range $a \leq 0.5$ which indicate the preferred pseudorapidities of groups of emitted particles.
- When the azimuthal structures of produced particles have been investigated using the S_2-method the additional groups of produced particles in the region of the ring-like structures ($S_2/\langle S_2\rangle < 1$) and the jet-like structures ($S_2/\langle S_2\rangle > 1$) in comparison to the FRITIOF model calculations have been observed.

Acknowledgments

Financial support from the Scientific Agency of the Ministry of Education of Slovak Republic and the Slovak Academy of Sciences (Grant No.1/0080/08) is cordially acknowledged.

References

[1] E. Stenlund et al., Nucl. Phys. **A498**, 1989, p.541c.
[2] L. Van Hove , Z. Phys. **C21**, 1984, p.93.
[3] M.I. Adamovich et al., J. Phys. G: Nucl.Part. Phys. **19**, 1993, p.2035.
[4] V. Uzhinsky et al., Preprint JINR, P1-2001-119, Dubna, 2001.
[5] M. Blažek , Int. Journal of Mod. Phys. **A12**, 1997, p.839.
[6] A.S. Gaitinov et al., Proc. Of the XVII Meeting of the EMU01 Collaboration, Dubna, Russia, May 18-20, 1999, Dubna, 2000, p.143.
[7] M.I. Adamovich et al., Eur. Phys. J.**A5**, 1999, p.429.
[8] B. Nilsson-Almquist, E. Stenlund, Comp. Phys. Com. **43**, 1987, p.387.
[9] V. Uzhinsky, Preprint JINR, E2-96-192, Dubna, 1996.
[10] G.Musulmanbekov, Preprint JINR, P-2-99-59, Dubna,1999, also in: AIP, 1995, 428.1
[11] S. Vokál S. et al., Physics of Atomic Nuclei **71**, 2008, p.1395.
[12] G.I. Orlova, A. Kravčáková, S. Vokál, V.V. Prosin, Proc. of the Hadron Structure 2002, Herľany, Sept. 22-27, 2002, Košice, 2003, p.155.
[13] S. Vokál et al., Preprint JINR, E1-2004-173, Dubna, 2004.
[14] S. Vokál, S. Lehocká, G.I. Orlova, Preprint JINR, E1-2005-66, Dubna, 2005.
[15] J. Fedorišin, S. Vokál, Preprint JINR, E1-2007-4, Dubna, 2007.
[16] J. Fedorišin, S. Vokál, Preprint JINR, E1-2007-66, Dubna, 2007.
[17] A. Bialas, R. Peschanski, Nucl.Phys. B **273**,1986, 703.
[18] A. Bialas, R. Peschanski R, Nucl.Phys. B **308**,1988, 857.
[19] M.I. Adamovich et al., APH N.S., Heavy Ion Physics **13**, 2001, 213.
[20] J. Vrláková, S.Vokál, A.Dirner, Acta Physica Slovaca **56**, 2006, 83.
[21] B.Wosiek, Acta Physica Slovaca **46**, 1996, 531.
[22] J. Vrláková, S.Vokál, Zborník príspevkov 14. konf. slov. a českých fyzikov, Plzeň, 9.-12.9. 2002, ZU Plzeň, ČR, 2002, p.178
[23] A. Bialas, K. Zalewski, Phys. Lett. **B238**, 1990, 413.
[24] D. Ghosh et al., Europhys. Lett. **41**, 1998, 371.
[25] E. K. Sarkisyan et al., Phys. Lett. **B347**, 1995, 439.
[26] R. J. Wilkes et al.(EMU01 col.), Nucl.Phys. A **544**,1992, 153c.

Study of hadron production in nucleus-nucleus collisions in NA49 and project NA61 at CERN SPS

G. L. Melkumov[1]
for NA61 and NA49 Collaborations

Abstract

The present report addresses the current status and future plans of the NA49 experiment with special emphasis on the JINR activity regarding the analysis of the vast data samples accumulated in the experiment as well as the continuation of the JINR group to participate in a new measurements within the NA61 project by use of the upgraded NA49 apparatus.

1 Introduction

The primary purpose of heavy ion programme at the CERN SPS is the search for evidence of a transient deconfined state of strongly interacting matter during the early stage of nucleus–nucleus collisions The NA49 experiment Fig. 1 [1] was designed for investigation of hadron production in the most violent Pb+Pb interactions at the CERN SPS. With its large acceptance tracking in TPCs and particle identification by means of dE/dx and TOF measurements. It is in addition an excellent detector for the study of nucleon-nucleus collisions of controlled centrality and of nucleon-nucleon reactions in order to elucidate the particle production mechanism in elementary collisions and for studying the effects of cold nuclear matter on particle production yields.

The JINR has actively been taking part in the NA49 project for many years. Its primary contribution to the experiment is the multichannel time-of-flight (TOF) detector designed and built at Dubna. The 2.5 m^2 TOF wall containing 900 scintillator pixels situated behind the large TPCs and operates with the overall time resolution of 60-70 ps. Such a high resolution provides a powerful identification of the charged particles and the produced light nuclei in the momentum range from 3 to 14 GeV/c. The latter became the basic motivation for Dubna group to be involved not only in maintenance of the TOF detector and calibration for a global production chain, but also in the data processing and the physics analysis. Their primary engagement is the study of the identified charged particle production, which play an important role for understanding of the dynamics of relativistic heavy ion collisions and the evolution of the systems created

[1]E-mail:Georgui.Melkoumov@cern.ch

in these reactions. The results of the data analysis prompty related to the principal contribution of the Dubna team as well as a plans of the future activity to follow.

A unique data have been recorded in Pb+Pb collisions at $20A$, $30A$, $40A$, $80A$ and $158A$ GeV beam energies by this bridging the gap in the data between AGS and SPS top energies. The only NA49 data for C+C and Si+Si interactions at 158 and 40 AGeV have also been measured using the fragmentation beams produced by the primary Pb projectiles. Moreover, extensive data sets have been taken for nucleon-nucleon (p+p, d+p, π+p) and nucleon-nucleus (p+Pb, π+Pb, p+C) reactions at 158 and 100 GeV/c. More than 30.000.000 events are recorded.

A comprehensive written status report of the NA49 collaboration on the results obtained from A+A collisions was submitted to the SPSC in 2005 [2]. The results and analysis plans for p+p and p+A reactions were described in [3]. An oral presentation of the main results of NA49, concentrating mainly on the evidence for the onset of deconfinement at low SPS energies, was presented at the open SPSC session on October 3, 2006. The analysis program as outlined in [2] has been successfully pursued leading to numerous physics results and publication. In the last Memorandum to the SPSC of October 2, 2007 [4] the NA49 collaboration confirmed that a vigorous analysis activity is continuing for another 3 years.

Along with this activity the proposal for a new measurements at the CERN SPS by use of the upgraded NA49 apparatus has been developed. Firstly, it was the Expression of Interest [5] and the Letter of Intent [6] submitted to the SPSC in November 2003 and January 2006, respectivelly. The proposal [7] supplemented with a number of Addendums upon the requests by SPSC was approved in June 2007 under the name of the experiment NA61 [8]. It is a fixed-target experiment at the CERN SPS accelerator based on the upgraded setup of the NA49 apparatus [9]. In particular, the most expensive components are inherited from the NA49. These are the two superconducting magnets, the four large volume TPCs and the two TOF walls.

The proposed physics program of the NA61 mainly concerns the following objectives:

- Measurements of hadron production in nucleus-nucleus collisions, in particular fluctuations and long range correlations, to identify the properties of the onset of deconfinement and search for a possible evidence for the critical point of strongly interacting matter,

- Measurements of hadron production in proton-proton and proton-nucleus interactions needen as a reference datafor better understanding of nucleus-nucleus reactions; in particular correlations, fluctuations and high transverse momenta will be focus of this study,

- Measurements of hadron production production in hadron-nucleus interactions needed for neutrino (T2K) and cosmic-ray (Pierre Auger Observatory and KASCADE) experiments.

At present, the participants of this experiment, the NA61 Collaboration, are 114 physicists from 24 institutes and 14 countries.

The first pilot run was already performed during September-October 2007[10].

2 Review of physics results

The data taking for $20A$, $30A$, $40A$, $80A$ and $158A$ GeV in Pb+Pb collision was carried out by NA49 for completion of the energy scan program at the CERN SPS. A numerous important results was obtained by the NA49 collaboration in the study of the energy dependence of particle production as well as in the dependence on the collision centrality. Summary of the physics results prompty related to the principal contribution of the JINR team since 2005 as well as the plans for the future activity are given in the following sections. For the first time, the transverse spectra for $\pi^{\pm}$, $K^{\pm}$, p and $\bar{p}$ and light nuclei d, $\bar{d}$, t, and ^{3}He most of them in the energy range

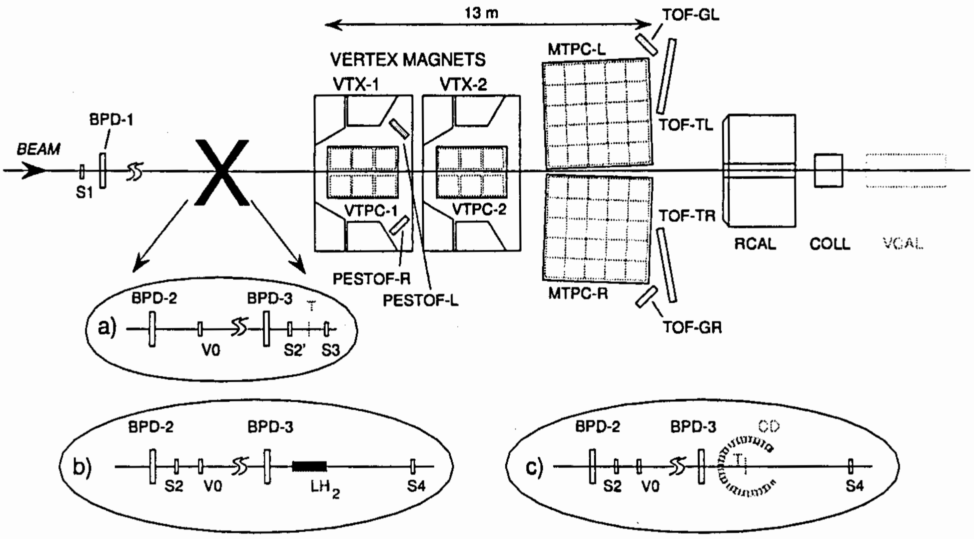

Figure 1: Schematic layout of the NA49 experiment at the CERN SPS showing beam detectors, superconducting dipole magnets, time projection chambers (VTPC, MTPC), time-of-flight arrays (TOF) and calorimeters (RCAL, VCAL). A thin solid target T is used for A+A collisions (a), which is surrounded by a detector of slow protons (CD) for p+A collisions (c). A liquid H_2 target is employed for p+p collisions (b)

$20A$-$158A$ GeV were obtained and employed for the physics analysis.

3 Proton and antiproton production

3.1 Baryon stopping

It is important in relativistic heavy ion experiments to understand nuclear stopping in details since it is a requisite for the formation of hot and dense nuclear matter. Stopping is a necessary ingradient in our overall understanding of the reaction and the expectations to form and study the properties of QGP.

- New results on rapidity spectra of protons and antiprotons in central Pb+Pb reactions at $20A$ - $80A$ GeV in combination with previously published results [12, 15] allow to study the energy evolution of stopping. Based on the measured rapidity spectra for p, $\bar{p}$ Λ, $\bar{\Lambda}$, $\Xi^-$and $\bar{\Xi}^+$, all corrected for feed down from weak decays, the net-baryon distributions $\mathrm{d}N_{(\mathrm{B}-\bar{\mathrm{B}})}/\mathrm{d}y$ are constructed:

$$B - \bar{B} = S_n \cdot (p - \bar{p}) + S_{\Sigma^\pm} \cdot (\Lambda - \bar{\Lambda}) + S_{\Xi^0} \cdot (\Xi^- - \bar{\Xi}^+). \qquad (1)$$

The contribution of unmeasured baryons (n, $\Sigma^\pm$, Ξ^0) was estimated using a scaling factors S_x obtained from statistical hadron gas model fits [16]. The results are plotted in Fig. 2 (left). A clear evolution is seen from a peak to a dip structure in the SPS energy range.

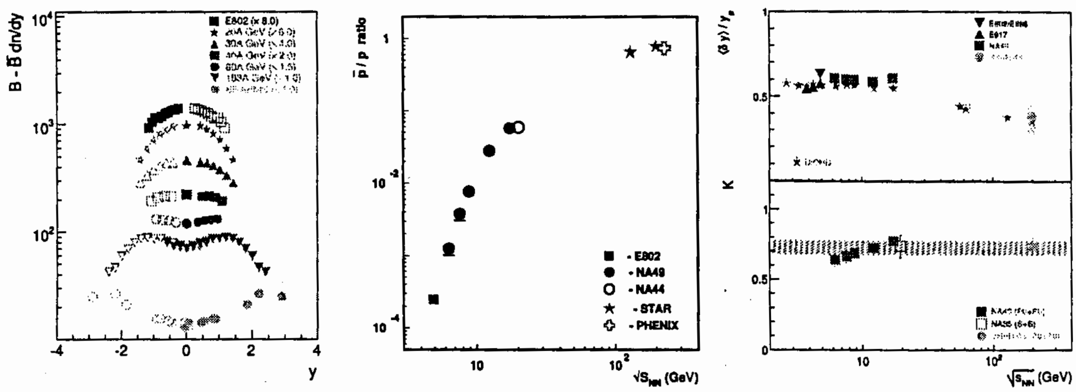

Figure 2: (left) Net baryon rapidity distributions at AGS[11], SPS[12] and RHIC[13] energies in central Pb+Pb or Au+Au collisions. Open data points were obtained by reflection. (center) $\bar{p}/p$ ratio at midrapidity as a function of $\sqrt{s_{NN}}$ in central Pb+Pb (Au+Au) collisions reviwed in [15]. (right top) Relative rapidity shifts of projectile nucleons extracted from net baryon distributions compared to results (stars) from the UrQMD model calculations [14]. (right bottom) Dependence of the inelasticity factor K on $\sqrt{s_{NN}}$.

- Another measure promptly related to the stopping power is the $\bar{p}/p$ ratio and its dependence on the energy and centrality of the interactions. Fig. 2 (center) displays the midrapidity $\bar{p}/p$ ratio for central collisions as a function of energy at the AGS, SPS and RHIC early reviewed in [15]. The ratio rises steeply within the SPS energy range by nearly two orders of magnitude. The figure illustrates how the collisions evolve from producing a net baryon-rich system at the AGS through the SPS energy range to an almost net baryon-free midrapidity region at the RHIC.

- The averaged rapidity shift of projectile nucleons $\langle \delta y \rangle$, which is commonly used to quantify stopping in $A - A$ collisins, can be derived from:

$$\langle \delta y \rangle = y_{proj} - \frac{2}{N_{part}} \int_0^{y_{proj}} y \frac{dN_{B-\bar{B}}}{dy} dy, \tag{2}$$

  where y_{proj} is the projectile rapidity and $N_{\rm part}$ is the number of participating nucleons. As seen from Fig. 2 (upper right), $\langle \delta y \rangle$ is approximately 0.6 at AGS and SPS and then slowly decreases in the RHIC energy range. This behaviour is well reproduced by the UrQMD model calculations [14].

- The partial stopping of incident nucleons observed in A-A collisions provides the energy for particle production, which can be estimated in terms of the inelasticity. Using $\mathrm{d}N_{(\mathrm{B}-\bar{\mathrm{B}})}/\mathrm{d}y$ and the measured $\langle m_{\rm t} \rangle$ the inelastic energy per net-baryon:

$$E_{\rm inel} = \frac{\sqrt{s_{\rm NN}}}{2} - \frac{1}{N_{(\mathrm{B}-\bar{\mathrm{B}})}} \int_{-y_{proj}}^{y_{proj}} \langle m_{\rm t} \rangle \frac{\mathrm{d}N_{(\mathrm{B}-\bar{\mathrm{B}})}}{\mathrm{d}y} \cosh y \, \mathrm{d}y \tag{3}$$

  and the inelasticity factor $K = 2\, E_{\rm inel}/(\sqrt{s_{\rm NN}} - 2m_{\rm p})$ can be calculated. Fig. 2 (right bottom) indicates that K is approximatly energy independent and the average energy loss of projectiles amounts to about 70 - 80 % at all energies.

3.2 Spectra and yields of $\bar{p}$ and p and the $\bar{\Lambda}/\bar{p}$ ratio

Abundances of antibaryons as well as a copious strangeness production in relativistics heavy ion collisions have been suggested as a signatures for exotic states and possible phase transition to a new state of matter, called the quark-gluon plasma (QGP), in which the quarks and gluons are deconfined. The enhancement could be created due to gluon fragmentation (fusion) into quark-antiquark ($q\bar{q}$) pairs, which have significantly lower threshold relative to that of the baryon-antibaryon pair production. However, in the baryon reach colliding systems, there can be significant annihilation losses before antibaryons escape the collision zone.

The midrapidity transverse mass distributions for antiprotons and protons were measured in Pb+Pb collisions at $20A$, $30A$, $40A$, $80A$ and $158A$ GeV. The yields were obtained by integration of these distributions. In addition they are compared to the relevant data for antilambda production. The main observations from analysis of the data and their interpretation are briefly explained below.

- The shapes of m_t-spectra show a strong dependence on collision centrality. In central collisions and at small m_t the spectra exhibit a pronounced deviation from the exponential Boltzmann shape. The data reveal the shoulder-arm structure characteristic of prominent radial collective expansion flow.
- The $\bar{p}$ and p transverse mass spectra reveal within errors quite similar shapes (Fig. 3 left) in spite of the fact that at these energies a significant fraction of protons carry baryon number from the incoming nuclei, while antiprotons are predominantly pair produced. This observation may indicate similar expansion dynamics for both particles comprised of thermal motion and collective radial flow that determine the transverse spectra of particles at the late stage of the expansion.

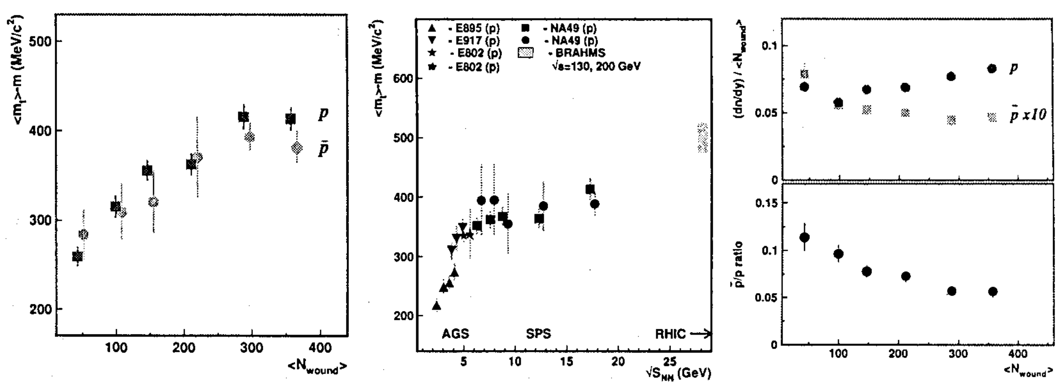

Figure 3: (left) Mean transverse mass $\langle m_t \rangle - m$ for $\bar{p}$ and p as a function of N_{wound} at midrapidity in $158A$ GeV Pb+Pb collisions. (center) Mean transverse mass $\langle m_t \rangle - m$ for $\bar{p}$ and p at midrapidity as a function of the c.m. energy per nucleon pair $\sqrt{s_{NN}}$ in central Pb+Pb collisions at SPS energies (NA49) together with data for central Au+Au collisions from the AGS [18, 19, 20] and RHIC [21]. Yield dn/dy of $\bar{p}$ and p per N_{wound} (right top) and the $\bar{p}/p$ ratio (right bottom) plotted as a function of N_{wound} at midrapidity in $158A$ GeV Pb+Pb collisions. Errors are statistical.

- In contrast to the strong centrality dependence, the shape of the measured transverse mass spectra does not change noticeably in central Pb+Pb collisions within SPS energy range (Fig. 3 center). A similar non trivial energy dependence was also observed by NA49 for kaon and pion production [17] which was considered a possible manifestation of the coexistence of partonic and hadronic phases or more generally a very soft equation of state in the SPS energy regime [22, 23, 24]. The behavior of the m_t spectra may thus be taken to support the indication for an onset of deconfinement in the early stage of the collisions at low SPS energies as obtained from the energy dependence of pion and kaon yields [25].

- The yield of p normalized to the number of wounded nucleons increases with centrality while this quantity for $\bar{p}$ exhibits a decrease (Fig. 3 upper right). The former effect can be understood as the result of an increase of baryon stopping with collision centrality which leads to contraction of the proton rapidity distribution around midrapidity. The decrease of the yield of $\bar{p}$ per wounded nucleon may point to some contribution from annihilation.

- The different dependence of $\bar{p}$ and p yields on N_{wound} results in significant centrality dependence of the $\bar{p}/p$ ratio as shown in the bottom panel of Fig. 3 right. This ratio steadily decreases with centrality by a factor of about two within the considered centrality range. A similar result was obtained in Au+Au collisions at $11.7A$ GeV [20]. In contrast, the $\bar{p}/p$ ratio measured at RHIC shows very weak variation with centrality at the collision energy $\sqrt{s_{NN}}$=130 GeV [26] and almost no dependence on centrality at $\sqrt{s_{NN}}$=200 GeV [27]. Thus, the net baryon density, which is significant at lower energies, strongly affects the midrapidity p and $\bar{p}$ abundances through baryon stopping and baryon-antibaryon annihilation in central collisions at the AGS and SPS, but not at RHIC energies.

- The $\bar{p}/p$ ratio is found to increase by almost two orders of magnitude in central Pb+Pb collisions at $158A$ GeV as compared to $20A$ GeV beam energy (Fig. 2 center), reflecting the rapid decrease of the net baryon density at midrapidity with collision energy. The ratio rises steeply within the SPS energy range by nearly two orders of magnitude. The data illustrate how the collisions evolve from producing a net baryon-rich system at the AGS through the SPS energy range to an almost net baryon-free midrapidity region at the RHIC.

- In central Pb+Pb collisions the $\bar{\Lambda}/\bar{p}$ ratio shows a steady increase with decreasing beam energy approaching a value of almost 2 at the energies of 20 and 30 A GeV (Fig. 4 left). This confirms earlier evidence for this ratio to significantly exceed unity at AGS energies which remains unexplained by theory, i.e. by the commonly used thermal and hadronic cascade models that, in turn, well reproduce a large number of other particle ratios. Moreover, these observations are considered as an intriguing results because they may point to a strangeness enhancement effect and possible QGP formation. There may be an analogy to the K^+/π^+ maximum also observed [25] in the domain of top AGS to lowest SPS energies.

- The centrality dependence of the midrapidity $\bar{\Lambda}/\bar{p}$ ratio has been suggested to be particulary sensitive to the interplay between production and subsequent absorption. It is shown that the $\bar{\Lambda}/\bar{p}$ ratio increases from peripheral to central collisions by about a factor 2 (Fig. 4 right). A much stronger increase with centrality has been observed at the AGS

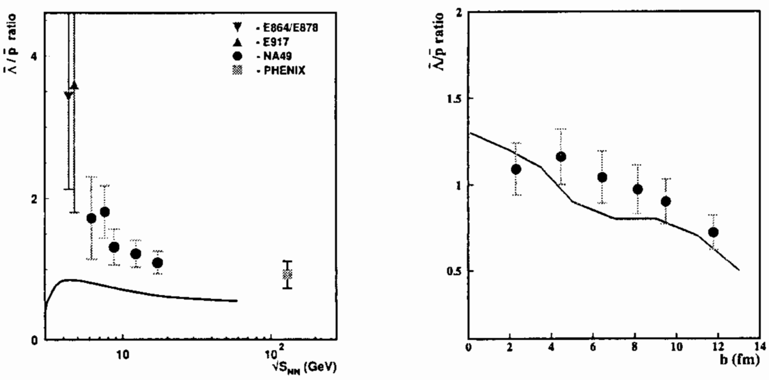

Figure 4: (left) $\bar{\Lambda}/\bar{p}$ ratio at midrapidity as a function of the c.m. energy per nucleon pair $\sqrt{s_{NN}}$ in central Pb+Pb collisions at SPS energies (NA49) together with the data from AGS [28, 29] and RHIC [30]. Total error bars are drawn. The curve shows the prediction of the statistical hadron gas model [31]. (right) Impact parameter dependence of the $\bar{\Lambda}/\bar{p}$ ratio at midrapidity in central Pb+Pb collisions at 158A GeV. Errors are statistical. Curve presents the result of hadronic cascade (UrQMD) calculation [32].

[28, 29]. Interestingly, the obtained results at 158A GeV are in agreement with a UrQMD model calculation [32] which incorporates antibaryon absorption.

4 Production of light nuclei and antinuclei

There is a notion that abandances of light nuclei probe the latest stage of the evolution of a systems created in relativistic heavy ion collision. The light nuclei production enables the study of several topics, including the mechanism of composite particle production, freeze-out temperature, size of the interaction region and enrtopy of the system.

Recently NA49 has measured the energy dependence of deuteron and tritons production at midrapidity, and ^3He nuclei in a wide rapidity range. A rare process of the antideuteron production at midrapidity in central Pb+Pb collisions at 158A GeV beam energy was also studied. It is of significant interest because the initial colliding system contains no antibaryons therefore their yields and spectra are determined solely by the post collision dynamics. Additionally, the produced antideuterons have no contribution from spectator fragments.

In these investigations the identification of the produced nuclei is of primary importance. The Fig. 5 (left) demonstrates the clean identification of d, t and ^3He from measurements of the energy loss dE/dx in the TPC gas and mass squared M^2 computed from momentum and time of flight measurements in TOF detector. As shown in Fig. 5 (center), for doubly charged ^3He nuclei the dE/dx measerement was sufficient to uniquely and cleanly determine its identity thus providing a large coverage in rapidity for measuring ^3He in TPCs. The M^2 distribution after all identification cuts is shown on Fig. 5 (right). Antideuterons are clearly visible at about $M^2 \approx 3.5$ GeV$^2/c^4$.

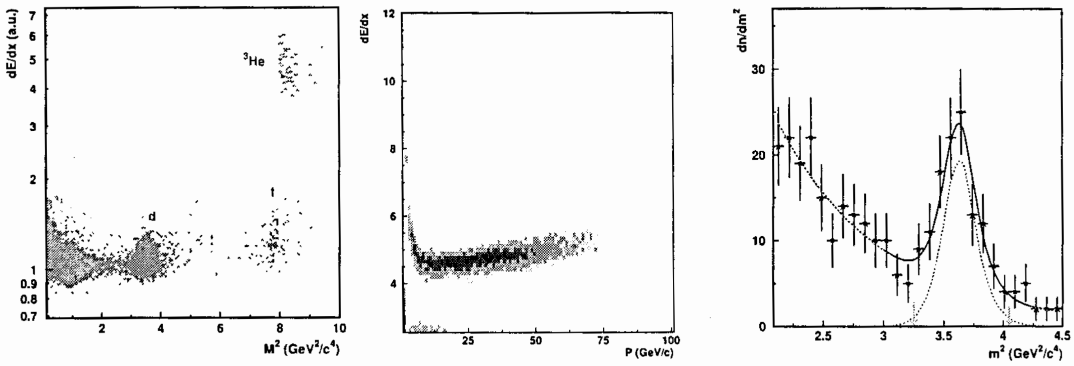

Figure 5: (left) Energy loss dE/dx in TPC versus mass squared M^2 from measurements in TOF for ^3He, t, and d produced in central Pb+Pb collisions. (center) Momentum dependence of the ^3He energy loss dE/dx. (right) Mass squared distribution for $\bar{d}$ after dE/dx and TOF identication cuts.

4.1 ^3He and triton nuclei

New results on triton and ^3He production in central Pb+Pb collisions at $20A$ - $80A$ GeV are shown in Fig. 6.

- Rapidity distributions dn/dy of the ^3He yield, displayed in the left panel of Fig. 6, were obtained by integration of the m_t distributions in small bins of rapidity. One sees from the figure that the dn/dy distributions have a concave shape at all investigated energies. This is in constrast to the case of protons, where the shape of rapidity distributions is rather convex and strongly energy dependent (see Fig. 2 left).

- The total yields of ^3He have been estimated by fitting and integrating a parabolic parameterisation up to beam rapidity. These values shown in Fig. 6 (center) agree very well with a prediction of a statistical hadron gas model [16].

- It is an overlooked aspect of the thermal model to compute the yields of composite particles reproduced with the chemical freeze-out parameters used to describe baryon and meson ratios [33]. In these investigations, an observed exponential decrease of composite particles implies a penalty factor for each additional nucleon. In the relevant Boltzmann approximation this penalty factor, $R_p \approx exp\frac{m \pm \mu_b}{T}$, where m is a nucleon mass, can be easily derived. Using the chemical freeze-out parameters μ_b and T appropriate for SPS energies obtained from the statistical model fit [34] to the NA49 data, the penalty factors were calculated as well as the yields of ^3He. Fig. 6 (right) illustrates the results for the penalty factor R_p as determined from $dn_A/dy = const/R_p^{A-1}$ for AGS and SPS energies using the yields of p, d, and ^3He. The values increase linearly with $\sqrt{s_{NN}}$ and are largest for $p_t = 0$ yields. For p_t-integrated midrapidity yields dn/dy the penalty factors decrease because of transverse flow. One finds their values to be in surprising agreement with the statistical hadron gas model predictions [16]. As was mentioned above this agreement also holds for total ^3He yields. Both these observations might imply that ^3He is already formed at the chemical freeze-out, which might be in contradiction to the assumption of cluster formation via coalescence at possibly lower thermal freeze-out temperatures.

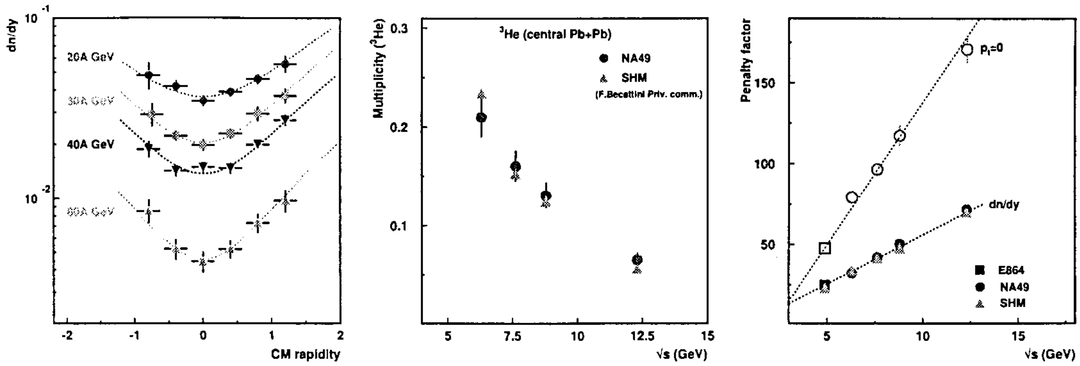

Figure 6: (left) Rapidity distributions of ^3He. The dashed lines are fits with a parabola used to extract the total multiplicities. (center) Total multiplicity of ^3He in central Pb+Pb collisions as a function of the c.m. energy per nucleon pair $\sqrt{s_{NN}}$ (solid points). The triangles represent predictions of a statistical hadron gas model [16]. (right) Penalty factor derived from the midrapidity ^3He, d and p production yields in central Pb+Pb collisions (dots) for p_t=0 and p_t-integrated yields compared to predictions of the statistical hadron gas model [16] (triangles).

4.2 Coalescence formation of ^3He, d and $\bar{d}$ nuclei

Using a general prescription of coalescence model which relates the invariant yield of light nuclei with mass A to the Ath power of the proton yield [35], assuming the neuteron and proton distributions are identical:

$$E_A \frac{d^3N_A}{dp_A^3} = B_A \left(E_p \frac{d^3N_p}{dp_p^3} \right)^A, p_A = Ap_p, \tag{4}$$

the coalescence parameters B_2 and B_3 were extracted for deuterons and ^3He, respectively. Their values measured by NA49 at SPS energies are shown in Fig. 7 (left) and compared to results from lower and higher energies. One observes a gradual decrease with increasing beam energy which would suggest an increasing effective coalescence volume in the coalescence model scenario.

Analysis of antideuteron production was provided using 2.6 million of the 23% most central events recorded in 158A GeV Pb+Pb collisions in rapidity range $2.0 < y < 2.5$. Further off-line selection of the data for two classes of events corresponding to (0-10)% and (10-23)% centralities was used in analysis.

The coalescence parameter for antideuterons $B_2(\bar{d})$ for the 23% most central Pb+Pb events as a function of p_t is plotted in Fig. 7 (center). As seen from the data the $B_2(\bar{d})$ is almost independent on p_t and its average value is calculated $B_2(\bar{d}) = (9.1 \pm 0.9) \cdot 10^{-4}$ GeV^2/c^3. The coalescence parameters for $\bar{d}$ and d as a function of the number of wounded nucleons for two selected centrality classes are shown in Fig. 7 (right). Being equal within errors B_2 for both $\bar{d}$ and d increases with centrality of 158A GeV Pb+Pb collisions. This trend might be attributed to the developed radial flow and strong transverse expansion of the system created in relativistic heavy ion rections.

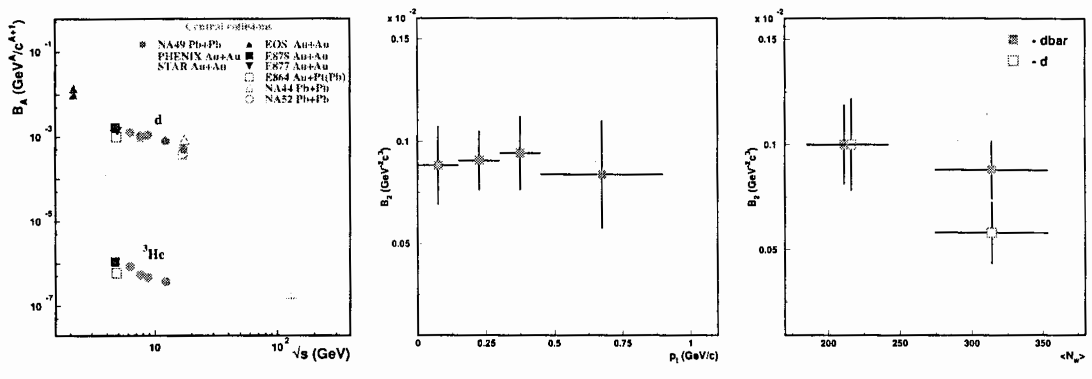

Figure 7: (left) Energy dependence of coalescence parameters B_2 and B_3 for d and ^3He, respectively. Coalescence parameter B_2 for antideuterons as a function of p_t (center) and the number of wounded nucleons $\langle N_w \rangle$ (right).

5 Kaon and pion production

The energy scan program program at the CERN SPS initiated by the NA49 was motivated by the prediction of [36] that the onset of deconfinement should lead to a steeping of the increase of the pion yield with collision energy and to a sharp maximum in the energy dependence of the strangeness to pion ratio. The analysis of the data at $40A$, $80A$ and $158A$ GeV was published early in [25] and the results confirmed the predictions of [36]. This finding motivated an extension of the energy scan to the lower SPS energies of $30A$ and $20A$ GeV. The analysis at these energies was recently complited. It is combined with those from [25] and compared to available model calculations, together with lower and higher energy data from AGS and RHIC. The final results [37] has been published this year. The TOF analysis of the K and π transverse spectra at midrapidy accomplished by the JINR group became essential contribution to this study. The primary results of this investigations could briefly be summarized as follows:

- A close approximation of the total strangeness to pion production ratio calculated from measured yields via the observable $E_S = (\langle K+\bar{K}\rangle + \langle\Lambda\rangle)/\langle\pi\rangle$ is plotted in Fig. 8 (left) as a function of collision energy. As expected, it shows the same sharp peak followed by a plateau as the $\langle K^+\rangle/\langle\pi^+\rangle$ ratio, which is not seen in p+p collisions and not reproduced by hadronic models. On the other hand this feature can be understood in a reaction scenario with the onset of deconfinement around $30A$ GeV as proposed in the statistical model of the early stage (SMES [36], dash-dotted curve in Fig. 8 (left)). E_S, a measure of the ratio of strange to non-strange degrees of freedom in the model, drops to the value expected in the QGP.

- At the same energy the rate of increase of the number of produced pions per participating nucleon (a measure of the entropy per baryon in the model) was predicted to increase. As seen in Fig. 8 (center), this seems to be confirmed by the measurements for collisions of heavy nuclei, while there is no change in energy dependence for p+p reactions.

- The transverse mass spectrum of kaons at midrapidity is well described by an exponential function $e^{-m_T/T}$. As shown in Fig. 8 (right) for K^+ the effective temperature parameter

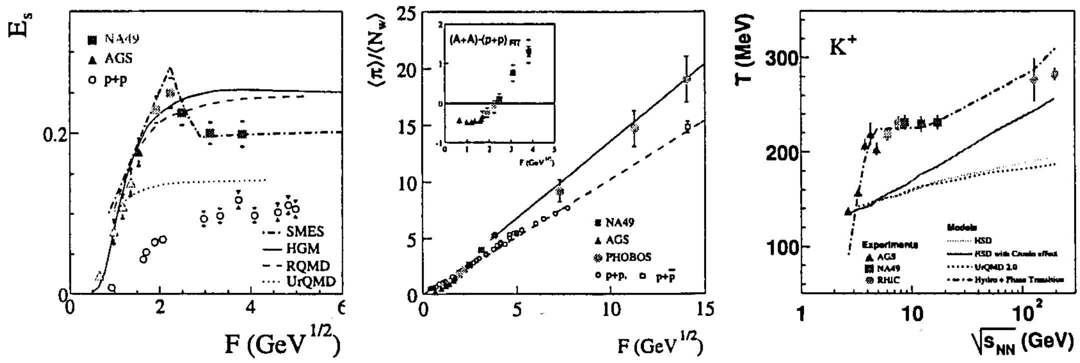

Figure 8: (left) Relative strangeness yields $\mathrm{E}_S = (\langle \mathrm{K} + \bar{\mathrm{K}}\rangle + \langle\Lambda\rangle)/\langle\pi$ rangle versus Fermi energy variable F$\approx$ $s_{NN}^{0.25}$. (center) Pion yield per participating nucleon $\langle\pi\rangle/\langle \mathrm{N}_W\rangle$ versus F. (right) Energy dependence of the effective temperature parameter T of K^+ transverse mass spectra measured at midrapidity. Results from p+p collisions are shown as open circles, model predictions for Pb+Pb collisions as curves.

T rises steeply at low energies, stays at an approximately constant value through the SPS energy range and ends up slighly higher at RHIC energy. Similar behavior is seen for the transverse spectra of K^- and pions (not shown), but is not observed in p+p collisions. These features have been attributed [38] to the constant pressure and temperature when a mixed phase is present in the early stage of the reaction. In fact, a hydrodynamic calculation [39] modeling both the deconfined and the hadronic phases can provide a quantitative description (dash-dotted curve in Fig. 8 (right)).

6 Forthcoming data analysis

In the last Memorandum to the SPS committee "Status and further Analysis Plans of the NA49 Collaboration", CERN-SPSC-2007-026 (October 2, 2007) [4] the NA49 collaboration confirmed that a vigorous analysis activity is continuing for another 3 years with numerous publications either in the pipeline or planned. To facilitate this work collaboration request support from the CERN IT division at the present level (25 KSI2000 units in lxbatch). These resources are required for the simulation work connected with determining corrections during the physics analysis. This work has to use raw data which are stored on the CASTOR system.

The JINR group also firmly intents to proceed the data analysis employing an experience accumulated for many years. A number of significant analysis objectives has to be studied.

First of all, the final data from the analysis of light nucleus and antinucleus production has to be obtained and the physics results has to be submitted for for publication.

However, the most important point regarding the future analysis is that the vast data sets for p+p, p+Pb and central C+C and Si+Si interactions at 158 A GeV accumulated by the NA49 collaboration are still waiting for the TOF analysis for physics. The data for the TOF identified hadrons in above reactions at midrapidity will be obtained and analysed together with available data for central Pb+Pb collision in order to understand the role of the volume of strongly interacting matter in high energy nucleus-nucleus collisions. The following observations for strangeness production (relative to pions) illustrate importance of these studies.

The most recent measurements of particle production in relativistic nucleus-nucleus collisions focused on heavy reaction partners because of the expectation that the transition to a deconfined state of strongly interactiong matter is more likely to occure in larger collision systems. However, earlier experiments with lighter beams had demonstrated that already in S+S collisions relative strangeness production is significantly enhanced compared to p+p collisions and, as found later, close to the situationn in Pb+Pb.

Another observation is that the data obtained for near-central symmetric nucleus-nucleus collisions with increasing number of participating nucleons show a steep rise of the relative strangeness content in the produced hadrons reaching a saturation value at around N_{part}=60.

Thus, a systematic study of hadron production and its dependence on the size of the collision systems is of great interest.

7 NA61 physics and data sets

It was early mentioned in the Introduction that the NA61 is a new fix-target experiment at the CERN SPS accelerator based essentially on use of the NA49 detector. The physics programme of NA61 is the systematic measurements of hadron production in proton-proton, proton-nucleus, hadron-nucleus and nucleus-nucleus collisions.

A summary of all data sets planned to be registered by NA61 are given in Table 1 marked by acronyms of physics which motivates them. In the following the physics cases are briefly explained for more clarification.

- Data for T2K. High precision measurements of the differential cross-section (momentum and polar angle) for charged pion and kaon production in p+C interactions at 30, 40 and 50 GeV. These data are needed by the T2K neutrino experiment for a detailed simulation of the initial neutrino flux which is necessary to achieve the required precision on the neutrino oscillation parameters.

- Data for C-R. High precision measurements of the differential cross-section of identified hadrons in p+C interactions at 30, 40, 50 and 400 GeV. These data are needed by the cosmic-ray experiments (KASCADE and Pierre Auger Observatory) in order to reduce uncertainties of hadron production models used in the analysis of data on high energy cosmic-ray reactions. The new results will significantly improve the resolution of cosmic-ray experiments.

- High p_T. Large statistics measurements of hadron production in p+p and p+Pb interactions at 158 GeV needed as reference data for better understanding of hadron spectra at high transverse momenta in nucleus-nucleus reactions. Suppression of hadron yield at high transverse momenta in central heavy ion collisions relative to the p+p and p+A interactions is one of the most important RHIC results. It reflects properties of high energy density matter created in the collisions. The discriminating power of the corresponding results at SPS is poor due to the absence of high statistic measurements in p+p and p+Pb interactions.

- CP&OoD. Measurements of hadron production in nucleus-nucleus collisions in the SPS energy range with the aim to identify the properties of the onset of deconfinement and find evidence for the critical point of strongly interacting matter. For the first time in the history of heavy ion collisions a comprehensive scan in two dimensional parameter space, size of colliding nuclei versus interaction energy, will be performed.

The new data can answer the questions:
- what is the nature of the transition from the anomalous energy dependence measured in central Pb+Pb collisions at SPS energies (interpreted as evidence of the onset of deconfinement), to the smooth dependence suggested by the existing p+p results ? and
- does the critical point of strongly interacting matter exist in nature and, if it does, where is it located ?

- $\overline{\text{CP\&OoD}}$ Measurement of energy dependence of hadron production in p+p and p+Pb interactions at SPS. These results are needed to test alternative explanations of the effects which are, or will be, considered as signals of the onset of deconfinement and the critical point. The alternative interpretations are based on string-hadronic approaches which use as input results from p+p and p+Pb reactions [40, 41] .

Reaction	Energy (A GeV)	Year	Event statistics	Physics
p+C	30	2007	$3 \cdot 10^6$	Data for T2K, C-R
p+C	30, 40, 50	2008	$25 \cdot 10^6$	Data for T2K, C-R
p+ C	400	2008	$5 \cdot 10^6$	Data for C-R
p+p/Pb	158	2008	$55 \cdot 10^6$	High p_T
p+p	158	2010	$60 \cdot 10^6$	High p_T
In+In	10, 20, 30, 40, 80, 158	2009	$36 \cdot 10^6$	CP&OoD
Si+Si	10, 20, 30, 40, 80, 158	2010	$36 \cdot 10^6$	CP&OoD
C+C	10, 20, 30, 40, 80, 158	2011	$36 \cdot 10^6$	CP&OoD
p+p	10, 20, 30, 40, 80, 158	2009	$36 \cdot 10^6$	CP&OoD, $\overline{\text{CP\&OoD}}$
p+Pb	10, 20, 30, 40, 80, 158	2011	$36 \cdot 10^6$	$\overline{\text{CP\&OoD}}$

Table 1: Summary of the data sets to be taken and the physics which motivates them.

The proposed physics program has the potential for an important discovery - the experimental observation of the critical point of strongly interacting matter. Other proposed studies belong to the class of precision measurements.

The critical point is expected to be found by a measurement of a maximum of fluctuations in transverse momentum and multiplicity in the two dimensional plane of system size and collision energy. In the physics of the critical point the relevant parameters are the temperature and the baryo-chemical potential at the freeze-out of strongly interacting matter.

Particle yield ratios in A+A (as well as elementary) collisions are consistent with statistical model predictions from threshold to the highest energies using only 3 parameters: a temperature T, a baryo-chemical potential μ_B and a strangeness suppression parameter γ_s. These parameters characterize the freezeout of particle composition after which only the momentum distributions further evolve via elastic scattering.

The resulting parameters T and μ_B [34] are plotted in the phase diagram of hadronic matter in fig. 9 (left) together with the phase boundary predicted by lattice QCD [42]. One observes

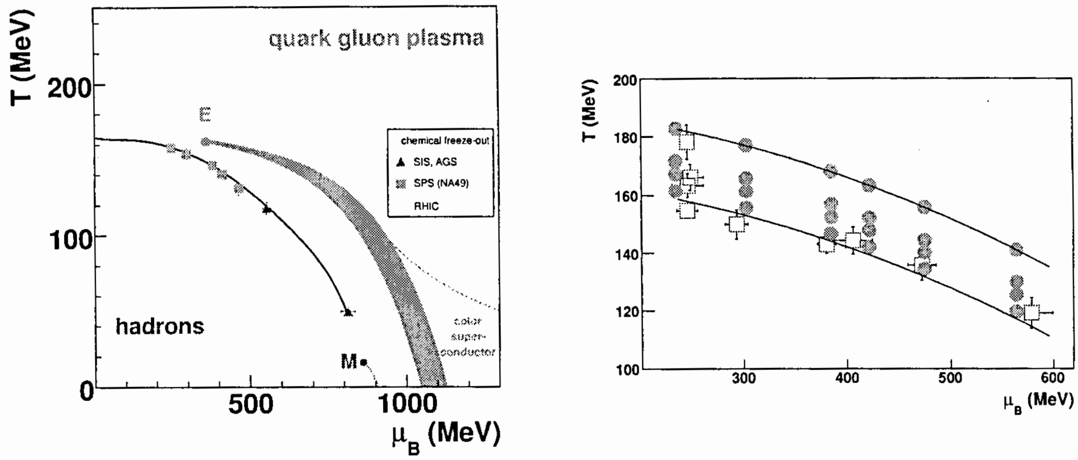

Figure 9: (left) Phase diagram of hadronic matter showing the hadron species freezeout points obtained from statistical model fits [34]. The solid curve represents the empirical freezeout condition 1 GeV/hadron [31]. The grey band is a lattice QCD [42] estimate of the first order phase boundary between QGP and hadrons which ends in a critical point E. (right) Hypothetical positions of the chemical freeze-out points of the reactions (In+In, S+S, C+C and p+p from bottom to top at 158A, 80A, 40A, 30A, 20A and 10A GeV from left to right) to be studied by NA61 in the (temperature)- (baryo-chemical potential) plane are shown by full dots. The open squares show the existing data.

that the freezeout points at SPS energies approach the phase boundary and are closest to the critical point at about 60A GeV.

These parameters vary under changes of the system size and collision energy. The hypothetical positions of the chemical freeze-out points for central In+In, S+S and C+C collisions (full dots from bottom to top) at 158A, 80A, 40A, 30A, 20A and 10A GeV (full dots from left to right) are shown in Fig. 9 (right). These positions are also calculated using a parametrization [16] of the dependence of T and μ_B on collision energy and system size based on the existing data. These data are shown by the open squares. The upper open and the corresponding full dots indicate the upper limit of the temperature obtained for p+p interactions. The lower solid line shows the parametrization for the central Pb+Pb collisions.

8 Critical point search

This chapter summarizes basic elements of the NA61 strategy in a search for the critical point of strongly interacting matter.

- The critical point is expected to lead to an increase of multiplicity and transverse momentum fluctuations [43] provided the freeze-out of the matter takes place in its vicinity ($\Delta T \approx 10$ MeV and $\Delta\mu_B \approx 50$ MeV [44]).

- Freeze-out parameters, the temperature T and baryo-chemical potential μ_B, depend on the collision energy and the size of the colliding nuclei.

- NA61 plans to perform a first comprehensive scan in energy and the system size (see Table 1) which will allow for a detailed study of matter properties as a function of T and

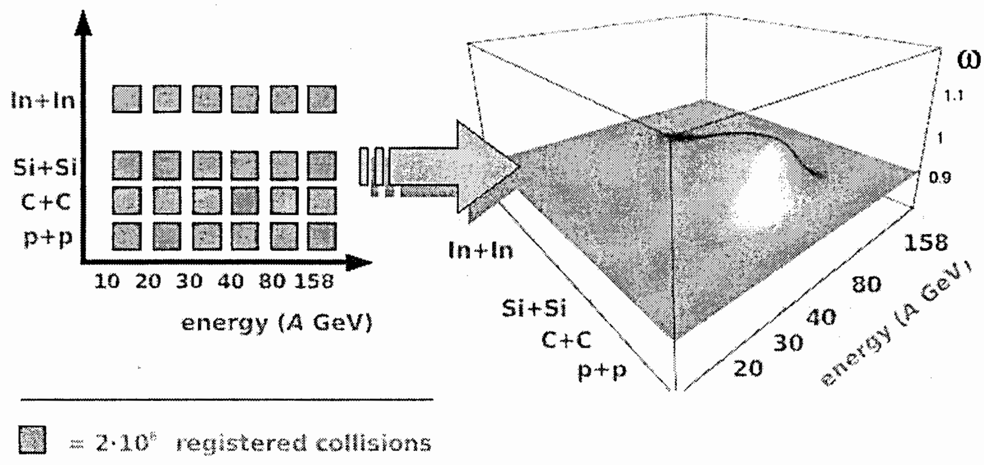

Figure 10: An qualitative illustration of the NA61 strategy in search for the critical point of strongly interacting matter.

μ_B.

- Thus, if the critical point is located in the scanned region of the phase diagram as suggested by the lattice QCD calculations [42], it should be signaled by a "hill" of fluctuations over smoothly varying background in the (collision energy)-(system size) plane. This qualitative prediction (see Fig. 10 for its graphical illustration), if confirmed by the data, will serve as a strong argument [45] for the existence of the critical point and its location in the phase diagram of strongly interacting matter.

- The QCD-inspired calculations [43] predict that the critical point should lead to an increase of the scaled variance of the multiplicity fluctuations by about 10% and an increase of the Φ_{p_T} measure of the transverse momentum fluctuations by about 10 MeV/c. NA61 will measure the scaled variance and Φ_{p_T} in central A+A collisions and p+p interactions with statistical errors smaller than 0.5% and about 0.15 MeV/c, respectively. The corresponding systematic errors will be about 1% and 0.5 MeV/c. The above estimates are performed based on the NA49 results.

- The background fluctuations are influenced by several physics phenomena. In particular these are a variation in the collision geometry, conservation laws, quantum statistics, resonances decays and production of mini-jets. The resulting fluctuations are expected to vary smoothly with collision energy and the system size.

- The pioneering NA49 results on fluctuations show several unexpected effects:
  - non-monotonic centrality and system size dependence of the transverse momentum fluctuations at 158A GeV [46],
  - non-monotonic centrality dependence of the multiplicity fluctuations in Pb+Pb collisions at 158A GeV [47] and
  - an increase of the kaon to pion ratio fluctuations with decreasing collision energy in central collisions [48].

An interpretation of these results and their possible relation to the critical point is unclear. This is because comprehensive precision measurements of fluctuations are missing.

- The proposed NA61 measurements with the upgraded NA49 detector would qualitatively improve the experimental situation and consequently allow for a quantitative understanding of fluctuations and at the same time would give the opportunity to discover the critical point of strongly interacting matter.

9 Complementary projects

The SPS energy range is of particular importance for the study of nucleus-nucleus collisons for two reasons. Firstly, at the low SPS energies anomalies in the energy dependence of hadron production properties are observed. They are attributed to the onset of deconfinement. Secondly, at high SPS energies the critical point of strongly interacting matter can be discovered. This expectation is based on the recent estimate of the location of the critical point from lattice QCD and the freeze-out parameters determined from measured hadron yields using the hadron-resonance gas model.

The heavy ion accelerators RHIC at BNL can potentially run in the SPS energy range. It was decided to start preparation for a low energy RHIC program and the first tests of the accelerator complex were performed. The physics run with Au beams at several energies which correspond to the NA61 setting may be scheduled for 2009. The SPS program proposed here and the suggested new RHIC program are to a large extent complementary. This is due to different collision kinematics and different priorities in data taking.

Starting from 2013-2015 the study of nucleus-nucleus collisions at 10A-40A GeV beam energy range will continued by the CBM experiment at SIS-300 (FAIR, Darmstadt) and by the NICA-MPD experiment in a heavy ion collider at JINR(Dubna), which is being proposed for construction also to cover the low SPS energy range.

References

[1] S. Afanasiev *et al.*, (NA49 Collababoration), *The NA49 large acceptance hadron detector*, Nucl. Instrum. Meth. **A430**, 210 (1999).

[2] C. Alt *et al.*, (NA49 Collaboration), *Main Physics Results and further Analysis Plans of the NA49 Collaboration on Nucleus–Nucleus Collisions at SPS Energies*, CERN-SPSC-2005-041 (November 10, 2005).

[3] V. Cerny *et al.*, (NA49 Collaboration), *Status and Plans of NA49 p+p and p+A Programme*, CERN-SPSC-2005-035 (2005)

[4] C. Alt *et al.*, (NA49 Collaboration), *Status and further Analysis Plans of the NA49 Collaboration*, CERN-SPSC-2007-026 (October 2, 2007) .

[5] J. Bartke *et al.*, *A New Experimental Programme with Nuclei and Proton beams at the CERN SPS*, NA49-future expression of interest, CERN-SPSC-2003-031, SPSC-EOI-001 (2003).

[6] N. Antoniou *et al.*, *Study of Hadron Production in Collisions of Protons and Nuclei at the CERN SPS*, NA49-future letter of intent, CERN-SPSC-2006-001, SPSC-1-I-235 (January 6, 2006).

[7] N. Antoniou *et al.*, *Study of Hadron Production in Hadron-Nucleus and Nucleus-Nucleus Collisions at the CERN SPS*, CERN-SPSC-2006-034 (November 3, 2006) and addendums CERN-SPSC-2007-004 (January 25, 2007) , CERN-SPSC-2007-019 (June 15, 2007).

[8] N. Abgrall *et al.*, (NA61/SHINE Collabotarion), *NA61/SHINE at the CERN SPS*, arXiv:0709.1867v2 [nucl-ex] (14 Sep 2007).

[9] N. Antoniou *et al.*, *Report from tests of the NA49 experimental facility and the NA49-future prototypes*, NA49-future status report, CERN-SPSC-2006-023, SPSC-SR-010 (2006).

[10] N. Abgrall *et al.*, (NA61/SHINE Collabotarion), *Report from the NA61/SHINE pilot run performed in October 2007*, CERN-SPSC-2007-033 (November 16, 2007).

[11] L. Ahle *et al.*, Phys. Rev. C **60** (1999) 064901.

[12] H. Appelshäuser *et al.*, (NA49 Collaboration) Phys. Rev. Lett. **82** (1999) 2471.

[13] I.G. Bearden *et al.*, Phys. Rev. Lett. **93** (2004) 102301.

[14] H. Weber *et al.*, Phys. Lett. B **545** (2002) 285; H. Petersen and M. Bleicher, [nucl-th/0611001] and private communication.

[15] C. Alt *et al.*, (NA49 Collaboration), Phys. Rev. **C73**, 044910 (2006).

[16] F. Becattini, J. Manninen and M. Gazdzicki, Phys. Rev. C **73**, 044905 (2006).

[17] Ch. Blume *et al.*, (NA49 Collaboration), J. Phys. G: Nucl. Part. Phys. **31**, 685 (2005); Ch. Meurer, (NA49 Collaboration), J. Phys. G: Nucl. Part. Phys. **30**, 1325 (2004).

[18] J. L. Klay *et al.*, (E895 Collaboration), Phys. Rev. Lett. **88**, 102301 (2002).

[19] B. B. Back *et al.*, (E917 Collaboration), Phys. Rev. C **66**, 054901 (2002).

[20] I. Ahle *et al.*, (E802 Collaboration), Phys. Rev. Lett. **81**, 2650 (1998).

[21] I. Arsene *et al.*, (BRAHMS Collaboration), Nucl. Phys. **A757**, 1 (2005).

[22] L. van Hove *et al.*, Phys. Lett. B **118**, 138 (1982).

[23] M. Gorenstein *et al.*, Phys. Lett. B **567**, 175 (2003).

[24] B. Mohanty *et al.*, Phys. Rev. C **68**, 021901 (2003).

[25] S. V. Afanasiev *et al.*, (NA49 Collaboration), Phys. Rev. C **66**, 054902 (2002).

[26] K. Adcox *et al.*, (PHENIX Collaboration), Phys. Rev. C **69**, 024904 (2004).

[27] S. S. Adler *et al.*, (PHENIX Collaboration), Phys. Rev. C **69**, 034909 (2004).

[28] B. B. Back *et al.*, (E917 Collaboration), Phys. Rev. Lett. **87**, 242301 (2001).

[29] T. A. Armstrong *et al.*, (E864 Collaboration), Phys. Rev. C **59**, 2699 (1999); T.A.Armstrong *et al.*, (E864 Collaboration), Phys. Rev. Lett. **79**, 3351 (1997); D. Beavis *et al.*, (E878 Collaboration), Phys. Rev. Lett. **75**, 3633 (1995).

[30] K. Adcox *et al.*, (PHENIX Collaboration), Phys. Rev. Lett. **89**, 092302 (2002).

[31] J. Cleymans and K. Redlich, Phys. Rev. Lett. **81** 5284 (1998).

[32] M. Bleicher *et al.*, Phys. Rev. C **59**, 1844 (1999); S. A. Bass *et al.*, Prog. Part. Nucl. Phys **41**, 225 (1998); X. Zhu, UrQMD group, private communication.

[33] P. Braun-Munzinger and J. Stachel, J.Phys. **G28**, 1971-1976 (2002).

[34] F. Becattini *et al.*, Phys. Rev. **C69** 024905 (2004).

[35] V. J. Llope *et al.*, Phys. Rev. **C52**, 2004 (1995).

[36] M. Gaździcki and M. I. Gorenstein, Acta Phys. Polon. **B30** 2705 (1999); M. Gaździcki and D. Röhrich, Z. Phys. **C65** 215 (1995); M. Gaździcki, Z. Phys. **C66** 659 (1999).

[37] C. Alt *et al.*, (NA49 Collaboration), Phys. Rev. C **77**, 024903 (2008).

[38] M. Gorenstein, M. Gazdzicki and K. Bugaev, Phys. Lett. **B567** 175 (2003).

[39] F. Hama *et al.*, Acta Phys. Polon. **B35** 179 (2004).

[40] B. A. Cole, Phys. Lett. B **639**, 210 (2006)

[41] H. G. Fischer *et al.*, http://indico.cern.ch/conferenceDisplay.py?confId=a057199.

[42] Z. Fodor and S. D. Katz, JHEP **0404**, 050 (2004)

[43] M. A. Stephanov, K. Rajagopal and E. V. Shuryak, Phys. Rev. D **60**, 114028 (1999)

[44] Y. Hatta and T. Ikeda, Phys. Rev. D **67**, 014028 (2003)

[45] M. Stephanov, Acta Phys. Polon. B **35**, 2939 (2004)

[46] T. Anticic *et al.*, (NA49 Collaboration), Phys. Rev. C **70**, 034902 (2004).

[47] M. Rybczynski *et al.*, (NA49 Collaboration), J. Phys. Conf. Ser. **5**, 74 (2005).

[48] C. Roland *et al.*, (NA49 Collaboration), J. Phys. G **30**, S1381 (2004).

ELEMENTARY STRUCTURE OF TWO-BODY SYSTEMS AT LARGE TRANSFER MOMENTA

A.F. Krutov[a,1], V.E. Troitsky[b,2] and N.A. Tsirova[c,3]

a) Samara State Universite, 443011 Samara, Russia
b) D.V. Skobeltsyn Institute of Nuclear Physics, 119992 Moscow, Russia
c) Laboratoire de Physique Corpusculaire, 63170 Aubiere, France

Abstract

We present an investigation of the electromagnetic structure of the deuteron and pion in the case of large transfer momenta in the range of modern and future JLab experiments. It is shown that this range could be considered as asymptotical for these systems. We perform an asymptotical analysis of the deuteron and pion form factors in a relativistic approach. We find that our relativistic calculations coincide with pQCD predictions, if some restrictions are imposed.

1. Introduction

We investigate the electromagnetic structure of composite systems in the framework of relativistic quantum mechanics (RQM) in the case of high momentum transfer. The motivation of our work is closely connected with the JLab 12 GeV Upgrade program. One of the most important parts of this program is the investigation of the electromagnetic structure of composite systems at high momentum transfer [1]. At low energies the electromagnetic structure of such systems is described by well-known nonrelativistic methods. If energies increase, these methods fail and we should use relativistic ones. In the case of the highest energies, perturbative QCD (pQCD) should provide the most reliable description [2]. However, the question when pQCD starts to become valid is still open.

Here we investigate the electromagnetic structure of the deuteron as the simplest nucleon-nucleon system and the pion as the simplest $q\bar{q}$ system. In future experiments of JLab the predicted behaviour of the form factors is expected to coincide with pQCD predictions for both the deuteron and the pion [1].

pQCD predictions are available for asymptotically high momentum transfers. So the region of future JLab experiment could be considered as asymptotical. That's why it is interesting to study the asymptotics of the deuteron and pion form factors. In this paper the asymptotical regime of the instant form of relativistic quantum mechanics [3, 4, 5] is investigated for the deuteron and the pion.

2. Instant form of relativistic quantum mechanics

Let us describe briefly our model of relativistic quantum mechanics. In this section we also present the derivation of the electromagnetic pion form factor (see also [3]).

The charge form factor of a pion can be obtained from the electromagnetic current matrix element for a composite system in an arbitrary coordinate frame

$$\langle p_\pi |\, j_\mu \,| p'_\pi \rangle = (p_\pi + p'_\pi)_\mu \, F_\pi(Q^2), \tag{1}$$

[1]E-mail: krutov@ssu.samara.ru
[2]E-mail: troitsky@theory.sinp.msu.ru
[3]E-mail: natalia.tsirova@clermont.in2p3.fr

$F_\pi(Q^2)$ – the electromagnetic form factor of the pion, describing the transition dynamics is an invariant function, the four-vector $(p_\pi - p'_\pi)_\mu$ describes the geometric (transformation) properties of the matrix element, p_π – the four-momentum of the pion.

In RQM the Hilbert space of composite particle states is the tensor product of single particle Hilbert spaces: $\mathcal{H}_{q\bar{q}} \equiv \mathcal{H}_q \otimes \mathcal{H}_{\bar{q}}$ and the state vector in RQM is a superposition of two-particle states. As a basis in $\mathcal{H}_{q\bar{q}}$ one can choose the following set of vectors:

$$|\,\vec{p}_1\,, m_1;\, \vec{p}_2\,, m_2\rangle = |\,\vec{p}_1\,, m_1\rangle \otimes |\,\vec{p}_1\,, m_2\,\rangle\;,$$

$$\langle\vec{p}\,, m\,|\,\vec{p}\,'\,, m'\rangle = 2p_0\,\delta(\vec{p} - \vec{p}\,')\,\delta_{mm'}\;, \tag{2}$$

Here $\vec{p}_1$, $\vec{p}_2$ — are particle momenta, m_1 , m_2 — spin projections.

Since we consider the two-quark system as one composite system, the natural basis is one with separated center-of-mass motion:

$$|\,\vec{P},\ \sqrt{s},\ J,\ l,\ S,\ m_J\,\rangle\;, \tag{3}$$

with $P_\mu = (p_1 + p_2)_\mu$, $P_\mu^2 = s$, $\sqrt{s}$ — the invariant mass of two-particle system , l — the angular momentum in the center-of-mass frame, S — the total spin, J — the total angular momentum, m_J — the projection of the total angular momentum.

The basis (3) is connected with (2) through the Clebsch – Gordan decomposition of the Poincaré group [6].

Now the decomposition of the electromagnetic current matrix element for the composite system (1) in the basis (3) has the form

$$(p_\pi + p'_\pi)_\mu\, F_\pi(Q^2) = \sum \int \frac{d\vec{P}}{N_{CG}}\,\frac{d\vec{P}'}{N'_{CG}}\, d\sqrt{s}\, d\sqrt{s'}\,\langle p_\pi|\vec{P}, \sqrt{s}, J, l, S, m_J\rangle$$

$$\times\langle\vec{P}, \sqrt{s}, J, l, S, m_J\mid j_\mu\mid \vec{P}', \sqrt{s'}, J', l', S', m_J{}'\rangle\langle\vec{P}', \sqrt{s'}, J',{}', S', m_J{}'|p_\pi{}'\rangle\;. \tag{4}$$

Here the sum is over the discrete variables of the basis (3). $\langle\vec{P}\,,\ \sqrt{s},\ J,\ l,\ S,\ m_J|p_\pi\rangle$ is the composite system wave function,

$$\langle\vec{P}\,',\ \sqrt{s'},\ J',\ l',\ S',\ m'_J|\,p_\pi\rangle = N_\pi\delta(\vec{P}\,' - \vec{p}_c)\delta_{JJ'}\delta_{m_Jm'_J}\delta_{ll'}\delta_{SS'}\,\varphi^J_{lS}(k)\;. \tag{5}$$

$s = 4(k^2 + M^2)$, M is the quark mass, N_π, N_{CG} are factors due to normalization. The concrete form of N_π and N_{CG} will not be used.

The basis (3) is the relativistic analogue of the basis of generalized spherical functions of nonrelativistic quantum mechanics (see, e.g. [7]). In this basis the pion wave function is the eigenfunction of the operators $\hat{J}^2$, $\hat{J}_3$, $\hat{l}^2$ as well as of the operator of the total spin squared $\hat{S}^2$, defined in an invariant way (see, e.g. [8]). All the operators have zero eigenvalues, because in the pion $J = l = S = 0$. The quark spin properties are taken into account in the basis (3) by the corresponding Clebsh–Gordan decomposition.

In this approach we represent the pion electromagnetic form factor in the relativistic impulse approximation by the following integral form:

$$F_\pi(Q^2) = \int d\sqrt{s}\, d\sqrt{s'}\,\varphi(k)\, g_0(s, Q^2, s')\,\varphi(k')\;. \tag{6}$$

Here $g_0(s, Q^2, s')$ is the so called free two-particle form factor to be derived by the methods of relativistic kinematics [6], $\varphi(k)$ is a phenomenological wave function normalized with account of the relativistic density of states [6]:

$$\varphi(k) = \sqrt[4]{4(k^2 + M^2)}\, k\, u(k), \qquad \int dk\, k^2\, u^2(k) = 1\ . \tag{7}$$

Here $u(k)$ is a nonrelativistic wave function.

While obtaining (6) we do not use a fixed coordinate frame (for example, Breit frame) or fixed ("good") current components, as one usually does in other RQM approaches [9]. In this respect our calculations are Lorentz-covariant. Our current matrix element satisfies conservation laws, so that the current operator of the composite system does not only contain the contribution of one-particle currents, but of two-particle currents too [6].

The deuteron form factors could be obtained in the same way. They have the following form:

$$G_C(Q^2) = \sum_{l,l'} \int d\sqrt{s}\, d\sqrt{s'}\, \varphi_l(s)\, g_{0C}^{ll'}(s\,, Q^2\,, s')\, \varphi_{l'}(s')\ ,$$

$$G_Q(Q^2) = \frac{2\, M_d^2}{Q^2} \sum_{l,l'} \int d\sqrt{s}\, d\sqrt{s'}\, \varphi_l(s)\, g_{0Q}^{ll'}(s\,, Q^2\,, s')\, \varphi_{l'}(s')\ , \tag{8}$$

$$G_M(Q^2) = -\, M_d \sum_{l,l'} \int d\sqrt{s}\, d\sqrt{s'}\, \varphi_l(s)\, g_{0M}^{ll'}(s\,, Q^2\,, s')\, \varphi_{l'}(s')\ .$$

Here $\varphi_l(s)$, $l, l' = 0, 2$ are the deuteron wave functions in the sense of RQM, $g_{0i}^{ll'}$, $i = C, Q, M$ are the relativistic free two-particles charge, quadrupole, and magnetic form factors [10].

3. Deuteron form factors asymptotics

First, let us make some remarks about the deuteron wave functions used in (8). In modern calculations the deuteron wave functions usually are of the following analytic form in the momentum representation (see, e.g., Refs. [11, 12, 13]):

$$u_0(k) = \sqrt{\frac{2}{\pi}} \sum_j \frac{C_j}{(k^2 + m_j^2)}, \qquad u_2(k) = \sqrt{\frac{2}{\pi}} \sum_j \frac{D_j}{(k^2 + m_j^2)}\ , \tag{9}$$

or in the coordinate representation:

$$u_0(r) = \sum_j C_j \exp\left(-m_j\, r\right)\ , \quad u_2(r) = \sum_j D_j \exp\left(-m_j\, r\right) \left[1 + \frac{3}{m_j\, r} + \frac{3}{(m_j\, r)^2}\right]\ , \tag{10}$$

here $m_j = \alpha + m_0\,(j-1)$, $\alpha = \sqrt{M\, |\varepsilon_d|}$, M is the average nucleon mass, ε_d – the binding energy of the deuteron. The coefficients C_j, D_j, the maximal value of the index j and m_0 are determined by the best fit of the corresponding solution of the Schrödinger equation.

The standard behavior of the functions at short distances:

$$u_0(r) \sim r\,, \quad u_2(r) \sim r^3\,, \tag{11}$$

is provided by imposing the following conditions on the coefficients in (10):

$$\sum_j C_j = 0\,, \quad \sum_j D_j = \sum_j D_j m_j^2 = \sum_j \frac{D_j}{m_j^2} = 0\,. \tag{12}$$

Now let us turn to the asymptotics. In our paper [14] we obtain the asymptotic series for the deuteron form factors. The main asymptotic term for the deuteron form factor
$F_d(Q^2) = \sqrt{G_C^2(Q^2) + \frac{8}{9}\eta^2\, G_Q^2(Q^2) + \frac{2}{3}\eta\, G_M^2(Q^2)}$ has the form:

$$F_d(Q^2) \sim \frac{1}{(Q^2)^4}. \tag{13}$$

Let us compare the obtained asymptotic predictions with experimental data. Fitting the existing experimental points for the seven highest attained values of momentum transfer [15] in the region 3.040–5.955 $(\mathrm{GeV/c})^2$ by a power-law function we obtain the following estimate for Eq. (13) with a normalized $\chi^2 = 1.34$:

$$F_d^{exp}(Q^2) \sim \frac{1}{(Q^2)^{3.76\pm0.41}}\,. \tag{14}$$

So, comparing Eqs. (13) and (14) one can see that up to fitting accuracy, the experimental data are described by the relativistic formula (13).

Let us note that this result does not depend on the actual model of the NN-interaction and in fact is due to the general conditions (11) and (12) only. So, in the recent JLab experiments the range of momentum transfers, which can be characterized as an asymptotic one for our relativistic two-nucleon model of deuteron, is reached. Let us emphasize that this concerns our relativistic approach only. For example, in the relativistic approach of Ref. [16] the asymptotic decrease is faster than the experimental one and even faster than that of the quark-counting prediction.

Let us compare our results with those of the quark approach and of QCD in more detail. At $Q^2 \to \infty$ there exists the well established prediction in the framework of these approaches [17, 18]:

$$F_d(Q^2) \sim Q^{-10}\,. \tag{15}$$

As one can see, this prediction does not agree with the current experiment (14). So let us discuss the possibility to incorporate the QCD predictions in the nucleon–nucleon dynamics. We formulate the problem in the following way: what kind of behavior at small distances should the deuteron wave function have, or, in other words, how has the nucleon-nucleon potential at short distances to be modified, in order to obtain the asymptotic behavior of the electromagnetic deuteron form factors predicted by QCD? The answer can be obtained easily and the analysis shows that the quark-model asymptotic behavior could be derived in the nucleon dynamics formalism if in addition to the conditions (12) for the s-wave function (9) the following condition is imposed:

$$\sum_j C_j m_j^2 = 0\,. \tag{16}$$

This condition means that in the vicinity of zero the wave function has the following form:

$$u_0(r) \sim r + a\, r^3 \;, \; u_0''(0) = 0 \;. \tag{17}$$

So, we have solved some kind of inverse problem: we found a condition for the deuteron wave function to give the asymptotic behavior of the deuteron electromagnetic form factors (in the framework of the two-nucleon model of deuteron) given by the quark approach.

4. Pion form factor and its asymptotics

The main asymptotic term for the electromagnetic pion form factor in the relativistic constituent quark model is of the following form:

$$F_\pi(Q^2) \sim \frac{2^{5/2} M}{Q} \mathrm{e}^{-\frac{\mathrm{QM}}{4\mathrm{b}^2}} . \tag{18}$$

Here the quark mass M and b are parameters of the constituent quark model [3]. Let us note, that this formula is obtained for structureless quarks. In our relativistic approach it is possible to take into account quark structure by introducing quark form factors [3]. But quark form factors don't influence the decrease of the pion form factor, they just add logarithmic corrections. So in this paper we will work with structureless quarks.

We also present the main asymptotic term in the small quark-mass limit:

$$F_\pi(Q^2) \sim \frac{14\sqrt{2}b^2}{Q^2} \;. \tag{19}$$

In $e\pi$ scattering in the case of low momentum transfer, the electron interacts not only with the constituent quarks but also with the sea-quarks cloud, so with an object of bigger mass. But if the energy is increased this cloud becomes smaller and smaller for the electron. So asymptotically high momentum tranfers lead us to asymptotically small quark masses. One can see that the main asymptotic term coincides with the pQCD predictions ($F_\pi(Q^2) \sim 1/Q^2$).

We also investigate pion electromagnetic structure without asymptotic decomposition. We use the following wave functions: wave function of harmonic oscillator, wave function of power law decreasing and wave function of Coulomb interaction at small distances and linear confinement. Let us represent expressions for these functions:

$$u(k) = N_{HO} \exp\left(-k^2/2b^2\right) . \tag{20}$$

$$u(k) = N_{PL} \left(k^2/b^2 + 1\right)^{-n} \;, \quad n = 2\;,3 \;. \tag{21}$$

$$u(r) = N_T \, \exp(-\alpha r^{3/2} - \beta r) \;, \quad \alpha = \frac{2}{3}\sqrt{2\, M_r\, a} \;,$$

$$\beta = M_r\, b \;, \tag{22}$$

where a , b are parameters of linear and Coulomb parts of potential respectively, M_r is a reduced mass of the two-particle system.

Graphical results of our calculations are presented in Fig.1. It is evident that we should use small quark masses at high momentum transfer, that is a confirmation of

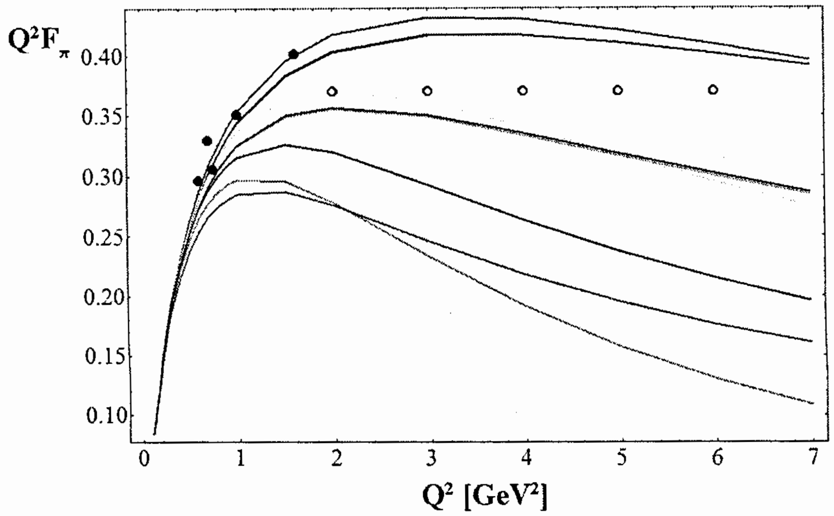

Figure 1: The pion form factor with wave functions (20) - (22). Upper curves respect to the constituent quark mass $M = 0.22$ GeV, medium to $M = 0.25$ GeV, and lower to $M = 0.33$. Existing experimental dots are represented as black dots, expected in the future JLab experiments ones as white dots.

our asymptotic result. From the presented results it is also evident that the product $Q^2F_\pi(Q^2)$ is not a constant now (it is constant in the framework of pQCD). But we can reproduce this result in our relativistic constituent quark model, if we introduce the following dependence of quark mass on the transferred momenta:

5. Conclusion

JLab predicts the pQCD-coinciding behavior of form factors of the deuteron and pion in future experiments. In our work we show that this behavior could be obtained in a relativistic two-nucleon model for the deuteron and a relativistic constituent-quark model for the pion with some restrictions.

Acknowledgments

This work was supported in part by Russian Foundation for Basic Researches (grant No 07-02-00962). N.T. thanks the Organizing Committee of the RNP2009 Workshop for the hospitality and financial support.

References

[1] J. Arrington, R.J. Holt, P.E. Reimer *et al.*, Hall A 12 GeV Upgrade. Pre-Conceptual Design Report, 2005.

[2] R. Gilman and F. Gross, J.Phys G. **28**, R37 (2002).

[3] A.F. Krutov and V.E. Troitsky, Eur.Phys.J. C **20**, 71 (2001).

[4] A. F. Krutov and V. E. Troitsky, Phys. Rev. C **65**, 045501 (2002).

[5] A. F. Krutov and V. E. Troitsky, Phys. Rev. C **68**, 018501 (2003).

[6] E.V. Balandina, A.F. Krutov, and V.E. Troitsky, Teor. Math. Phys. **103**, 381 (1995).

[7] R.Newton, *Scattering theory of waves and particles*, 2nd ed., (Springer Verlag, New York, 1982).

[8] V.P. Kozhevnikov, V.E. Troitsky, S.V. Trubnikov, Yu.M. Shirokov, Theor.Math.Fiz. **10**, 47, (1972).

[9] B.D. Keister and W. Polyzou, Adv.Nucl.Phys. **21**, 225, (1991).

[10] A. F. Krutov and V. E. Troitsky, Phys. Rev. C **75**, 014001 (2007).

[11] M. Lacombe, B. Loiseau, R. Vinh Mau, J. Coté, P. Pirés, R. de Tourreil, Phys. Lett. B **101**, 139 (1981).

[12] R. Machleidt, Phys.Rev.C **63**, 024001 (2001).

[13] A.F. Krutov and V.E. Troitsky, Phys. Rev. C **76**, 017001 (2007).

[14] A. F. Krutov, V. E. Troitsky, and N. A. Tsirova, J. Phys. A: Math. Theor. **41**, 255401 (2008).

[15] L.C. Alexa *et al.* (The Jefferson Lab Hall A Collaboration), Phys. Rev. Let. **82**, 1374 (1999).

[16] R. G. Arnold, C. E. Carlson, and F. Gross, Phys.Rev. C **21**, 1426 (1980).

[17] S. J. Brodsky and G. R. Farrar, Phys. Rev. Lett. **31**, 1153 (1973).

[18] V. A. Matveev, R. M. Muradyan and A. N. Tavkhelidze, Lett. Nuovo Cim. **7**, 719 (1973).

STUDY OF LIGHT NUCLEI SPIN STRUCTURE FROM (d,p) AND (d,^3He) REACTIONS

A.K. Kurilkin[a,e,1], L.S. Azhgirey[a], V.V. Fimushkin[a], Yu.V. Gurchin[a], A.P. Ierusalimov[a], A.Yu. Isupov[a], K. Itoh[g], M. Janek[a,c], J.-T. Karachuk[a,d], T. Kawabata[b], A.N. Khrenov[a], A.S. Kiselev[a], A.B. Kurepin[i], P.K. Kurilkin[a,e], V.A. Krasnov[a,i], V.P. Ladygin[a,e], N.B. Ladygina[a], D. Lipchinski[d], A.N. Livanov[a,i], G.I. Lykasov[a], Y. Maeda[b], A.I. Malakhov[a], G. Martinska[c], S. Nedev[f], S.M. Piyadin[a], E.B. Plekhanov[a], J. Popovichi[d], A.N. Prokofichev[a], S. Rangelov[f], S.G. Reznikov[a], P.A. Rukoyatkin[a], S. Sakaguchi[h], H. Sakai[b], Y. Sasamoto[b], K. Sekiguchi[h], K. Suda[b], A.A. Terekhin[a,j], T. Uesaka[b], J. Urban[c], T.A. Vasiliev[a,e], I.E. Vnukov[j].

a) Joint Institute for Nuclear Research, Dubna, Russia
b) Center for Nuclear Study, University of Tokyo, Tokyo, Japan
c) P.J.Šafarik University, Košice, Slovakia
d) Advanced Research Institute for Electrical Engineering, Bucharest, Romania
e) Moscow State Institute of Radio-engineering, Electronics and Automation (Technical University), Moscow, Russia
f) University of Chemical Technology and Metallurgy, Sofia, Bulgaria
g) Saitama University, Saitama, Japan
h) RIKEN (the Institute for Physical and Chemical Research, Saitama, Japan)
i) Institute for Nuclear Research, Moscow, Russia
j) Belgorod State University, Belgorod, Russia

Abstract

The data on the vector A_y and tensor A_{yy}, A_{xx}, A_{xz} analyzing powers for the $dd \to {}^3Hp$ and $dd \to {}^3Hen$ reactions at E_d=200 and 270 MeV are presented. The tensor analyzing powers for these reactions demonstrate the sensitivity to the ^3H, ^3He and deuteron spin structure. The essential disagreements between the experimental results and the theoretical calculations within the framework of the one-nucleon exchange model are observed. Obtained experimental data are important for the preparation of the experiments at the LHEP-JINR Nuclotron-M at higher energies. It is planned to obtain new experimental data on the polarization observables for the $p(d,p)d$, $^3He(d,p)^4He$ and $d(d,p)^3H$ reactions at intermediate and high energies in the wide angular range. These data will ensure new information on the spin structure of light nuclei at the short internucleonic distances, where the relativistic effects and the three-nucleon forces play an important role.

1. Introduction

At the present time, there is a great deal of interest in understanding the short-range spin structure of deuteron and other light nuclei, as ^3H and ^3He. They represent an important testing ground for models of the NN interaction and for studies of the many-body aspects of the strong interaction in nuclei. In addition, ^3H and ^3He are the simplest systems in which the effects of possible three-body nuclear forces can be explored.

The essential amount of the experimental data sensitive to the structure of light nuclei, have been accumulated at several last decades. Cross section[1]-[6] and spin

[1]E-mail: akurilkin@jinr.ru

observables, such as analyzing powers[7]-[10], spin correlation coefficient[11] and polarization transfer coefficient[12],[13] have been measured for Nd elastic scattering. Large discrepancies between the Nd data and theoretical predictions based on exact solution of the Faddeev equations with only modern NN potential are reported. These discrepancies are particularly significant in the angular region of the cross section minimum and at energies of incoming nucleons above 60 MeV[14]. The inclusion 2π-exchange 3NF models into theoretical calculations removes many of them and also solves underbinding problem[14]-[17]. This result clearly shows the significance of the 3NFs in the nucleus. In contrast, theoretical calculations with 3NFs still have difficulties in the reproducing of some spin observables. At higher energies, not only spin observables but also cross sections at backward scattering indicate the deficiencies of the present 3NF models[18]-[20].

The study of reactions with participation of the four nucleons present a special interest, because four-nucleon systems have a number of features not found for three nucleons. Some of them are the existence of excited states, a complicated reaction mechanism, many channels in [3+1] and [2+2] configurations, and much larger polarization effects. The essential progress in theoretical description of the four-nucleon reactions was performed at last decade. Theoretical calculations for all possible 4N reactions below three-body breakup threshold were performed in ref [21]-[25]. These results have shown that the agreement between data and theory the best by using non-local model[26]. However, specific observables such as A_y for $p - {}^3He$ reaction and $n - {}^3H$ cross section show large discrepancies with data. Also, it was found that the Urbana IX 3N force, when added to AV18 2N force bears almost no effect on the total cross section in the $n - {}^3H$ resonance region[24]. In contrary, there was a good agreement between the $p - {}^3He$ cross section data and the calculations there a 3N potential was included[25]. One of the tools for understanding of the reason of these disagreements is the investigation of the processes sensitive to the deuteron, ${}^3He({}^3H)$ spin structure and 3-nucleon forces(3NFs). It gives additional important information about reaction mechanisms and the structure of the lightest nuclei(d, ${}^3H$, ${}^3He$).

Binary reactions like $dd \to {}^3Hp$, $dd \to {}^3Hen$, $dp \to pd$ and $d^3He \to p^4He$ are sensitive to the structure of deuteron and 3-nucleon forces. In additional, the $dd \to {}^3Hp({}^3Hen)$ reaction can be used as an effective tool to investigate the structure ${}^3H$ and ${}^3He$ at short distances, because they are the simplest ONE reactions where the three nucleon structure is relevant. These reactions were intensively studied at low energy both experimentally and theoretically[27]-[34]. But the polarization data for dd scattering at intermediate energies are scare. The tensor analyzing power T_{20} have been obtained in the $\vec{d}d \to {}^3He(0^0)n({}^3H(0^0)p)$ reactions at the energy of deuteron 140, 200 and 270 MeV at RIKEN. The positive values and the behavior of T_{20}[35] depending from the deuteron energy are in the agreement with the calculations of the ONE model. However, recent data on the tensor A_{yy}, A_{xx} and A_{xz} analyzing powers for the $\vec{d}d \to {}^3Hen$ reaction [36] obtained at 270 MeV demonstrate strong disagreement with the predictions of ONE at the angles larger than 15° in the c.m.s. This difference may indicate that the knowledge of short-range structure and applied reaction mechanism are not reasonable. To understand the reason of such deviation, data at different energies are necessary.

In this report the data on the angular distributions of the vector A_y and tensor A_{yy}, A_{xx}, A_{xz} analyzing powers in the $\vec{d}d \to {}^3Hp$ and $\vec{d}d \to {}^3Hen$ reactions at 200 and 270 MeV of the deuteron kinetic energy are presented. These data are data are important for the preparation of the experiments at the LHEP-JINR Nuclotron-M at higher energies. It is planned to obtain new experimental data on the polarization observables for the $p(d,p)d$, $^3He(d,p)^4He$ and $d(d,p)^3H$ reactions at intermediate and high energies in the wide angular range. These data will ensure new information on the spin structure of light nuclei at the short internucleonic distances, where the relativistic effects and the three-nucleon forces play an important role.

2. Experiment

Experiment was performed at the acceleration complex RARF(Fig1.). The polarized beam of deuterons, was ensured by the polarized ion source(PIS), and was accelerated by AVF and Ring Cyclotrons up to energy of 140, 200 and 270 MeV. The accelerated beam was directed to the target, located in hall E4.

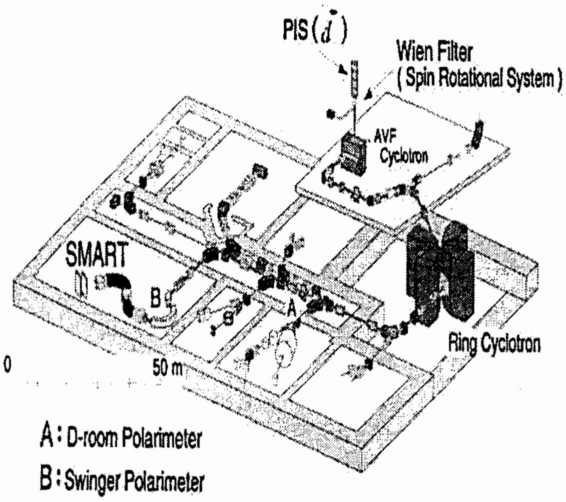

Figure 1: RIKEN Accelerator Research Facility

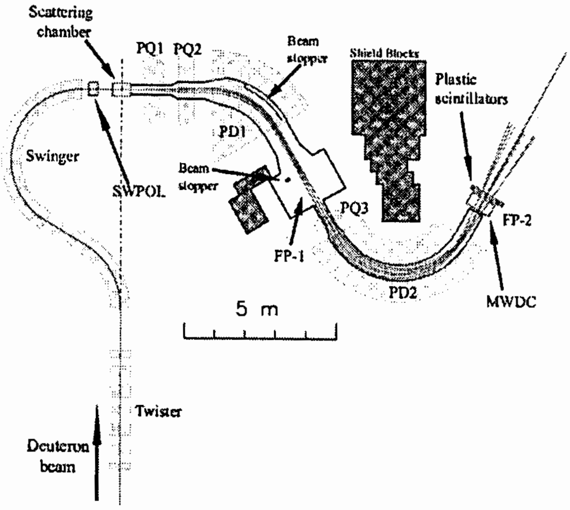

Figure 2: Spectrometer SMART

The measurement of the polarization of beam was carried out with the help of Swinger polarimeter (SwingerPOL) and Droom polarimeter (DroomPOL). These polarimeters are based on the measurement of asymmetry in $\vec{d}p$ elastic scattering. Two kinds of deuterized polyethylene(CD_2) sheets were used as the target. The carbon targets were used for evaluating the background events. The scattered particles (^3He, ^3H and p) were registered by spectrometer SMART(Fig2.). The identification of particles was based on the time-of-flight and the value of ionization losses in the plastic of scintillation detectors. Scattering angle and momentum of the particle were determined by the information of multiwire drift cambers (MWDC) and optical characteristics of the spectrometer.

The energy spectrum on carbon target was measured to take account for the contribution of carbon content of CD_2 target. The quality of the $CD_2 - C$ subtraction procedure for the $\vec{d}d \to {}^3Hp$ reactions at 200 MeV is demonstrated in Fig.3 for several angles in the center of mass system. The spectra are plotted as a function of the excitation energy E_x defined as follows:

$$E_x = \sqrt{(E_0 - E_{3N})^2 - (\mathbf{P}_0 - \mathbf{P}_{3N})^2} - M_N,$$

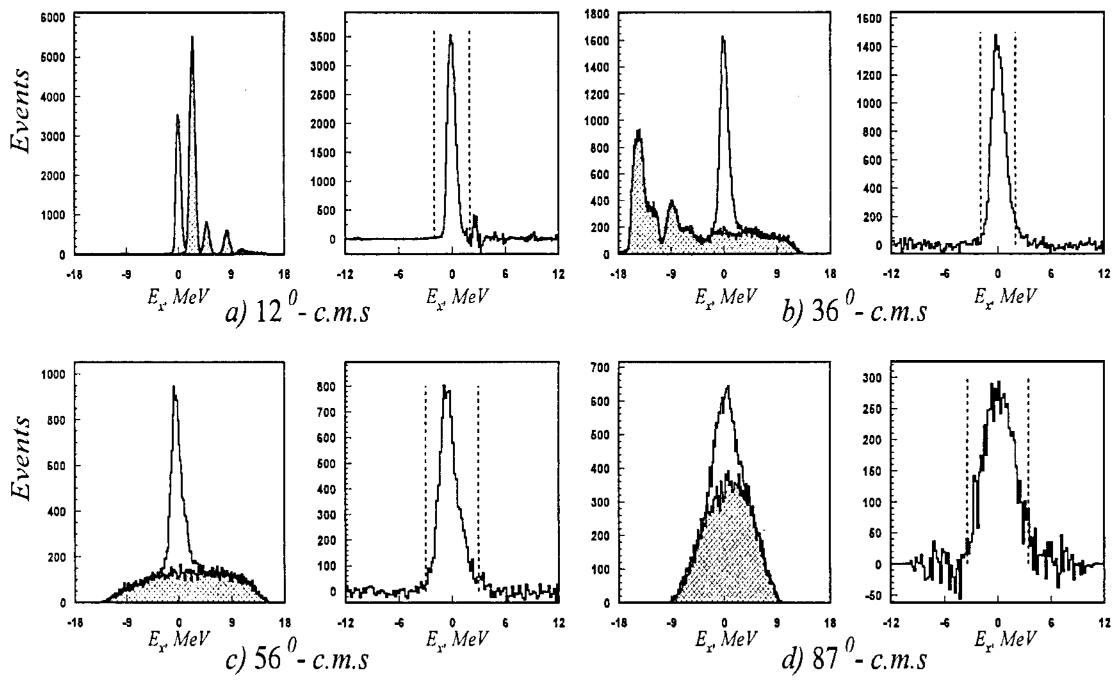

Figure 3: $CD_2 - C$ subtraction procedure for $dd \to {}^3Hp$ reaction at 200 MeV. The open and shadowed histograms in the left panels correspond to the yields from CD_2 and carbon targets, respectively. The right panels demonstrate the quality of the $CD_2 - C$ subtraction. The peaks at E_x=0 MeV correspond to ^3H production from the $dd \to {}^3Hp$ reaction.

where $\mathbf{P}_0$ is the incident momentum; $E_0 = 2M_d + T_d$ is the total initial energy; E_{3N} and $\mathbf{P}_{3N}$ are the energy and momentum of the three-nucleon system, respectively; M_N is the nucleon mass. The analyzing powers A_y, A_{yy}, A_{xx} and A_{xz} were obtained from the number of the events after the $CD_2 - C$ subtraction and beam polarization. The number of the events was normalized on the dead-time effect, the detection efficiency, and beam intensity.

3. Results

The experimental results on the vector and tensor analyzing powers of the $\vec{d}d \to {}^3Hp({}^3Hen)$ reactions are presented in Fig.4. The errors of the experimental values include both the statistical and the systematic errors. The systematic errors were derived from the errors of the beam polarizations measurements.

The solid curves are the results of ONE calculations using CD-Bonn deuteron and ^3He wave functions[37]. The long-dashed curves are the results of ONE calculations using Paris deuteron and ^3He wave functions[37]. The positive values and the behavior of T_{20}[35] versus the deuteron energy at forward angles are qualitative agree with the calculations of the ONE model, but these calculations predict slightly large values of the tensor analyzing power. The predictions show sharper decrease of the T_{20} than the experimental values obtained at 180 degrees. The signs of the tensor A_{yy}, A_{xx} and A_{xz} analyzing powers at forward and backward angles are same for the data and ONE calculations. The shapes of distributions for A_{yy} and A_{xz} are similar at both energies

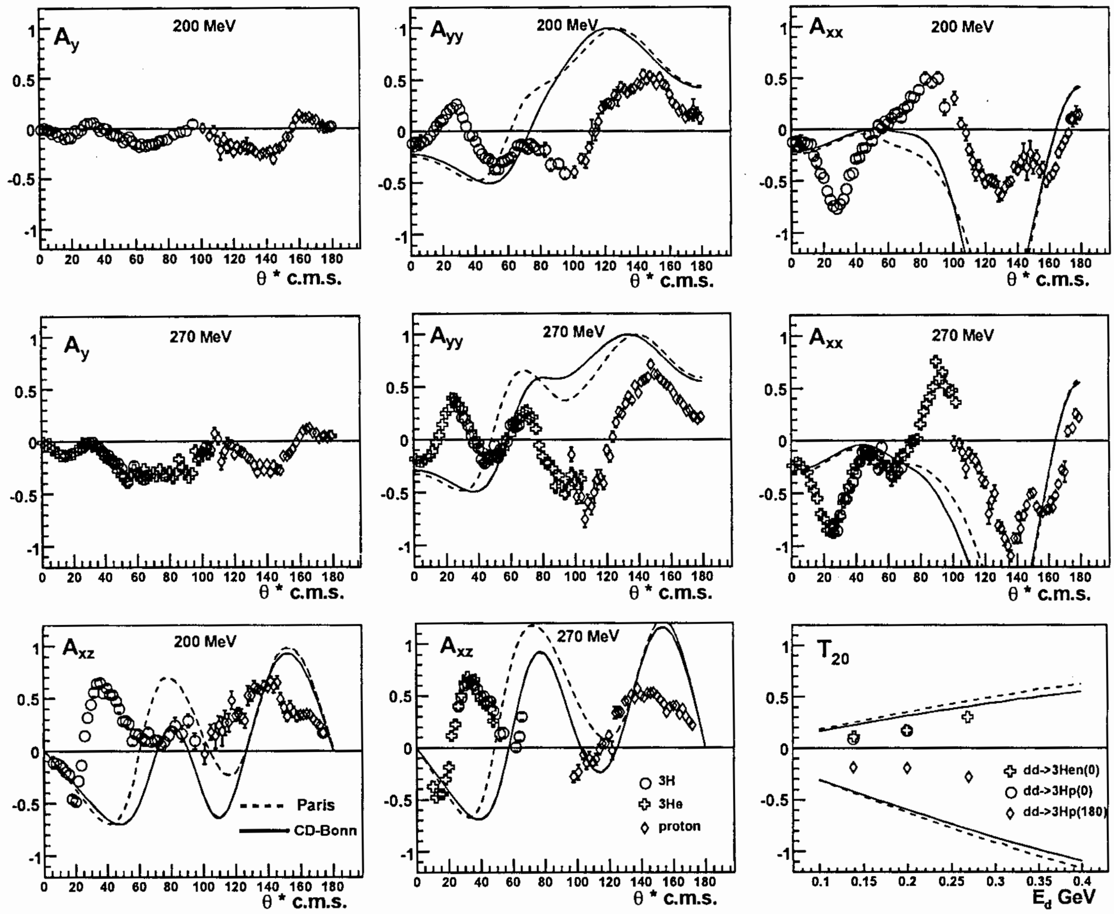

Figure 4: The experimental results on the vector and tensor analyzing powers. The circles, crosses, rhombus are results of the analyzing powers in the cases when ^3H, ^3He and proton were registered.

in contrast with the data on A_{xx} where an additional structure at 270 MeV is observed. The vector analyzing power A_y equals zero in the ONE model. Some structures in the experimental results on A_y indicate possibility other than ONE mechanisms in these reactions.

One can see that ONE calculations qualitatively reproduce the behavior of the tensor analyzing powers at the angles smaller than 15^0 and larger than 160^0 only. However, the ONE calculations strongly disagree with the data in the whole angular range of the measurements. This is especially noticeable at the angles smaller than 90 degrees. The reason of the discrepancy can be in the non-adequateness of the 3N-bound state spin structure and/or more complicated reaction mechanism. The multiple scattering calculations are in progress now[38].

4. Measurements of the *dp* elastic scattering.

We plan to measure the cross section, vector A_y and tensor A_{yy} and A_{xx} analyzing powers in *dp*-elastic scattering at large angles in c.m.s. in the energy range 0.3-2.0 GeV[39,40] and in dp-non-mesonic breakup at the energies below 500 MeV for different kinematic configurations of two final protons[41] at Internal Target Station[42,43] at Nuclotron-M.

The deuteron-proton, deuteron-neutron and breakup reactions are used for the intensive studies of the three-nucleon force effect. At deuteron energies below 300 MeV, Faddeev calculations can provide good description of cross section data, by introducing a three nucleon force, over the whole angular range. However, their reproduction of the polarization observables are not so good as that for cross section data, which may be regarded as an insufficiency of our knowledge on spin dependence of three nucleon force. Measurement of energy dependences of polarization observables in the region of cross section minimum can give an irreplaceable clue to the problem.

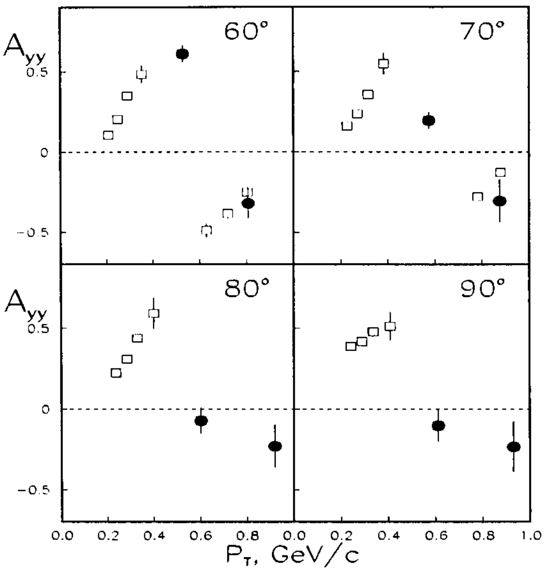

Figure 5: The dependence of the tensor A_{yy} analyzing power in *dp*- elastic scattering at the fixed angles in the c.m.s. as a function of transverse momentum p_T. The open and solid symbols represent data obtained at RIKEN, Saclay, ANL and at Nuclotron(Dubna), respectively.

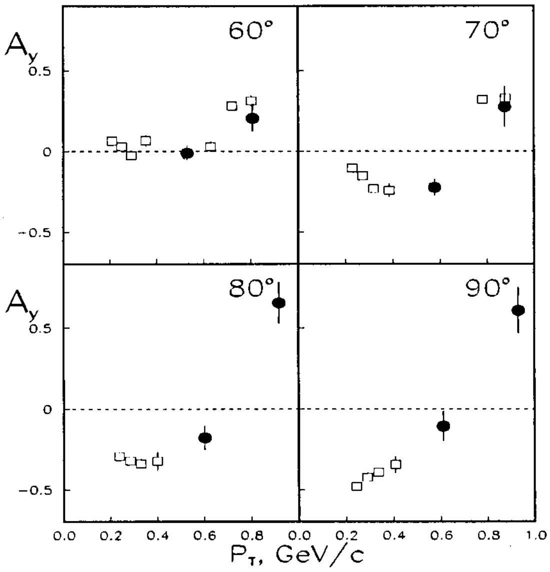

Figure 6: The dependence of the vector A_y analyzing power in *dp*- elastic scattering at the fixed angles in the c.m.s. as a function of transverse momentum p_T. The open and solid symbols represent data obtained at RIKEN, Saclay, ANL and at Nuclotron(Dubna), respectively.

The Fig.5 and Fig.6 show the dependences of the vector A_y and tensor A_{yy} analyzing powers in *dp*- elastic scattering at the fixed angles in the c.m.s. as a function of transverse momentum p_T. The open and solid symbols represent data obtained at RIKEN, Saclay, ANL and at Nuclotron(Dubna), respectively. The change of the sign in the both A_y and A_yy analyzing powers values at p_T 600-700 MeV is observed. Further precise measurements are required to understand the reason of such behavior.

5. Measurements of the $^3He(d,p)^4He$ reaction spin observables.

The goal of the $^3He(d,p)^4He$ reaction study at Nuclotron-M is to understand the reason of the long staying puzzle, namely, the behavior, of the tensor analyzing power T_{20} in *dp* - backward elastic scattering[44,45]. While t_{20} data in *ed*- elastic scattering obtained at JLAB[46] and T_{20} data in *dp*- inclusive breakup[47,48] can be explained by using the conventional deuteron structure functions and additional to the Born approximation mechanisms, the T_{20} in dp- backward elastic scattering(Fig.7) demonstrate unexplained the strange structure at the internal momentum $k \sim$0.3–0.5 GeV/c in the vicinity of the D-wave dominance.

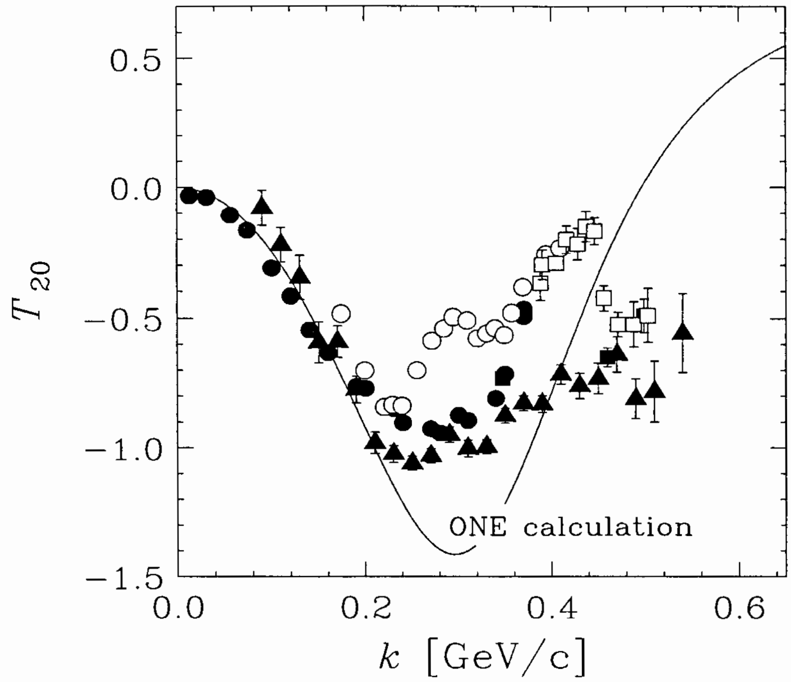

Figure 7: T_{20} data taken at Dubna and Saclay plotted as a function of the internal momentum k. Open circles and squares denote data for the dp- backward elastic scattering obtained at Saclay[44] and at Dubna[45], respectively. Closed circles, squares and triangles indicate data for the deuteron inclusive breakup on hydrogen target obtained at Saclay[47] and at Dubna[48], respectively. Solid curve represent the result of ONE calculation.

The experiments performed at RIKEN at the energies below 270 MeV have shown that the polarization correlation coefficient, $C_{//} = 1-\frac{1}{2\sqrt{2}}T_{20}+\frac{3}{2}C_{y,y}$, for the $^3He(d,p)^4He$ reaction may be a unique probe to the D-state admixture in deuteron[49]. In the ONE, the expression for $C_{//}$ is proportional to the D-state fraction in deuteron as

$$C_{//} = \frac{9}{4}\frac{w^2}{u^2 + w^2}, \tag{1}$$

where u and w are the S- and D-state wave functions of deuteron in momentum space. This is a marked contrast to T_{20} and κ_0 for dp backward elastic scattering which include S- and D-state interference term (uw-term) together with a w^2-term. It is thus expected that $C_{//}$ may be a candidate to provide an information on the deuteron structure complementary to those from T_{20} and κ_0 obtained in dp- backward elastic scattering.

Tensor analyzing power T_{20}, spin correlation $C_{y,y}$ and polarization correlation coefficient $C_{//}$ for the ^{3}He$(d,p)^4$He reaction are shown in Fig.8. Solid lines in the figures represent calculations based on an impulse approximation proposed in Ref.[50]. In the

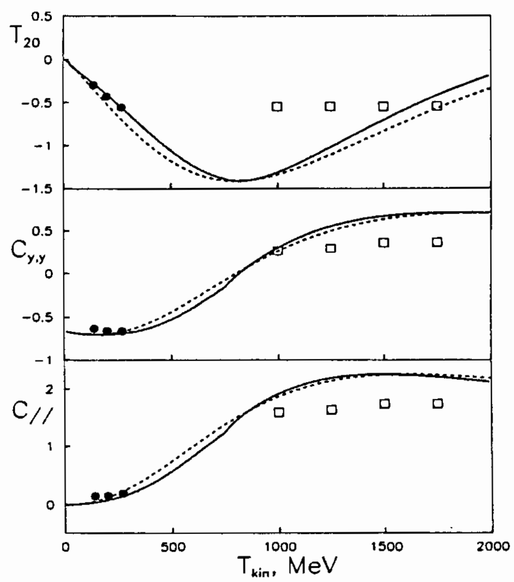

Figure 8: Tensor analyzing power T_{20}, spin correlation $C_{y,y}$ and polarization correlation coefficient $C_{//}$ for the ^{3}He$(d,p)^4$He reaction. The dashed and solid lines represent one-nucleon exchange calculations without[50] and taking into account the Fermi motion in the target nucleus, respectively. The full symbols are the data obtained at RIKEN[51]. The open squares show the expected precision for the data at Nuclotron-M.

calculation, the Fermi motion in the target nucleus is taken into account [51]. The full symbols are the data obtained at RIKEN[51] . The open squares show the expected precision for the data at Nuclotron.

The main goal of the experiment is to obtain the data on $C_{//}$ in the energy region of 1.0–1.75 GeV, where the contribution from the deuteron D-state is expected to reach a maximum in one-nucleon exchange approximation, to obtain new information on the strange structure observed in the behavior of T_{20} in the *dp*- backward elastic scattering and to realize experiment on the full determination of the matrix element of the ^{3}He$(d,p)^4$He reaction in the model independent way. These data will help us also to understand the short-range spin structure of deuteron and effects of non-nucleonic degrees of freedom. For these purposes polarized deuteron beam from new PIS[52] and polarized ^{3}He target developed at CNS of Tokyo University[53] and modified for present experiment at Nuclotron-M will be used.

6. Conclusion.

The results on the vector A_y and tensor A_{yy}, A_{xx} and A_{xz} analyzing powers in the $\vec{d}d \rightarrow {}^3Hp({}^3Hen)$ reactions at the energy of initial deuterons 200 and 270 MeV have been obtained. The data demonstrate large values of the analyzing powers. The calculations performed within one-nucleon-exchange approximation[38] using standard wave functions fail to reproduce the data. The reason of the discrepancy can be in the non-adequateness of the 3N-bound state spin structure and/or more complicated reaction mechanism. The multiple scattering calculations are in progress now[38].

Obtained experimental data are important for the preparation of the experiments at the LHEP-JINR Nuclotron-M at higher energies. It is planned to obtain new experimental data on the polarization observables for the $p(d,p)d$, ${}^3He(d,p)^4He$ and $d(d,p)^3H$ reactions at intermediate and high energies in the wide angular range. Further precise measurements of the polarization observables for the dp elastic scattering are required to understand the reason of the change of the sign in the both A_y and A_{yy} analyzing powers values at $p_T \sim$ 600-700 MeV. The goal of the ${}^3He(d,p)^4He$ reaction study at Nuclotron-M is to understand the reason of the long staying puzzle, namely, the behavior, of the tensor analyzing power T_{20} in dp - backward elastic scattering[44].

New experimental data will ensure the important information on the spin structure of light nuclei at the short internucleonic distances, where the relativistic effects and the three-nucleon forces play an important role.

Acknowledgments

The work has been supported in part by the Russian Foundation for Basis Research (travel grant *No.* 09-02-09262-mob-3, grant *No.* 07-02-00102a), by the Grant Agency for Science at the Ministry of Education of the Slovak Republic (grant *No.* 1/4010/07), by a Special program of the Ministry of Education and Science of the Russian Federation(grant RNP2.1.1.2512).

References

[1] K.Sekiguchi, *et al.*, Phys. Rev. Lett **95**, 162301 (2005).
[2] H.Ruhl, *et al.*, Nucl. Phys. A **524**, 377 (1991).
[3] H.Sakai, *et al.*, Phys. Rev. Lett. **84**, 5288 (2000).
[4] N.Sakamoto, *et al.*, Phys. Lett. B **367**, 60 (1996).
[5] K.Sekiguchi, *et al.*, Phys. Rev. C **65**, 034003 (2001).
[6] K.Ermisch, *et al.*, Phys. Rev. Lett. **86**, 5862 (2001).
[7] R.Bieber, *et al.*, Phys. Rev. Lett. **84**, 606 (2000).
[8] H.Witala, *et al.*, Few-Body Syst. 15, 67 (1993).
[9] J.Arvieux, *et al.*, Phys. Rev. Lett. **50**, 19 (1983).
[10] E.J.Stephenson, *et al.*, Phys. Rev. C **60**, 061001(R) (1999).
[11] R.V.Gadman, *et al.*, Phys. Rev. Lett. **86**, 967 (2001).
[12] K.Sekiguchi, *et al.*, Phys. Rev. C **70**, 014001 (2004).
[13] K.Hatanaka, *et al.*, Phys. Rev. C **66**, 044002 (2002).
[14] H.Witala, *et al.*, Phys. Rev. Lett. **81**, 1183 (1998).
[15] A.Nogga, H.Kamada, and W.Glockle, Phys.Rev.Lett. **85**, 944 (2000).
[16] A.Nogga, H.Kamada, W.Glockle, and B.R.Barrett, Phys.Rev.C **65**, 054003 (2002).
[17] R.B.Wiringa, *et al.*, Phys. Rev. C **62**, 014001 (2000).
[18] Y.Maeda, *et al.*, AIP Conf. Proc. Volume **915**, pp.781-784 (2007).
[19] Y.Maeda, *et al.*, Phys. Rev. C **76**, 014004 (2007).
[20] W.R.Falk, Phys. Rev. C **50**, 1574-1593 (1994).
[21] A.Deltuva, A.C.Fonseca, P.U.Sauer Phys.Lett. B **660**, 471-477 (2008).
[22] A.Deltuva, A.C.Fonseca, P.U.Sauer Phys.Rev. C **76**, 021001 (2007).
[23] R.Lazauskas, J.Carbonell, Phys. Rev. C **70**, 044002 (2004).
[24] R.Lazauskas, *et al.*, Phys. Rev. C **71**, 034004 (2005).

[25] B.M.Fisher, *et al.*, Phys. Rev. C **74**, 034001 (2006).
[26] P.Doleschall, Phys. Rev. C **69**, 054001 (2004).
[27] E.M. Bernstein et al., Nucl.Phys. A **126**, 641 (1969);
[28] W. Grüebler et al., Nucl.Phys. A **193**, 129 (1972);
[29] L.G. Dries et al., Phys.Lett. B **80**, 176 (1979);
[30] V. König et al., Nucl.Phys. A **331**, 1 (1979).
[31] A.C. Fonseca, Few-Body Syst.Suppl. **10**, 359 (1999);
[32] F. Ciesielski and J. Carbonell, Phys.Rev. C **58**, 58 (1998);
[33] R. Lazauskas and J. Carbonell, Few-Body Syst. **34**, 105 (2004);
[34] M. Viviani, A. Kievsky and S. Rosati, Phys.Rev. C **71**, 024006 (2005);
[35] V. P. Ladygin, et al., Phys. Lett.B, **589**,47 (2004) ; Phys. At. Nucl. **69**, 1271 (2006).
[36] M. Janek, et al., Eur.Phys.J., **A33**, 39 (2007).
[37] V. Baru, *et al.*, Eur.Phys.J., A **16**, 437-446 (2003)
[38] N.B. Ladygina, private communication.
[39] Ladygin V.P. XV-th ISHEPP, 25-29 September 2000, Dubna, Russia.
[40] T. Uesaka, V.P. Ladygin et al., Part.Nucl.Lett. 3[114] N^o5 (2006), 58.
[41] S.M. Piyadin et al., talk at SPIN-Praha-08 Conference, Czech Republic, to be published.
[42] A.I. Malakhov, et al., Nucl.Instr.Meth. in Phys.Res. **A440** (2000) 320.
[43] Yu.S. Anisimov, et al., Proc. of RNP-2003, 25-30 August 2003, Slovak Republic, p.117.
[44] V. Punjabi et al., Phys.Lett. **B350** (1995) 178.
[45] L.S. Azhgirey et al., Phys.Lett. **B391** (1997) 22.
[46] D. Abbott et al., Phys.Rev.Lett. **84** (2000) 5053.
[47] V. Punjabi et al., Phys.Rev. **C39** (1989) 608.
[48] L.S. Azhgirey et al., Phys.Lett. **B387** (1996) 37.
[49] T. Uesaka et al., Phys.Lett. **B467** (1999) 199.
[50] H. Kamada et al., Prog.Theor.Phys. **104** (2000) 703.
[51] T. Uesaka et al., Phys. Lett. **B533** (2002) 1.
[52] T. Uesaka et al., Nucl.Instr. and Meth. in Phys.Res. **A402** (1998) 212.
[53] V.V. Fimushkin et al., Eur.Phys.J. ST **162** (2008) 275.

EXPERIMENT ON THE STUDY OF DEUTERON-PROTON BREAKUP AT ITS AT NUCLOTRON-M

S.M. Piyadin[a,1], Yu.V. Gurchin[a], M. Janek[a,b], A.Yu. Isupov[a], J.T. Karachuk[a,c], A.N. Khrenov[a], A.S. Kiselev[a], V.A. Krasnov[a], A.K. Kurilkin[a], P.K. Kurilkin[a], V.P. Ladygin[a], A.N. Livanov[a], G. Martinsky[b], S.G. Reznikov[a], T.A. Vasiliev[a].

a) LHE-JINR, 141-980 Dubna, Moscow region, Russia
b) P.J.Safarik University, Kosice, Slovakia
c) Advanced Research Institute for Electrical Engineering, Bucharest, Romania

Abstract

The experiment on *dp*-non-mesonic breakup at the Internal Target Station (ITS) at Nuclotron-M is discussed. The status of the setup upgrade (detectors, high voltage and DAQ systems etc.) is presented.

1. Introduction

The purpose of Light Nuclei Structure experimental program is to obtain the information on the spin dependent parts of 2-nucleon and 3-nucleon forces from two processes: *dp*-elastic scattering in a wide energy range and *dp*- non-mesonic breakup with two protons detection at energies 300 - 500 MeV.

Properties of few-nucleon system at moderate energies are determined mainly by pairwise nucleon-nucleon interactions. Models of NN forces describe the long range interaction part according to the meson-exchange, while the short range is based on phenomenology, adjusted by fitting a certain number of parameters to the NN scattering data. Nowadays a new generation of the NN potentials (AV-18[1], CD-Bonn[2], Nijmegen[3] etc.) was obtained. They reproduce data on the nucleon nucleon scattering up to 350 MeV with very good accuracy. However, these modern 2N forces fail to provide the experimental binding energies of few-nucleon systems. Moreover the data on the *dp*- elastic scattering and deuteron breakup are not described properly.

Precise predictions for observables in the $3N$ system can be obtained via exact solutions of the $3N$ Faddeev equations for any nucleon-nucleon (NN) interaction, even with the inclusion of a $3NF$ model [4]. Incorporation of the 3N forces makes it possible to reproduce the binding energy of the three-nucleon bound systems and also data on unpolarized *dp*- interaction. Nevertheless, polarization data for the reactions with participation of three and more nucleons are not described even with inclusion of 3NF. Therefore, the obtaining of the additional polarization data in the *dp*- interaction in the wide energy range more is very desirable for the study of the spin structure of 2N and 3N forces [5]. To investigate the details of the dynamics of the $3N$ system, in addition to elastic Nd scattering data, reliable deuteron breakup data sets, covering large regions of the available phase space, are needed.

The experimental data on the deuteron analyzing powers for large phase space were obtained at 130 MeV at KVI [6]. A_y, A_{yy} and A_{xx} analyzing powers in *dp*-breakup will be investigated at Internal Target Station at 200-500 MeV. The predictions for tensor analyzing power A_{yy} and differential cross section in the selected *dp*-breakup

[1]E-mail: piyadin@jinr.ru

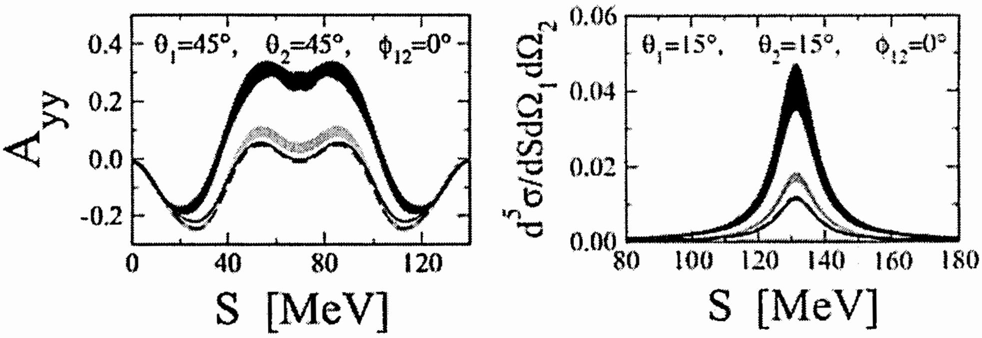

Figure 1: The tensor analyzing power A_{yy} (left) and differential cross section in selected breakup configurations at 400 MeV (right)[7]. The curves are explained in the text.

configurations at 400 MeV are shown in Fig.1. The light shaded band contains the theoretical predictions based on CD-Bonn, AV18, Nijm I, II and Nijm 93. The darker band represents predictions when these NN forces are combined with the TM 3NF. The solid line is for AV18+Urbana IX and the dashed line for CD Bonn+TM. One can see large sensitivity of these observables to the model of 3NF.

In this report the status of the experiment at ITS at Nuclotron-M preparation and first beam test results are presented.

2. ΔE-E detector.

The *dp* breakup reaction will be investigated using ΔE-E techniques for the detection of protons. 8 detectors of this kind are planned to use in experiment. The detector consists of two scintillators ΔE and E.

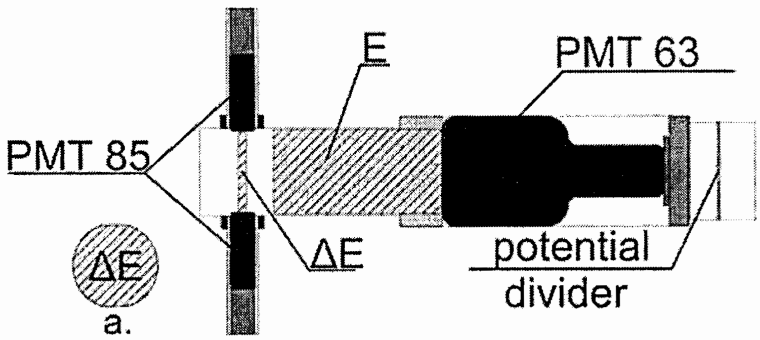

Figure 2: The schematic view of the ΔE-E detector for *dp* breakup reaction study.

The first scintillator has the cylindrical form with the height 10 mm and the diameter 100 mm. Two PMTs-85 view through given scintillator and they are located the friend opposite to the friend. Two planes have been made on the scintillator to increase the area of the optical contact between the scintillator and photocatode of the PMT-85. These planes have been polished. (see Figure 2). ΔE scintillator it is covered by a white paper. Digital dividers of pressure are used for PMT-85.

E scintillator also has the cylindrical form with height 200 mm and diameter 100 mm. PMT-63 view through this scintillator. Given PMT has been chosen because of the suitable size of the cathode (100 mm) both good time and amplitude properties. E scintillator has been wrapped by a white paper. The part which is located to ΔE scintillator has been covered by a black paper. It is made to exclude possibility of hit the light from one plastic scintillator to another.

3. Divider of the high voltage of PMT-63.

Divider of voltage for PMT-63 was used standard (not individual) without feed of last cascades (see Figure 3). The divider consists of resistors, without use of stabilitrons on the last dynodes. The general resistance of a divider makes 1736 kOm, and the current is equal 1,1 - 1,4 mA at working voltage.

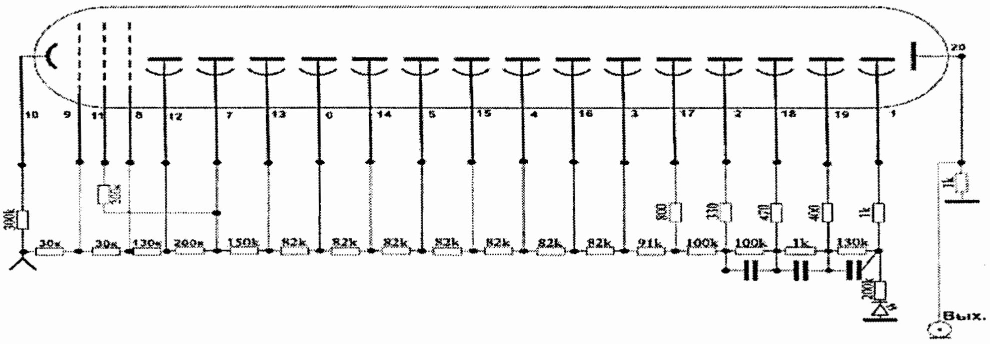

Figure 3: The scheme of a divider of voltage PMT 63.

The resistor of 300 kOm in the cathode chain extinguishes the large amplitudes pulses arising sometimes from PMT-63 punching the shaper. Resistors on the last dynodes dump parasitic oscillatory contours (improve the pulse form).

Condensers between the last dynodes serve only for improvement of the form of an impulse.

The resistor 1 kOm between the anode and the earth is intended for shaper protection. The charge flows down on this resistor from the anode when last is disconnected from the shaper. The light-emitting diode informs about current presence in a divider.

4. Testing for ΔE-E counters.

The signal amplitudes for PMT-85, PMT-63 and correlation for the PMT-85 and PMT-63 obtained on cosmic muons are show in Figure 4.

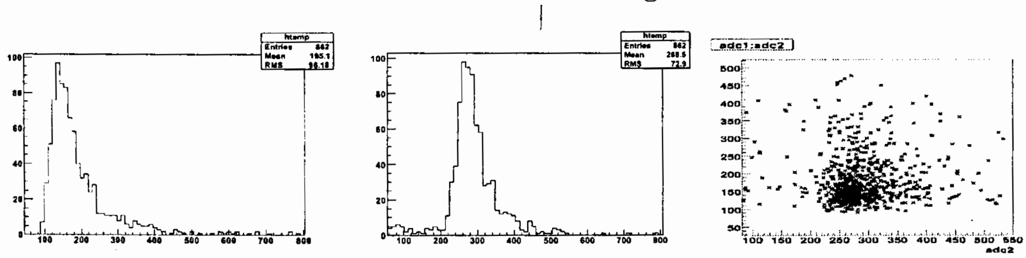

Figure 4: Signal amplitudes obtained on cosmic muons. Left panel is the amplitude from one PMTs 85. Center panel is the amplitude from PMTs 63. Right panel is the correlation of these amplitudes.

The beam test of two ΔE-E detectors at ITS has been performed at the initial deuteron kinetic energy of 2.3 GeV in June 2008. During this test a new DAQ-system based on the trigger LT320D module has been used. One of the important advantages of this module is the possibility to control the status of majority coincidence circuit on-line. The trigger used was the coincidence of the signals from 2 ΔE-E detectors located in the horizontal plane on the left and right from the initial beam direction.

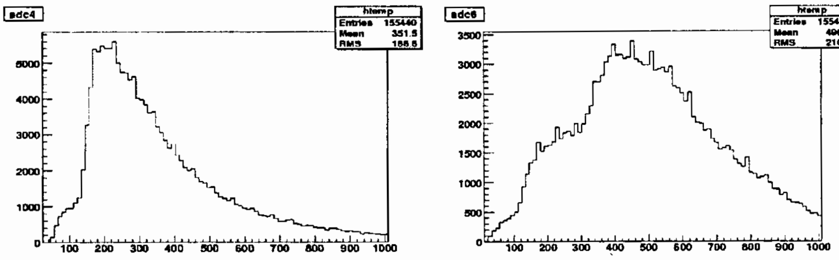

Figure 5: The amplitude from one of the PMTs 85 and the amplitude from PMTs 63 of the same detector.

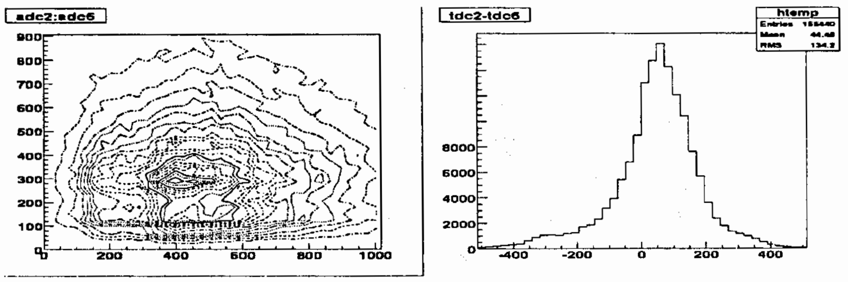

Figure 6: The correlation of amplitudes from two E-detectors and their time-of-flight difference.

First results for the beam test of ΔE-E counters are presented in Figs.5,6. The signal amplitudes from the thin and thick plastic scintillator are shown in the left and right panels of the Fig.5, respectively. The results on the correlation of the energy depositions in two E- scintillation counters and their time-of-flight difference are given in Fig.6.

5. Modernization of ΔE-E detectors.

The modernization of ΔE-E detectors consists in diminution of diameter of ΔE scintillator to 8 cm. It has allowed to reduce the solid angle for detected nucleons. Solid angle reduction allows to exclude nucleons which take off through a E - scintillator lateral side. This detector was tested with cosmic muons. Results of calibration are presented on Figure 7. Pedestal is disposed in 23 bin. Mean size of amplitude distribution from E - scintillator is equal 243 channels. 10 channels are equal 1.8 MeV for this configuration of the detector.

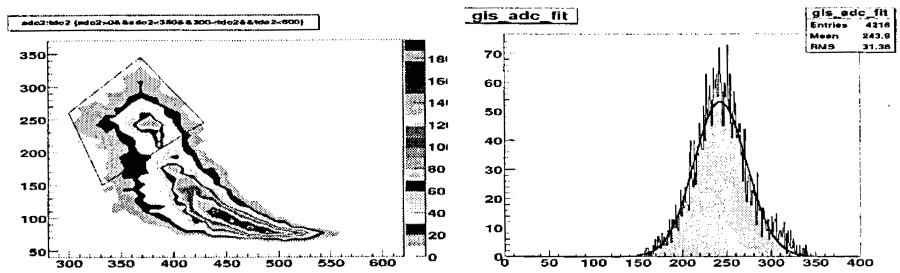

Figure 7: Results of calibration ΔE-E detector with cosmic muons.

6. The high voltage system.

The high voltage digital dividers of PMTs-85 were controlled by the module connected with computer through the bus RS-232. This system was designed at LHEP-JINR [8]. The high voltage system for PMTs-63 is based on "Wenzel Electronik" module, whose voltage is adjusted and checked on-line using DAC and ADC CAMAC modules (see Figure 8).

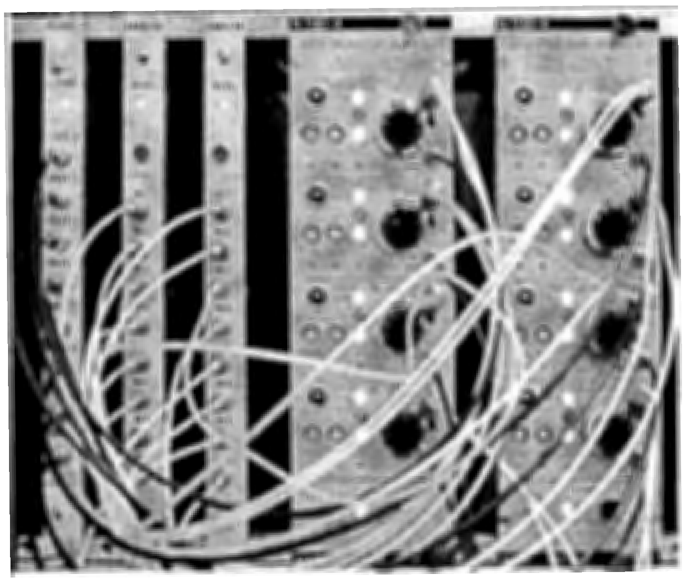

Figure 8: The high voltage system for PMTs-63

The versatile DAQ system for middle range physics experiments MIDAS [9] was used for on-line control of high voltage provided by "Wenzel Electronik". The system demonstrated good time stability during beam test.

7. Hardware bay.

Hardware bay consists of 4 vertical steel arc. Each arc can move in the horizontal plane(see Figure 9). Two carriages for ΔE-E counters can take up position on the arc. Counters move relatively to arc in the vertical plane.

Figure 9: The hardware bay for 8 ΔE-E counters.

8. Conclusion

The following results of the preparation of the setup for the investigation of dp-breakup was obtained:

- Systems of high-voltage system and DAQ were modernized;
- ΔE-E scintillation counter to study dp-breakup was designed and manufactured;
- First results on the the ΔE-E counters tests with cosmic muons and with beam at the Internal Target Station at Nuclotron were obtained.

Acknowledgments.

The authors are grateful to Experimental Workshop staff. The work has been supported in part by the RFBR under (grant N^o 07-02-00102a, grant N^o 09-02-09264-mob-z), grant JINR and by the Grant Agency for Science at the Ministry of Education of the Slovak Republic (grant N^o 1/4010/07).

References

[1] R.B. Wiringa, V.G.J. Stoks, and R. Schiavilla., Rhys. Rev. **C51**, (1995) 38.
[2] R. Machleidt, Phys.Rev. **C63**, (2001) 024001.
[3] V.G.J. Stoks, R.A.M. Klomp, C.P.F. Terheggen, and J.J. de Swart., Rhys. Rev. **C49**, (1994) 2950.
[4] W. Glockle, H. Witala, D. Huber, H. Kamada, and J.Golak, Phys. Rep. **274**, 107 (1996).
[5] T. Uesaka, V.P. Ladygin, et al., Phys.Part.Nucl.Lett. **3**, (2006) 305.
[6] St. Kistryn et al. **nucl-ex/0508012v1**, (2005).
[7] J. Kuros-Zolnierczuk et al. **nucl-th/0203017v1**, (2002).
[8] http://hvsys.dubna.ru.
[9] http://midas.psi.ch.

DEUTERON BEAM POLARIMETER AT THE INTERNAL TARGET STATION AT NUCLOTRON

P.K. Kurilkin[a,k,1], K. Suda[b], T. Uesaka[c], V.P. Ladygin[a,k], Yu.V. Gurchin[a], A.Yu. Isupov[a], K. Itoh[d], M. Janek[a,e], J.–T. Karachuk[a,f], T. Kawabata[c], A.N. Khrenov[a], A.S. Kiselev[a], V.A. Kizka[a], V.A. Krasnov[a,g], N.B. Ladygina[a], A.N. Livanov[a,g], Y. Maeda[h], A.I. Malakhov[a], S.G. Reznikov[a], S. Sakaguchi[c], H. Sakai[c,i], Y. Sasamoto[c], K. Sekiguchi[b], M.A. Shikhalev[a], T.A. Vasiliev[a,k] and H. Witala[j]

a) JINR, 141980, Dubna, Moscow region, Russia
b) IPCR (RIKEN), Saitama 351-0198, Wako, Japan
c) CNS, University of Tokyo, Saitama 351-0198, Wako, Japan
d) Department of Physics, 255 Shimo-Okubo, Saitama University, Urawa, Saitama 338, Japan
e) IEP SAS, 04001, Košice, Slovak Republic
f) Advanced Research Institute for Electrical Engineering, 74204, Bucharest, Romania
g) INR RAS, 117312, Moscow, Russia
h) Kyushi University, Fukuoka 812-8581, Hakozaki, Japan
i) University of Tokyo, 113-0033, Tokyo, Japan
j) M. Smoluchowski Institute of Physics, Jagiellonian University, PL-30-059, Kraków, Poland
k) Moscow State Institute of Radio-engineering, Electronics and Automation (Technical University), Moscow, Russia

Abstract

A polarimeter based on the asymmetry measurement of the deuteron-proton elastic scattering has been constructed at Internal Target Station of Nuclotron-M(JINR). The polarimeter allows to measure vector and tensor components of the deuteron beam polarization. The results of the deuteron beam polarization completed at the energy of 270 MeV are given.

The analyzing powers A_y, A_{yy} and A_{xx} in $d-p$ elastic scattering at the energy of 0.88 and 2.0 GeV are obtained. The analyzing powers of the reaction have the sufficiently large values for conducting the efficient polarimetry in a wide energy region of deuteron.

1. Introduction

Spin physics studies with intermediate energy polarized deuteron beams have been proposed at different facilities. Measurement of the beam polarization is an important element in such experiments. Since deuteron is a spin−1 particle, the deuteron beam has vector and tensor polarization in general. The polarimetry should have a capability to determine both components of polarization, if possible, simultaneously.

The polarimetry based on zero−degree inclusive deuteron breakup from a proton target[1] and pp quasi−elastic scattering[2] are currently used at LHEP Accelerator Complex to provide the polarimetry of the deuterons at GeV−energies. However, these reactions have not vector and tensor analyzing power, respectively. On the other hand, the $d-p$ elastic scattering at forward scattering angles is traditionally used for the tensor and vector polarimetry at intermediate energies. The polarization of the

[1]E–mail: `pkurilkin.jinr.ru`

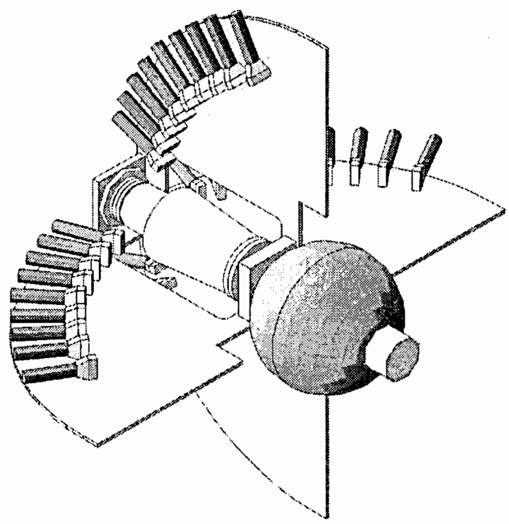

Figure 1: Schematic view of the detector setup.

deuteron beam was measured using the $d-p$ elastic scattering at 1600 MeV at forward angles where vector A_y and tensor A_{yy} analyzing powers have large values with two-arm magnetic spectrometer ALPHA[3]. It was demonstrated recently at COSY at ANKE spectrometer[4] at the initial deuteron energy of 1170 MeV that the vector and tensor analyzing powers for $d-p$ elastic scattering are also large. The $d-p$ elastic scattering at large angles has been successfully used for deuteron beam polarimetry at RIKEN[5].

The aim of the experiment is to obtain the A_y, A_{yy}, and A_{xx} analyzing powers in the $d-p$ elastic scattering at large angles at the 270–2000 MeV energy range. Also the possibility to the use this reaction for the efficient polarimetry of deuterons is studied. It has several advantage as a beam–line polarimetry over the others. Firstly, both vector and tensor analyzing powers for the reaction have large values[6]-[9]. Secondly, the kinematical coincidences measurement of deuteron and proton with plastic scintillation counters suffices for event identification. This is mainly due to a small background event rate, compared with the forward angles.

The analyzing powers data at the energies in a GeV region are necessary for the DSS project at Nuclotron–M[10]. For the measurements of the polarization observables in the ^{3}He(d,p)^{4}He reaction it is necessary to know of the both vector and tensor polarization of the deuteron beam. New facility RIBF at RIKEN will have polarized deuterons at 880 MeV and, therefore, also require the development of the high energy polarimetry.

2. Polarimeter

The polarimeter was constructed at the Internal Target Station(ITS) of Nuclotron-M[11]. This target station is composed of a spherical hull, a beam duct and the target stage where the target holder currying up to six different targets is located. The details of ITS can be found in Ref.[11].

A schematic view of the polarimeter is shown in Fig.1. A detector support to install deuteron and proton detectors is placed downstream of the ITS. 48 plastic scintillation counters are placed in horizontal and vertical planes. Each of them coupled to a photomultiplier tube Hamamatsu H7416MOD is arranged on the left, right, up and down of the beam axis to allow determination of spin-dependent asymmetry of the reaction. A detector for quasielastic-pp scattering is used as the monitor of beam intensity. Proton detectors are placed 630 mm from the target, while deuteron and quasifree-pp detectors in front of proton detectors. The scattered deuterons and recoil proton were detected in kinematical coincidence over the center-of-mass(CM) range of $60 - 140°$. The angular span of one proton detector is $\sim 2°$ in the laboratory frame, which corresponds to $\sim 4°$ in CM system.

The coincidences of the signal from any of LEFT detectors (LP1-9,LD1-4,PPL) and any of RIGHT detectors(RP1-9,RD1-4,PPR) trigger the data taking. VME-CAMAC based DAQ[12] has been used for data taking. The monitor counts as well as a signal about the type of the spin mode of ion source was stored for each beam spill. Quasi-elastic pp scattering at 90° in c.m. (in the horizontal plane) has been used as a luminosity monitor.

The information on the target position across the beam pipe has been used to tune the trajectory of the internal target and accelerator parameters in order to provide the position of the interaction point as much as close to the beam pipe center. These data are important to fix the kinematics and were used also in offline analysis. The typical uncertainty of the interaction point at 270 MeV is ± 1 mm. The details of the target position monitor operation are described in Ref.[13].

3. Experimental procedure

Analyzing powers for the $d-p$ elastic scattering at the energies 880 and 2000 MeV were measured with the newly-constructed polarimeter in June 2005.

Polarized deuterons were provided by PIS("polarized ions sources") POLARIS[14]. In the present experiment the data were taken for unpolarized, "2-6" and "3-5" spin modes of POLARIS [14] which had the following theoretical maximum polarization (p_z, p_{zz})=(0,0),(1/3,1) and (1/3,-1), respectively. The quantization axis is perpendicular to the beam circulation plane of Nuclotron. The spin states of POLARIS were changed spill by spill.

The typical beam intensity in Nuclotron ring was 2-3$\times 10^7$ deuterons per spill. The $10 \mu m$ CH_2 foil was used as a proton target, while the measurements with carbon target were made to estimate the background originating from quasifree scattering on carbon. Prior to the analyzing powers measurement at 880 and 2000 MeV, the beam polarization measurement was carried out at 270 MeV, where well established data on the analyzing powers exist[6]-[9].

4 Data analysis

4.1 Measurement of the beam polarization at 270 MeV.

The beam polarization was determined by using asymmetry of the $d-p$ elastic scattering yields and known analyzing powers of the reaction[7]-[9]. Data at several scattering angles were used in the polarization determination: 75°, 86.5°, 95°, 105°, 115°, 126.3°, and 135°. The analyzing powers values A_y, A_{yy}, A_{xx} and A_{xz} and their errors at these angles were obtained by the cubic spline interpolation of the data from Refs.[7]-[9].

The spin-dependent cross section $\sigma(\Theta)$ for $d-p$ elastic scattering has the following

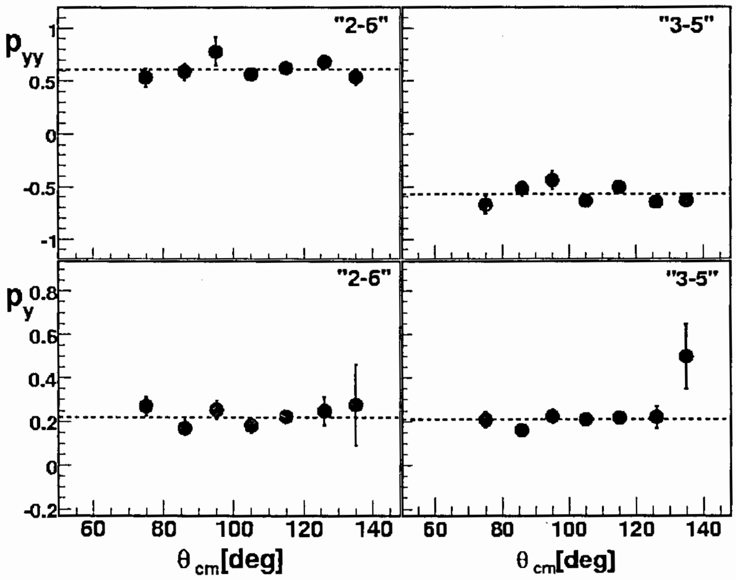

Figure 2: The vector p_y and tensor p_{yy} polarizations of the deuteron beam for "2-6" and "3-5" spin modes of POLARIS[14] obtained at different angles. The error bars include both statistical and systematical uncertainties.

Table 1: Vector p_y and tensor p_{yy} polarizations of the beam for the "2-6" and "3-5" spin modes of POLARIS[14].

Spin mode	P_y	ΔP_y	P_{yy}	ΔP_{yy}
"2-6"	0.216	0.015	0.605	0.025
"3-5"	0.208	0.012	-0.575	0.020

form

$$\sigma(\theta) = \sigma_0(\theta)[1+\frac{3}{2}p_yA_y(\theta)+\frac{2}{3}p_{xz}A_{xz}(\theta)+\frac{1}{3}(2p_{xx}+p_{yy})A_{xx}(\theta)+\frac{1}{3}(2p_{yy}+p_{xx})A_{yy}(\theta)] \quad (1)$$

where $\sigma_0(\Theta)$ is unpolarized cross section, A_y, A_{yy}, A_{xx} and A_{xz} are the deuteron analyzing powers, p_y, p_{yy}, p_{xx} and p_{xz} are the components of the beam polarization[15].

The normalized yields of the $d-p$ elastic events for scattering left (L), right (R), up (U) and down (D) were used for the beam polarization evaluation at the scattering angles $\Theta_{c.m.} \geq 105°$, while only scattering L, R, and D were used at the angles 75°, 86.5° and 95°. The values of the tensor p_{yy} and vector p_y polarizations of the beam for "2-6" and "3-5" spin modes of POLARIS[14] obtained at different angles are presented in Fig.2. The error bars include both statistical and systematical uncertainties. The weighted average values of the beam polarization are given in the table 1. The values of the tensor polarizations obtained at 270 MeV are in a good agreement with the values obtained by the low energy polarimeter based on $^3He(d,p(0°))^4He$ reaction at

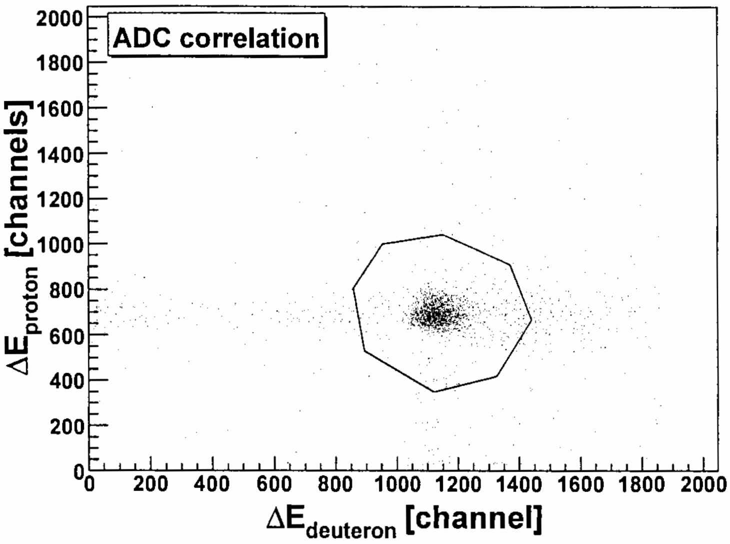

Figure 3: The correlation of the amplitude signals for one pair of the deuteron and proton detectors at 880 MeV. The solid line is the graphical cut for the selection of the $d-p$ elastic events.

10 MeV which where 0.69±0.13 and -0.67±0.16 for the spin modes "2-6" and "3-5" respectively[16]. The value of the angle between the beam direction and polarization axis was found $\beta = -91.0 \pm 1.3°$, therefore, the polarization axis is perpendicular to the plane containing the mean beam orbit in the accelerator.

4.2 Selection of the $d-p$ elastic events at high energies.

The $d-p$ elastic events have been selected using the information on the energy losses in the plastic scintillators by protons and deuterons, their time-of-flight difference and interaction point position.

The contribution of carbon background and accidental coincidences was negligible small at the energy of 270 MeV[17]. The contribution from the carbon content of the CH_2 target was increasing as the initial deuteron energy was increasing. Therefore, the $d-p$ elastic events selection procedure at 880 MeV was different from the procedure at 270 MeV. The $d-p$ elastic events candidates were selected by the correlation of the amplitude signals from the conjugated deuteron and proton detectors obtained on CH_2 target. The typical amplitude correlation for CH_2 target is presented in Fig.3. The graphical cut for the selection of the $d-p$ elastic events candidates is marked by the solid line. The same graphical cut was imposed for the data obtained on the carbon target. The procedure of the $d-p$ elastic events allocation is demonstrated in Fig4. The time difference spectra ΔT_{d-p} for one pair of conjugated deuteron and proton detectors obtained with the criteria on the amplitude signals correlation for the CH_2 and carbon target are shown in Fig.4a by the open and solid histograms, respectively. The CH_2-C subtraction procedure was applied for each pair of the conjugated deuteron and proton detectors at each spin mode of the ion source. The quality of the CH_2-C subtraction is demonstrated in Fig.4b. The $d-p$ elastic events were selected inside

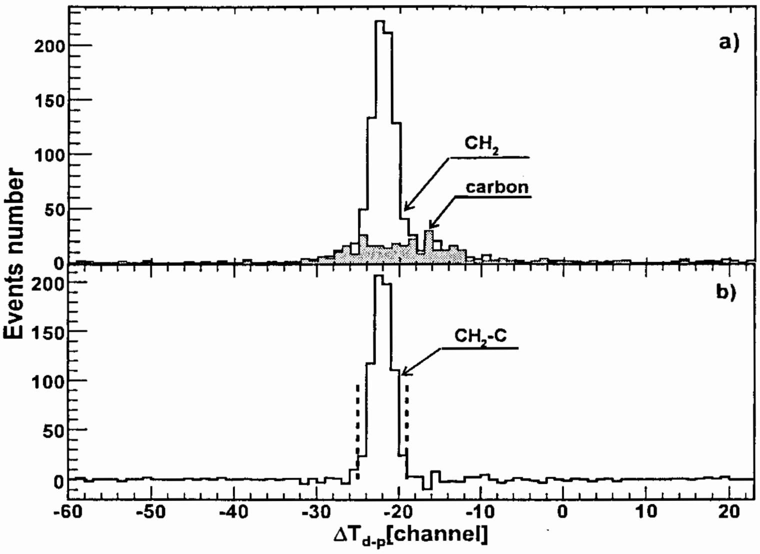

Figure 4: Selection of the $d-p$ elastic events by the time difference ΔT_{d-p} between the signal appearance from deuteron and proton detectors at E_d=880 MeV obtained with the criteria on the amplitude signal correlation.

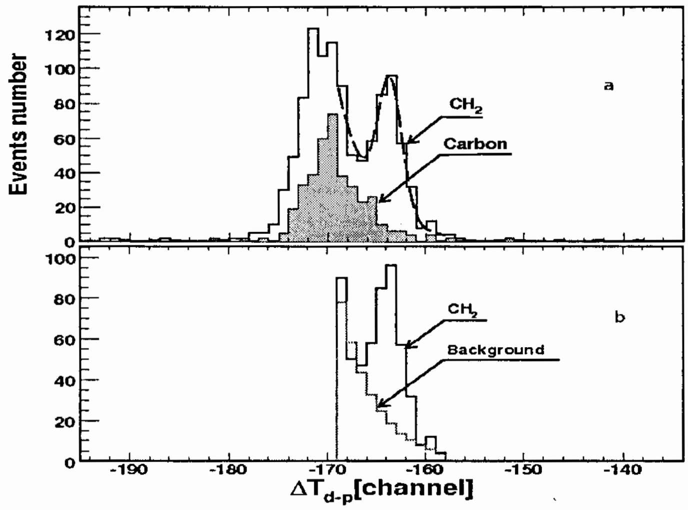

Figure 5: Selection of the $d-p$ elastic events by the time difference ΔT_{d-p} between the signal appearance from deuteron and proton detectors at E_d=2000 MeV obtained with the criteria on the amplitude signal correlation.

the imposed time window shown in Fig.4b by the dashes lines. The contribution from carbon content of CH_2 inside the prompt time window varied between 10 and 25% depending on the detection angle at the energy of 880 MeV.

The allocation of the $d-p$ elastic events at the energy 2000 MeV is different from the procedure of the elastic events getting at the energy 880 MeV. The graphical cut was imposed on the correlation ADC signal from deuteron and proton detectors. The procedure of the $d-p$ elastic events selection is shown in Fig.5. The time difference spectra ΔT_{d-p} for one pair of conjugated deuteron and proton detectors obtained with the criteria on the amplitude signal correlation for the CH_2 target is presented by open histogram in Fig.5a. The like unnormalized spectra obtained on unpolarized spin mode of POLARIS for the carbon target is shown by solid histogram in Fig.5a. The time difference spectra on CH_2 target was fitted a sum of the gaussian and exponential functions. The background was reconstructed by the exponential function. Fig.5b presents the time difference spectra for CH_2 target and reconstructed background spectra. The time gate were imposed to select the $d-p$ elastic events after background subtraction.

4.3 Evaluation of the analyzing powers at 880 and 2000 MeV.

The values of the analyzing powers A_y and A_{yy} at 880 and 2000 MeV were obtained from the following expressions

$$A_y = \frac{3(L-R)}{2p_y} \tag{2}$$

$$A_{yy} = \frac{L+R-2}{p_{yy}} \tag{3}$$

Here L and R are the normalized yields of the selected events to the yield for unpolarized beam for scattering left and right, respectively. Tensor polarization of the beam p_{xx} equal to the p_{yy}, since the beam polarization axis is perpendicular to the plane containing the mean beam orbit in the accelerator. The values of the tensor analyzing power A_{xx} for the scattering angles 70°-140° were obtained as

$$A_{xx} = \frac{U,D-1}{p_{yy}} \tag{4}$$

where U and D are the normalized yields of the selected events for scattering up and down, respectively.

5 Results at 880 and 2000 MeV

The final results on the analyzing powers A_y, A_{yy} and A_{xx} in $d-p$ elastic scattering at 880 MeV are compared with several theoretical predictions in Fig.6. The solid, dash and dash-dotted lines are the calculation performed within Faddeev techniques[18], relativistic multiple scattering model[19] and optical potential framework[20]. The A_y consists with zero at the angle of 60° in c.m.s, while it is about -0.2 at large angles. The A_{xx} has large negative values in the angular region of 60°-90° in c.m.s., nevertheless the A_{yy} is sizable only at the angles 60° and 70°. This make it possible to conduct the efficient deuteron beam polarimetry at the energy of 880 MeV using the $d-p$ elastic scattering at large angles in c.m.s. On the other hand theoretical calculations[18]-[20] predict the large values A_y , A_{yy} and A_{xx} at the angles $\theta_{c.m.} \leq 60°$. It is very desirable to conduct the analyzing powers measurements at these angles.

The results on the vector A_y and tensor A_{yy} analyzing powers at fixed angles in c.m.s are plotted as function of transverse momentum p_T in Fig.7 and in Fig.8, respectively.

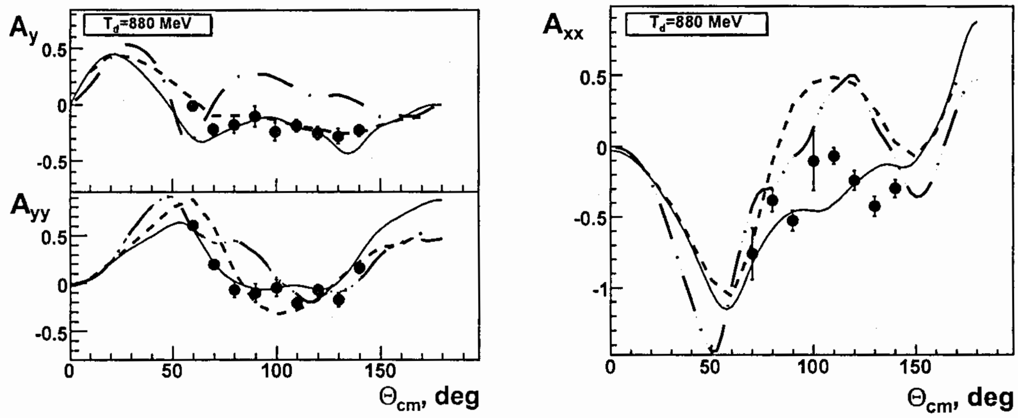

Figure 6: The vector A_y and tensor A_{yy} analyzing powers compared with different theoretical predictions[18]-[20].

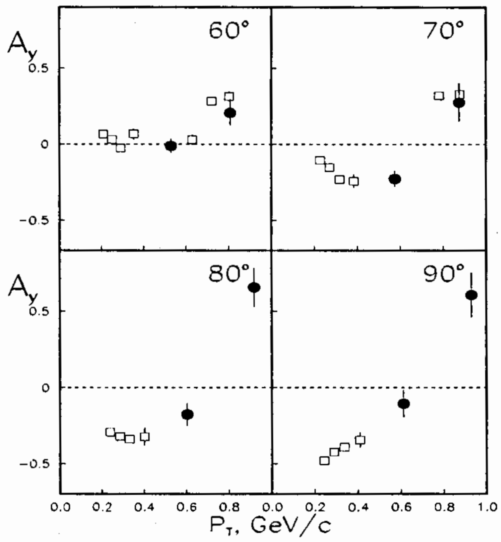

Figure 7: The dependence of the tensor A_y analyzing power in *dp*- elastic scattering at the fixed angles in the c.m.s. as a function of transverse momentum p_T. The open and solid symbols represent data obtained at RIKEN[8], Saclay[23], ANL[24]-[26] and at Nuclotron(Dubna)[21]-[22], respectively.

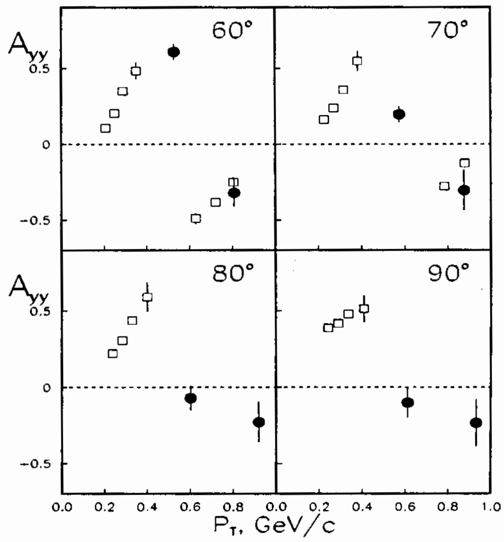

Figure 8: The dependence of the vector $A_y y$ analyzing power in *dp*- elastic scattering at the fixed angles in the c.m.s. as a function of transverse momentum p_T. The open and solid symbols represent data obtained at RIKEN[8], Saclay[23], ANL[24]-[26] and at Nuclotron(Dubna)[21]-[22], respectively.

The open symbols represent the data obtained at RIKEN[7], Saclay[23] and ANL[24]-[26]. Nuclotron data obtained at the energies 880 and 2000 MeV are shown by solid symbols[21]-[22]. Both vector A_y and tensor A_{yy} analyzing powers change the sign at p_T ~600-700 MeV/c. The additional measurement are necessary to understand of such behavior. The absolute values of the analyzing powers at 2000 MeV are sufficiently large to provide the efficient polarimetry of the deuteron beam. However, the measurements with larger statistics are needed.

6. Conclusion

A polarimeter based on the asymmetry measurement of the deuteron-proton elastic scattering has been constructed at Internal Target Station of Nuclotron-M(JINR). The polarimeter allows to measure vector and tensor components of the deuteron beam polarization.

The final results on the vector A_y and tensor A_{yy} and A_{xx} analyzing powers in $d-p$ elastic scattering at the energy of 880 MeV are obtained. The analyzing powers values are sufficiently large to provide the efficient polarimetry of the deuteron beam at this energy. The theoretical models[18]-[20] obtained within the different approaches predict the sizable values of the A_y, A_yy and A_{xx} at the angles $\theta_{c.m.} \leq 60^\circ$. The additional calibration data on the vector and tensor analyzing powers at angles less then 60° are needed.

The results on the vector A_y and tensor A_{yy} are also large, that can provide the deuteron beam polarimetry at this energy. However, the measurements with larger statistic are required.

Obtained experimental data are important for the preparation of the future experiments at LHEP-JINR at Nuclotron-M. The ITS polarimeter will be calibrate at the energies 270-2000 MeV with the expected error bars for analyzing powers ± 0.02.

Acknowledgments

The authors would like to express their gratitude to the Nuclotron accelerator staff. We thank Yu. S. Anisimov, A. F. Elishev, Z. P. Kuznezova, J. Kliman, A. P. Laricheva, A. G. Litvinenko, V. Matoucek, M/Morchar, V. G. Perevozchikov, I. Turso and V. N. Zhmyrov for the help during the preparation and performance of the experiment. This work was supported in part by the Russian Foundation for Basic Research (Grants N^o 07-02-00102a and N^o 09-02-09261-mob-3), the Grant-in-Aid for Scientific Research (Grant N^o 14740151), by the Grant Agency for Science at the Ministry of Education of the Slovak Republic (grant N^o 1/4010/07) and by a Special program of the Ministry of Education and Science of the Russian Federation(grant RNP2.1.1.2512).

References

[1] L.S.Zolin, et al., JINR Rapid Comm. 2[88]-98, p.27, 1998;
Yu.K.Pilipenko, et al., AIP Conf. Proc. **570** p.801, 2001

[2] L.S.Azhgirey, et al., Nucl.Instr.Meth. in Phys.Res. **A497**, p.340, 2003

[3] V.G.Ableev, et al., Nucl.Instr.Meth. **A306** p.73, 1991

[4] D.Chiladze, et al., Phys.Rev.ST Accel.Beams **9** 050101, 2006

[5] K.Suda, et al., Nucl.Instr.Meth. in Phys.Res. **A572**, p.745, 2007

[6] N.Sakamoto, et al., Phys.Lett. **B367** p.60, 1996
[7] K.Sekiguchi, et al., Phys.Rev. **C65** 034003, 2002
[8] K.Sekiguchi, et al., Phys.Rev. **C70** 014001, 2004
[9] K.Suda, et al., Nucl.Instr.Meth. in Phys.Res. **A572**, p.745, 2007
[10] T.Uesaka, et al., DSS Project, (Unpublished)
[11] A.I.Malakhov et al., Nucl. Instrum. Methods. A **440** p.320, 2000.
[12] H.Okamura, Nucl. Instr. Meth. in Phys. Res. A **443** p.194, 2000.
[13] Yu.V.Gurchin, et al., Phys. Part. Nucl. Lett. 4, p.263, 2007
[14] N.G.Anishchenko, et al., AIP Conf.Proc. **95**, p.445, 1983
[15] G.G.Olsen, Rep.Prog.Phys. 35, p.717, 1972
[16] V.P.Ladygin, et al., Proc of the 11-th Intern. Workshop on Polarized Sources and Targets, 14-17 November, 2005 Tokyo, Japan; Eds. T.Uesaka, H.Sakai, A.Yoshimi, K.Asahi, World Scientific Publishing Co.Pte.Ltd., Singapore p.117, 2007
[17] T.Uesaka, et al., Phys.Part.Nucl.Lett. **3**, p.305, 2006
[18] H.Witala, private communications
[19] N.B.Ladygina, Phys. Atom. Nucl. 71:2039-2051, 2008
[20] M.A.Shikhalev, Phys. Atom. Nucl. 72:588-595, 2009
[21] K.Suda, et al., AIP Conf. Proc. **1011** 241, 2008
[22] P.K.Kurilkin, et al., Eur. Phys.J. ST **162** 137, 2008
[23] M.Garson, et al., Nucl. Phys. **A458**, 287-300, 1986
[24] Bleszynski, et al., Phys. Lett. B. **87**, 178, 1979
[25] Bleszynski, et al., Phys. Lett. B. **106**, 42, 1981
[26] M.Haji-Saied, et al., Phys. Rev. C. **36**, 2010, 1987

EFFECTIVE RELATIVISTIC MEAN-FIELD PARAMETERIZATION OF THE DBHF RESULTS

K. Petrík[a,1] and Š. Gmuca[a]

a) Institute of Physics, Slovak Academy of Sciences, Dubravska cesta 9, SK-845 11 Bratislava 45, Slovakia

Abstract

Microscopic calculations based on the Dirac-Brueckner-Hartree-Fock (DBHF) approach with realistic nucleon-nucleon potential are used to adjust a relativistic mean-field theory (RMFT) parameterization. RMFT allows a clear interpretation of the role of the mesons, especially the isoscalar-scalar σ, the isoscalar-vector ω, the isovector-vector ρ, and the isovector-scalar δ in the equation of state. The new results are compared with several older microscopic approaches that allows an adequate investigation of the main differences between them. Different self-interactions and vector ω-ρ cross-interaction with their effects were examined in order to get a proper reproduction of the new DBHF data. It is shown that inclusion of vector cross-interaction is inevitable for correct description of the predicted nuclear symmetry energy.

1. Introduction

An *ab initio* description of dense nuclear matter which is based on QCD as the fundamental theory of strong interaction is presently not possible. The main reason lies in the highly non-perturbative character of the formation of hadronic bound states and their interactions. Therefore a quantitative description of nuclear many-body systems has to be based on effective theories. Particularly successful are theories which effective degrees of freedom are hadrons - nucleons (and their excited states) and mesons. However, also within microscopic hadronic theories a perturbative approach to the strong interacting nuclear systems is not possible [1]. A systematic summation of diagrams up to infinite order in terms of the Brueckner hole-line expansion turned out to be one of appropriate treatments. Already in lowest order which corresponds to standard nonrelativistic Brueckner theory the saturation of nuclear matter can be described at least qualitatively [2, 3, 4]. The another advantage of the Brueckner theory is that the free NN interaction is used, thus, there are no parameters in the force which are adjusted in the many-body problem. Nevertheless, nonrelativistic Brueckner calculations are not able to meet the empirical saturation point of nuclear matter. The results obtained using a variety of NN potentials show a systematic behaviour: the predictions for nuclear matter saturation are located along a band which does not meet the empirical area. This phenomenon is denoted by the "Coester band" [3]. The failure of this model to explain nuclear saturation indicates that one may have to extend the model.

In the last few years, the study of the equation of state (EoS) of nuclear matter has instigated strong theoretical activity. The interest for the nuclear EoS lies, in the main, on the study of supernovae and compact objects - mostly neutron stars. In particular, the structure of a neutron star is very sensitive to the compressibility and the symmetry energy of nuclear matter. For that, several phenomenological and microscopic models of the EoS have been developed. The former models include nonrelativistic mean field

[1]E-mail: kristian.petrik@savba.sk

theory based on Skyrme interactions [8] and relativistic mean field theory based on meson exchange interactions - Walecka's quantum hadrodynamics (QHD) [9]. The latter ones include nonrelativistic Brueckner–Hartree–Fock (BHF) theory [10] and the nonrelativistic variational approach corrected by relativistic effects [11].

Inspired by successes of relativistic description of nuclear systems, a relativistic extension of BHF theory has been suggested by Shakin and collaborators [12, 13], frequently called the Dirac-Brueckner approach. When first relativistic Dirac-Brueckner-Hartree-Fock (DBHF) calculations were performed in the eighties [12, 14, 15] a breakthrough was achieved. The common feature of all Dirac-Brueckner results was that a repulsive relativistic many-body effect was obtained which is strongly density-dependent such that the empirical nuclear matter saturation can be explained. The Coester line was shifted much closer towards the empirical area of saturation.

Despite evident successes of Dirac-Brueckner approach the DBHF framework is very complex and elaborate. Relativistic calculations are not straightforward and the methods of various groups are similar but differ in details, depending on solution techniques and the particular approximations made. Due to its complexity, this advanced approach is successfully manageable for nuclear matter properties only; fully consistent application to finite nuclei description has not been achieved yet. These difficulties can be partially overcome by fitting of the free parameters of relativistic mean-field theory to the results of DBHF calculations for symmetric and asymmetric nuclear matter, which provides an effective parametrization of DBHF theory and indirect connection to bare NN potential. Numerous calculations have established that relativistic mean-field (RMF) models, like quantum hadrodynamics, with such effective parameterization provide a reliable tool for realistic description of the bulk properties of finite nuclei and nuclear matter [16,17]. In addition to this successful low-energy phenomenology, these models are often extrapolated into regimes of high density and temperature to extract the nuclear equation of state. The relativistic mean field theory has been also widely used in determining total masses and radii of neutron stars. The QHD approach to the dense nuclear matter is therefore believed to be the eligible tool that can help us to better understand the role of EoS in the physics of compact stars.

The main objective of this contribution is to obtain a reliable mean-field parametrization that could be applied to asymmetric nuclear matter study and compact stars calculations, using different degrees of freedom in order to investigate the influence of different meson self- and cross-interactions on quality of reproduction of the DBHF results as well as their effects on calculated nuclear matter properties, especially on the nuclear symmetry energy.

The article is organized as follows. In Section 2, we discuss the main details of the theoretical framework for the nonlinear relativistic mean-field (RMF) model based on nucleon-meson interactions. Fitting procedure of mean-field parameterization and following results on the isospin-dependent properties of asymmetric nuclear matter are analyzed in Section 3. A summary is then given in Section 4.

2. Formalism

The detailed dynamics of the relativistic nuclear many-body problem must be specified by choosing a particular Lagrangian density. In the case of nonlinear RMF model Lagrangian generally includes the nucleon field in the form of isospinor ψ, the isoscalar-scalar meson field σ, the isoscalar-vector meson field ω, the isovector-vector meson field

$\boldsymbol{\rho}$, and the isovector-scalar meson field $\boldsymbol{\delta}$,

$$
\begin{aligned}
\mathcal{L} = \bar{\psi}\Big[& i\gamma^\mu\partial_\mu - (m_N - g_\sigma\hat{\sigma} - g_\delta\boldsymbol{\tau}\cdot\hat{\boldsymbol{\delta}}) - g_\omega\hat{\omega}_\mu\gamma^\mu - g_\rho\boldsymbol{\tau}\cdot\hat{\boldsymbol{\rho}}_\mu\gamma^\mu\Big]\psi \\
&+\frac{1}{2}\partial_\mu\hat{\sigma}\partial^\mu\hat{\sigma} - \frac{1}{2}m_\sigma^2\hat{\sigma}^2 - \frac{1}{4}\hat{\omega}_{\mu\nu}\hat{\omega}^{\mu\nu} + \frac{1}{2}m_\omega^2\hat{\omega}_\mu\hat{\omega}^\mu \\
&+\frac{1}{2}\partial_\mu\hat{\boldsymbol{\delta}}\partial^\mu\hat{\boldsymbol{\delta}} - \frac{1}{2}m_\delta^2\hat{\boldsymbol{\delta}}^2 - \frac{1}{4}\hat{\boldsymbol{\rho}}_{\mu\nu}\cdot\hat{\boldsymbol{\rho}}^{\mu\nu} + \frac{1}{2}m_\rho^2\hat{\boldsymbol{\rho}}_\mu\cdot\hat{\boldsymbol{\rho}}^\mu \\
&-\frac{1}{3}b_\sigma m_N(g_\sigma\hat{\sigma})^3 - \frac{1}{4}c_\sigma(g_\sigma\hat{\sigma})^4 + \frac{1}{4}c_\omega(g_\omega^2\hat{\omega}_\mu\hat{\omega}^\mu)^2 + \frac{1}{4}c_\rho(g_\rho^2\hat{\boldsymbol{\rho}}_\mu\cdot\hat{\boldsymbol{\rho}}^\mu)^2 \\
&+\frac{1}{2}\Lambda_{vv}(g_\rho^2\hat{\boldsymbol{\rho}}_\mu\cdot\hat{\boldsymbol{\rho}}^\mu)(g_\omega^2\hat{\omega}_\mu\hat{\omega}^\mu) + \frac{1}{2}\Lambda_{vs}(g_\rho^2\hat{\boldsymbol{\rho}}_\mu\cdot\hat{\boldsymbol{\rho}}^\mu)(g_\sigma^2\hat{\sigma}^2),
\end{aligned}
\tag{1}
$$

where antisymmetric tensors are of the form

$$
\begin{aligned}
\hat{\omega}_{\mu\nu} &= \partial_\mu\hat{\omega}_\nu - \partial_\nu\hat{\omega}_\mu, \\
\hat{\phi}_{\mu\nu} &= \partial_\mu\hat{\phi}_\nu - \partial_\nu\hat{\phi}_\mu, \\
\hat{\boldsymbol{\rho}}_{\mu\nu} &= \partial_\mu\hat{\boldsymbol{\rho}}_\nu - \partial_\nu\hat{\boldsymbol{\rho}}_\mu.
\end{aligned}
\tag{2}
$$

In addition to nucleon-meson interactions the Lagrangian density includes the scalar b_σ, c_σ and the vector c_ω self-interactions, and the isovector vector c_ρ self-interaction [18, 19, 20, 21]. Finally, the nonlinear cross-interactions Λ_{vv} and Λ_{vs} [22, 23] are included to modify the density dependence of the symmetry energy $a_{sym}(\rho_B)$. We neglect the electromagnetic field in the following since in the present work we are interested in the properties of infinite nuclear matter.

The free parameters entering the Lagrangian are baryon and meson masses and dimensionless coupling constants, which define the strength of interaction terms, other symbols have their usual meanings.

The field equations for this model follow from the Euler-Lagrange equations in a standard way. The resulting Dirac equation for the baryon field is of the form

$$
[i\gamma^\mu\partial_\mu - (m_N - g_\sigma\hat{\sigma} - g_\delta\boldsymbol{\tau}\cdot\hat{\boldsymbol{\delta}}) - g_\omega\hat{\omega}_\mu\gamma^\mu - g_\rho\boldsymbol{\tau}\cdot\hat{\boldsymbol{\rho}}_\mu\gamma^\mu]\psi = 0. \tag{3}
$$

Meson fields with *spin 0* are described by the Klein-Gordon equations

$$
\begin{aligned}
g_\sigma\bar{\psi}\psi &= (\Box + m_\sigma^2)\hat{\sigma} + b_\sigma m_N g_\sigma^3\hat{\sigma}^2 + c_\sigma g_\sigma^4\hat{\sigma}^3 - \Lambda_{vs}g_\rho^2 g_\sigma^2(\hat{\boldsymbol{\rho}}_\nu\cdot\hat{\boldsymbol{\rho}}^\nu\hat{\sigma}), \\
g_\delta\bar{\psi}\boldsymbol{\tau}\psi &= (\Box + m_\delta^2)\hat{\boldsymbol{\delta}},
\end{aligned}
\tag{4}
$$

and meson fields with *spin 1* by the Proca equations

$$
\begin{aligned}
g_\omega\bar{\psi}\gamma_\mu\psi &= (\Box + m_\omega^2)\hat{\omega}_\mu - \partial_\mu\partial^\nu\hat{\omega}_\nu + c_\omega g_\omega^4(\hat{\omega}^\nu\hat{\omega}_\nu\hat{\omega}_\mu) + \Lambda_{vv}g_\rho^2 g_\omega^2(\hat{\boldsymbol{\rho}}_\nu\cdot\hat{\boldsymbol{\rho}}^\nu\hat{\omega}_\mu), \\
g_\rho\bar{\psi}\gamma_\mu\boldsymbol{\tau}\psi &= (\Box + m_\rho^2)\hat{\boldsymbol{\rho}}_\mu - \partial_\mu\partial^\nu\hat{\boldsymbol{\rho}}_\nu + c_\rho g_\rho^4(\hat{\boldsymbol{\rho}}_\mu\hat{\boldsymbol{\rho}}_\nu\cdot\hat{\boldsymbol{\rho}}^\nu) \\
&\quad + \Lambda_{vv}g_\rho^2 g_\omega^2(\hat{\boldsymbol{\rho}}_\mu\hat{\omega}_\nu\hat{\omega}^\nu) + \Lambda_{vs}g_\rho^2 g_\sigma^2(\hat{\boldsymbol{\rho}}_\mu\hat{\sigma}^2).
\end{aligned}
\tag{5}
$$

When quantized, meson field equations become nonlinear quantum field equations, whose exact solutions are very complicated, moreover, the coupling constants are large, so perturbative solutions are not useful. Two approximations are necessary to circumvent this problem: *relativistic mean-field approximation* in which operators of meson fields are replaced by their expectation values and *no-sea approximation* introduced by exclusion of the filled Dirac sea of negative energy states.

For a static, homogenous infinite nuclear matter, all derivative terms drop out and expectation values of space-like components of vector fields vanish due to rotational symmetry and translational invariance of the nuclear matter. In addition, only the third component of isovector fields needs to be taken into account due to rotational invariance around the third axis in the isospin space.

In brief,

$$\hat{\sigma} \longrightarrow \bar{\sigma}, \quad \hat{\omega}_\mu \longrightarrow \bar{\omega}_0, \quad \hat{\boldsymbol{\rho}}_\mu \longrightarrow \bar{\rho}_{03}, \quad \hat{\boldsymbol{\delta}} \longrightarrow \bar{\delta}_3, \quad \hat{\sigma}^* \longrightarrow \bar{\sigma}^*, \quad \hat{\phi}_\mu \longrightarrow \bar{\phi}_0. \tag{6}$$

This greatly simplifies the remaining problem; consequently the meson equations could be expressed in a reduced form

$$\begin{aligned}
g_\sigma\bar{\sigma} &= \left(\frac{g_\sigma}{m_\sigma}\right)^2 \left[\bar{\rho}_s - b_\sigma m_N (g_\sigma\bar{\sigma})^2 - c_\sigma (g_\sigma\bar{\sigma})^3 + \Lambda_{vs}(g_\sigma\bar{\sigma})(g_\rho\bar{\rho}_{03})^2\right], \\
g_\omega\bar{\omega}_0 &= \left(\frac{g_\omega}{m_\omega}\right)^2 \left[\bar{\rho}_v - c_\omega (g_\omega\bar{\omega}_0)^3 - \Lambda_{vv}(g_\omega\bar{\omega}_0)(g_\rho\bar{\rho}_{03})^2\right], \\
g_\rho\bar{\rho}_{03} &= \left(\frac{g_\rho}{m_\rho}\right)^2 \left[\bar{\rho}_{iv} - c_\rho (g_\rho\bar{\rho}_{03})^3 - \Lambda_{vv}(g_\rho\bar{\rho}_{03})(g_\omega\bar{\omega}_0)^2 - \Lambda_{vs}(g_\rho\bar{\rho}_{03})(g_\sigma\bar{\sigma})^2\right], \\
g_\delta\bar{\delta}_3 &= \left(\frac{g_\delta}{m_\delta}\right)^2 \bar{\rho}_{is},
\end{aligned}$$

where the source scalar density $\bar{\rho}_s$, isovector scalar density $\bar{\rho}_{is}$, baryon vector density $\bar{\rho}_v$, and isovector vector density $\bar{\rho}_{iv}$ are as follows

$$\bar{\rho}_s = \langle\bar{\psi}\psi\rangle_{GS} = \sum_{B=p,n} \rho_{sB} = \sum_{B=p,n} \frac{2J_B+1}{2\pi^2} \int_0^{k_{FB}} \frac{k^2 m_B^*}{\sqrt{k^2 + m_B^{*2}}} dk, \tag{7}$$

$$\bar{\rho}_{is} = \langle\bar{\psi}\tau_3\psi\rangle_{GS} = \sum_{B=p,n} \rho_{isB} = \sum_{B=p,n} \tau_{3B} \frac{2J_B+1}{2\pi^2} \int_0^{k_{FB}} \frac{k^2 m_B^*}{\sqrt{k^2 + m_B^{*2}}} dk, \tag{8}$$

$$\bar{\rho}_v = \rho_B = \langle\bar{\psi}\gamma_0\psi\rangle_{GS} = \sum_{B=p,n} \rho_{vB} = \sum_{B=p,n} \frac{2J_B+1}{2\pi^2} \int_0^{k_{FB}} k^2 dk = \sum_{B=p,n} \frac{k_{FB}^3}{3\pi^2}, \tag{9}$$

$$\bar{\rho}_{iv} = \langle\bar{\psi}\gamma_0\tau_3\psi\rangle_{GS} = \sum_{B=p,n} \rho_{ivB} = \sum_{B=p,n} \rho_{vB}\tau_{3B} = \sum_{B} \tau_{3B} \frac{2J_B+1}{2\pi^2} \int_0^{k_{FB}} k^2 dk. \tag{10}$$

The set of coupled equations for the baryon and meson fields can be solved self-consistently using the iteration procedure, and the properties of the nuclear matter can be then obtained from these fields. Subsequently, from the energy-momentum tensor [24]

$$T^{\mu\nu} = \frac{\partial\mathcal{L}}{\partial(\partial_\mu\psi)}\partial^\nu\psi - g^{\mu\nu}\mathcal{L} = (\epsilon + P)u_\mu u_\nu - g^{\mu\nu}P, \tag{11}$$

we can calculate the energy density ϵ and pressure P of asymmetric nuclear matter, and the results are given by

$$
\begin{aligned}
\epsilon = &\frac{1}{2}m_\sigma^2\bar{\sigma}^2 - \frac{1}{2}m_\omega^2\bar{\omega}_0^2 + \frac{1}{2}m_\delta^2\bar{\delta}_3^2 - \frac{1}{2}m_\rho^2\bar{\rho}_{03}^2 \\
&+\frac{1}{3}b_\sigma m_N(g_\sigma\bar{\sigma})^3 + \frac{1}{4}c_\sigma(g_\sigma\bar{\sigma})^4 - \frac{1}{4}c_\omega(g_\omega\bar{\omega}_0)^4 - \frac{1}{4}c_\rho(g_\rho\bar{\rho}_{03})^4 \\
&-\frac{1}{2}\Lambda_{vv}(g_\rho\bar{\rho}_{03})^2(g_\omega\bar{\omega}_0)^2 - \frac{1}{2}\Lambda_{vs}(g_\rho\bar{\rho}_{03})^2(g_\sigma\bar{\sigma})^2 \\
&+\sum_{B=p,n} g_\omega\bar{\omega}_0\Big(\frac{2J_B+1}{2\pi^2}\int_0^{k_{FB}} k^2 dk\Big) + \sum_{B=p,n} g_\rho\bar{\rho}_{03}\tau_{3B}\Big(\frac{2J_B+1}{2\pi^2}\int_0^{k_{FB}} k^2 dk\Big) \\
&+\sum_{B=p,n}\Big(\frac{2J_B+1}{2\pi^2}\int_0^{k_{FB}} k^2\sqrt{k^2+m_B^{*2}}dk\Big),
\end{aligned}
\tag{12}
$$

and

$$
\begin{aligned}
P = &-\frac{1}{2}m_\sigma^2\bar{\sigma}^2 + \frac{1}{2}m_\omega^2\bar{\omega}_0^2 - \frac{1}{2}m_\delta^2\bar{\delta}_3^2 + \frac{1}{2}m_\rho^2\bar{\rho}_{03}^2 \\
&-\frac{1}{3}b_\sigma m_N(g_{\sigma N}\bar{\sigma})^3 - \frac{1}{4}c_\sigma(g_{\sigma N}\bar{\sigma})^4 + \frac{1}{4}c_\omega(g_{\omega N}\bar{\omega}_0)^4 + \frac{1}{4}c_\rho(g_{\rho N}\bar{\rho}_{03})^4 \\
&+\frac{1}{2}\Lambda_{vv}(g_{\rho N}\bar{\rho}_{03})^2(g_{\omega N}\bar{\omega}_0)^2 + \frac{1}{2}\Lambda_{vs}(g_{\rho N}\bar{\rho}_{03})^2(g_{\sigma N}\bar{\sigma})^2 \\
&+\frac{1}{3}\sum_{B=p,n}\Big(\frac{2J_B+1}{2\pi^2}\int_0^{k_{FB}} \frac{k^4}{\sqrt{k^2+m_B^{*2}}}dk\Big).
\end{aligned}
$$

The binding energy per baryon can be obtained from the energy density via

$$
E_{\mathcal{B}} = \frac{\epsilon}{\rho_{\mathcal{B}}} - m_N, \tag{13}
$$

while the symmetry energy can be expressed from generic series

$$
E(\rho_{\mathcal{B}},\alpha) = E(\rho_{\mathcal{B}},0) + E_{sym}(\rho_{\mathcal{B}})\alpha^2 + \mathcal{O}(\alpha^4), \tag{14}
$$

where $\rho_{\mathcal{B}} = \rho_p + \rho_n$ is the baryon density, $\alpha = (\rho_n - \rho_p)/(\rho_p + \rho_n)$ is the isospin asymmetry and $E(\rho_{\mathcal{B}},0)$ is the binding energy per nucleon in symmetric nuclear matter. Nuclear symmetry energy is thus given by

$$
E_{sym}(\rho_{\mathcal{B}}) = \frac{1}{2}\frac{\partial^2 E(\rho_{\mathcal{B}},\alpha)}{\partial\alpha^2}\Big|_{\alpha=0}. \tag{15}
$$

The absence of odd order terms in α in Eq. (14) is due to the charge symmetry of nuclear forces, moreover, the higher-order terms in α are negligible, which has been verified by all many-body theories to date, at least for densities up to moderate values.

3. Results and Discussion

The new RMFT parameterization was obtained by adjusting free parameters of QHD model to fit the DBHF results for nuclear matter obtained by van Dalen, Fuchs and Faessler [25]. This group has investigated the properties of asymmetric nuclear matter in the DBHF framework based on projection techniques using the Bonn A potential and bare NN matrix elements. The potential matrix elements have been adapted for isospin asymmetric nuclear matter in order to account for the proton-neutron mass splitting. Furthermore, additional parameterizations were acquired using two older DBHF data calculated by Lee, Kuo, Li, and Brown [26, 27], and Huber, Weber, and Weigel [28, 29]. Again, the Bonn A potential was employed in both cases. This was done to compare the new fit with the older ones and to investigate and discuss the main differences. All of these Brueckner calculations are still too complex to utilize them to finite nuclei, on the other hand they can be used as a guidance to construct a RMF theory, which can be easily applied to finite nuclei or nuclear matter. In our case, the mean-field model was fitted to DBHF results by use of the optimization process, employing the least squares method based on principle of maximum likelihood. The DBHF binding energies per baryon for various asymmetries along with the neutron effective mass were taken as an input to the fitting procedure. In the case of older DBHF results also the scalar and the vector potentials were considered.

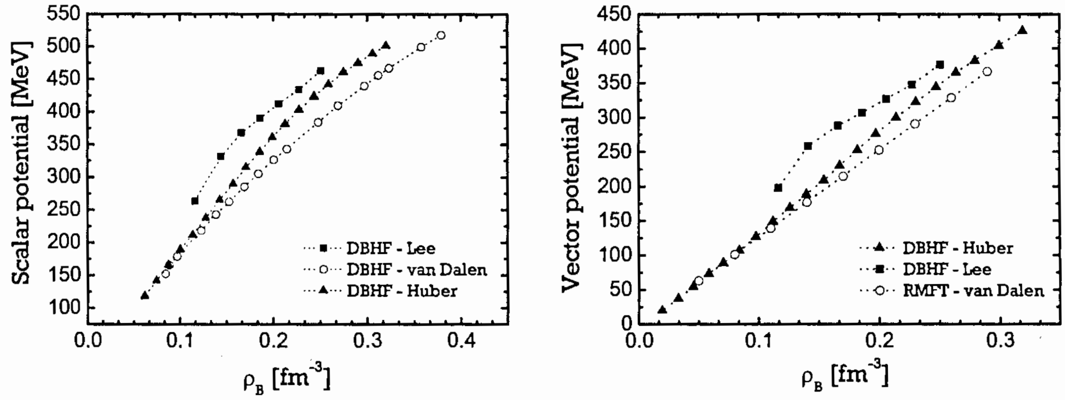

Figure 1: Density dependencies of the scalar and vector potentials leading from the DBHF theory of various groups.

Initial data were weighted correspondingly to their physical significance - uncertainties 0.3 MeV for binding energy and 5 MeV for potentials have been chosen. Value 0.3 MeV is the usual estimation which stems from empirical evaluations of nuclear matter properties, whereas 5 MeV originates from the violation of the Hugenholtz-Van Hove's theorem within the DBHF theory. In the process of mapping of the RMF model on this microscopic theory one should cover this fact by introducing an additional uncertainty in the potentials, which value is related to the extent of violation.

The fit was performed in the first step using nucleons N, scalar σ, vector ω and vector ρ mesons as degrees of freedom, then scalar cubic b_σ and quartic c_σ self-interactions, and vector quartic c_ω self-interaction.

Some of the DBHF data could not be properly reproduced by the fitted functions without introducing the isovector-scalar channel - δ meson. It is due to important role of this meson in the description of nucleon effective mass-splitting as well as the properties of asymmetric nuclear matter. This fact is straightforward because the DBHF calculations based on projection techniques predict a Dirac effective mass splitting of $m_n^* < m_p^*$ in whole density range. The DBHF result of van Dalen *et al.* is example of such an approach. The RMF theories with the isovector ρ and δ mesons included predict the same Dirac mass splitting.

The data of Lee *et al.* and Huber *et al.* were successfully parameterized using standard RMFT, in the latter case with help of δ meson. The related parameter sets can be found in Tab.1.

TAB.1: Parameter sets resulting from fit to DBHF data of Lee [26, 27], Huber [28, 29], and van Dalen *et al.* [25], respectively.

	Lee	Huber	van Dalen (with Λ_{vv})
g_σ^2	102.116	86.877	76.949
g_ω^2	146.802	108.096	100.842
g_ρ^2	9.6695	31.112	40.806
g_δ^2	-	29.499	49.3978
b_σ	0.00082	0.00316	0.00115
c_σ	0.00126	-0.00295	0.00053
c_ω	0.00520	-	-
c_ρ	-	-	-
Λ_{vv}	-	-	0.02362
χ^2/N	2.9106	4.2833	13.6029
m_σ [MeV]	550.	550.	550.
m_ω [MeV]	783.	783.	783.
m_ρ [MeV]	770.	770.	769.
m_δ [MeV]	-	980.	980.
m_N [MeV]	939	939.	939.

However, the van Dalen's *et al.* data were not satisfactorily reproduced by these mean-field models. Although the calculated effective neutron mass was in good accord with the DBHF theory, the fitted binding energy had fairly different behaviour, mostly for the high asymmetries. Improvement of the binding energy fit was reached after

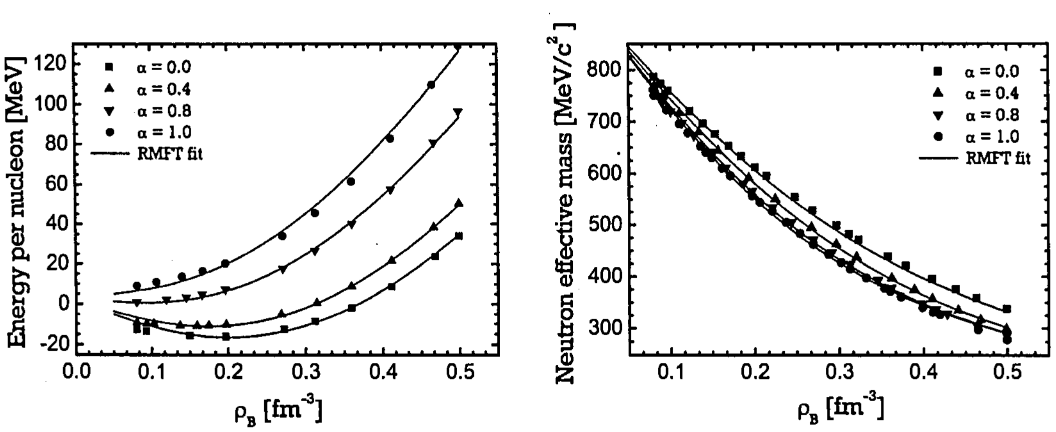

Figure 2: Density dependence of binding energy per baryon and neutron effective mass for different asymmetries as resulted from the RMF fit (lines) to the DBHF results (symbols) of van Dalen *et al.* [25].

inclusion of the isovector vector c_ρ self-interaction, which indicates the importance of isovector sector. Unfortunately, the fit leads to nonphysical value of c_ρ implying too strong isovector self-interaction. In addition, it can be shown that the parameterization arising from such fit is not able to reproduce the predicted nuclear symmetry energy resulting from the DBHF calculations of van Dalen. Mean-field model with c_ρ gives the value of the symmetry energy at saturation density far too high than $E_{sym} = 34.36$ MeV of van Dalen. On the one hand, the isovector vector c_ρ self-interaction can positively affect the fit, but on the other hand, it has no direct effect on the symmetry energy dependence. Presumably, that is why its incorporation enhanced the fitting procedure but failed in symmetry energy description. Fortunately, we have found that the use of

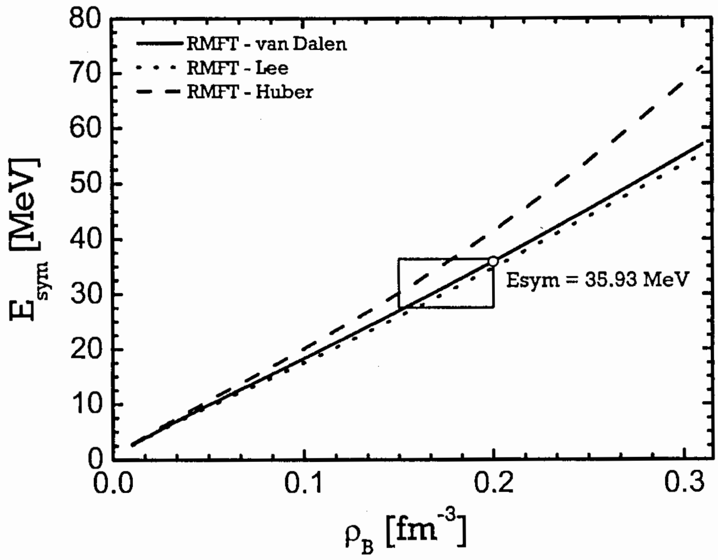

Figure 3: Mean-field symmetry energy results given by different RMF models are compared. Saturation value of E_{sym} following from fit to van Dalen data ? is depicted. Rectangular region represents an empirical area of typical symmetry energy values at saturation.

Λ_{vv} cross-interaction instead the c_ρ self-interaction can solve the remaining difficulties. The vector ω-ρ cross-interaction contrary to the ρ self-interaction directly influences the symmetry energy through the effective ρ mass. Not only it improved the binding energy fit as it is shown in Fig.2 but also it suitably reproduced the symmetry energy value - RMF model with Λ_{vv} gives $E_{sym} = 35.93$ MeV. Fig.3 displays the comparison of the RMFT symmetry energy dependencies as resulting from different DBHF calculations as well as the differences between applied mean-field models. The parameter set of the mean-field model with Λ_{vv} cross-interaction can be found in the Tab.1. One can see that the strength of the scalar and vector couplings is somewhat smaller in this case than usual. However, this is not so surprising. The simple explanation for this lies in the original DBHF data. Fig.1 shows the comparison of the density dependencies of the scalar as well as the vector potentials calculated within the different approaches to the DBHF theory considered in this work. It can be clearly seen that the van Dalen's calculations predict the smallest potentials. The second thing, which one can observe from the Tab.1 is that van Dalen's data lead to significantly stronger isovector coupling constants than in the Huber case. This again confirms the crucial role of the isovector mesons in the mapping of the mean-field theory on the Dirac-Brueckner approach.

4. Summary

The QHD in the mean-field approximation is an effective field theory, in other words it is not parameter free like microscopic approaches, therefore one needs to anchor its free parameters to bulk or single-particle nuclear properties, or to fit them to the more fundamental DBHF results, which is a reasonably accurate way to parametrize the many-body effects. In this work the relativistic mean-field theory was used to obtain an effective parametrization of the properties of asymmetric nuclear matter by adjusting it to reproduce the DBHF calculations of different groups. The binding energy per nucleon and effective neutron mass were fitted, in some cases along with the scalar and the vector potentials. New parameterization was obtained through the use of van Dalen *et al.* DBHF data. We have employed two different mean-field models in the fitting procedure, both included nucleons N, scalar σ, vector ω, isovector vector ρ and isovector scalar δ mesons as degrees of freedom, then scalar cubic b_σ and quartic c_σ self-interactions. The first model additionally contained the c_ρ self-interaction and the second the Λ_{vv} cross-interaction. Both models were satisfactorily capable to describe the binding energy together with the neutron effective mass resulting from DBHF theory, however, the former showed overly strong isovector self-interaction and failed in reproduction of the symmetry energy. It has been shown that the vector ω-ρ cross-interaction is necessary for obtaining the proper fit in the whole density range as well as that the mean-field symmetry energy calculated within this model is in good agreement with the DBHF predictions.

References

[1] Ch. Fuchs, Lect. Notes Phys. **641** (2004) 119-146.

[2] K. A. Brueckner, J. L. Gammel, Phys. Rev. **107**, 1023 (1958).

[3] F. Coester, S. Cohen, B. D. Day and C. M. Vincent, Phys. Rev. C **1**, 769 (1970).

[4] J. P. Jeukenne, A. Lejeuene, C. Mahaux, Phys. Rep. **25**, 83 (1976).

[5] L. D. Miller and A. E. S. Green, Phys. Rev. C **5**, 241 (1972).

[6] L. G. Arnold, B. C. Clark, and R. L. Mercer, Phys. Rev. C **19**, 917 (1979).

[7] S. J. Wallace, Ann. Rev. Nucl. Part. Sci. **37**, 267 (1987).

[8] P. Bonche, E. Chabanat, P. Haensel, J. Meyer and R. Schaeffer, Nucl. Phys. **A635**, 231 (1998).

[9] J. D. Walecka, Ann. Phys. (N.Y.) **83** (1974) 491.

[10] M. Baldo, Nuclear Methods and the Nuclear Equation of State (International Review of Nuclear Physics vol 8) (Singapore: World Scientific) (1999).

[11] A. Akmal, V. R. Pandharipande and D. G. Ravenhall, Phys. Rev. C **58** 1804 (1998).

[12] M. R. Anastasio, L. S. Celenza, W. S. Pong, and C. M. Shakin, Phys. Reports **100**, 327 (1983).

[13] L. S. Celenza and C. M. Shakin, Rel. Nucl. Phys.: *Theories of Structure and Scattering*, Lecture Notes in Physics Vol. 2 (World Scientific, Singapore, 1986).

[14] B. ter Haar and R. Malfliet, Phys. Rep. **149**, 207 (1987).

[15] R. Brockmann, R. Machleidt, Phys. Rev. C **42**, 1965 (1990).

[16] J. K. Bunta and S. Gmuca, Phys. Rev. C **68**, 054318 (2003).

[17] B. Liu, V. Greco, V. Baran, M. Colonna, and M. Di Toro, Phys. Rev. C **65**, 045201 (2002).

[18] J. Boguta and A. R. Bodmer, Nucl. Phys. **A292**, 413 (1977).

[19] A. R. Bodmer, Nucl. Phys. **A292**, 703 (1991).

[20] S. Gmuca, Nucl. Phys. **A547**, 447 (1992).

[21] H. Mueller and B. D. Serot, Nucl. Phys. **A606**, 508 (1996).

[22] C.J. Horowitz and J. Piekarewicz, Phys. Rev. Lett. **86**, 5647 (2001).

[23] C.J. Horowitz and J. Piekarewicz, Phys. Rev. C **64**, 062802 (2001).

[24] A. L. Fetter and J. D. Walecka: Theoretical Mechanics of Particle and Continua, MacGraw-Hill, New York (1980).

[25] E. N. E. van Dalen, C. Fuchs, and Amand Faessler, Nucl. Phys. **A744** 227-248 (2004).

[26] C. H. Lee, T. T. S. Kuo, G. Q. Li, and G. E. Brown, Phys. Lett. B **412**, 235 (1997).

[27] C. H. Lee, T. T. S. Kuo, G. Q. Li, and G. E. Brown, Phys. Rev. C **57**, 3488 (1998).

[28] H. Huber, F. Weber, and M. K. Weigel, Phys. Lett. B **317**, 485 (1993).

[29] H. Huber, F. Weber, and M. K. Weigel, Phys. Rev. C **51**, 1790 (1995).

SEPARABLE KERNELS FOR UNCOUPLED PARTIAL STATES OF THE NEUTRON-PROTON SYSTEM

E.P.Rogochaya[1], S.G.Bondarenko, and V.V.Burov

JINR, 141980, Dubna, Moscow region, Russia

Abstract

The multirank separable kernels of the neutron-proton interaction for uncoupled S and P partial waves (with the total angular momentum J=0,1) are proposed. Using the constructed kernels the experimental data for phase shifts in the elastic neutron-proton scattering for the laboratory energy up to 3 GeV and low-energy parameters are described. The comparison of our results with other model calculations are presented.

1 Introduction

The problem of an adequate description of nuclear interactions arose many years ago. At present there is no consistent theory of these interactions. Therefore to calculate many processes defined by nuclear forces various theoretical models were elaborated. They are potentials or interaction kernels parameters of which are defined from the description of relatively simple reactions with hadrons, like neutron-proton scattering, or systems composed of them, like deuteron.

There are a lot of works devoted to the description of the deuteron. The first models were based on the nonrelativistic Shrödinger equation (see, for example, [1, 2]). In numerous papers mesonic exchange currents, relativistic corrections were investigated and then were added to nonrelativistic solutions [3]-[9]. These approaches could describe properties of the deuteron such as binding energy, magnetic and quadruple momenta, electromagnetic form factors, tensor polarization and so on. However, with increasing of the precision of experimental data and obtaining new data at larger energies it became evident that it was necessary to take into account relativistic effects more carefully.

One of the most consistent approaches is based on the solution of the Bethe-Salpeter (BS) equation [10]. In this case, we have to deal with a nontrivial integral equation. There is no method to get its exact solution. So various approximations were worked out. At present, the most known and developed approaches are the so-called quasipotential [11]-[22].

They consist in the simplification of the equations under consideration by some assumption. In most cases it means the deliverance from the relative energy, according to some physical reasons. There is another class of approaches called the relativistic quantum mechanics which was successfully developed and applied to explain the electromagnetic properties of the deuteron. One of the most elaborated is the light front (LF) dynamics [23]. In this approach, the state vector describing the system is expanded by Fock components defined on a hypersphere in the four-dimensional space-time.

An alternative approach based on the exact solution of the BS equation is to use the separable ansatz for the interaction kernel in the BS equation [24]. In this case

[1]E-mail: rogoch@theor.jinr.ru

we can transform an integral equation to a system of linear equations. Parameters of the kernel are fitted by the description of phase shifts for respective partial states and low-energy parameters.

First separable parametrizations were worked out within nonrelativistic models. The form factors in the interaction kernel had no poles on a real axis in the relative energy complex plane [25, 26]. However, after the construction of a relativistic generalization such poles appeared [24]. In some cases they do not prevent to perform the calculations. As an example, such parametrizations are successfully used in the consideration of the deuteron photodisintegration [27], elastic electron-deuteron scattering, deuteron electrodisintegration on the threshold, and the deep inelastic scattering [24]. However, at high energies, one would have to deal with several thresholds corresponding to the production of one, two and more mesons of different types. This is clearly not feasible. A more practical approach is to employ phenomenological covariant separable kernel, which do not exhibit the meson-production thresholds, and can even be constructed in a singularity-free fashion, with the form factors chosen in the present paper and our Wick-rotation prescription. Thus, an accurate description of on-shell nucleon-nucleon data is possible, up to quite high energies. One then hopes that the used separable interactions also have a reasonable off-shell behaviour, so that realistic applications to other reactions can be done. The parametrization like that was proposed in [28]. In the present work, we develop this approach increasing the rank of the kernels and trying to describe the data for the phase shifts of uncoupled partial states in the energy range up to 3 GeV taken from the SAID program (http://gwdac.phys.gwu.edu).

2 Bethe-Salpeter formalism

Within the relativistic field theory, the elastic NN scattering can be described by the scattering T matrix which satisfies the inhomogeneous BS equation. In momentum space, the BS equation for the T matrix can be (in terms of the relative four-momenta p' and p and the total four-momentum P) represented as:

$$T(p',p;P) = V(p',p;P) + \frac{i}{4\pi^3}\int d^4k\, V(p',k;P)\, S_2(k;P)\, T(k,p;P), \qquad (1)$$

where $V(p',p;P)$ is the interaction kernel and $S_2(k;P)$ is the free two-particle Green function

$$S_2^{-1}(k;P) = (\frac{1}{2}\,P\cdot\gamma + k\cdot\gamma - m)^{(1)}(\frac{1}{2}\,P\cdot\gamma - k\cdot\gamma - m)^{(2)},$$

γ are the Dirac gamma-matrices. The square of the total momenta $s=(p_1+p_2)^2$ and the relative momentum $p=(p_1-p_2)/2$ $[p'=(p_1'-p_2')/2]$ are defined via the nucleon momenta p_1, p_2 $[p_1',\ p_2']$ of initial [final] nucleons.

To solve the BS equation (1) we perform the partial-wave decomposition of it, i.e. we introduce relativistic two-nucleon basis states $|aM\rangle \equiv |\pi,\ {}^{2S+1}L_J^{\rho}M\rangle$, where S denotes the total spin, L is the orbital angular momentum, and J is the total angular momentum with the projection M; relativistic quantum numbers ρ and π refer to the relative-energy and spatial parity with respect to the change of sign of the relative energy and spatial vector, respectively. In that case we obtain a system of linear integral equations for the off-shell partial-wave amplitudes:

$$T_{ab}(p_0',|\mathbf{p}'|;p_0,|\mathbf{p}|;s) = V_{ab}(p_0',|\mathbf{p}'|;p_0,|\mathbf{p}|;s) \qquad (2)$$

$$+\frac{i}{4\pi^3}\sum_{cd}\int_{-\infty}^{+\infty}dk_0\int_0^{\infty}\mathbf{k}^2d|\mathbf{k}|\,V_{ac}(p_0',|\mathbf{p}'|;k_0,|\mathbf{k}|;s)S_{cd}(k_0,|\mathbf{k}|;s)\,T_{db}(k_0,|\mathbf{k}|;p_0,|\mathbf{p}|;s),$$

where the two-particle propagator S_{ab} depends only on ρ-spin indices.

We use the normalization condition for the T matrix in the on-mass-shell form for the singlet case:

$$T_{ll}(s)\equiv T_{ll}(0,\bar{p};0,\bar{p};s)=-\frac{16\pi}{\sqrt{s}\sqrt{s-4m^2}}\exp\{i\delta_l\}\sin\delta_l, \tag{3}$$

where $\bar{p}\equiv|\bar{\mathbf{p}}|=\sqrt{s/4-m^2}=\sqrt{mT_{\mathrm{Lab}}/2}$ is the on-mass-shell momentum, m is a nucleon mass. In Eq.(3) l denotes ${}^SL_J$ states for simplicity. Low-energy parameters, the scattering length a_0, and the effective range r_0 are derived from the expansion of the T-matrix into a series of $\bar{p}$-terms, according to [30]:

$$\bar{p}\cot\delta_l(s)=-\frac{1}{a_0^l}+\frac{r_0^l}{2}\bar{p}^2+\mathcal{O}(\bar{p}^3). \tag{4}$$

To solve the equations for the T matrix and BS amplitude, we should use some assumption for the interaction kernel.

3 A separable kernel

We assume that the interaction kernel V conserves parity, total angular momentum J and its projection, and isotopic spin. Due to the tensor nuclear force, the orbital angular momentum L is not conserved. Moreover, the negative-energy two-nucleon states are switched off, which leads to the total spin S conservation. The partial-wave-decomposed BS equation is therefore reduced to the following form:

$$\begin{aligned}T_{l'l}(p_0',|\mathbf{p}'|;p_0,|\mathbf{p}|;s)&=V_{l'l}(p_0',|\mathbf{p}'|;p_0,|\mathbf{p}|;s)\\&+\frac{i}{4\pi^3}\sum_{l''}\int_{-\infty}^{+\infty}dk_0\int_0^{\infty}\mathbf{k}^2d|\mathbf{k}|\,\frac{V_{l'l''}(p_0',|\mathbf{p}'|;k_0,|\mathbf{k}|;s)\,T_{l''l}(k_0,|\mathbf{k}|;p_0,|\mathbf{p}|;s)}{(\sqrt{s}/2-E_{\mathbf{k}}+i\epsilon)^2-k_0^2},\end{aligned} \tag{5}$$

where $l=l'=J$ for spin-singlet and uncoupled spin-triplet states.

Supposing the separable (rank N) ansatz for the kernel of the NN interaction:

$$V_{l'l}(p_0',|\mathbf{p}'|;p_0,|\mathbf{p}|;s)=\sum_{i,j=1}^{N}\lambda_{ij}(s)g_i^{[l']}(p_0',|\mathbf{p}'|)g_j^{[l]}(p_0,|\mathbf{p}|), \tag{6}$$

where the form factors $g_j^{[l]}$ represent the model functions, we can obtain the solution of equation (6) in a similar separable form for the T matrix:

$$T_{l'l}(p_0',|\mathbf{p}'|;p_0,|\mathbf{p}|;s)=\sum_{i,j=1}^{N}\tau_{ij}(s)g_i^{[l']}(p_0',|\mathbf{p}'|)g_j^{[l]}(p_0,|\mathbf{p}|), \tag{7}$$

where

$$\tau_{ij}(s)=1/(\lambda_{ij}^{-1}(s)+h_{ij}(s)), \tag{8}$$

$$h_{ij}(s) = -\frac{i}{4\pi^3}\sum_l \int dk_0 \int \mathbf{k}^2 d|\mathbf{k}| \frac{g_i^{[l]}(k_0,|\mathbf{k}|)g_j^{[l]}(k_0,|\mathbf{k}|)}{(\sqrt{s}/2 - E_{\mathbf{k}} + i\epsilon)^2 - k_0^2}, \tag{9}$$

$\lambda_{ij}(s)$ is a matrix of model parameters.

The form factors $g_i^{[l]}$ used in the separable representation of the interaction kernel (6) are obtained by a relativistic generalization of the initially nonrelativistic Yamaguchi-type functions depending on the three-dimensional squared momentum $|\boldsymbol{p}|$. There are two methods to derive covariant relativistic generalizations of nonrelativistic form factors. They are considered below.

Calculating the T matrix we can connect the parameters of the internal kernel with observables.

4 Methods of a covariant relativistic generalization

Two methods of a covariant relativistic generalization of the Yamaguchi- or Tabakin-type functions are considered by the example of the nonrelativistic Yamaguchi-type function

$$g(|\mathbf{p}|) = \frac{1}{\mathbf{p}^2 + \beta^2}. \tag{10}$$

1. One of the common methods is to replace three-momentum squared by four-momentum squared:

$$\mathbf{p}^2 \to -p^2 = -p_0^2 + \mathbf{p}^2. \tag{11}$$

This formal procedure converts three-dimensional functions to covariant four-dimensional ones:

$$g_p(p,P) = \frac{1}{-p^2+\beta^2} \xrightarrow{\text{c.m.}} \frac{1}{-p_0^2 + \mathbf{p}^2 + \beta^2 + i\epsilon}. \tag{12}$$

2. The other method is based on the introduction of the formal four-vector Q via the relative p and total P four-momenta of the two-body system by the following relation:

$$Q = p - \frac{P\cdot p}{s}P, \tag{13}$$

with the total momentum squared $s = P^2$.

$$g_Q(p,P) = \frac{1}{-Q^2+\beta^2} \xrightarrow{\text{c.m.}} \frac{1}{\mathbf{p}^2+\beta^2}. \tag{14}$$

Note that in the two-particle center-of-mass system where $P = (\sqrt{s}, \mathbf{0})$ the four-vector Q is defined by the components $Q = (0, \mathbf{p})$ and, thus,

$$\mathbf{p}^2 = -Q^2 \tag{15}$$

can be formally converted to the Lorentz invariant.

The presented functions have rather different properties in the relative energy p_0 complex plane in c.m. The function g_p has two poles on the real axis for p_0 at $\pm\sqrt{\mathbf{p}^2+\beta^2} \mp i\epsilon$ while the function g_Q has no poles on it.

5 Pole structure of the BS solution

The solution of the Bethe-Salpeter equation with the separable kernel of interaction contains the function h_{ij} (9). To simplify the investigation of the pole structure, let us consider h_{ij} for the one-rank kernel ($i = j = 1$) for single l state. Then the value to be calculated is $h(s)$:

$$h(s) = -\frac{i}{4\pi^3} \int dp_0 \int \mathbf{p}^2 d|\mathbf{p}| \frac{g(p_0, |\mathbf{p}|)^2}{(\sqrt{s}/2 - E_{\mathbf{p}} + i\epsilon)^2 - p_0^2}. \tag{16}$$

To obtain the function $h(s)$, the two-dimensional integral on p_0 and $|\mathbf{p}|$ should be calculated. To perform the integration over p_0, the Cauchy theorem is used. As it can be seen from Eq.(16), there are two types of singularities on the real axis in the p_0 complex plane: one is poles of the function $S(p; s)$:

$$p_0^{(1,2)} = \pm\sqrt{s}/2 \mp E_{\mathbf{p}} \pm i\epsilon, \tag{17}$$

and the other is poles of the function $g(p)$.

The function g_p has four poles:

$$\begin{aligned} p_0^{(3,4)} &= \pm\sqrt{\mathbf{p}^2 + \beta^2 + i\alpha^2}, \\ p_0^{(5,6)} &= \pm\sqrt{\mathbf{p}^2 + \beta^2 - i\alpha^2}, \end{aligned} \tag{18}$$

and to perform the p_0 integration, residues in three poles of Eqs.(17) and (18) should be calculated. These calculations are performed analytically. All poles and the contour of integration are pictured in Fig.1. The idea how to choose the contour appeared owing to [31, 32]. It consists in that the contour must envelope the poles from form factors which will be inside the standard contour after the $\alpha \to 0$ limit. "Standard" means the one used in the quantum field theory calculations with a propagator which has poles only on the real axis in the p_0 complex plane; one of them is rounded from below and the other, from above. So the path of integration is defined by an appropriate contour for the propagator. The calculation over the presented path leads to the pure real contribution from the form factor poles and, therefore, to the unitary T matrix. We also obtain a correct transition to ordinary form factors of type $g \sim 1/(p_0^2 - \mathbf{p}^2 - \beta^2)^2$ in the $\alpha \to 0$ limit.

The function g_Q has no poles on the p_0 real axis and, therefore, the only poles of Eq.(17) should be taken into account. The result for $h(s)$ can be written as:

$$h(s) = \frac{1}{2\pi^2} \int \mathbf{p}^2 d|\mathbf{p}| \frac{g_Q(0, |\mathbf{p}|)^2}{\sqrt{s} - 2E_{\mathbf{p}} + i\epsilon}. \tag{19}$$

This equation formally coincides with that could be obtained within the Blankenbeckeler-Sugar-Logunov-Tavkhelidze (BSLT) approximation [11, 12] which consists in replacing the Green function in Eq.(16) by the expression

$$S_{BSLT}(p; s) = -2\pi i(\sqrt{s} - 2E_{\mathbf{p}} + i\epsilon)^{-1}\delta(p_0). \tag{20}$$

Although the solutions of the equation with functions g_Q and within the BSLT approximation coincide in c.m., the difference becomes evident when the reaction with the two-particle system is considered. In that case, the arguments of the function g_Q

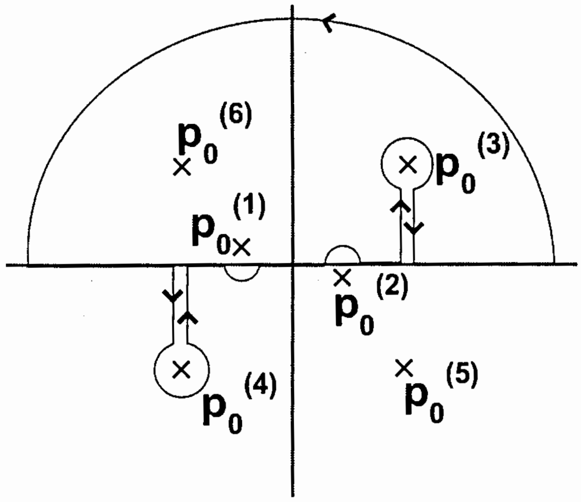

Figure 1: Contour for integration over p_0.

are calculated with the help of the Lorentz transformations in the system different from c.m. The functions become similar to g_p but with a more complicated dependence of the p argument.

In following sections some separable presentations of the interaction kernel for the partial waves with $J = 0, 1$ are considered. Form factors are constructed by the relativization procedure, according to the first method. The functions with Q can be obtained from them by the change $p^2 \to Q^2$.

6 Separable presentations of the kernel

We consider the partial states using the separable kernels with modified Yamaguchi-type functions of N rank (MYN, MYQN).

For the description of the P partial waves the two-rank separable kernel of interaction with the modified Yamaguchi-type functions is used. Its form factors have the following form:

$$g_1^{[P]}(p) = \frac{\sqrt{-p_0^2 + \mathbf{p}^2}}{(p_0^2 - \mathbf{p}^2 - \beta_1^2)^2 + \alpha_1^4}, \tag{21}$$
$$g_2^{[P]}(p) = \frac{\sqrt{(-p_0^2 + \mathbf{p}^2)^3 (p_{c2} - p_0^2 + \mathbf{p}^2)}}{((p_0^2 - \mathbf{p}^2 - \beta_2^2)^2 + \alpha_2^4)^2}.$$

For the description of the ${}^1S_0^+$ partial state the three-rank kernel is used. Increasing the rank is connected with the circumstance that the two-rank kernel leads to results which are not much better than the one-rank ansatz [29]. The form factors of our three-rank kernel are:

$$g_1^{[S]}(p) = \frac{(p_{c1} - p_0^2 + \mathbf{p}^2)}{(p_0^2 - \mathbf{p}^2 - \beta_1^2)^2 + \alpha_1^4}, \tag{22}$$

5 Pole structure of the BS solution

The solution of the Bethe-Salpeter equation with the separable kernel of interaction contains the function h_{ij} (9). To simplify the investigation of the pole structure, let us consider h_{ij} for the one-rank kernel ($i = j = 1$) for single l state. Then the value to be calculated is $h(s)$:

$$h(s) = -\frac{i}{4\pi^3} \int dp_0 \int \mathbf{p}^2 d|\mathbf{p}| \frac{g(p_0, |\mathbf{p}|)^2}{(\sqrt{s}/2 - E_{\mathbf{p}} + i\epsilon)^2 - p_0^2}. \tag{16}$$

To obtain the function $h(s)$, the two-dimensional integral on p_0 and $|\mathbf{p}|$ should be calculated. To perform the integration over p_0, the Cauchy theorem is used. As it can be seen from Eq.(16), there are two types of singularities on the real axis in the p_0 complex plane: one is poles of the function $S(p; s)$:

$$p_0^{(1,2)} = \pm\sqrt{s}/2 \mp E_{\mathbf{p}} \pm i\epsilon, \tag{17}$$

and the other is poles of the function $g(p)$.

The function g_p has four poles:

$$\begin{aligned} p_0^{(3,4)} &= \pm\sqrt{\mathbf{p}^2 + \beta^2 + i\alpha^2}, \\ p_0^{(5,6)} &= \pm\sqrt{\mathbf{p}^2 + \beta^2 - i\alpha^2}, \end{aligned} \tag{18}$$

and to perform the p_0 integration, residues in three poles of Eqs.(17) and (18) should be calculated. These calculations are performed analytically. All poles and the contour of integration are pictured in Fig.1. The idea how to choose the contour appeared owing to [31, 32]. It consists in that the contour must envelope the poles from form factors which will be inside the standard contour after the $\alpha \to 0$ limit. "Standard" means the one used in the quantum field theory calculations with a propagator which has poles only on the real axis in the p_0 complex plane; one of them is rounded from below and the other, from above. So the path of integration is defined by an appropriate contour for the propagator. The calculation over the presented path leads to the pure real contribution from the form factor poles and, therefore, to the unitary T matrix. We also obtain a correct transition to ordinary form factors of type $g \sim 1/(p_0^2 - \mathbf{p}^2 - \beta^2)^2$ in the $\alpha \to 0$ limit.

The function g_Q has no poles on the p_0 real axis and, therefore, the only poles of Eq.(17) should be taken into account. The result for $h(s)$ can be written as:

$$h(s) = \frac{1}{2\pi^2} \int \mathbf{p}^2 d|\mathbf{p}| \frac{g_Q(0, |\mathbf{p}|)^2}{\sqrt{s} - 2E_{\mathbf{p}} + i\epsilon}. \tag{19}$$

This equation formally coincides with that could be obtained within the Blankenbeckeler-Sugar-Logunov-Tavkhelidze (BSLT) approximation [11, 12] which consists in replacing the Green function in Eq.(16) by the expression

$$S_{BSLT}(p; s) = -2\pi i(\sqrt{s} - 2E_{\mathbf{p}} + i\epsilon)^{-1}\delta(p_0). \tag{20}$$

Although the solutions of the equation with functions g_Q and within the BSLT approximation coincide in c.m., the difference becomes evident when the reaction with the two-particle system is considered. In that case, the arguments of the function g_Q

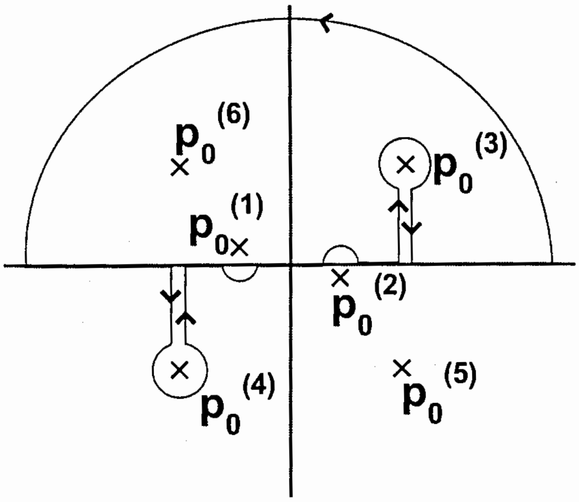

Figure 1: Contour for integration over p_0.

are calculated with the help of the Lorentz transformations in the system different from c.m. The functions become similar to g_p but with a more complicated dependence of the p argument.

In following sections some separable presentations of the interaction kernel for the partial waves with $J = 0, 1$ are considered. Form factors are constructed by the relativization procedure, according to the first method. The functions with Q can be obtained from them by the change $p^2 \to Q^2$.

6 Separable presentations of the kernel

We consider the partial states using the separable kernels with modified Yamaguchi-type functions of N rank (MYN, MYQN).

For the description of the P partial waves the two-rank separable kernel of interaction with the modified Yamaguchi-type functions is used. Its form factors have the following form:

$$g_1^{[P]}(p) = \frac{\sqrt{-p_0^2 + \mathbf{p}^2}}{(p_0^2 - \mathbf{p}^2 - \beta_1^2)^2 + \alpha_1^4},$$
$$g_2^{[P]}(p) = \frac{\sqrt{(-p_0^2 + \mathbf{p}^2)^3 (p_{c2} - p_0^2 + \mathbf{p}^2)}}{((p_0^2 - \mathbf{p}^2 - \beta_2^2)^2 + \alpha_2^4)^2}. \tag{21}$$

For the description of the ${}^1S_0^+$ partial state the three-rank kernel is used. Increasing the rank is connected with the circumstance that the two-rank kernel leads to results which are not much better than the one-rank ansatz [29]. The form factors of our three-rank kernel are:

$$g_1^{[S]}(p) = \frac{(p_{c1} - p_0^2 + \mathbf{p}^2)}{(p_0^2 - \mathbf{p}^2 - \beta_1^2)^2 + \alpha_1^4}, \tag{22}$$

$$g_2^{[S]}(p) = \frac{(p_0^2 - \mathbf{p}^2)(p_{c2} - p_0^2 + \mathbf{p}^2)^2}{((p_0^2 - \mathbf{p}^2 - \beta_2^2)^2 + \alpha_2^4)^2},$$
$$g_3^{[S]}(p) = \frac{(p_0^2 - \mathbf{p}^2)}{(p_0^2 - \mathbf{p}^2 - \beta_3^2)^2 + \alpha_3^4}.$$

The functions are numerated by angular momenta $L = 0([S]), 1([P])$. The numerator with p_c in $g_2^{[P]}$ and $g_{1,2}^{[S]}$ is introduced to compensate an additional dimension in the denominator to provide the total dimension as GeV^{-2} [29].

7 Calculations and results

Using the np scattering data we analyze the parameters of the separable kernels distinguishing two different cases:

1. There are no sign change in phase shifts or bound state (${}^1P_1^+$, ${}^3P_1^+$ partial states). In this case
$$\lambda_{ij}(s) = \bar{\lambda}_{ij} = const. \tag{23}$$
This is sufficient for most of the higher partial waves.

2. One sign change and no bound state (${}^1S_0^+$, ${}^3P_0^+$ partial states). In this case the energy-dependent expression for $\lambda_l(s)$ is used (see [28] and references therein):
$$\lambda_{ij}(s) = (s_0 - s)\bar{\lambda}_{ij}, \tag{24}$$
Here the parameter s_0 is introduced to reproduce the sign change in the phase shifts at the position of the experimental value for the kinetic energy T_{Lab} where they are equal to zero. It is added to the other parameters of the kernel.

The calculation of the parameters is performed by using Eqs.(3), (4) and expressions given in the previous sections to reproduce experimental values for all available data from the SAID program (http://gwdac.phys.gwu.edu) for the phase shifts. The the low-energy scattering parameters are taken from [33].

The calculations are performed in two independent ways. The first one is based on using the Cauchy theorem for the integration over p_0 component of the nucleon four-momentum. The integration over $|\boldsymbol{p}|$ is performed numerically. The second one is based on using the Wick rotation [32]. All integrals are calculated numerically with the technique elaborated in the paper [34].

The introduced parameters of the kernels are found on base of minimization procedure realized by the Minuit algorithm (CERN library).

The description of P waves by the two-rank kernel is denoted by MY2 for the first case of a relativization procedure; MYQ2, for the second one. For the ${}^1S_0^+$ partial state the notation MY3 and MYQ3, respectively, are used.

The calculated parameters of the considered kernels are listed in Tables 1 and 2 (here the values of s_0 are presented, too). In Table 3, the calculated low-energy scattering parameters for the ${}^1S_0^+$ wave are compared with their experimental values.

In Figs.2,3, the results of the phase shift calculations are compared with experimental data (the used notation is described in the following Section 8) and two alternative descriptions by CD-Bonn [35] and SP07 [36]. In the discussion of the ${}^1S_0^+$ channel the nonrelativistic Graz II [25], as an alternative model with a separable kernel, is also presented.

Table 1: Parameters of the two-rank kernel with modified Yamaguchi functions for P waves; $s_0 = 3.8682\,\mathrm{GeV}^2$.

	MY2		
	${}^1P_1^+$	${}^3P_0^+$	${}^3P_1^+$
$\bar\lambda_{11}$ (GeV^4)	0.05412952	-923.8881	0.06125619
$\bar\lambda_{12}$ (GeV^4)	1.925	-102.0961	2.068215
$\bar\lambda_{22}$ (GeV^4)	7.975	4.346553	24.48148
β_1 (GeV)	0.1244769	0.958602	0.1224502
β_2 (GeV)	0.6228701	1.897255	0.5822389
α_1 (GeV)	0.2	0.759970	0.2107709
α_2 (GeV)	0.5984991	0.687087	0.5927882
p_{c2} (GeV^2)	1.035	-133.2385	0.9476951
	MYQ2		
	${}^1P_1^+$	${}^3P_0^+$	${}^3P_1^+$
$\bar\lambda_{11}$ (GeV^4)	0.3086486	-55.88270	0.07648584
$\bar\lambda_{12}$ (GeV^4)	1.606382	-763.1649	1.567463
$\bar\lambda_{22}$ (GeV^4)	-5.797411	-5325.327	21.25497
β_1 (GeV)	0.2150637	0.5008744	0.2109235
β_2 (GeV)	0.9582849	2.4269161	0.4260685
α_1 (GeV)	0.2	0.6863803	0.2
α_2 (GeV)	0.2	0.2	0.2
p_{c2} (GeV^2)	12.47736	5.866078	0.007380749

8 Discussion

In this section, the review of the results of our calculations with two methods of relativization is performed.

In. Fig.2, the phase shifts for P partial states are depicted. We can see that all of the calculations including nonrelativistic CD-Bonn give a quite good description of the ${}^1P_1^+$ state. As for the ${}^3P_0^+$ partial state, the comparison of our and other model calculations demonstrates a reasonable agreement with the experimental data in the whole range of energies except the nonrelativistic CD-Bonn which works till $T_{\rm Lab} \sim 0.75\,\mathrm{GeV}$. Virtually the same can be said about the ${}^3P_1^+$ partial state. All models except CD-Bonn give various but acceptable within the limits of error results. The CD-Bonn works for $T_{\rm Lab} \leq 0.66\,\mathrm{GeV}$. From Fig.3, where the results of calculations for ${}^1S_0^+$ are presented, it can be seen that CD-Bonn is quite good till $T_{\rm Lab} \sim 0.66\,\mathrm{GeV}$. All the other results are in agreement with measured phase shifts except Graz II which works for $T_{\rm Lab} \leq 2\,\mathrm{GeV}$.

Table 2: Parameters of the three-rank kernel with modified Yamaguchi functions for $^1S_0^+$ state; $s_0 = 4.0279\,\mathrm{GeV}^2$.

	MY3		
$\bar{\lambda}_{11}$ (GeV^2)	-0.2922173	β_1 (GeV)	0.7018063
$\bar{\lambda}_{12}$ (GeV^2)	-3.953624	β_2 (GeV)	4.381178
$\bar{\lambda}_{13}$ (GeV^2)	1.035416	β_3 (GeV)	1.137604
$\bar{\lambda}_{22}$ (GeV^2)	-11268.52	α_1 (GeV)	1.297282
$\bar{\lambda}_{23}$ (GeV^2)	331.1130	α_2 (GeV)	4.612956
$\bar{\lambda}_{33}$ (GeV^2)	70.37369	α_3 (GeV)	0.6752485
p_{c1} (GeV^2)	38.20462	p_{c2} (GeV^2)	34.53211
	MYQ3		
$\bar{\lambda}_{11}$ (GeV^2)	723.7399	β_1 (GeV)	2.463736
$\bar{\lambda}_{12}$ (GeV^2)	550.4827	β_2 (GeV)	1.266692
$\bar{\lambda}_{13}$ (GeV^2)	-1583.031	β_3 (GeV)	7.714815
$\bar{\lambda}_{22}$ (GeV^2)	132.7836	α_1 (GeV)	3.752405
$\bar{\lambda}_{23}$ (GeV^2)	-14.26609	α_2 (GeV)	2.117966
$\bar{\lambda}_{33}$ (GeV^2)	-26005.23	α_3 (GeV)	1.338336
p_{c1} (GeV^2)	-44.84322	p_{c2} (GeV^2)	247.2476

Table 3: The low-energy scattering parameters and for the singlet (s) $^1S_0^+$ wave.

	a_s(fm)	r_{0s}(fm)
MY3	-23.750	2.70
MYQ3	-23.754	2.78
Experiment	-23.748(10)	2.75(5)

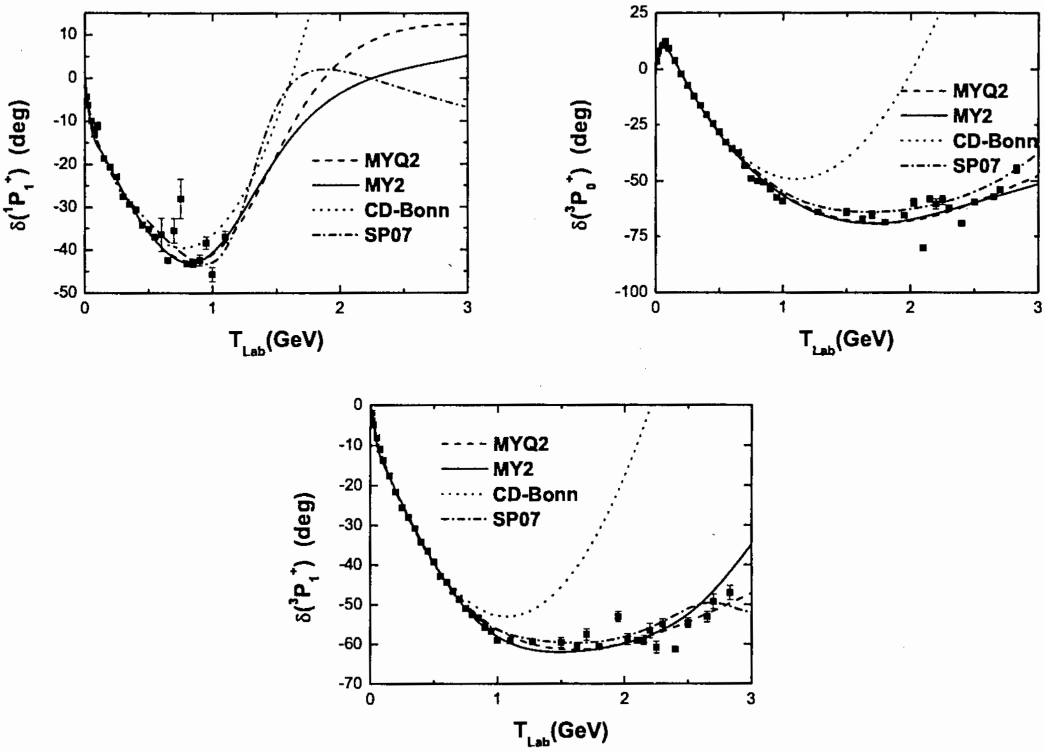

Figure 2: Phase shifts for the P waves.

From the presented figures the similarity of the calculations with the MY and MYQ form factors can be noted. Thus, as for the description of phase shifts and low-energy parameters there is no difference which variant of a relativistic generalization to choose. The choice should be dictated by the convenience of performing calculations within some concrete problem.

9 Conclusion

Using the multirank kernels (two-rank for P waves, three-rank for the ${}^1S_0^+$ partial state) we have constructed an adequate description of all existent experimental data for phase shifts taken from SAID and low-energy parameters with capable accuracy.

The results for two different methods of a relativistic generalization of initially nonrelativistic Yamaguchi-type form factors were considered. As it was shown they lead to slightly different descriptions of phases and low-energy parameters. Hence, the choice of the concrete form of functions for performing calculations of any process is governed only by convenience.

In spite of the fact that the model functions have a simple form there are quite a few parameters in the description of the data. This is necessitated by introduction of an additional parameter α so that integrands containing form factors of the separable kernel could not have poles. In particular, using this type of kernels will make the numerical calculations of the electrodisintegration far from the threshold possible without resorting quasipotential or nonrelativistic models.

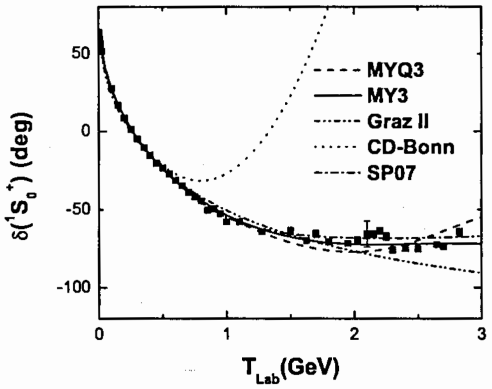

Figure 3: Phase shifts for the $^1S_0^+$ wave.

10 Acknowledgements

This work was supported by the Russian Foundation for Basic Research Grant No. 09-02-09260.

References

[1] G.E.Brown and A.D.Jackson, RX-707 (NORDITA).

[2] J.F.Mathiot, Nucl. Phys., **A412**, p.201, 1984.

[3] M.Gari and H.Hyuga, Nucl. Phys., **A278**, p.372, 1977.

[4] V.V.Burov, V.N.Dostovalov, and S.E.Suskov, JETP Lett., **44**, p.457, 1986.

[5] V.V.Burov, V.N.Dostovalov, Z. Phys., **A326**, p.245, 1987.

[6] V.V.Burov, A.A.Goi, and V.N.Dostovalov, Sov. J. Nucl. Phys., **45**, p.616, 1987.

[7] W.Y.P.Hwang and T.W.Donnelly, Phys. Rev., **C33**, p.1381, 1986.

[8] R.F.Wagenbrunn and W.Plessas, Few Body Syst. Suppl., **8**, p.181, 1995.

[9] T.Wilbois, G.Beck, and H.Arenhovel, Few-Body Syst., **15**, p.39, 1993.

[10] E.E.Salpeter and H.A.Bethe, Phys. Rev., **84**, p.1232, 1951.

[11] A.A.Logunov and A.N.Tavkhelidze, Nuovo Cim., **29**, p.380, 1963.

[12] R.Blankenbecler and R.Sugar, Phys. Rev., **142**, p.1051, 1966.

[13] V.G.Kadyshevsky, Nucl. Phys., **B6**, p.125, 1968.

[14] F.Gross, Phys. Rev., **186**, p.1448, 1969.

[15] W.W.Buck and F.Gross, Phys. Rev., **D20**, p.2361, 1979.

[16] F.Gross, Nucl. Phys., **A358**, 215c., 1981.

[17] F.Gross, World Scientific, 1991.

[18] F.Gross, J.W.Van Orden, and K.Holinde, Phys. Rev., **C45**, p.2094, 1992.

[19] V.Pascalutsa and J.A.Tjon, Phys. Rev., **C61**, p.054003, 2000; nucl-th/0003050.

[20] J.Adam, J., F.Gross, S.Jeschonnek, P.Ulmer, and J.W.Van Orden, Phys. Rev., **C66**, p.044003, 2002; nucl-th/0204068.

[21] R.A.Gilman and F.Gross, J. Phys., **G28**, p.R37, 2002; nucl-th/0111015.

[22] M.Garcon and J.W.Van Orden, Adv. Nucl. Phys., **26**, p.293, 2001; nucl-th/0102049.

[23] J.Carbonell, B.Desplanques, V.A.Karmanov, and J.F.Mathiot, Phys. Rept., **300**, p.215, 1998; nucl-th/9804029.

[24] S.G.Bondarenko, V.V.Burov, A.V.Molochkov, G.I.Smirnov, and H.Toki, Prog. Part. Nucl. Phys., **48**, p.449, 2002; nucl-th/0203069.

[25] L.Mathelitsch, W.Plessas, and M.Schweiger, Phys. Rev., **C26**, p.65, 1982.

[26] J.Haidenbauer and W.Plessas, Phys. Rev., **C30**, p.1822, 1984.

[27] S.G.Bondarenko, V.V.Burov, K.Y.Kazakov, and D.V.Shulga, Phys. Part. Nucl. Lett., **1** p.178, 2004; nucl-th/0402056.

[28] K.Schwarz, J.Frohlich, and H.F.K.Zingl, Acta Phys. Austriaca, **53**, p.191, 1981.

[29] S.G.Bondarenko, V.V.Burov, W.-Y.Pauchy Hwang, and E.P.Rogochaya, JETP Lett., **87**, p.753, 2008; 0804.3525.

[30] H.A.Bethe, Phys. Rev., **76**, p.38, 1949.

[31] R.E.Cutkosky, P.V.Landshoff, D.I.Olive, and J.C.Polkinghorne, Nucl. Phys., **B12**, p.281, 1969.

[32] T.D.Lee and G.C.Wick, Nucl. Phys., **B9**, p.209, 1969.

[33] O.Dumbrajs et al., Nucl. Phys., **B216**, p.277, 1983.

[34] J.Fleischer and J.A.Tjon, Nucl. Phys., **B84**, p.375, 1975.

[35] R.Machleidt, Phys. Rev., **C63**, p.024001, 2001; nucl-th/0006014.

[36] R.A.Arndt, W.J.Briscoe, I.I.Strakovsky, and R.L.Workman, Phys. Rev., **C76**, p.025209, 2007; 0706.2195.

THEORETICAL STUDY OF LIGHT ATOMIC NUCLEI

J. Leja[a,1] and Š. Gmuca[b]

a) Slovak University of Technology, Bratislava, Slovakia
b) Slovak Academy of Sciences, Bratislava, Slovakia

Abstract

The paper deals with the calculations of the binding energies of light atomic nuclei. The calculations have been performed in the framework of the relativistic mean-field theory. The results obtained for magnesium and silicon isotopes are presented and compared with experimental data.

1. Introduction

In recent years the relativistic mean-field theory has been frequently used for calculations of bulk and single-particle properties of nuclei. The calculations have been successfully performed from light to superheavy nuclei, but still exist nuclei where the model predictions are in poor agreement with experimental results.

2. Relativistic mean-field theory

The relativistic mean-field theory [1, 2] is a relativistic quantum field theory describing atomic nucleus as a system of relativistic particles interacting through effective meson exchange. The model starts from a Lagrangian density that includes nucleon field (ψ_i), isoscalar-scalar meson field (σ), isoscalar-vector meson field (ω^μ), isovector-vector meson field ($\vec{\rho}^\mu$) and electromagnetic field (A^μ):

$$\mathcal{L} = \bar{\psi}_i \left[i\gamma_\mu \partial^\mu - M + g_\sigma \sigma - g_\omega \gamma_\mu \omega^\mu - g_\rho \gamma_\mu \vec{\rho}^\mu \cdot \vec{\tau} - e\gamma_\mu \frac{(1-\tau_3)}{2} A^\mu \right] \psi_i +$$

$$+\frac{1}{2}\partial_\mu \sigma \partial^\mu \sigma - m_\sigma^2 \sigma^2 - \frac{1}{3} b_\sigma \sigma^3 - \frac{1}{4} c_\sigma \sigma^4 - \frac{1}{4} O^{\mu\nu} O_{\mu\nu} + \frac{1}{2} m_\omega^2 \omega_\mu \omega^\mu$$

$$+\frac{1}{4} c_\omega \left(\omega_\mu \omega^\mu\right)^2 - \frac{1}{4} \vec{R}_{\mu\nu} \vec{R}^{\mu\nu} + \frac{1}{2} m_\rho^2 \vec{\rho}_\mu \vec{\rho}^\mu - \frac{1}{4} F_{\mu\nu} F^{\mu\nu}. \tag{1}$$

M, m_σ, m_ω, m_ρ denote nucleon mass and meson masses, g_σ, g_ω, g_ρ, are nucleon-meson coupling constants and the strengths of the selfinteractions are given by constants b_σ, c_σ, c_ω. The field tensors are given by standard expressions:

$$O_{\mu\nu} = \partial_\mu \omega_\nu - \partial_\nu \omega_\mu, \quad \vec{R}_{\mu\nu} = \partial_\mu \vec{\rho}_\nu - \partial_\nu \vec{\rho}_\mu, \quad F_{\mu\nu} = \partial_\mu A_\nu - \partial_\nu A_\mu. \tag{2}$$

[1] E-mail: jozef.leja@stuba.sk

The field equations follow from the Euler-Lagrange equations in a standard way. Two approximations are necessary for solution of field equations:

- the mean-field approximation introduced by replacing the field operators for meson fields and electromagnetic field by their expectation values,
- the no-sea approximation realized by exclusion of the filled Dirac sea of negative energy states.

The nucleon spinor for axially symmetric case can by written in form [3]:

$$\psi_i(r_\perp, z, \varphi) = \frac{1}{\sqrt{2\pi}} \begin{pmatrix} f_i^+(r_\perp, z)\exp^{i(\Omega_i - \frac{1}{2})\varphi} \\ f_i^-(r_\perp, z)\exp^{i(\Omega_i + \frac{1}{2})\varphi} \\ ig_i^+(r_\perp, z)\exp^{i(\Omega_i - \frac{1}{2})\varphi} \\ ig_i^-(r_\perp, z)\exp^{i(\Omega_i + \frac{1}{2})\varphi} \end{pmatrix} \zeta_{t_i}. \tag{3}$$

The components of nucleon spinor obey the set of Dirac equations:

$$(M + S + V_0)\, f_i^+ + \partial_z g_i^+ + \left[\partial_{r_\perp} + \frac{\left(\Omega_i + \frac{1}{2}\right)}{r_\perp}\right] g_i^- = \varepsilon_i f_i^+, \tag{4}$$

$$(M + S + V_0)\, f_i^- - \partial_z g_i^- + \left[\partial_{r_\perp} - \frac{\left(\Omega_i - \frac{1}{2}\right)}{r_\perp}\right] g_i^+ = \varepsilon_i f_i^-, \tag{5}$$

$$(M + S - V_0)\, g_i^+ + \partial_z f_i^+ + \left[\partial_{r_\perp} + \frac{\left(\Omega_i + \frac{1}{2}\right)}{r_\perp}\right] f_i^- = -\varepsilon_i g_i^+, \tag{6}$$

$$(M + S - V_0)\, g_i^- - \partial_z f_i^- + \left[\partial_{r_\perp} - \frac{\left(\Omega_i - \frac{1}{2}\right)}{r_\perp}\right] f_i^+ = -\varepsilon_i g_i^-. \tag{7}$$

where S and V_0 represent scalar potential and vector potential:

$$S = g_\sigma \sigma, \tag{8}$$

$$V_0 = g_\omega \omega_0 + g_\rho \tau_3 \rho_0^{(3)} + e\frac{(1-\tau_3)}{2} A_0. \tag{9}$$

The meson fields and electromagnetic field obey the set of Klein-Gordon equations:

$$\left(-\frac{1}{r_\perp}\partial_{r_\perp} r_\perp \partial_{r_\perp} - \partial_z^2 + m_\sigma^2\right)\sigma = -g_\sigma \rho_S - b_\sigma \sigma^2 - c_\sigma \sigma^3, \tag{10}$$

$$\left(-\frac{1}{r_\perp}\partial_{r_\perp} r_\perp \partial_{r_\perp} - \partial_z^2 + m_\omega^2\right)\omega_0 = g_\omega \rho_V + c_\omega \omega_0^3, \tag{11}$$

$$\left(-\frac{1}{r_\perp}\partial_{r_\perp} r_\perp \partial_{r_\perp} - \partial_z^2 + m_\rho^2\right)\rho_0^{(3)} = g_\rho \rho_I, \tag{12}$$

$$\left(-\frac{1}{r_\perp}\partial_{r_\perp} r_\perp \partial_{r_\perp} - \partial_z^2\right) A_0 = e\rho_C. \tag{13}$$

THEORETICAL STUDY OF LIGHT ATOMIC NUCLEI

J. Leja[a,1] and Š. Gmuca[b]

a) Slovak University of Technology, Bratislava, Slovakia
b) Slovak Academy of Sciences, Bratislava, Slovakia

Abstract

The paper deals with the calculations of the binding energies of light atomic nuclei. The calculations have been performed in the framework of the relativistic mean-field theory. The results obtained for magnesium and silicon isotopes are presented and compared with experimental data.

1. Introduction

In recent years the relativistic mean-field theory has been frequently used for calculations of bulk and single-particle properties of nuclei. The calculations have been successfully performed from light to superheavy nuclei, but still exist nuclei where the model predictions are in poor agreement with experimental results.

2. Relativistic mean-field theory

The relativistic mean-field theory [1, 2] is a relativistic quantum field theory describing atomic nucleus as a system of relativistic particles interacting through effective meson exchange. The model starts from a Lagrangian density that includes nucleon field (ψ_i), isoscalar-scalar meson field (σ), isoscalar-vector meson field (ω^μ), isovector-vector meson field ($\vec{\rho}^\mu$) and electromagnetic field (A^μ):

$$\mathcal{L} = \bar{\psi}_i \left[i\gamma_\mu \partial^\mu - M + g_\sigma \sigma - g_\omega \gamma_\mu \omega^\mu - g_\rho \gamma_\mu \vec{\rho}^\mu \cdot \vec{\tau} - e\gamma_\mu \frac{(1-\tau_3)}{2} A^\mu \right] \psi_i +$$

$$+\frac{1}{2}\partial_\mu \sigma \partial^\mu \sigma - m_\sigma^2 \sigma^2 - \frac{1}{3} b_\sigma \sigma^3 - \frac{1}{4} c_\sigma \sigma^4 - \frac{1}{4} O^{\mu\nu} O_{\mu\nu} + \frac{1}{2} m_\omega^2 \omega_\mu \omega^\mu$$

$$+\frac{1}{4} c_\omega \left(\omega_\mu \omega^\mu\right)^2 - \frac{1}{4} \vec{R}_{\mu\nu} \vec{R}^{\mu\nu} + \frac{1}{2} m_\rho^2 \vec{\rho}_\mu \vec{\rho}^\mu - \frac{1}{4} F_{\mu\nu} F^{\mu\nu}. \qquad (1)$$

M, m_σ, m_ω, m_ρ denote nucleon mass and meson masses, g_σ, g_ω, g_ρ, are nucleon-meson coupling constants and the strengths of the selfinteractions are given by constants b_σ, c_σ, c_ω. The field tensors are given by standard expressions:

$$O_{\mu\nu} = \partial_\mu \omega_\nu - \partial_\nu \omega_\mu, \quad \vec{R}_{\mu\nu} = \partial_\mu \vec{\rho}_\nu - \partial_\nu \vec{\rho}_\mu, \quad F_{\mu\nu} = \partial_\mu A_\nu - \partial_\nu A_\mu. \qquad (2)$$

[1]E-mail: jozef.leja@stuba.sk

The field equations follow from the Euler-Lagrange equations in a standard way. Two approximations are necessary for solution of field equations:

- the mean-field approximation introduced by replacing the field operators for meson fields and electromagnetic field by their expectation values,
- the no-sea approximation realized by exclusion of the filled Dirac sea of negative energy states.

The nucleon spinor for axially symmetric case can by written in form [3]:

$$\psi_i(r_\perp, z, \varphi) = \frac{1}{\sqrt{2\pi}} \begin{pmatrix} f_i^+(r_\perp, z) \exp^{i\left(\Omega_i - \frac{1}{2}\right)\varphi} \\ f_i^-(r_\perp, z) \exp^{i\left(\Omega_i + \frac{1}{2}\right)\varphi} \\ i g_i^+(r_\perp, z) \exp^{i\left(\Omega_i - \frac{1}{2}\right)\varphi} \\ i g_i^-(r_\perp, z) \exp^{i\left(\Omega_i + \frac{1}{2}\right)\varphi} \end{pmatrix} \zeta_{t_i}. \tag{3}$$

The components of nucleon spinor obey the set of Dirac equations:

$$(M + S + V_0) f_i^+ + \partial_z g_i^+ + \left[\partial_{r_\perp} + \frac{\left(\Omega_i + \frac{1}{2}\right)}{r_\perp}\right] g_i^- = \varepsilon_i f_i^+, \tag{4}$$

$$(M + S + V_0) f_i^- - \partial_z g_i^- + \left[\partial_{r_\perp} - \frac{\left(\Omega_i - \frac{1}{2}\right)}{r_\perp}\right] g_i^+ = \varepsilon_i f_i^-, \tag{5}$$

$$(M + S - V_0) g_i^+ + \partial_z f_i^+ + \left[\partial_{r_\perp} + \frac{\left(\Omega_i + \frac{1}{2}\right)}{r_\perp}\right] f_i^- = -\varepsilon_i g_i^+, \tag{6}$$

$$(M + S - V_0) g_i^- - \partial_z f_i^- + \left[\partial_{r_\perp} - \frac{\left(\Omega_i - \frac{1}{2}\right)}{r_\perp}\right] f_i^+ = -\varepsilon_i g_i^-. \tag{7}$$

where S and V_0 represent scalar potential and vector potential:

$$S = g_\sigma \sigma, \tag{8}$$

$$V_0 = g_\omega \omega_0 + g_\rho \tau_3 \rho_0^{(3)} + e\frac{(1 - \tau_3)}{2} A_0. \tag{9}$$

The meson fields and electromagnetic field obey the set of Klein-Gordon equations:

$$\left(-\frac{1}{r_\perp}\partial_{r_\perp} r_\perp \partial_{r_\perp} - \partial_z^2 + m_\sigma^2\right) \sigma = -g_\sigma \rho_S - b_\sigma \sigma^2 - c_\sigma \sigma^3, \tag{10}$$

$$\left(-\frac{1}{r_\perp}\partial_{r_\perp} r_\perp \partial_{r_\perp} - \partial_z^2 + m_\omega^2\right) \omega_0 = g_\omega \rho_V + c_\omega \omega_0^3, \tag{11}$$

$$\left(-\frac{1}{r_\perp}\partial_{r_\perp} r_\perp \partial_{r_\perp} - \partial_z^2 + m_\rho^2\right) \rho_0^{(3)} = g_\rho \rho_I, \tag{12}$$

$$\left(-\frac{1}{r_\perp}\partial_{r_\perp} r_\perp \partial_{r_\perp} - \partial_z^2\right) A_0 = e\rho_C. \tag{13}$$

The nucleon densities can be calculated through expressions:

$$\rho_S = 2\sum_{i>0}^{occ} n_i \left[\left(|f_i^+|^2 + |f_i^-|^2\right) - \left(|g_i^+|^2 + |g_i^-|^2\right)\right], \tag{14}$$

$$\rho_V = 2\sum_{i>0}^{occ} n_i \left[\left(|f_i^+|^2 + |f_i^-|^2\right) + \left(|g_i^+|^2 + |g_i^-|^2\right)\right], \tag{15}$$

$$\rho_I = 2\sum_{i>0}^{occ} n_i \tau_3 \left[\left(|f_i^+|^2 + |f_i^-|^2\right) + \left(|g_i^+|^2 + |g_i^-|^2\right)\right], \tag{16}$$

$$\rho_C = 2\sum_{i>0}^{occ} n_i \frac{(1-\tau_3)}{2} \left[\left(|f_i^+|^2 + |f_i^-|^2\right) + \left(|g_i^+|^2 + |g_i^-|^2\right)\right]. \tag{17}$$

Proton and neutron pairing correlations have been included using the BCS theory [4]. The occupation numbers n_i are obtained in the constant gap approximation through the expression:

$$n_i = \frac{1}{2}\left[1 - \frac{\varepsilon_i - \lambda}{\sqrt{(\varepsilon_i - \lambda)^2 + \Delta^2}}\right] \tag{18}$$

where λ denotes the chemical potential and Δ is the pairing gap. The pairing energy is calculated as:

$$E_{pairing} = -\Delta \sum_i \sqrt{n_i(1-n_i)}.$$

The center of mass correction has been introduced through the approximation [5]:

$$E_{cm} = -17.2\ A^{-0.2}\ \text{MeV}. \tag{19}$$

The total energy is given by formula:

$$E = \sum_i^{occ} \varepsilon_i - \frac{1}{2}\int \left(g_\sigma \sigma_0 \rho_S + g_\omega \omega_0 \rho_V + g_\rho \rho_0^{(3)} \rho_I + eA_0 \rho_C\right) d^3x +$$
$$- \int \left(\frac{1}{3} b_\sigma \sigma_0^3 + \frac{1}{4} c_\sigma \sigma_0^4 - \frac{1}{4} c_\omega \omega_0^4\right) d^3x + E_{pairing} + E_{cm}. \tag{20}$$

3. Lagrangian parameters

Four different sets of Lagrangian parameters have been used for calculations:

- NL3 [6] is very successful parameter set for the description of nuclear properties in the entire mass region which originates from the original non-linear NL1 parameter set. The NL3 has removed the unwanted feature on NL1 of not being able to obtain stable state for ^{12}C due to too large attractive contribution of the non-linear terms while keeping the good properties of the NL1 for heavy nuclei.

- NL-BA [7] is a parameter set dealing with a fit to a large body of observables related to ground-state properties of selected doubly-magic nuclei covering a wide variation of isospin. The predicted properties of nuclear matter indicate improvement for the incompressibility coefficient while the symmetry energy remains practically the same as in the other parameterizations.

- TM2 [8] is a parameter set invented for description of properties of light nuclei. It includes ω-meson selfinteraction term, the necessity of which is suggested by the relativistic Brueckner-Hartree-Fock theory of nuclear matter [9].

- TMA [10] is a global parameter set which interpolates parameter sets TM1 and TM2 with mass dependence. The parameter set TM1 is a parameter set suitable for description of heavy nuclei. We may interpret this mass dependence as a mean to effectively express the quantum fluctuations beyond the mean-field level or the softness of the nuclear ground states in deformation, pairing and alpha clustering in light nuclei.

Table 1: Lagrangian parameters

	NL3	NL-BA	TM2	TMA
M (MeV)	939.0	939.0	938.0	938.9
m_σ (MeV)	508.194	506.28	526.443	519.151
m_ω (MeV)	782.501	782.6	783.0	781.950
m_ρ (MeV)	763.0	769.0	770.0	768.100
g_σ	10.2169	10.129758	11.4694	$10.055 + 3.050/A^{0.4}$
g_ω	12.8675	12.722198	14.6377	$12.842 + 3.191/A^{0.4}$
g_ρ	4.4744	4.508614	4.6783	$3.800 + 4.644/A^{0.4}$
b_σ (fm^{-1})	-10.4307	-11.480161	-4.4440	$-0.328 - 27.879/A^{0.4}$
c_σ	-28.8851	-32.277332	4.6076	$38.862 - 184.191/A^{0.4}$
c_ω	0	0	84.5318	$151.590 - 378.004/A^{0.4}$

Table 2: Nuclear matter properties

	NL3	NL-BA	TM2	TMA
saturation density ρ_0 (fm^{-3})	0.148	0.1503	0.132	0.147
bulk binding energy/nucleon E_∞/A (MeV)	-16.24	-16.1949	-16.2	-16.0
incompressibility K (MeV)	272	248	344	318
bulk symmetry energy/nucleon a_{sym} (MeV)	37.4	37.7	35.8	30.68
effective mass ratio M^*/M	0.60	0.60	0.571	0.635

4. Results

We have calculated the binding energies of even-even magnesium isotopes from ^{20}Mg to ^{40}Mg and even-even silicon isotopes from ^{22}Si to ^{44}Si. The results have been compared with the experimental data taken from the atomic mass evaluation AME 2003 [11]. The calculated binding energies are listed in Table 3 and Table 4. The differences between calculated and experimental binding energies are plotted in Figure 1 and Figure 2.

The results obtained for both isotopic chains are similar. The parameter sets NL3 and NL-BA predict low binding energies around the N=Z nuclei ^{24}Mg and ^{28}Si. On the other hand both parameter sets provide high values for neutron-rich nuclei. The parameter set TM2 predicts high values for neutron-rich nuclei, but binding energies calculated in the N=Z region agree with experimental results. The mass dependent parameter set TMA predicts also acceptable values of binding energies in the N=Z region. The situation in the neutron rich region is different, TMA is the only parameter set which predicts good values also for the heaviest magnesium and silicon isotopes.

Table 3: Binding energies of even-even magnesium isotopes.

	BE (MeV) AME 2003	BE (MeV) NL3	BE (MeV) NL-BA	BE (MeV) TM2	BE (MeV) TMA
^{20}Mg	134.47	136.62	135.55	136.19	136.34
^{22}Mg	168.58	166.97	166.12	167.56	168.04
^{24}Mg	198.26	194.51	193.80	196.33	196.20
^{26}Mg	216.68	213.41	212.73	216.40	215.08
^{28}Mg	231.63	229.30	228.85	230.78	230.14
^{30}Mg	241.66	241.57	241.36	241.55	241.13
^{32}Mg	249.85	252.45	252.39	251.05	250.80
^{34}Mg	256.22	258.20	258.31	257.15	255.63
^{36}Mg	259.74	264.73	264.87	263.72	261.26
^{38}Mg	262.31	268.26	268.51	266.90	263.72
^{40}Mg	263.24	270.11	270.44	268.32	264.36

Table 4: Binding energies of even-even silicon isotopes.

	BE (MeV) AME 2003	BE (MeV) NL3	BE (MeV) NL-BA	BE (MeV) TM2	BE (MeV) TMA
^{22}Si	134.44	136.94	136.02	137.09	135.90
^{24}Si	172.00	170.61	169.81	172.23	171.41
^{26}Si	206.05	202.85	202.17	205.85	204.66
^{28}Si	236.54	232.21	231.77	236.32	234.10
^{30}Si	255.62	251.56	251.22	254.20	252.99
^{32}Si	271.41	268.95	268.78	270.11	269.74
^{34}Si	283.43	284.60	284.56	284.67	284.53
^{36}Si	292.10	293.00	292.93	293.79	292.59
^{38}Si	299.82	301.01	301.05	301.86	299.59
^{40}Si	306.44	307.66	307.84	308.30	305.20
^{42}Si	309.62	314.70	315.04	314.54	311.03
^{44}Si	311.34	318.26	318.68	317.58	313.56

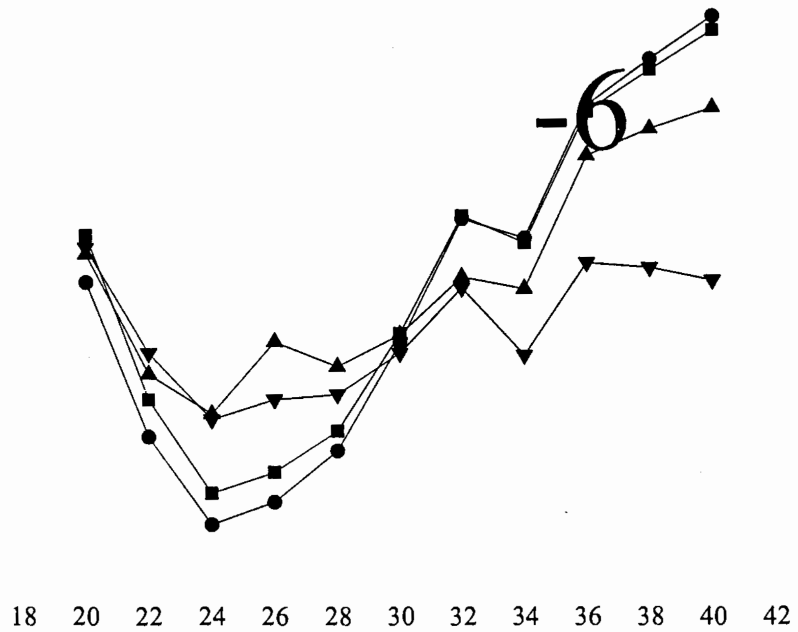

Figure 1: The binding energy differences for even-even magnesium isotopes.

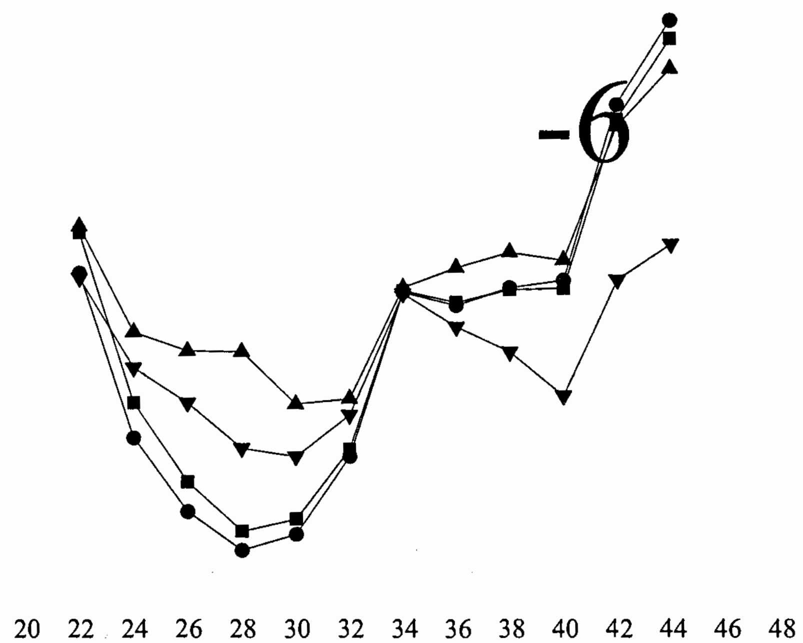

Figure 2: The binding energiey differences for even-even silicon isotopes.

4. Conclusion

Our results identify the areas in which the binding energies calculated in the relativistic mean-field framework disagree with the experimental data for magnesium and silicon isotopes. Comparison of results obtained with different sets of Lagrangian parameters shows two possibilities to improve the model predictions:

- the deviation in the N=Z region can be suppressed by the incorporation of ω-meson selfinteraction term into the Lagrangian,
- the disagreement in the neutron rich region can be cured using the mass dependent parameters set.

Acknowledgments

This work was supported by the Slovak Grant Agency for Science VEGA under the grants 2/7117/07.

References

[1] J.D. Walecka, Theoretical Nuclear and Subnuclear Physics, World Scientific, Singapore, 2004.

[2] L.N. Savushkin L.N. and H. Toki, The Atomic Nucleus as a Relativistic System, Springer-Verlag, Berlin Heidelberg, 2004.

[3] Y.K. Gambhir, P. Ring and A. Thimed, Ann. Phys., **198**, 132, 1990.

[4] P. Ring and P. Schuck, The Nuclear Many-Body Problem, Springer-Verlag, New York, 1980.

[5] P.G. Reinhard, M. Rufa, J.A. Maruhn, W. Greiner and J. Friedrich, Z. Phys, **A323**, p.13, 1986.

[6] G.A. Lalazissis, J. König and P. Ring, Phys. Rev., **C55**, p.540, 1997.

[7] Š. Gmuca, In: Proceedings of 2^{nd} International Conference "Fission and Properties of Neutron-Rich Nuclei", p.75, World Scientific, Singapore, 2000.

[8] Y. Sugahara and H. Toki, Nucl. Phys., **A579**, p.557, 1994.

[9] R. Brockmann and R. Machleidt, Phys. Rev., **C42**, p.1965, 1990

[10] Y. Sugahara Y., Doctor Thesis, Tokyo Metropolitan University, Tokyo, 1995.

[11] G.Audi, A.H. Wapstra and C. Thibault, Nucl. Phys., **A729**, p.337, 2003.

CORRECTION OF CONTINUOUS WAVELET SPECTRA FOR DETECTOR EFFECTS

J.Fedorišin[1]

1) Šafárik University, 040 01, Košice, Slovakia

Abstract

The Monte Carlo method is used to estimate errors in one-dimensional wavelet spectra. It is subsequently applied to estimate errors in wavelet spectra corrected for limited detector efficiency by the weighting method. Finally the necessary tests are carried out in order to judge efficiency and accuracy of both the methods and their results are presented and discussed.

1. Short introduction to the multiresolution analysis

Multiresolution analysis is applicable to variety of physical processes. In heavy-ion physics such analysis is useful for study of multiparticle collective flows of secondary particles produced in heavy nuclei collisions at ultrarelativistic energies. Although there are various approaches to perform such analysis, so-called wavelet transform provides substantial advantages over other analytical techniques. Its great virtue rests above all in providing handy mathematical apparatus which makes a study of processes on different scales more transparent and easily intrepretable.

A continuous wavelet transform of analyzed function or distribution $f(x)$ has form:

$$W_\Psi(a,b) = C_\Psi \int_{-\infty}^{\infty} f(x)\Psi_{a,b}(x)dx, \tag{1}$$

where

$$\Psi_{a,b}(x) = \Psi\Big(\frac{x-b}{a}\Big)$$

are daughter functions generated from mother wavelet function $\Psi(x)$ through its translations and dilations. Dilation parameter a and translation parameter b are usually reffered to as scale and phase, respectively. They are used to estimate typical widths and positions of structures present in a studied function $f(x)$. $C_\Psi = C_\Psi(a)$ is normalizing factor whose value depends on the form of wavelet function used in function decomposition. C_Ψ is defined by the normalizing condition

$$C_\Psi^2 \int_{-\infty}^{\infty} \Psi_{a,b}^2(x)dx = 1.$$

An interpretation of amplitudes $W_\Psi(a,b)$ is analogous to that of Fourier coefficients. They constitute contributions of basis functions $\Psi_{a,b}(x)$ to function $f(x)$.

In real experiment we deal with spectrum of n measurements x_1, x_2,..., x_n rather than with analytical expression $f(x)$. In such case integral wavelet transform (1) takes on the form of sum:

$$W_\Psi(a,b) = \frac{C_\Psi}{N}\sum_{i=1}^{N} \Psi\Big(\frac{x_i-b}{a}\Big), \tag{2}$$

[1]E–mail: jan.fedorisin@upjs.sk

Thus a wavelet amplitude at some scale a and phase b is calculated as a sum of wavelet contributions from all the measured values $x_1, x_2, \ldots, x_n$ which basically means that resulting wavelet spectrum can be interpreted as interference picture.

2. Examples of wavelet functions and their applications

The following wavelet functions Ψ are commonly employed:
1.) Morlet wavelet which is cosine-modulated Gaussian function with modulating frequency ω_m as a parameter:

$$\Psi(x) = m(x) = [\cos(\omega_m x) - \exp(-\omega_m^2/2)] \exp(-x^2/2),$$
$$C_\Psi(a) = \frac{1}{a^{1/2}\pi^{1/4}\sqrt{0.5 + 1.5\exp(-\omega_m^2) - 2\exp(-3\omega_m^2/4)}}.$$

2.) MHAT or g_2 wavelet, obtained as the second derivative of Gaussian function. It is again Gaussian function but now modulated by parabola:

$$\Psi(x) = g_2(x) = (1 - x^2)\exp(-x^2/2), \qquad C_\Psi(a) = \frac{2}{a^{1/2}\sqrt{3}\pi^{1/4}}.$$

The graphs of both the functions are shown in Fig.1. The modulating frequency ω_m of Morlet wavelet equals 6 for the presented example but in general its choice is arbitrary. Both the wavelets are normalized to zero when integrating from $-\infty$ to $+\infty$ which is a basic condition that all wavelet functions have to suit.

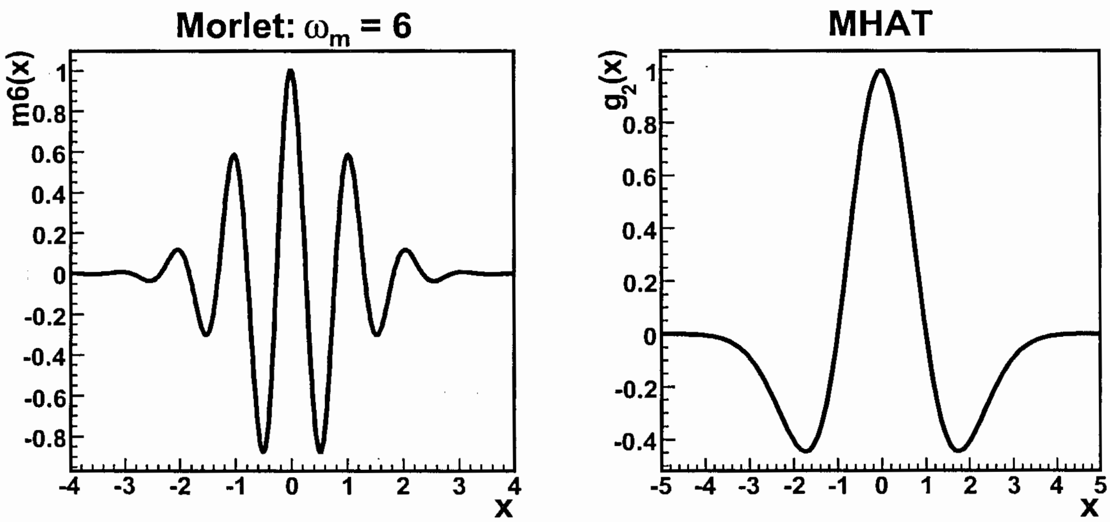

Figure 1: Morlet wavelet for $\omega_m = 6$ (left) and MHAT wavelet (right)

The constant term $\exp(-\omega_m^2/2)$ in the Morlet wavelet is added just to ensure this normalization. It can be neglected for high frequencies ω_m.

Example:

Fig.2 left presents histogram of the MC event containing a few peak structures with randomly distributed means and widths. The corresponding MHAT wavelet spectrum is shown on the right side of the figure.

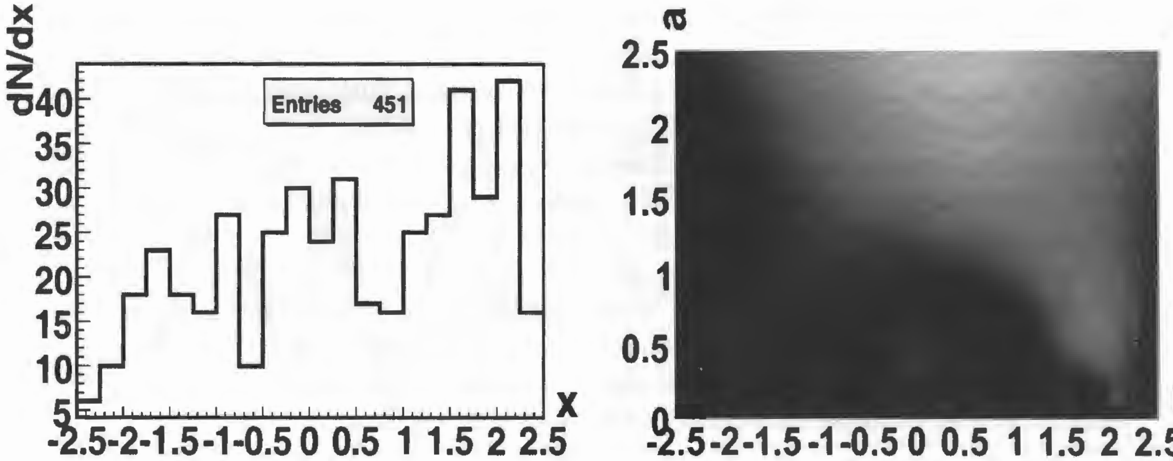

Figure 2: Distribution of the example event (left) and its corresponding MHAT wavelet spectrum (right)

The wavelet spectrum demonstrates dependence of amplitudes $W_{g_2}(a,b)$ on phase b and scale a. For better understanding the phase wavelet spectra of the studied event are shown in Fig.3.

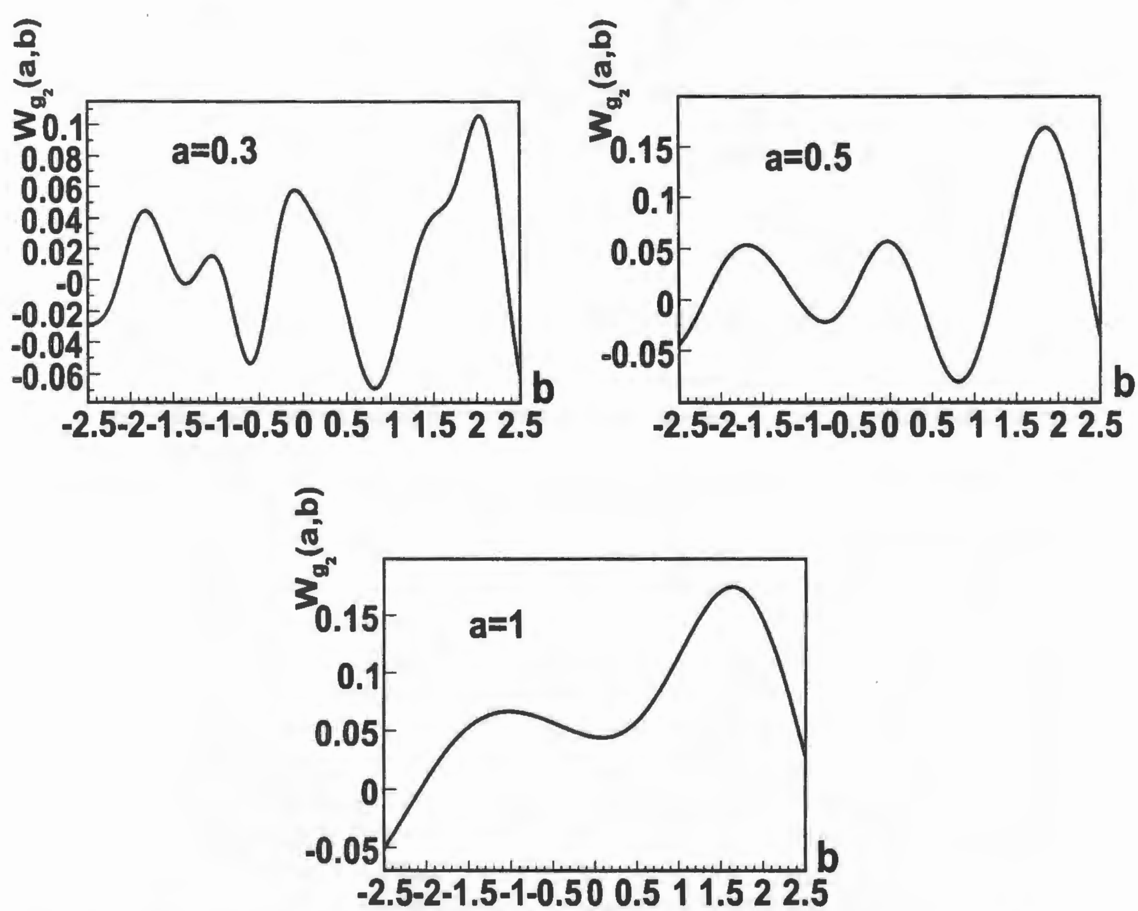

Figure 3: Phase wavelet spectra of the example event shown for the three different scales a

They are obtained by slicing the wavelet spectrum at some chosen scales a. Zero wavelet coefficients $W_{g_2}(a,b)$ correspond to average density of generated values while positive and negative coefficients indicate more and less densely populated regions respectively. To put it another way, non-zero values of wavelet coefficients correspond to deviations from average density of meausured values. Such interpretation suggests that this analysis is related also to probality density estimation. It becomes more evident when comparing the phase wavelet spectra with the original histogram. The comparison reveals clear correspondence between extrema in the wavelet spectra and the histogram.

The wavelet spectra in Fig.3 and especially in Fig.2 right disclose also evolution of merging process when shifting from small scales to large scales. Fine structures seen at small scales gradually merge to produce more robust structures at larger scales.

In heavy ion physics this feature of wavelet analysis offers possibility to study mutual relations among multiparticle collective flows of different sizes.

3. Statistical errors of the wavelet spectra

Before applying the above-described analysis to real data, a crucial question must be answered: What is statistical significance of structures observed in wavelet spectra? The question is justified since the wavelet coefficients (2) are calculated from the measured quantity x having properties of random variable, therefore it is natural to expect they will also behave like random quantities, i.e. they will fluctuate around their mean values. Standard deviations describing these fluctuations can be then interpreted as experimental errors of the resulting wavelet coefficients.

Since to calculate error propagation through wavelet transform analytically is nontrivial task, eventually it proved to be necessary to employ the Monte Carlo method. It consists of the following steps:

1. MC events are produced by introducing Poisson deviations to all values x_1, x_2,. . ., x_n of original spectrum.

2. Wavelet spectra are calculated for all these MC events.

3. Standard deviations of wavelet coefficients of these wavelet spectra are interpreted as statistical errors of wavelet coefficients in original wavelet spectrum.

The phase wavelet spectra of the previously shown event but now with error corridors indicated are presented in Fig.4. They demonstrate nontrivial dependence of statistical errors of wavelet coefficients on phase b, above all that the error sizes are not correlated with the magnitudes of wavelet coefficients. For instance, the extrema on the plot for scale $a = 0.5$ at phases $b \approx -1.7$, $b \approx 0$ and $b \approx 0.8$ have approximately same magnitude, but their errors are markedly different.

The scale wavelet spectra of the same event are presented in Fig.5. The plots are done at some chosen phases and they display error corridors as well. It is naturally expected that the errors should gradually decrease when shifting to large scales since such transition is analogous to bin merging. In general error sizes of the dependences presented in Fig.5 suggest decreasing trend when going to larger scales, but there are some parts of the studied scale range where this trend is temporarily reversed.

Finally the proposed method of error estimation is checked for its consistency by a simple test: 200 events with different probability density functions are generated and for each of them sample of new events with same p.d.f. is simulated. Compatibility of

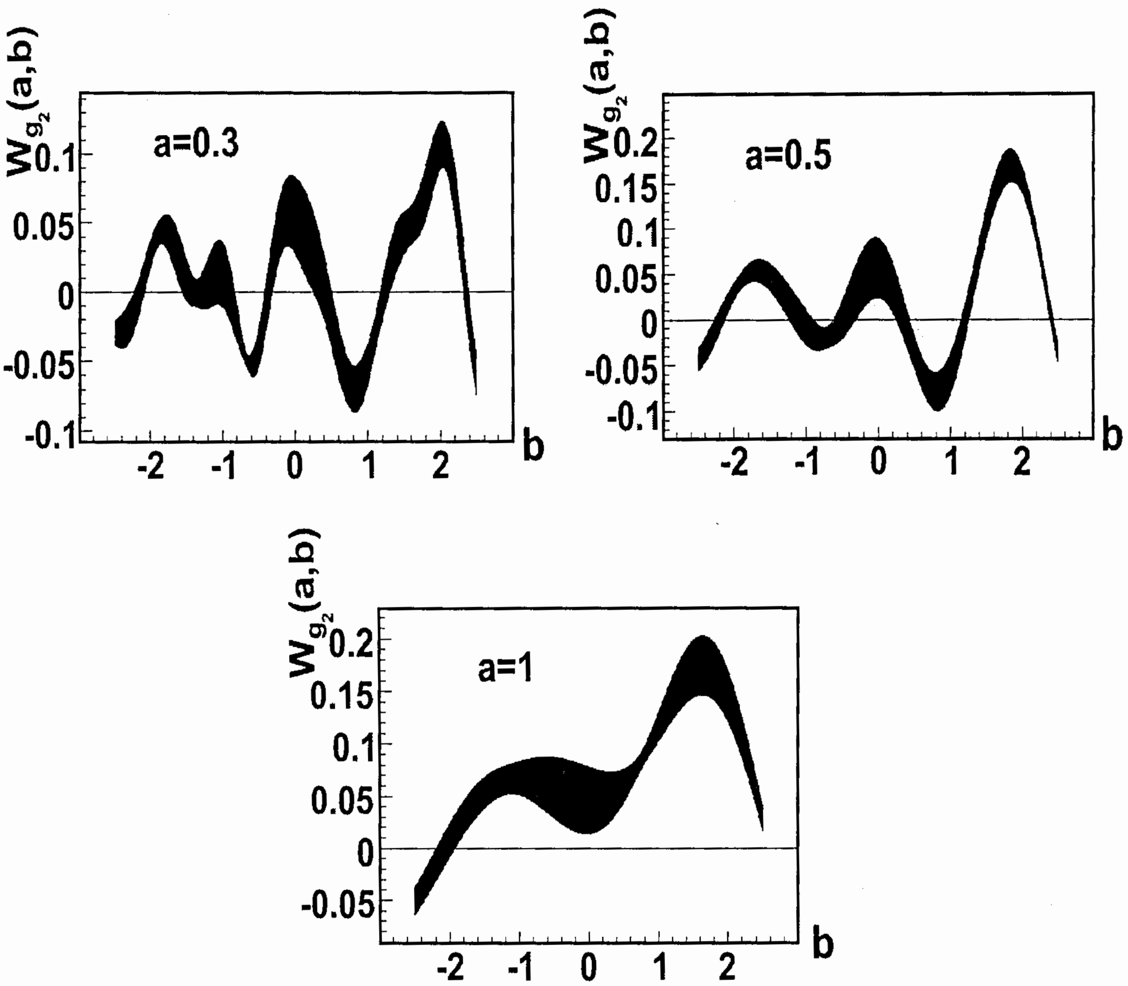

Figure 4: Error corridors of the phase wavelet spectra shown in Fig.3

the wavelet spectra of the original events and the wavelet spectra of the new events is checked through variable

$$z = \frac{[W_{orig}(a,b) - W_{new}(a,b)]}{\sigma(a,b)},$$

where $\sigma(a,b)$ are errors of $W_{orig}(a,b)$.

Wavelet coefficients $W_\Psi(a,b)$ are presumed to fluctuate normally but only in the region of large scales where the conditions for application of the central limit theorem are fulfilled. Therefore in ideal case the variable z should be a standard normal variable, i.e. with mean 0 and standard deviation 1. In general at least Gaussian-like behaviour of variable z with mean and sigma of standard Gaussian is expected.

The distribution of variable z for the studied sample of events is shown in Fig.6. The values of z are calculated for all the studied scales and phases. The mean value and the standard deviation of z are close to the anticipated values although the distribution little deviates from ideal Gaussian curve. This can be explained by presence of small scales where Gaussian behaviour may not be a good approximation. The another reason could be a finiteness of the samples of MC events from which errors of the original events are estimated or finiteness of samples of additional events that are

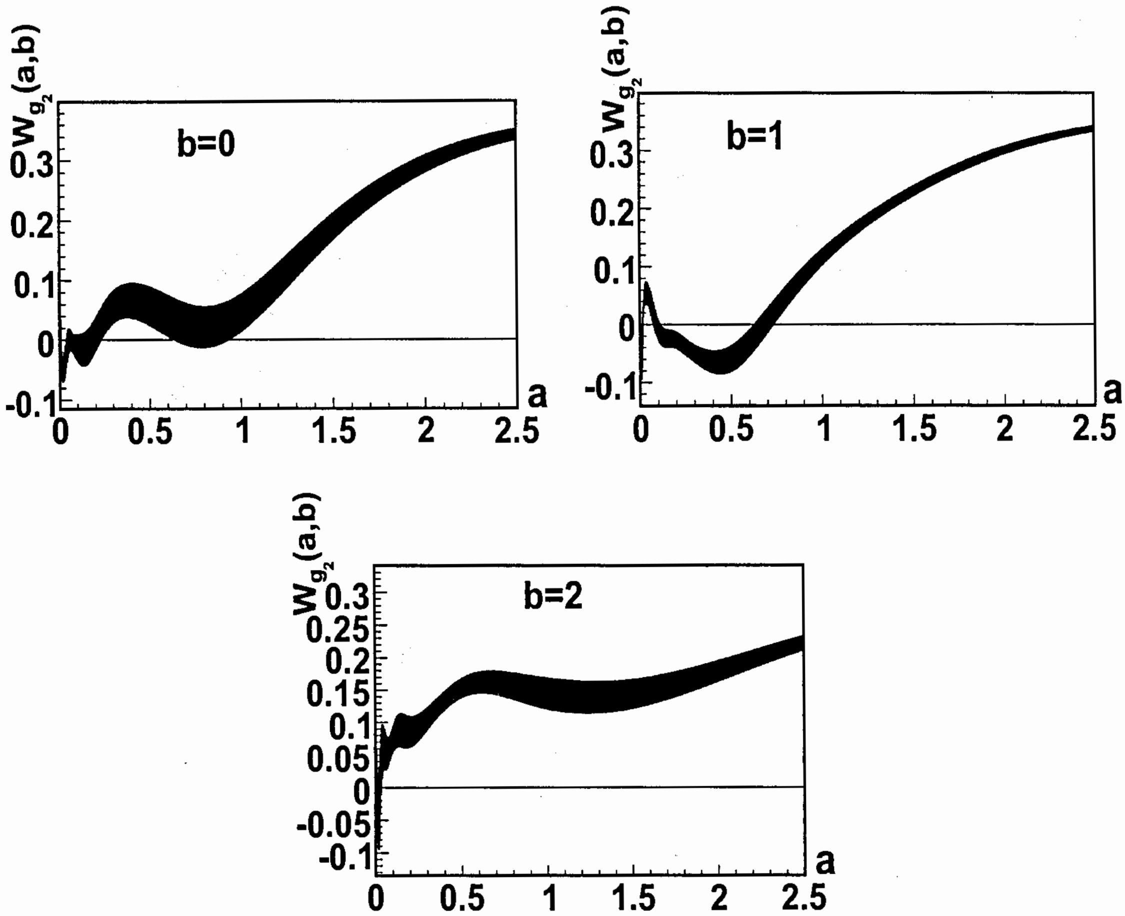

Figure 5: Error corridors of the scale wavelet spectra of the event shown in Fig.2

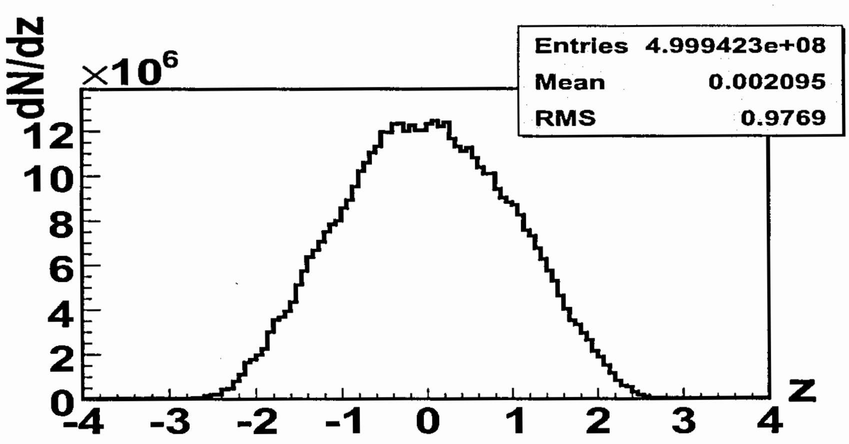

Figure 6: Distribution of variable z for the sample of 200 tested events

through variable z compared with the original events.

4. Correction of the wavelet spectra for limited detector efficiency

The next important problem that has to be solved especially when dealing with data measured in electronic experiment is to remove negative effects arising in the process of measurement. Part of physical data is due to limited detector efficiency irretrievably lost and must be corrected for. This data loss is in nontrivial way propagated to wavelet spectra which makes a correction even more difficult. In this section the procedure correcting the wavelet spectra for detector effects is proposed and discussed.

Fig.7 left shows efficiency of the imaginary detector that is employed in the next Monte Carlo study. The efficiency which is in fact generated by a process of random walk is displayed as function of x. The presented dependence is chosen because it has a few properties that are helpful for careful investigation of all aspects of the studied topic. Mainly, the dependence in Fig.7 left shows irregularities on all scales which ensures that the wavelet spectra are consequently distorted on all the examined scales as well. The next thing is that the efficiency distribution contains intervals with low, medium and high efficiencies. These features of the efficiency spectrum should enable to verify the proposed correction procedure as thoroughly as possible.

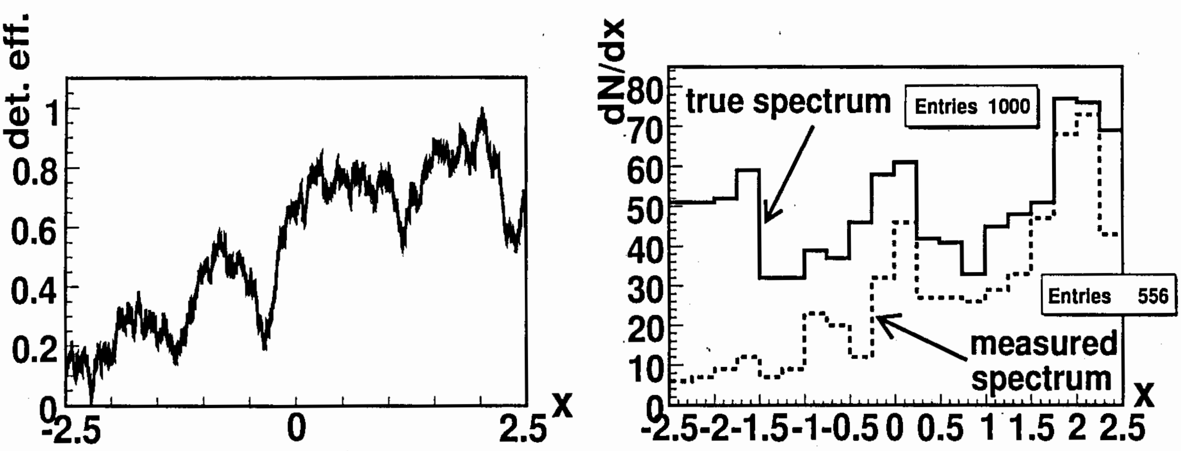

Figure 7: Efficiency of the model detector as function of x (left) and impact of this detector on the spectrum of the example event (right)

The impact of this detector measurement on the true spectrum of the example event is shown in Fig.7 right. The true spectrum consists of a few randomly scattered Gaussian spectra with different variances. Overall loss of statistics in the measurement is about 50% which at the same time implies average efficiency of the model detector.

Providing that detector response is known, correction of measured wavelet spectra can be done by the weighting method which is outlined below:

1. Detector response is applied to uniformly distributed spectrum whose size is hundred times larger than typical size of individual corrected events. Weights are calculated as a ratio of initial uniform spectrum and same spectrum after measurement.

2. Weights are calculated for each measured value separately. This is done to assure the correction will start to work from the smallest scales.

3. Measured distribution is corrected and then wavelet spectrum of corrected distribution is calculated using the modified formula (2):

$$W_\Psi(a,b) = \frac{C_\Psi}{\sum_{i=1}^{N} w_i} \sum_{i=1}^{N} w_i \Psi\left(\frac{x_i - b}{a}\right) \tag{3}$$

where w_i is weight of measured value x_i. The main drawback of this procedure consists in correcting wavelet spectra indirectly, through the correction of corresponding histograms.

Before proceeding further, it should be verified if the proposed correction method is feasible in real experiment. The main problem is to obtain a set of uniformly distributed data. Experimental data occurring in heavy-ion physics, concretely distributions of rapidities and azimuthal angles of produced particles, have certain unique features that offer possibility to overcome this obstacle. Uniform (mid)rapidity or azimuthal distribution can be produced from large number of events through their merging or mixing. Such operations produce uniform true distribution even though the true rapidity or azimuthal distributions of single events are not uniform. This argument follows from the assumption that multiparticle correlations which spoil uniformity of single events included in mixing operations occur randomly and therefore they get eventually wiped out. To better specify the multiparticle correlations just mentioned, they include above all jet-like structures or flow in case of azimuthal spectra or possibly some other multiparticle collective flows triggered by exotic physical mechanisms.

Of course, the proposed correction method is applicable only if detector efficiency does not change dramatically and erratically during the period when experimental events are measured. It should be also mentioned this method does not include correction for detector resolution.

The capability of the correction method is demonstrated in Fig.8 which shows three wavelet spectra of the studied event at the different stages of the measurement-correction process. Good visual agreement between the corrected spectrum and the true spectrum at least suggests the correction works, however, in order to estimate the *agreement of the spectra impartially, some quantitave criterion has to be introduced.*

Therefore the consistency of the wavelet spectra W_{true} and $W_{corrected}$ is compared through variable z defined as:

$$z = \frac{[W_{true}(a,b) - W_{corrected}(a,b)]}{\sigma(a,b)},$$

where $\sigma(a,b)$ are errors of $W_{corrected}(a,b)$.

Errors σ of the corrected spectrum arise mainly from uncertainties brought to the measured spectrum in the measurement process, and from uncertainties coming from weights. Both these uncertainties have statistical origin and they are described by binomial distribution since detector response is essentially binomial process (each particle is either detected or not). Therefore these errors are determined utilizing the MC method previously described with one exception – the MC events that are used for error estimation are produced from the measured event through binomial, not Poisson smearing.

For the reasons discussed in the previous section the distribution of variable z should be close to standard normal p.d.f..

The consistency test is performed not only for the presented example event but for much larger data set consisting of 100 events with different p.d.f.'s. Their multiplicities are same or very close to the presented example event. Another test is done also for

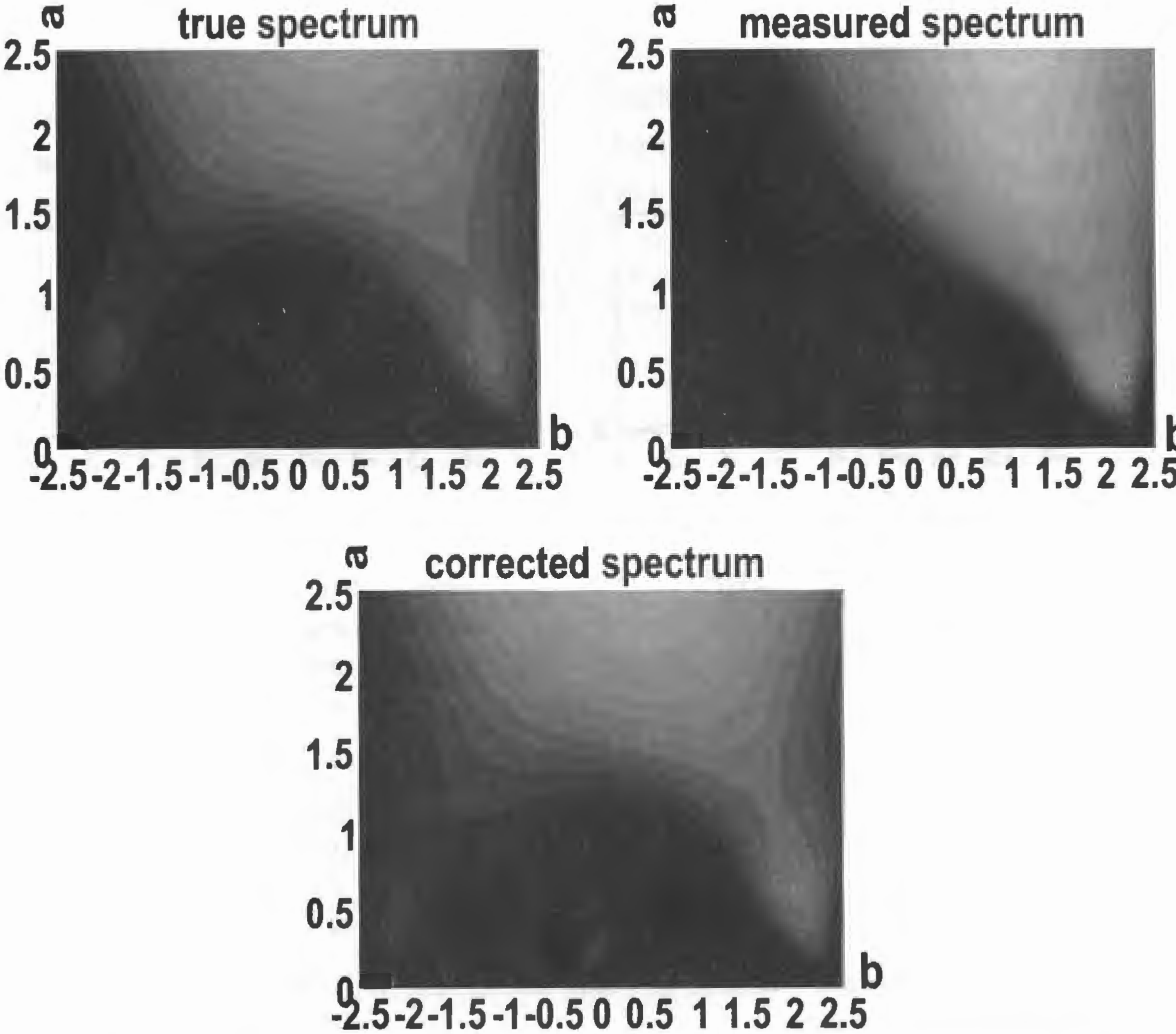

Figure 8: MHAT wavelet spectra of the studied event before the measurement (the true spectrum), after the measurement (the measured spectrum) and after the correction (the corrected spectrum)

events with ten times lower multiplicities but its results are not presented here since they are similar to those obtained for high multiplicity events.

The distributions of variable z for small, medium and large scales are shown in Fig.9. They suggest the errors are underestimated on small scales and overestimated on large scales. Furthermore, seems there is some bias that grows when going to large scales.

Possible explanations of why the empirical distributions of variable z differ from the idealized prediction:

- Small scales are problematic because they cannot be fully corrected by weighting method. If fine structure is removed from data during measurement, it cannot be restored anymore.
- The discrepancy on the large scales may arise from introducing binomial fluctuations to the measured events when creating the MC events. The measured events are already binomially smeared, thus the MC events are smeared twice which

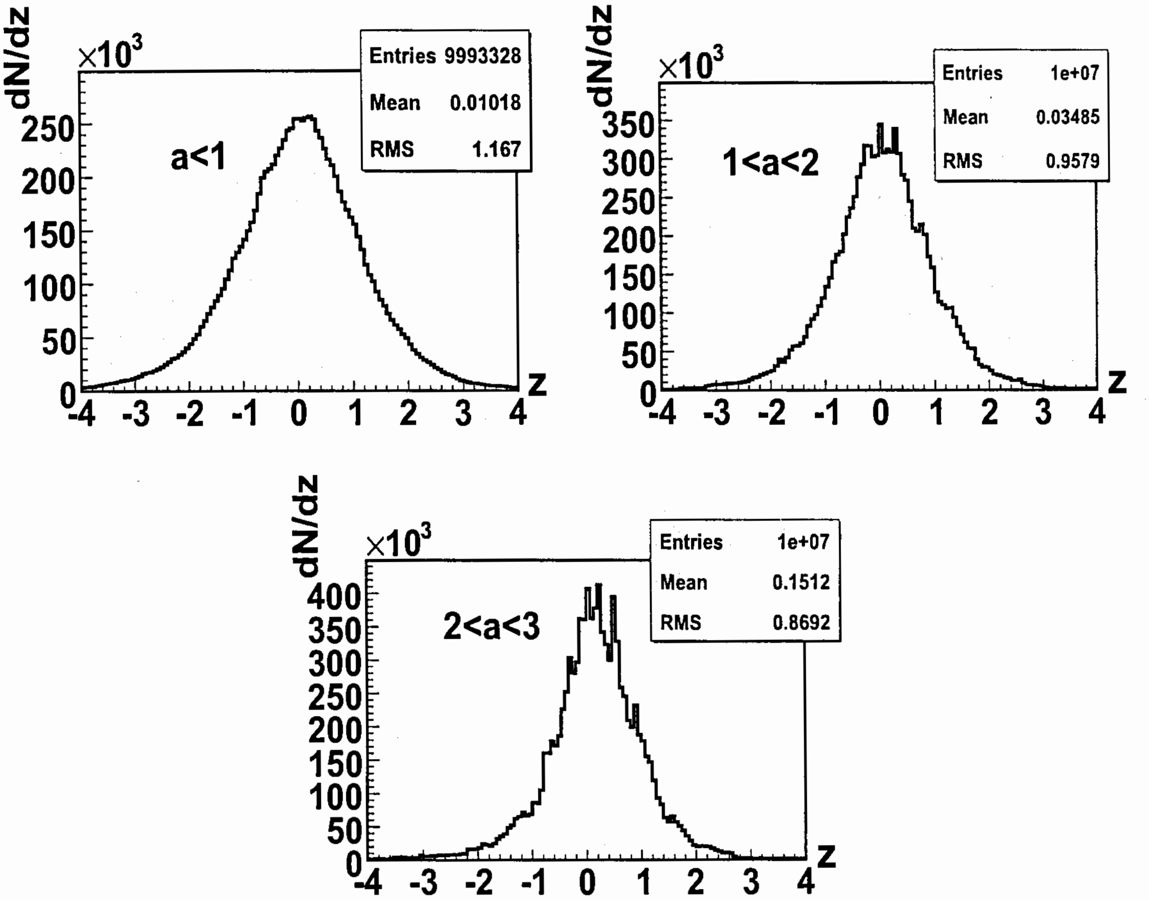

Figure 9: Distributions of z variable for small, medium and large scales a obtained for the studied sample of 100 events

may enlarge input binomial fluctuations. But this effect can be barely avoided in real experiment.

- Limited statistics of the MC events – only 10, in order not to spend to much computer capacity.

- The relationship variance $\Longleftrightarrow$ bias (that has not been investigated yet). It is known from statistics that variance and bias are complementary quantities.

5. Summary and conclusions

1. Propagation of statistical errors in the wavelet spectra was estimated by the MC method.

2. It was shown how to correct the wavelet spectra for limited detector efficiency utilizing the weighting method.

3. The basic tests were carried out to evaluate efficiency and accuracy of both the methods.

4. The results of the tests were presented and discussed. They suggest both the methods provide basically correct results albeit some minor issues need to be resolved.

Acknowledgments

The work was supported by the Scientific Grant Agency of the Ministry of Education of Slovak Republic and the Slovak Academy of Sciences under the contract No. VEGA 1/0080/08.

SEARCH FOR ETA-MESIC NUCLEI AT THE INTERNAL TARGET OF THE JINR NUCLOTRON

D.K.Dryablov[a,1], S.V.Afanasev[a], A.S.Artiomov[a], D.M.Zhomurodov[a], A.Yu.Isupov[a], Z.A.Igamkulov[a], V.I.Ivanov[a], A.I.Malakhov[a], E.B.Plekhanov[a], A.I.Lvov[b], L.N.Pavlyuchenko[b], V.V.Polyanskiy[b], S.S.Sidorin[b], G.A.Sokol[b], R.N.Bekmirzaev[c],

a) JINR, 141980, Dubna, Moscow region, Russia
b) LPI, 119991, Moscow, Russia
c) JSPI, 130114, Jizzakh, Uzbekistan

Abstract

In the present paper an experiment set-up on a search for and study of eta-mesic nuclei (quasi-stationary bound state of the η and a nucleus) is considered. We have prepared the SCAN spectrometer and tested this set-up for working at framework the "eta-nuclei" project. The test showed two-arm spectrometer allows to detect and perform spectrometric analysis of decay products of the S11 resonance, proton and pion.

Using this setup we obtained the first results on formation of η-mesic nuclei at internal beam of the Nuclotron (JINR, Russia). The reacting $d + C \to \pi + p + X$ at E_{beam}=1.5 and 2 Gev/n was investigated.

Some theoretical calculations, simulations and analysis of the obtained data is given.

1. Introduction

The study of in-medium properties of hadrons is one of the most interesting topics of contemporary nuclear physics. In particular, the in-medium meson masses depend on nuclear density and temperature. Theoretical estimation show that mesons masses are about 15~20% lighter then the vacuum values already at the normal nuclear density [1]. So far, several kinds of hadron-nucleus bound systems have been investigated such as pionic atoms, kaonic atoms, and $\overline{p}$ atoms [2]. Now extensions of the method to other meson-nucleus bound states are being widely considered both theoretically and experimentally [5,9].

In the papers [4,10] the structure of η-nucleus bound systems (η-mesic nuclei) is investigated as one of the tools to study in-medium properties of the $N(1535)$ (S_{11}) resonance. The level structure of bound states has been calculated and has find that this structure is sensitive to the in-medium properties of the resonance.

There are directions of studies of η-mesic nucleus:

- Determination of the energy levels $E_g(S_{11})$ and $E_g(\eta)$ and their widths $\Gamma_g(S_{11})$ and $\Gamma_g(\eta)$ in the η-nucleus is of the main interest. This serves for testing ηA potentials proposed in various works. Calculations of the energy levels of η-nuclei performed in a number of theoretical works [13, 14, 15, 16] give a very wide range of the energies E_g and widths Γ_g what is directly related with insufficient accuracy of determination of the ηN-scattering amplitude $f(\eta N)$ and the following reconstruction of the ηN and ηA interaction.

- A direct study of the process $\eta N \to \eta N$ is not possible because of absence of beams of η-mesons (($\tau_{1/2} \simeq 5 \cdot 10^{-19}$ s). Since the $\eta N \to \eta N$ process permanently

[1]E-mail: dryablov@sunse.jinr.ru, LHEP JINR, work phone number: +7 (49621) 62804

happens inside an η-mesic nucleus, one can hope to use experimental data on cross sections of η-nuclei formation for getting more precise characteristics of ηN interaction, the scattering amplitude $f(\eta N)$ and the scattering length ($a_{\eta N} = f(\eta N)$ at $E_\eta = 0$) being at the first place.

- It is of great interest to experimentally determine mass shifts $\Delta m(\eta)$ and $\Delta m(S_{11})$ for constituents of η-nuclei, the η-meson and the $S_{11}(1535)$ resonance, in the nuclear medium [17]. Such information will perhaps shed a new light on the fundamental problem of origin of hadron masses. Currently, such questions are widely discussed in papers devoted to the chiral symmetry breaking [18].

- Apart from the first-order potential, other potentials of the ηA interaction are considered in some works, in which the shift of particle masses depending on the nuclear density $\rho(r)$ is taken into account. In this relation, it is of interest to investigate radio-active η-mesic nuclei, for which the nuclear potential is large near the nuclear surface [19].

- Studies of interaction between the $S_{11}(1535)$ resonance and nucleons in the nucleus and determinations of the amplitude of the reaction $S_{11}N \to NN$ are very perspective. This direction of research is unique since such a reaction cannot be studied in other way because of the lack of beams of the $S_{11}(1535)$ resonances (($\tau_{1/2}(S_{11}) \sim 10^{-23}$ s). The present program of investigations makes it possible to measure the ratio of probabilities for an η-nucleus to decay through the $S_{11} \to \pi N$ and $S_{11}N \to NN$ channels. The ratio of widths Γ_i for these two options for S_11 to decay can be obtained from such data.

- Eta-mesic nuclei are formally rather close to hypernuclei which contains, apart from nucleons, a particle of another flavor (a strange Λ or Σ hyperon). In the case of η-mesic nuclei containing the η meson, the difference is that the η meson consists of two quarks rather than three quarks as in the case nucleons and hyperons. Still, the quark structure of the η meson is characterized by a large admixture of hidden strangeness in the form of the $s\bar{s}$ pair. This peculiarity is perhaps very important for understanding dynamics of the interaction between the η meson and nucleons in η-nuclei. In view of existence of hidden (sea) strangeness in the nucleon [20], it is natural to expect an essential role of exchange with strange quarks in ηN interaction. In this sense, η-mesic nuclei can be considered as objects of quark-gluon nuclear physics.

In this paper we describe the experimental results on search an η-mesic nucleus at the internal deuteron beam of the Nuclotron in the reaction

$$d + C \to (A_2)_\eta + \ldots \to \pi + p + \ldots , \tag{1}$$

where A_2-nucleus is the part of ^{12}C formed in dC collision. The hadrons emitted at the transverse direction are registered by the two-arms spectrometer. The flow of particles includes πp-pars are product of the η-nuclei decay. A bound state of η is expected to be seen as peak in the energy spectrum of these pairs.

2. Method of identification of η-mesic nuclei

A theoretical predictions (for example,[3,4]) for the energy dependence of the s-wave ηN scattering amplitude demonstrates that an attraction between η and N exist at energies $E_{kin}(\eta) \leq 70$MeV.

Eta-mesic nuclei are unstable, their life-time $\tau_{\eta A} \approx 10^{-22}$ s, and they decay mainly to the πN, $\pi\pi N$ and NN channels (see Fig.1). A method of identification of η-nuclei consists in detecting πN pair which emerge due to a decay of a slow $S_{11}(1535)$ nucleon resonance in the η-nucleus and which are correlated over the opening angle and energies of components. The $S_{11}(1535)$ resonance decay to an πN or ηN pair is almost equally probable ($\sim$ 50%). The decay to the ηN channel leads to a low kinetic energy, so that the η meson and the nucleon stays in the nucleus. Therefore, multiple $\eta N \rightarrow \eta N$ transitions are very probable inside the η-nucleus. Such transitions are over when a πN pair is produced, because kinetic energies of the components π and N are now sufficient for escaping the nucleus (see Fig.1):

$$\eta + N \rightarrow S_{11}(1535) \rightarrow \eta + N \rightarrow S_{11}(1535) \rightarrow ... \rightarrow S_{11}(1535) \rightarrow \pi + N. \qquad (2)$$

The resulting πN pair is correlated over the opening angle $\langle\Theta_{\pi N}\rangle$ and energies of pair components. The decaying, inside the η-mesic nucleus, $S_{11}(1535)$ resonance in the chain (2) has a low kinetic energy, because $E_{kin}(S_{11})$ is determined by the kinetic energy of the η-meson and the nucleon (Fermi motion). Since energies of π and N in the finally produced πN pairs are large ($\langle E_\pi\rangle \cong 350$ MeV and $\langle E_N\rangle \cong 100$ MeV), the opening angle of the pairs is close to 180 degrees ($\langle\Theta_{\pi N}\rangle \approx 180°$).

It is worth noticing that πN pairs with the angle $\langle\Theta_{\pi N}\rangle \approx 180°$ cannot be produced in a decay of the $S_{11}(1535)$ resonance emerging at the first stage of the reaction (see Fig.2), i.e. in the interaction of the primary proton with a nucleon in the nucleus,

$$p_0 + n \rightarrow n + S_{11}^{+} \rightarrow n + \pi^{+} + N, \qquad (3)$$

because such a $S_{11}(1535)$ resonance typically has a large momentum and gives $\langle\Theta_{\pi N}\rangle \approx 100°$.

In addition to the πN pair, the neutron and the proton produced at the stage of formation of an η-nucleus will be detected in the next experiments.

3. The experimental setup

A method of detection of events with formation of η-mesic nuclei is based on detection of πN pairs which are correlated over angle and energy and which emerge from decays of S_{11} resonances in nuclei. Although imitation of such πN-events by other events of an inelastic pC interaction is practically impossible, there is a rather high level of random coincidences. That is why, in the project, a necessity exits to strengthen the trigger for separation of events with formation of η-mesic nuclei.

The setup for studying of decay product particles of η-nucleus is shown in Fig.3. The setup include the following systems:

1) A monitor system that consists of 4 scintillator telescopes - two triple monitors (F_L, F_R) and two double monitors (B_L, B_R) installed in the horizontal plane on both sides of the beam pipe. As well as determining the luminosity of reactions, the pairs of monitors: F_L, B_R and F_R, B_L serve to extract a quasi-elastic pp channel. Depending on the beam energy, angles of monitor positions can be changed.

2) A 32-channel scintillator hodoscope H_M that consists of two concentric rings sectioned to 16 segments each. Each segment is supplied with an individual phototube. H_M is used for selection of the impact parameter by the multiplicity measurement method [21]. For the aims of the "Eta-nuclei" project, the hodoscope serve for detection of protons created in the reaction of η-meson production through $S_{11}^{+}(1535) \rightarrow p + \eta$.

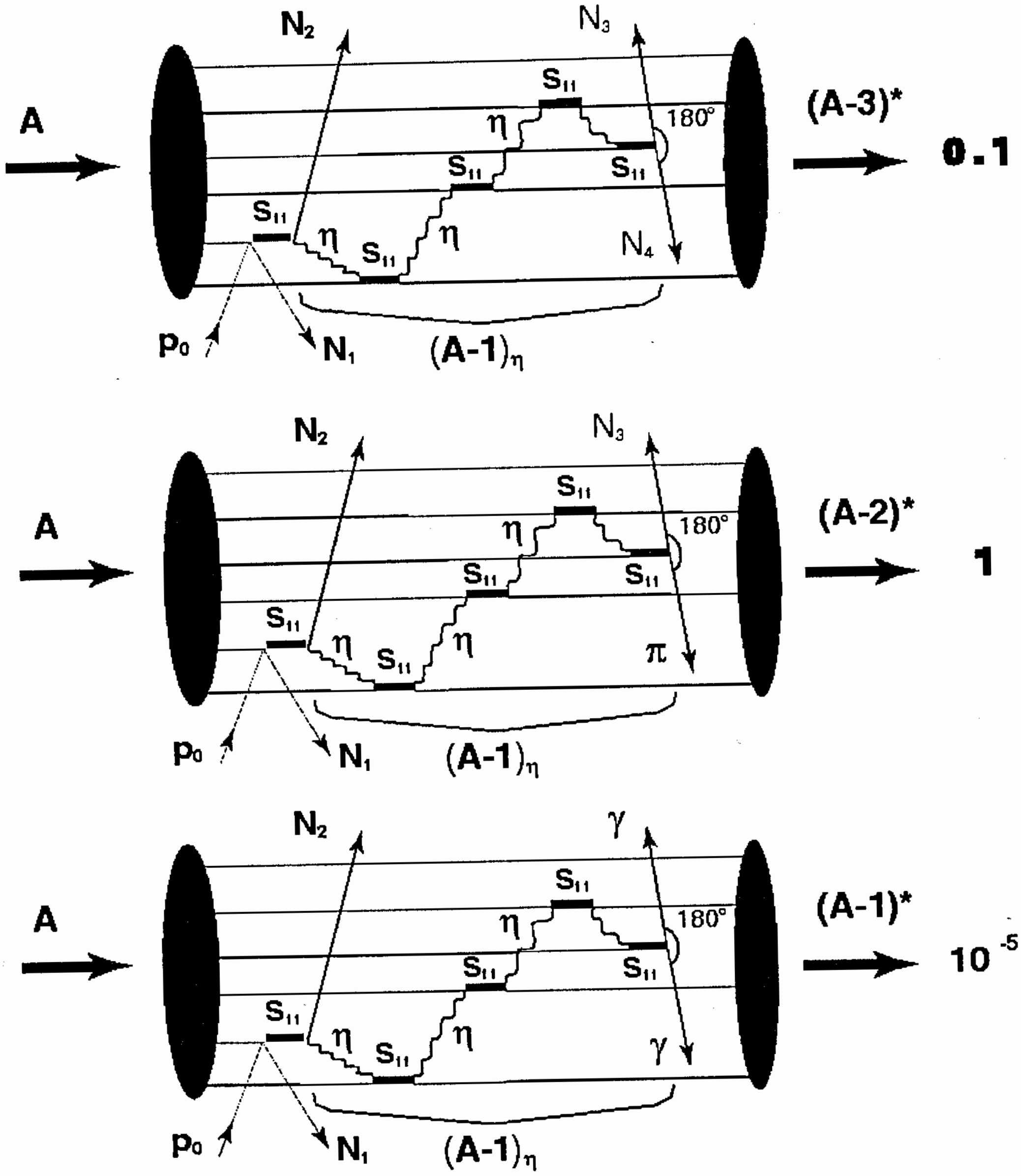

Figure 1: Formation, evolution, and decay of an η-nucleus, $(A-1)_\eta$, in a pA collision. Decay modes and their probabilities:
NN-channel(above), πN-channel(in the middle), $\gamma\gamma$-channel(below)

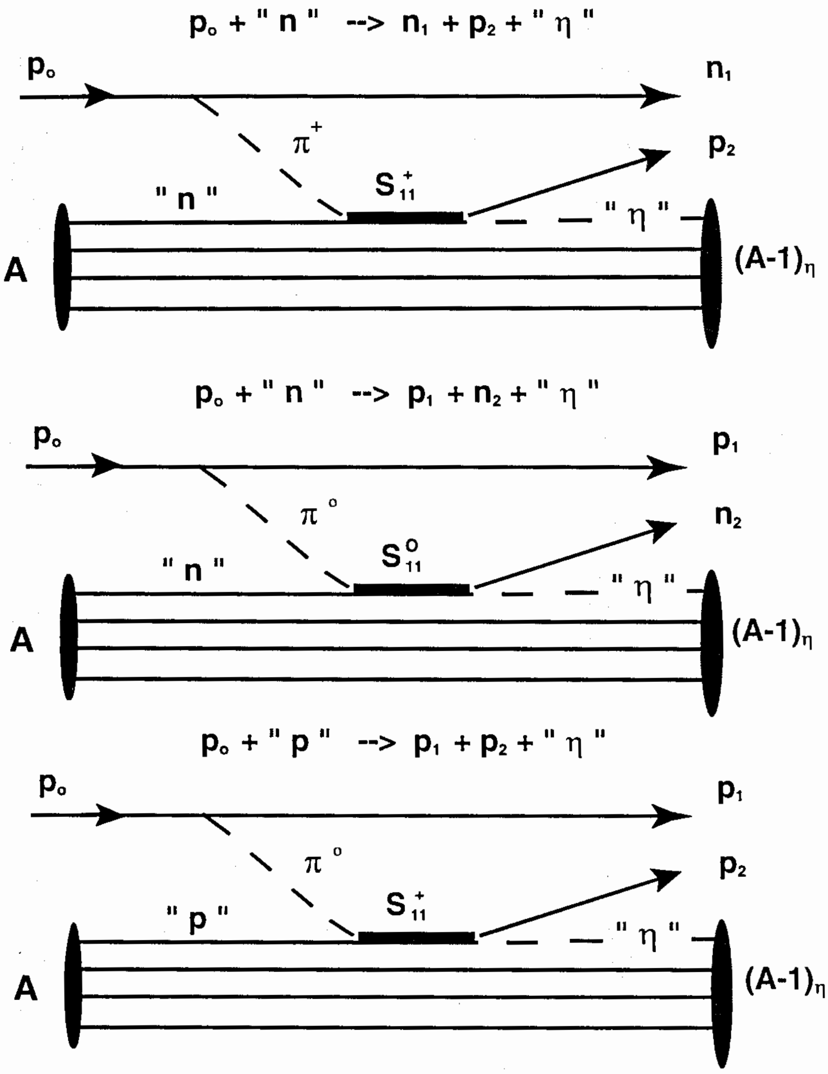

Figure 2: Formation of an η-mesic nucleus in a pA collision:
$p_0 + A \to n_1 + p_2 + {}_\eta(A-1)$(above);
$p_0 + A \to p_1 + n_2 + {}_\eta(A-1)$(in the middle);
$p_0 + A \to p_1 + p_2 + {}_\eta(A-1)$(below).

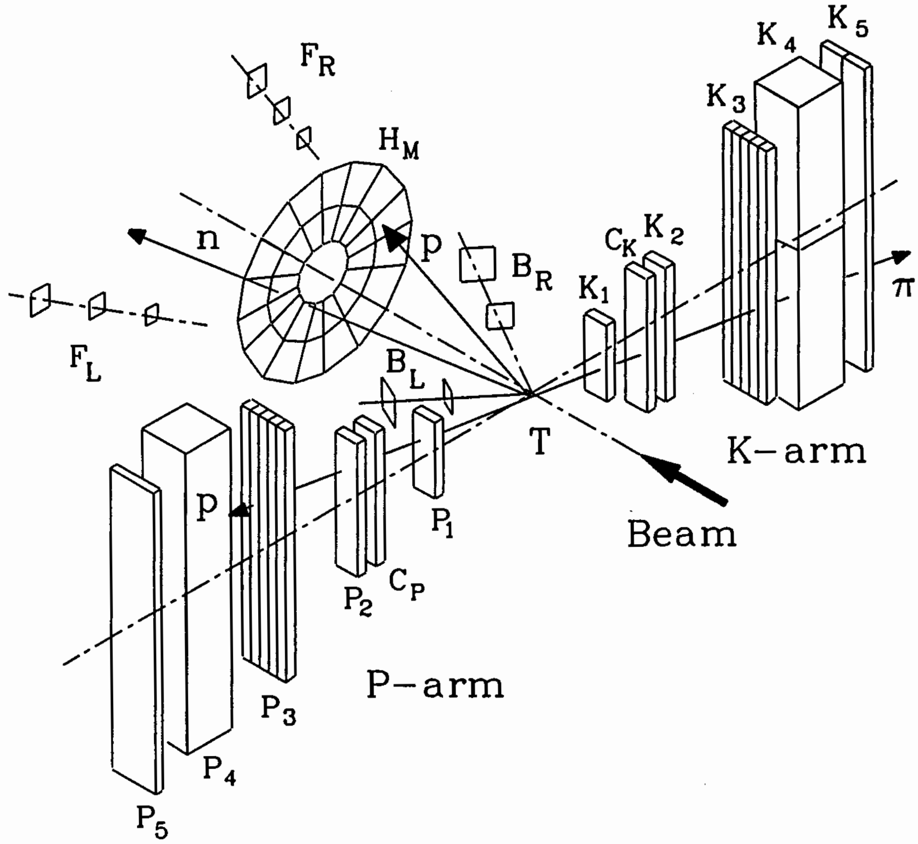

Figure 3: SCAN spectrometer. The experimental setup for study the in-medium properties of hadrons.

3) A spectrometer part that consists of two sets of decay-particle counters, located to the left (P-arm) and right (K-arm) of the target for back-to-back coincidence measurement. Each of coincidence counter sets consists of: fast timing counters ($P_1 \div P_3$; $K_1 \div K_3$), large volume counter (P_4; K_4), high-momentum particles detector (P_5; K_5), and the threshold Cerenkov counter (C_P; C_K) for pions separation. Each of these detectors has two photomultipliers at either end (at the bottom and top).

Using this spectrometer, it has become possible to make an absolute measurement of particle time of flight with an accuracy of about 0.2ns and a positional sensitivity of about 2.5cm.

The charged particles are identified by the three measured values: ΔE – the energy loss per unit length measured by all counters, TOF – the time-of-flight between $P_1(K_1)$ and $P_3(K_3)$ and E – the ADC sum of sequentially fired counters.

Protons and pions were clearly identified, and the proton contamination in the pion gate is less than 5%. The threshold Cerenkov counter rejects this contamination up to 50 times. The detection thresholds are 40 MeV/c for pions and 230 MeV/c for protons. The efficiency of the counter system was Monte Carlo simulated using the

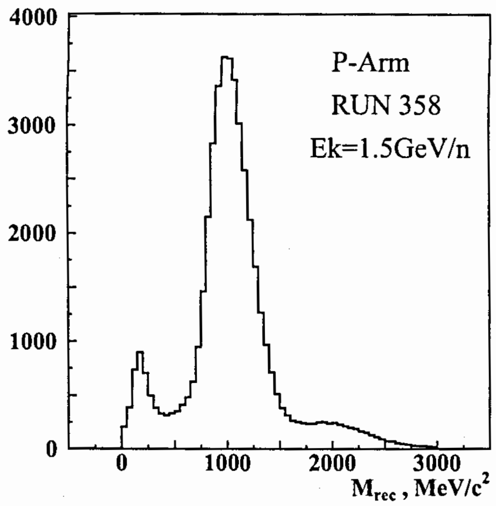

Figure 4: Mass reconstruction in the single-particle measurement.

GEANT code.

4. Event reconstruction

The experiment was carried out at the internal beam of Nuclotron with 1.5 and 2 GeV/nucl deuteron beam.

In order to resolve experimental difficulties, it is important unambiguously identify the two-body decay kinematics of the resonance. We have measured in coincidence two particles emitted in the back-to-back direction from the target, with the angle of two-arms setup around an open angle ($\Theta_{PK} = 180^o$). Also a contamination has been measured in not back-to-back kinematic with angle $\Theta_{PK} = 170^o$.

The collected data have been converted to the DST using calibration procedure described in [12] and analyzed in off-line. The particle type identified by determination the masses of particles. We have used the tradition method to measure two independent kinematic quantities involving the mass of particle. One of these quantities is velocity (β) and other is the energy (T). The velocity is calculated from the time of flight measurement and kinetic energy is proportion to ionization loss in the detectors:

$$\beta = \frac{L_{start-stop}}{t_{tof} \cdot c}; \qquad T = \sum_{i=1} k_i \cdot (dE/dx)_i,$$

where c – velocity of light, t_{tof} - time of light on a given basis $L_{start-stop}$ and i – number of activated detector. Finally a particle reconstruction mass was calculated from

$$M_{rec} = T\frac{\sqrt{1-\beta^2}}{1-\sqrt{1-\beta^2}} \tag{4}$$

The results of these calculation are plotted on Fig.4. All events within $0 < M_{rec} < 500$ are identified as π-mesons (m_π); within $500 < M_{rec} < 1500$ – as protons (m_p) and with $M_{rec} > 1500$ as deuterons (m_d). The masses m_1 and m_2 of these identified particles are applid to to the effective mass M_{eff} reconstruction:

$$M_{eff} = E_1 + E_2 = \frac{m_1}{\sqrt{1-\beta_1^2}} + \frac{m_2}{\sqrt{1-\beta_2^2}} \tag{5}$$

There are three good separated tiles of M_{eff}. They peaks are formed by the $\pi\pi$, πp and pp+πd pairs. M_{eff} resolution $\sigma \approx 8$ MeV

5. Additional simulation: effective mass correction.

An error of M_{rec} and M_{eff} follows from , in particular, an error of definition of kinetic energy and particles velocity. Except systematic errors, the error of kinetic energy is defined by losses of particle energy, which are not registered by set-up, the error of particles velocity is defined by particle braking in substance on the way from a target to detectors (P3 or K3). From the simulation data of passage of particles through set-up it is possible to receive true values kinetic energy T_{th} and particles velocity speed β_{th} after their start from a target:

$$\beta_{th} = \frac{p_0}{\sqrt{p_0^2+m^2}}, T_{th} = \sqrt{p_0^2+m^2} - m, \beta_{exp} = \frac{L}{t*c}, T_{exp} = e1+e2+e3+e4, \tag{6}$$

p_0 - particle momentum from simulation program output, m - tabular value of particle mass, t - time of light on a given basis L, c – velocity of light, $e1, e2, e3, e4$ - energy release in the detectors P1, P2, P3, P4 or K1, K2, K3, K4.

Experimental and theoretical values of kinetic energy and relative particle velocity for pions and protons it is possible to see on Figure5.

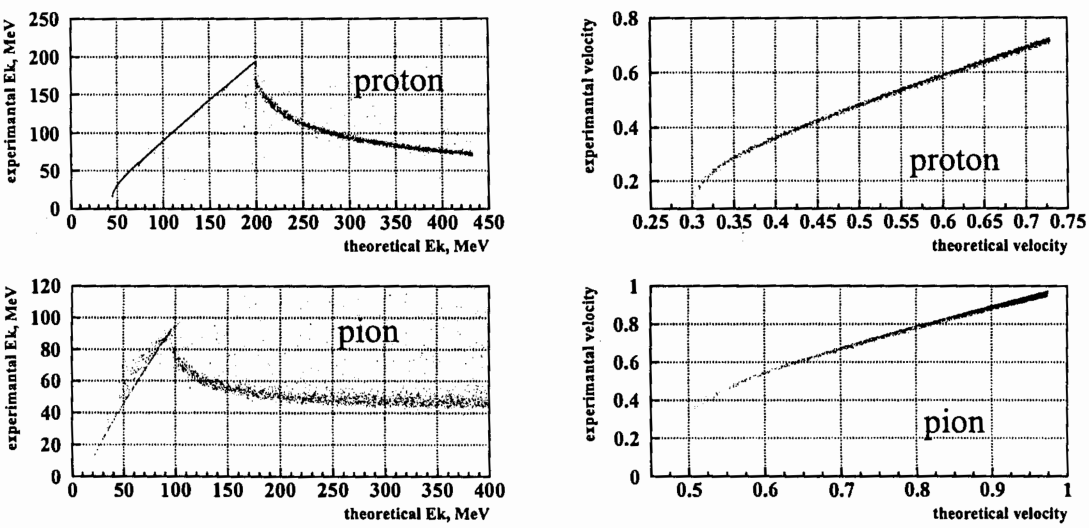

Figure 5: *The experimental kinetic energy and velocity dependence of the theoretical kinetic energy and velocity*

On the energy dependence graphs clearly visible two components of these graphs, the left component are the particles, which have not passed further last detector, right component are the particles, which have passed last detector.

To exact definition of effective mass it is necessary to enter the correction for relative velocity (and kinetic energy). If we do not enter this correction the total energy of each particle will be inaccurate, as shown, for example, in Figure 6. In particular, for a proton and a pion with $\beta_p \sim 0.44$ and $\beta_\pi \sim 0.96$ (from N(1535) resonance decay) the total energy sums error will be more than 50MeV.

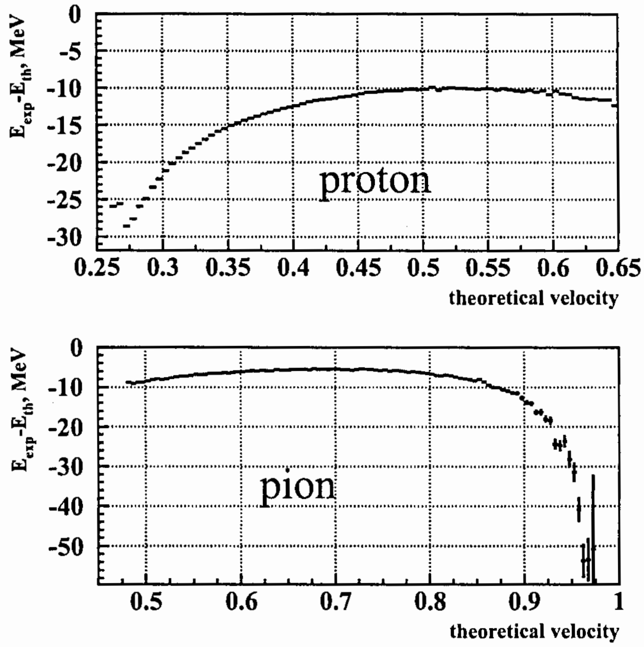

Figure 6: *The total energy error dependence of the theoretical velocity (without correction)*

6. Additional simulation: estimation of the cross section of Δ formation.

Realization of the "search for η-mesic nuclei" experiment is not a simple problem. The main difficulty is a small cross section of formation of η-mesic nuclei in pA or dA -collisions and a big background. In the case of the ^{12}C target, the total cross section of η-nucleus formation is expected to be $\sigma_t(_\eta A) \approx 3\ \mu b$. Meanwhile the total cross section of inelastic processes in a pC interaction is $\sigma_t(pC) \approx 250$ mb, i.e. 80000 times bigger.

Help with the decision of this problem is a research of the known reaction similar to reaction of η-mesic nuclei formation. Fortunately, such reaction is a formation of a stationary Δ-isobars (N1232) in a nucleus. The Δ-isobar cross section in pA-reactions is more (tens of mb) than the η-nuclei cross section in the same reaction (about 3 μb). The Δ-isobar can be used for analysis of hadrons behavior in nuclear matter and as a reference point in our measurements (search for η-nuclei). Therefore, process of the formation and the subsequent decay of Δ - isobars was chosen for our subsequent kinematic calculations.

Two-stage process of a Δ-resonance formation in a nucleus of a target is considered. Kinematic calculation of cross-section of pions production in p-A inelastic collisions and subsequent interaction of formed pions with a nucleus of target is analyzed.

We received the cross section of the Δ -resonance formation in $p^{12}C$-interaction for different kinetic energies of protons:

E_{kin}, GeV	1.4	1.5	1.7	1.9
σ_Δ, mb	13.15	12.42	10.8	9.86

By means of a Monte - Carlo method we have defined that SCAN set-up registers only one tenth part of the decay products of resting Δ resonance from from number of decay products flying in a direction of detectors (Figure 7).

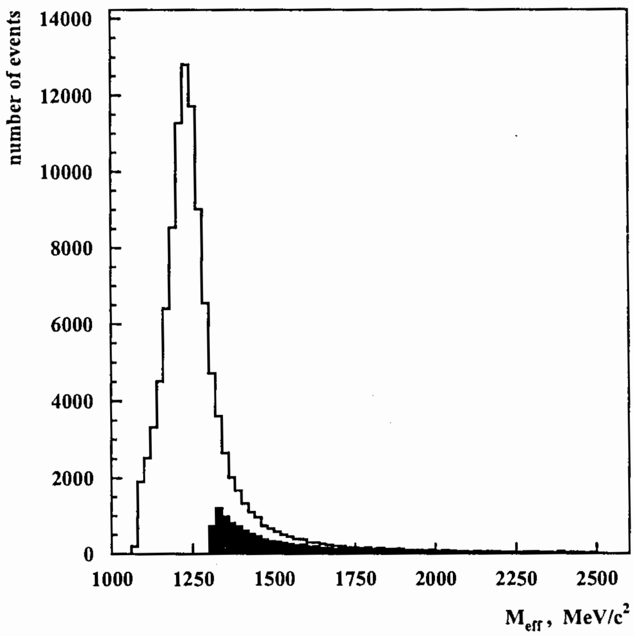

Figure 7: *Distributions of the effective mass of two particles from the Δ-resonance decay. The particles registered by spectrometer SCAN are shown by means of the shaded area*

The yield of the double-coincidence events (p, π^-) in the reaction of formation of Δ-resonance in pA collisions is equal to:

$$Y(p,\pi^-) = \sigma(p^{12}\mathrm{C} \to N_1N_2(A-1)_\Delta)\cdot N_t\cdot N_{\text{eff}}\cdot Br(\pi N)\cdot\xi\cdot\Omega_\pi\cdot n_c\cdot k\cdot f(\Omega p/\Omega_\pi)\cdot g, \quad (7)$$

where $N_{\text{eff}} = 3.0\cdot 10^{15}$ - the flux of protons hitting the target (per a 5 s/cycle), $\Omega_\pi = 8\cdot 10^{-3}$ sr - the solid angle of the π-spectrometer, $Br(\pi N) = 0.99$ - the branching ratio of Δ to decay to πN, $\xi(\pi^- p) = 0.5$ - the probability of $\Delta \to \pi^- + p$, a geometric fraction $f(\Omega_p/\Omega_\pi) \simeq 0.2$ of correlated πN pairs simultaneously hitting the pion and proton spectrometer (this fraction is determined by smearing of the angular 180°-correlation due to Fermi motion), $n_c = 360$ - the number of accelerator cycles per hour, $k = 3,3\cdot 10^{-3}$ - the ration of the transverse size of target and beam, $g = 0.5$ - the fraction of the Gaussian proton beam hitting the target, $N_t = 0.85\cdot 10^{20}$ cm^{-2} - the total number of ^{12}C nuclei in the 10 μm carbon filament target.

Estimates of the effect yield for different kinetic energies of protons:

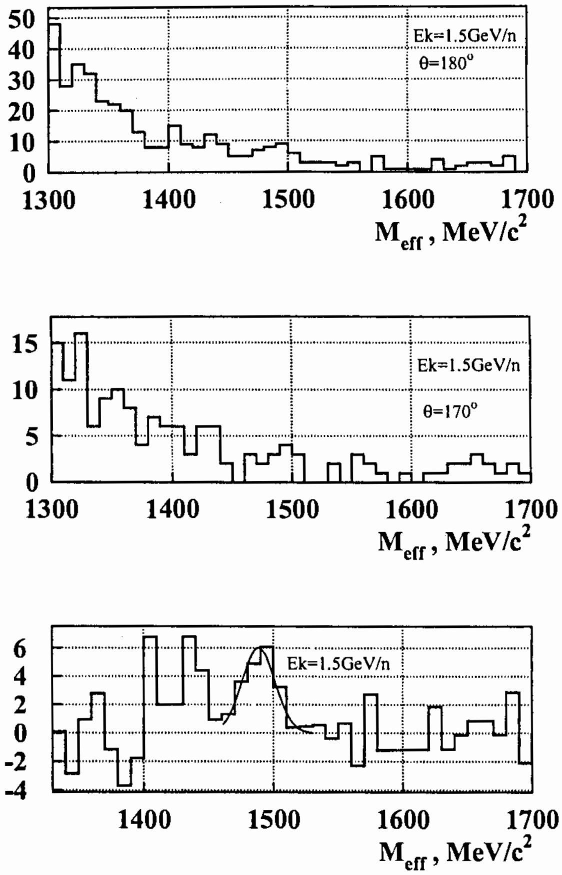

Figure 8: The $p\pi$ effective mass in the region of S_{11}-resonance for the energy of primary beam 1.5GeV/nucl and open angle of two-arm setup $180^o \pm 2.5^o$(top panel) and $170^o \pm 2.5^o$(center panel). Difference of both distributions (bottom panel)

E_{kin}, GeV	1.4	1.5	1.7	1.9
$Y_{p\pi^-}, event/hour$	960	906	789	720

7. Preliminary results on search for η-nuclei.

The experiment was carried out at the internal target of Nuclotron with 1.5 and 2 GeV/nucl deuteron beam.

Since the studied process is a two-body decay and emits nucleons with much higher momentum than the nuclear Fermi momentum, one can expect that the two emitted nucleons are strongly back-to-back correlated in their opening angle ($175^o < |\theta_{NN}| \leq 180^o$), and should have their sum of energy E_{sum} close to the value near 1535 MeV.

The distributions of the NN pair yields are shown in Fig. 8 versus M_{eff} of the pair nucleons. Only the pair events where each of the nucleons has an energy above 50 MeV are accounted. The histogram Fig.8(center panel) shows the contamination obtained at the arm angle $\Theta = 170^o$. The Fig.8(top panel) corresponds to a back-to-back correlation coming from the two-body decay. The histogram Fig.8(bottom panel) is the result of subtraction the back-to-back ($\Theta = 180^o$) and the contamination measurements.

The ratio of the nucleon pair numbers was $N_{170}/N_{180} = 0.42 \pm 0.08$(stat) in the mass region of $1450 < M_{eff} \leq 1550$MeV/c^2.

The Gauss fitting is applied to resulting histogram shows M_{eff}=1480 $\pm$ 18 MeV/c^2 and width is 23 MeV/c^2

The energy-sum resolution σ_{Esum} for πp pairs were estimated to be around 10 MeV. In the energy-sum spectrum of πp pairs, one can see the peak located at around the 1500 value of the E_{sum} as expected.

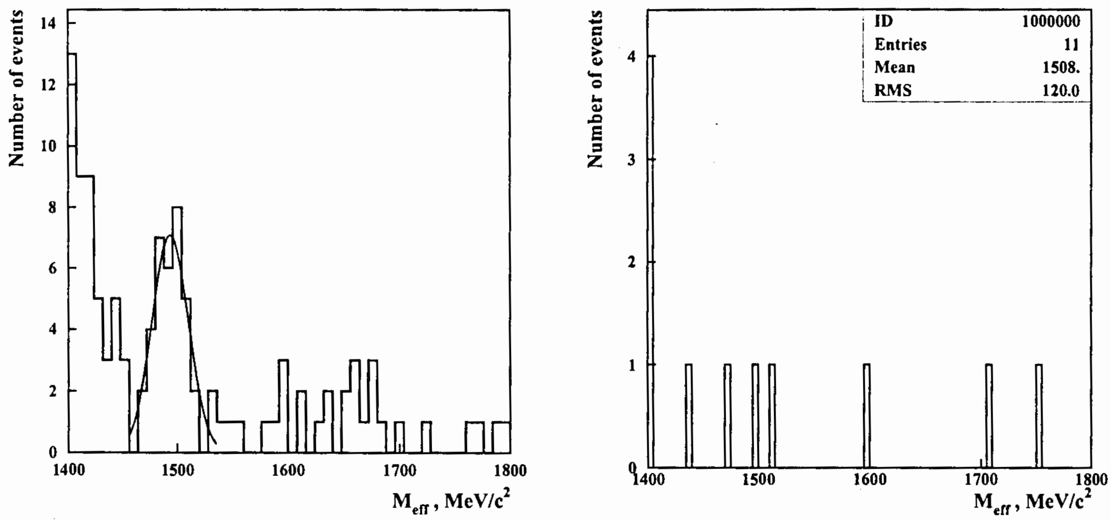

Figure 9: *The $p\pi$ effective mass in the region of S_{11}-resonance for the energy of primary beam 2GeV/nucl and open angle of two-arm setup 180$^o\pm$2.5^o(left panel) and 170$^o\pm$2.5^o(center panel).*

We observe a similar picture at E_{beam}=2GeV/n (Fig. 9). It is necessary to notice that in an investigated part of a spectrum of effective mass the peak, which disappears at background measurement, is observed.

For an estimation of a real part of scattering length of it is necessary to know a cross section of η-mesic nucleus formation. The cross section of $d + C \rightarrow A_\eta + ... \rightarrow \pi + p$ has been estimated:

$$\sigma_{A\eta} = (\sigma_{in} * (N_{eff} - N_{fon})/(\Omega * N_{in}) = 11.6 \pm 7.5 \pm 3.2\mu b, \tag{8}$$

where σ_{in}= 426$\pm$22 mb - cross section of inelastic $d^{12}C$ interaction at E_d=2.1GeV/n, N_{in}=1.5-2.2*10^9 - number of inelastic dC-interactions, which were measured under accounts of monitor telescopes and results of simulation with use of software packages GEANT and RQMD, Ω - the solid angle of the spectrometer, N_{fon} = 7.5 - reduced number of registered $p\pi$ pairs (background measurements, $1450 < M_{eff} < 1550MeV/c^2$). N_{eff} = 40 - number of registered $p\pi$ pairs ($1450 < M_{eff} < 1550MeV/c^2$)

7. Summary

We have measured the energy-sum and the angular correlation of two nucleon pairs πp emitted in the d+C reaction at E_{beam}=1.5 and 2 GeV. We have clearly observed a distinct πp back-to-back correlation coming from a target, which may be associated the signature of two-body final state.

Acknowledgments

We are grateful to JINR Nuclorton staff for their support of our experiment.

References

[1] T. Hatsuda and S.H. Lee, Phys. Rev. C46 R34 (1992)
[2] C.J. Batty, et. al., Phys. Rep. 287, 385 (1997)
[3] A.M. Green, S. Wycech, Phys.Rev. C55(1997) R 2167
[4] A.I. Lvov, nucl-th/9809054; 18 Sep 1998
[5] R.S. Hayano, S. Hirenzaki and A. Gillitzer, Eur. Phys. J. A6, 99 (1999).
[6] M. Pfeiffer, et. al., Phys.Rev.Lett. 92, 252001 (2004)
[7] M.Kh. Anikina, al., nucl-ex/0412036; (2004)
[8] G.A. Sokol, et al., nucl-ex/0011005; (2001)
[9] T. Falter et al., Progress in Particle and Nuclear Physics 53 (2004) 25-44
[10] D. Jido, H. Nagahiro and S. Hirenzaki, Nucl.Phys., A 721 (2003) 665-668
[11] S.V. Afanasev et al., JINR Rapid. Comm.,5[91]-98(1988) p.25
[12] S.V. Afanasev and D.K. Dryablov, Particles and Nuclei, Letters 2[125]-2005 pp.82-90
[13] A.I. Lvov, nucl-th/9810054
[14] Q. Haider, L.C. Liu, nucl-th/0209082
[15] C. Garcia-Recio et al., nucl-th/0206024
[16] V.A. Tryasuchev, Physics of Particles and Nuclei, 30, N 6, 606, 1999
[17] D. Jido et al., nucl-th/0206043
[18] T. Hatsuda, T. Kunihiro, Phys. Rep. 247 (1999) 241
[19] H. Nagahiro, D. Jido and S. Hirenzaki, nucl-th/0304068
[20] Particle Physics in Germany, Status and Perspectives, Nov. 2002 p.27
[21] P.L. Jain et al., Phys. Rev. C 47, 342 (1993)

STUDY OF NUCLEON STRUCTURE AT MESON PRODUCTION IN POLARIZED NUCLEONS COLLISIONS AT THE ENERGIES 1200 - 1400 MeV

A.N. Livanov[a,1], V.A. Krasnov[a], S.N. Kuznetsov[a], A.V. Pilyar[a]

a) JINR, 141980, Dubna, Moscow region, Russia

Abstract

The program on the study of the spin and medium effects in nucleon-nucleon and nucleon-nucleus collisions using DELTA-spectrometer is reported. The basic elements of the spectrometer: 150x2 channels Cherenkov detectors, monitoring system, proportional chambers, data acquisition electronics etc. are described.

1. Introduction.

Recent advances in accelerator and beam-target technology at JINR have opened up new possibilities for nuclear physics. Using slowly extracted polarized deuterons available at the Nuclotron accelerator complex of the Laboratory of High Energy Physics JINR, polarized quasi-monochromatic neutrons of moment from 1.1 to 4.5 GeV/c were generated. The momentum spread of the neutrons is ~5% (FWHM). The mean value for neutron beam polarization $|P_B(n)| = 0.535 \pm 0.009$. In addition, for the JINR physics program, the Argonne - Saclay frozen spin proton polarized target (used initially in the E704 experiment at FERMILAB) was updated and installed on the LHE polarized neutron beam line. The target material is 1.2 - propanediol $C_3H_6(OH)_2$ and contains $9 \times 10^{23}/cm^2$ polarized hydrogen atoms approximately. The maximum value of proton polarization was 0.842. The first measurements on the polarized beam-target complex were carried out, and the results of the neutron-proton total cross section difference $\Delta\sigma_L$ were obtained.

The physics program for new DELTA setup includes a search for the polarization phenomena of π^0 - and η - meson production in $\mathcal{NN}$ collisions with polarized nucleons (with probable deuteron production in the final state) at energies up to 2.5 GeV.

A major difference between the η and π^0 - meson is in their isospin and quark wave function: in addition to the $\overline{u}u$ and $\overline{d}d$ components, η also contains a $\overline{s}s$ pair, reflecting a relatively large mass of η. Another attractive feature of the η - meson is a selective excitation of the $N^*(1535)$ S_{11} - resonance in $\eta\mathcal{N}$ interaction (nearby the production threshold). The η - meson also decays into two photons with a large fraction (39%)similar to the π^0 - meson which decays predominantly into two photons.

2. Motivation.

DELTA-spectrometer has been designed and completely assembled to study neutral meson production at LHEP-JINR NUCLOTRON. It consists of two blocks with 150 lead-glass prisms (see Figure.1). The setup ensures a high-resolution and high-aperture detection of π^0 - and η - mesons for an energy of 100 MeV (for π^0) or 30 – 40 MeV (for η) and above.

The spectrometer is designed to determine the energies and emission angles of π^0 - and η - mesons coming from the target. The used experimental method consists

[1]E-mail: livanov@lhe.jinr.ru

in the detecting of two energetic photons, emitted in the decay of a neutral meson (99% and 39% probability for π^0 and for η, respectively), in an array of Cherenkov lead-glass detectors. The energies of photons emitted in the decay are of the order of $(m_0 + T_{kin})/2$ increasing with increasing particle kinetic energy. The photons tend to cluster about a laboratory opening angle $\theta_{1,2} = 2 \times \arcsin(m/E)$. This is merely due to "piling up" the spherical phase-space distribution of the photons in the decaying particle rest frame when transforming to laboratory coordinates. As the orientation of the photons in the meson rest frame is uncorrelated with the meson laboratory velocity, the observed $\gamma - \gamma$ opening angle for a given energy of particles is greater than or equal to $\theta_{1,2}$.

If $\theta_{1,2}$ is the laboratory opening angle between the two decay photons and E_1, E_2 are the laboratory photon energies, the mass m and total neutral meson energy E are:

$$m = 2 \times \sin(\theta/2) \times \sqrt{E_1 \times E_2}, \tag{1}$$

$$E = \sqrt{\frac{2m^2}{(1-\cos\theta)(1-X^2)}}, \tag{2}$$

$$X = \frac{E_1 - E_2}{E_1 + E_2}, \tag{3}$$

where X is the asymmetry parameter of γ - quanta energies.

In this case, the two photon energies are nearly equal, X^2 is small, and the measurement of θ with a good resolution can yield a good resolution for the total meson energy E.

3. Types of Pb-glass and their characteristics.

The shoulders of the spectrometer (CH1 and CH2) are two blocks. The blocks are built up from glass prisms made of F8-type *Pb*-glass with *PbO* 45% additions (see Table.1). The number of cells in each block is 150 (10 along the horizontal line and 15 along the vertical line) (see Figure.2). Each prism is shaped as a cut pyramid 400 mm high, that is $12X_0$. Its size is (36×36) mm^2 at the bottom and (22×22) mm^2 at the top. Each cell is viewed by a 34-mm FEU-84-3 photomultiplier tube.

The new principle is that glass prisms are designed as the cut pyramids with a cross dimension less than the Molier radius. This allows one to use "the center of gravity" method for avalanche coordinate measurements without converters and coordinate-sensitive detectors and increases the effective solid angle of the spectrometer. The main characteristics of the glass spectrometer are presented in Table 2.

The light output of the detector is the value about 0.3 photoelectrons for 1 MeV of γ - quantum input energy approximately. The approximating formula for the energy resolution for gammas looks like (numerical ratio):

$$\sigma(E)/E = 0.018 + 0.066/(E(GeV)). \tag{4}$$

4. Calibration experiment.

The work on starting up the setup was done on a neutron beam with carbon and polyethylene targets. The detectors were preliminary calibrated using cosmic radiation particles. About 2100 coincidence events appropriate to the np$\pi \rightarrow$ dπ^0 reaction on the polyethylene target and about 700 events on the hydrogen target were recorded using the neutron beam with an intensity of $\sim 5 \cdot 10^6$ neutrons per burst and an energy of 1.5 GeV. The level of random coincidence noise was of the order of 30% on hydrogen. As an example, (see Figure.3). The mass spectrum reconstructed from two measured gamma-quanta is shown in Figure.3. The average restored value (for 2 γ events) of mass equals 130 MeV at a 15% instrumental resolution.

5. π^0 energy spectrum.

For the first time, The energy spectra of prompt photons were measured for different mutual orientations of the longitudinally polarized proton target and polarized neutrons beam at 2.2 GeV of neutron beam energy and 80° of the average γ's angle. The preliminary results have shown the availability of the effect (relative difference of an exit at different directions of mutual polarization) at gamma-quantum energies close 400 MeV, at the level of 12% at a statistical precision of the measurements ±3%. For the analysis of detected effect the further measurements are planned. As an example, the spectrum a gamma quantum at parallel orientation of spins and 2,2 GeV neutron energy is shown on (see Figure.5). A total number of events in the spectrum is about 4.7×10 for 10 hours of measurements. It is clearly visible an amplification of an gamma - quantum exit at 400 MeV gamma energies. The relative difference of an exit, after statistic normalization (in %), is shown on (see Figure.6).

6. Data acquisition electronics.

The data acquisition is organized by the intelligent CAMAC crate controller of type CCPC5 containing PC compatible computer. The whole data acquisition system consists of 4 CAMAC crates (EUR4100) organized in a branch. The crate number 0 is controlled by the CCPC5 and contains branch driver. The other crates are connected via standard branch (EUR 4600) using the crate controller of type A1. The functional user modules placed in crates are described in brief in Appendices. The pulses from PMTs are led to analogue Summators. They are organized such that they allow to work with whole rows or columns summed or with pulses from individual PMT on the output. The control program switches the summators to the desired mode. The pulses from summators are led to QDC. The work of acquisition subsystem is triggered by the signals from laser and from the accelerator. These signals are processed in logical modules and led to CAMAC input or output register. The data from QDC are used for computing the correction codes for DACs which set up the high voltage. The role of this is to set the optimal working mode for photomultipliers and ensure the maximum stability during the experiments.

7. Functionality of stabilization system.

The block scheme of stabilization system is given in (see Figure.7). Secondary optical fibres collected on transmitting side into collector illuminated by isotropic light source are connected to all detectors of the setup (300 channels of Cherenkov's calorimeter CH1, CH2 and 28 channels of scintillation telescope ST). Light source is realized on the bases of standard plastic scintillator excitated by impulse light of UV laser. One part of the light (approx. 10%) of the laser beam is split for illumination of reference PIN diodes (D1, D2 of Hamamatsu S1406-03 type). They serve for stabilization of laser light flashes using programming way based on comparison of peak positions in amplitude spectrum of particle source Am^{241} of low activity (10 - 100 Bq). Collector of secondary optical fibres (1, 2, 3, 4) and reilluminating scintillator are located close to setup detectors. Laser is located in experimental box with distance approximately of 30m from the setup. The laser can be started either automatically in time periods between accelerator cycles (frequency 0.1 Hz)accumulating values of the order 1000 flashes per channel and scanning channels in the setup working time or calibration mode without measurement. In automatic working mode the comparison of average values of signal amplitudes from laser with predefined table data including corrections of HV power for each photomultiplier is carried out. Also the automatic data acquisition for correction of reference PIN diodes employing the measurement of amplitude distribution from irradiation source Am^{241} is carried out. The control system is realized on basis of CAMAC crate and crate controller CCPC4 equipped with PC. Using this computer the calibration system is connected to LHE LAN.

8. Laser system.

The laser of the type VSL-337 with illumination beam energy of the order of $120\mu J$ and duration of pulse 4ns is used. Analogical laser is used also in the setup CARMEN. Laser is positioned on base plate and covered by opaque shield. Inside of the shield, beam splitter for splitting the beam, absorption filters and system for illumination of primary fibres are placed. Output laser beam goes to beam splitter, which separates approximately 10% of beam to start the laser beam stability control system. Simultaneously with the TOF channels illumination also the illumination of the front sides of two optical quartz fibres (length approx. 0.5m) is going on. The light through this fibers goes to two silicone PIN photodiodes of the type S-1406 Hamamatsu with built-in preamplifier. The photodiodes are placed inside of separate shield and are irradiated by additional source Am^{241} with the activity of the order 100Bq and halftime of decay 433 years. Further the laser beam goes through the system of light absorption with thin aluminum filters for measurement of flash amplitudes. Filters with transparency coefficients 80%, 60%, 40%, 20%, 10%, 5%, 0% are used. After passing through filters the beam goes to the input of primary collector consisting of four quartz fibres with length of 30m placed in one shield. Then it goes to secondary collectors of reilluminating light positioned close to detector setup. Four independent quartz light isolating fibres with diameter 600 μm placed inside of common shield with length 30m are used. Near to the detector setup the primary fiber is divided to 4 separate light isolating threads with length 2m by using of which the laser light is passed to separate reilluminating collectors (1, 2, 3, 4). Each collector contains plastic scintillator with dimensions $5 \times 5mm^3$. The output box of light fibres is mounted into the scintillator. Further via the secondary light fibres the laser light goes to each detector of the setup. More detail description is given in Ref.3.

Acknowledgments

The authors are grateful to S.Gmuca, J.Kliman, V.Matoushek, M.Morkhach, I.Turzo (IP SAS, Bratislava), Yu.S.Anisimov, S.N.Bazilev, A.I.Malakhov (LHEP-JINR, Dubna) and A.B.Kurepin (INR RAS, Moscow) for the their help during the preparation, designs and performance of the present work. One of authors (ANL) has been supported by the RFBR travel grant 09-02-09270-mob-z.

Table 1: F8 and SF2 type Pb-glass main characteristics.

Tape	F8 (Russian)	SF2 (USA)
%PbO	45	50.8
Radiation length, X_0, cm	3.2	2.74
Critical energy, MeV	16	15.8
Refractive index, n	3.6	3.85
Density,ρ, g/cm_3	3.6	3.85
Transmittance, (400 nm, 10 X_0	0.96	0.8

Table 2: Main characteristics of the spectrometer.

Number of modules	2 arms×150
Material	F8 - type glass (45% PbO), light absorption <0.05%/cm
Module dimensions	22(front)×36(end)×400mm(12r.l.)
Light yield	$N_{ph.e.}$=0.3×Eγ(MeV)
γEnergy resolution (%)	$\sigma_E = 1.62\times(E(MeV))^{1/2}$
γCoordinate resolution	$\sigma_x = \sigma_y$ = 3mm (at 600 MeV)
Energy interval	π^0:0.03-2GeV; η:0.03-5GeV
Effective accepted solid angle	$\Delta\Omega \leq$(8-12) mster (for $\lvert X \rvert \leq$0.3)
Energy resolution (for 300 MeV π^0)	$\approx$(5-10)Mev(FWHM)

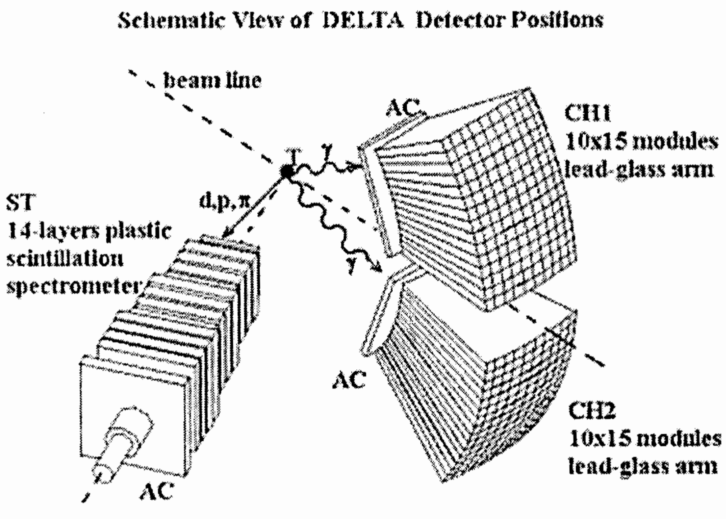

Figure 1: A schematic view of the DELTA detector positions. T- polarized proton target PPT; CH1, CH2 - two arms of the Cherenkov lead-glass spectrometer for two gammas after neutral meson decay measurements, ST - 14-layer fiber-optics scintillation telescope for multi - ΔE measurements of charged particles; AC - anticoincidence detectors.

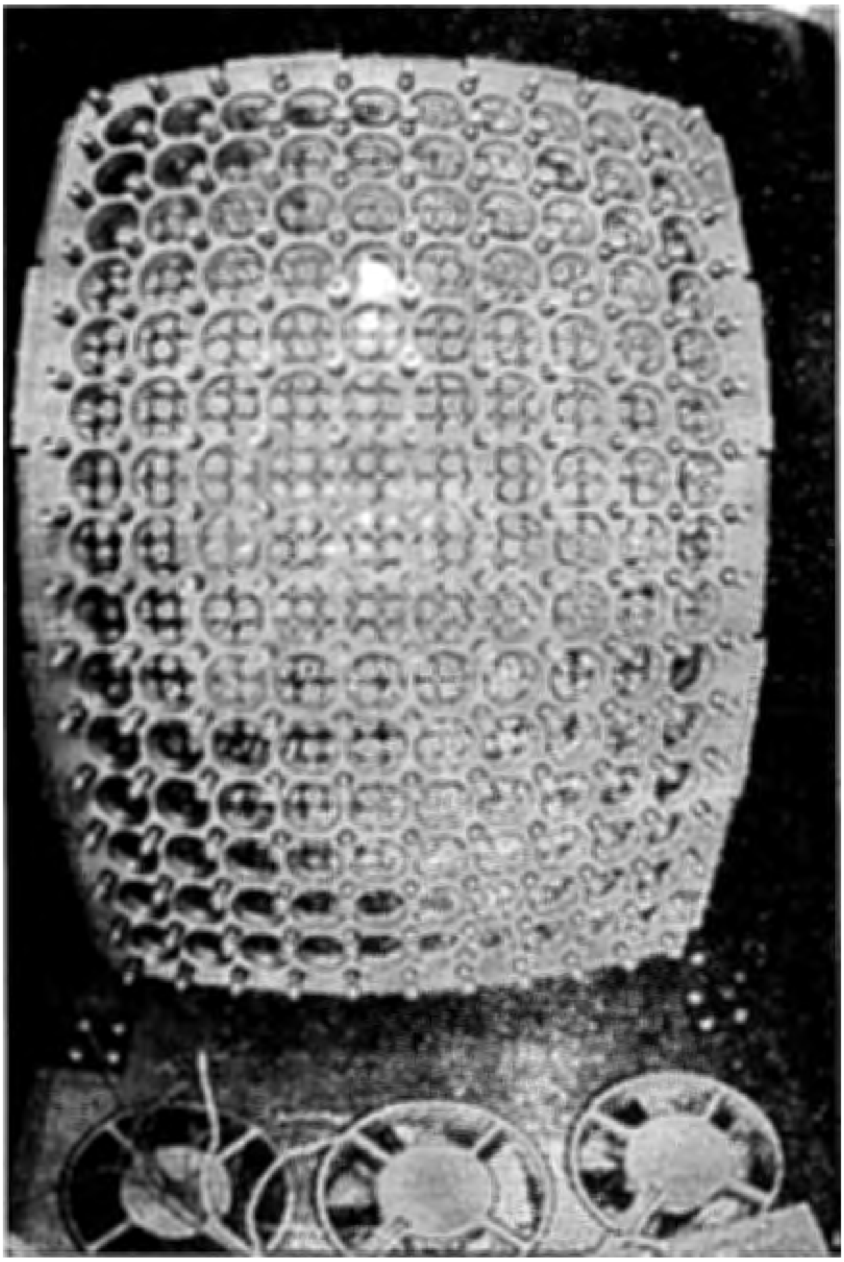

Figure 2: The general view on the back side of one arm of the spectrometer DELTA without photomultipliers.

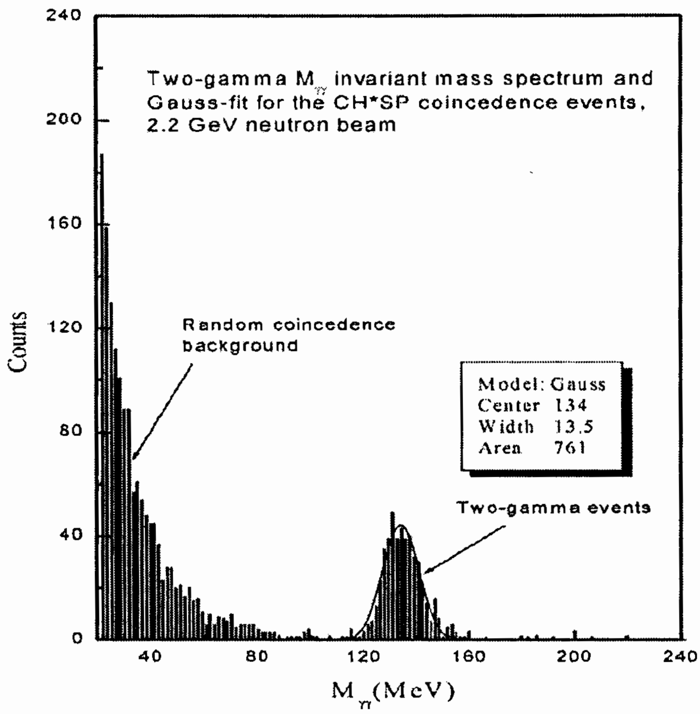

Figure 3: Reconstructed invariant mass spectrum of pions. The solid lines are the result of right peak Gaussian fitting.

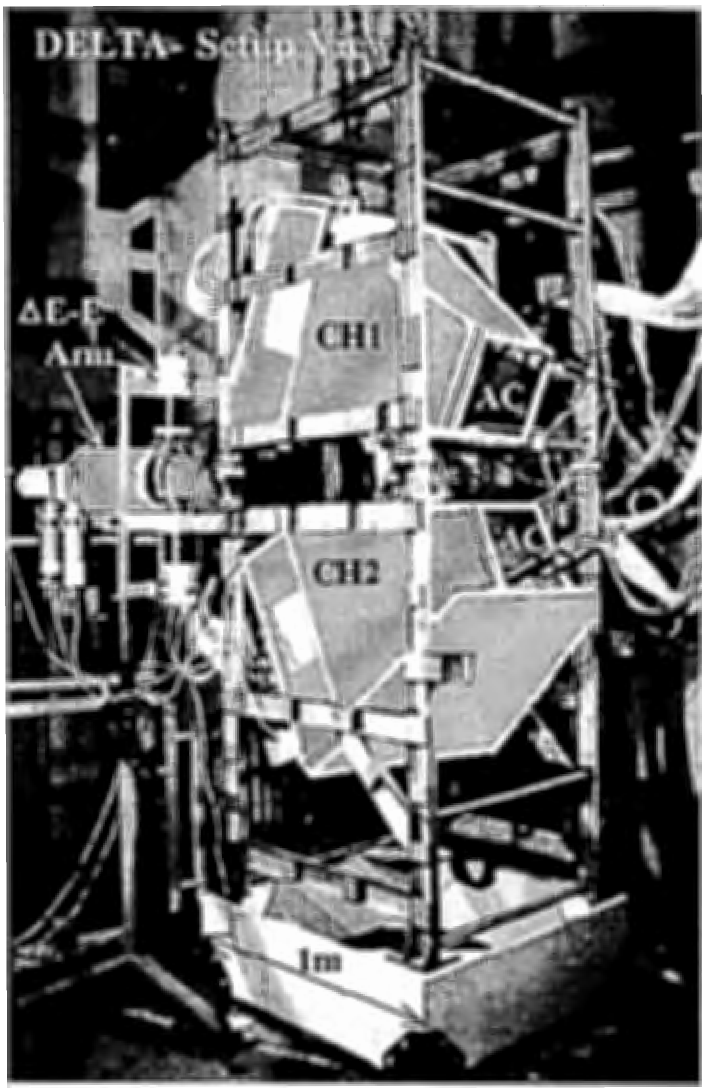

Figure 4: A general view of DELTA installation for use at the polarized proton target in 205 LHEP hall.

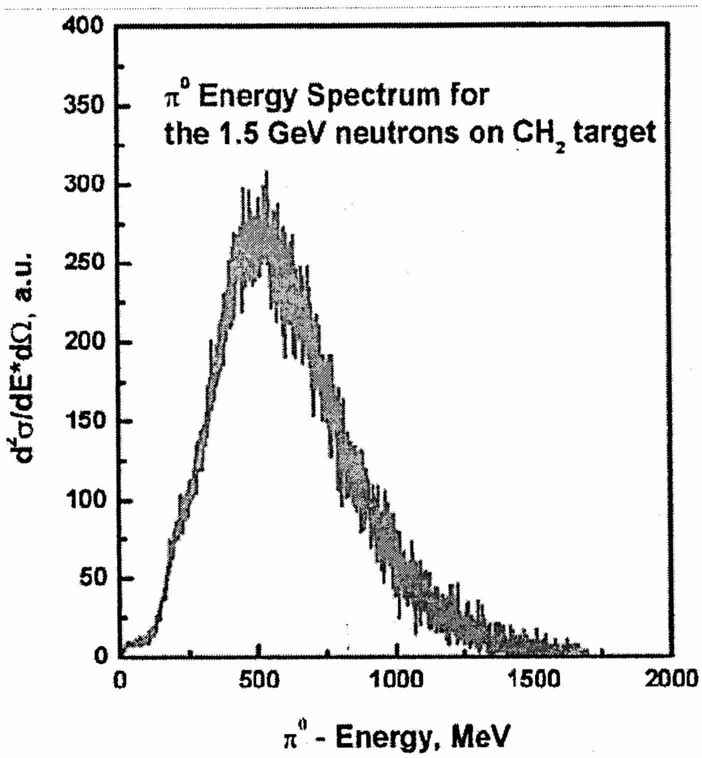

Figure 5: Example of the π^0 energy spectrum.

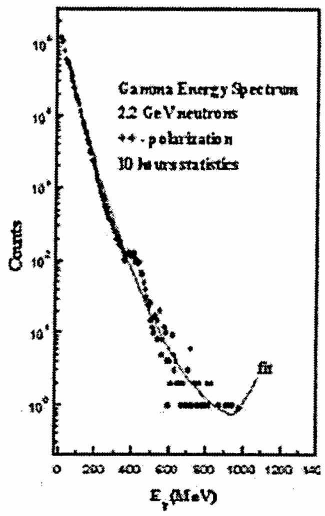

Figure 6: The spectrum a gamma quantum at parallel
orientation of spins and 2.2 GeV neutron energy.

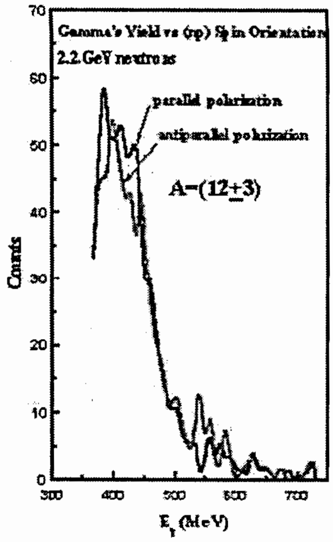

Figure 7: The relative difference of an exit, after statistic normalization (in %)

Figure 8: The construction of the DELTA laser calibration and stabilization system.

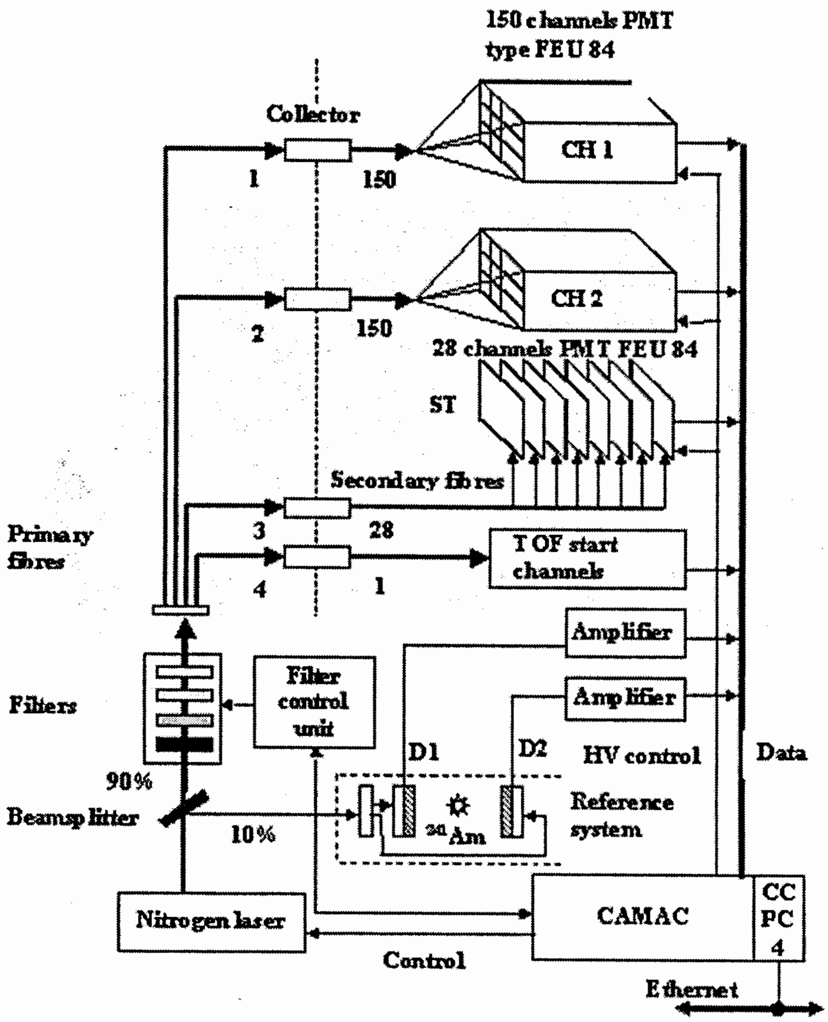

Figure 9: Block scheme of DELTA laser calibration system.

References

[1] V.A.Krasnov,et al., "The DELTA Laser Calibration System", Proceedings of the 7th Internal Workshop on Relativistic Nuclear Physics, 25–30 August 2004, Stara Lesna, Slovak Republic. P.117.

[2] V.A.Krasnov,et al., Nucl.Instrum.Meth.**A566** 413-421 (2006), "The laser-based calibration system of delta spectrometer.", ISSN 0168-9002.

[3] http://www.fu.sav.sk/nph/projects/Calib/Default.htm

FIRST RESULTS ON THE INTERACTIONS OF RELATIVISTIC ^{9}C NUCLEI IN NUCLEAR TRACK EMULSION

D. O. Krivenkov[a,1], D. A. Artemenkov[a], V. Bradnova[a], M. Haiduc[c], S. P. Kharlamov[a], V. N. Kondratieva[a], A. I. Malakhov[a], A. A. Moiseenko[a], G. I. Orlova[b], N. G. Peresadko[b], N. G. Polukhina[b], P. A. Rukoyatkin[a], V. V. Rusakova[a], V. R. Sarkisyan[e], R. Stanoeva[a], T. V. Shchedrina[a], S. Vokál[d], P. I. Zarubin[a], and I. G. Zarubina[a]

a) JINR, 141980, Dubna, Moscow region, Russia
b) LPI, 119991, Moscow, Leninskiy prospekt, 53, Russia
c) Institute of Space Sciences, Magurele, Romania
d) P. J. Šafărik University, Košice, Slovak Republic
e) Yerevan Physics Institute, Yerevan, Armenia

Abstract

First results of the exposure of nuclear track emulsions in a secondary beam enriched by ^{9}C nuclei at energy of 1.2 A GeV are described. The presented statistics corresponds to the most peripheral ^{9}C interactions. For the first time a dissociation $^9\mathrm{C} \to 3^3\mathrm{He}$ not accompanied by target fragments and mesons is identified.

1 Introduction

The most peripheral processes of the fragmentation of relativistic nuclei on heavy nuclei of the emulsion composition (i. e., Ag and Br) proceed without production of target fragments and mesons. They are called "white"stars aptly reflecting the images of events [1, 2]. The fraction of such events that are induced by electromagnetic diffraction and nuclear interactions is a few percent of inelastic interactions. The statistics of various configurations of relativistic fragments reflects the cluster features of light nuclei due to minimal transferred excitation [3, 4, 5, 6, 7, 8, 9, 10]. The use of emulsion provides a complete monitoring of relativistic fragments with an excellent angular resolution. This approach to the study of the nucleon clustering is used by the BECQUEREL collaboration [11] for the study of light nuclei at the proton drip line. Exploration of the dissociation of lighter nuclei ^{7}Be [8] and ^{8}B [9] formed the basis for the progress in the study of the next nucleus - ^{9}C. One can expect that in the peripheral ^{9}C dissociation the picture hitherto obtained for ^{8}B and ^{7}Be with the addition of one or two protons, respectively, should be reproduced.

The ^{3}He based clustering plays an equally important role in these nuclei as the α-particle one does. For the ^{9}C nucleus a cluster excitation 3^3He with a relatively low threshold (around 16 MeV) becomes available. In this case, a rearrangement of a neutron from the α-particle cluster into the emerging ^{3}He nucleus should occur. The search for the dissociation $^9\mathrm{C} \to 3^3\mathrm{He}$ without accompanying fragments of the target and mesons, i. e. "white"stars, becomes the main task of this study. In principle, this bright channel could be identified by a trident of doubly charged fragments. But

[1]E-mail: krivenkov@lhe.jinr.ru

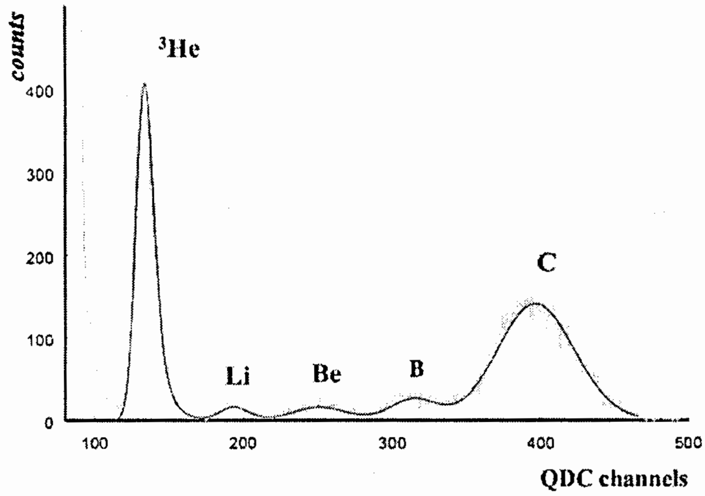

Figure 1: Charge spectrum of nuclei produced in the fragmentation of $^{12}C \rightarrow ^9C$ at secondary beam tuning $Z_{pr}/A_{pr} = 2/3$

the real situation with emulsion exposure in the secondary beams of relativistic radioactive nuclei is more complicated. There should be a detailed analysis of events of the "white"star type as the most clearly interpreted interactions for a reliable determination of the used beam composition. In what follows, first results on ^{9}C identified interactions are described.

2 Experiment

The fragmentation of 1.2 A GeV ^{12}C nuclei, accelerated at the JINR Nuclotron, was used to form a secondary beam with low magnetic rigidity for the best selection of ^{9}C nuclei [12]. The momentum acceptance of the separating channel was about 3%. The amplitude spectrum of a scintillation monitor of the secondary beam is presented Fig. 1. It shows that the major contribution comes from C nuclei. The main background was an admixture of nuclei ^{3}He, which have the same ratio of the charge Z_{pr} to the atomic mass A_{pr}, as ^{9}C ones have. ^{4}He nuclei could not penetrate into the channel because of a much greater magnitude of this ratio. A small admixture of fragments ^{7}Be and ^{8}B with slightly higher magnetic rigidity than that of ^{9}C entered the beam. These spectrum features indicate the correctness of the channel tuning.

The exposed stack consisted of 19 layers of BR-2 nuclear track emulsion with a relativistic sensitivity. The layer thickness and dimensions were 0.5 mum and 10×20 cm^2. Stack exposure was performed in a beam directed in parallel to the plane of the stack along the long side. The presented analysis is based on a complete scanning of 13 layers along the primary tracks with charges visually assessed as $Z_{pr} > 2$. ^{3}He nuclei were rejected at the primary stage of selection. The ratio of intensities $Z_{pr} > 2$ and $Z_{pr} = 2$ was about 1:10. The presence of particles $Z_{pr} = 1$ in the ratio $Z_{pr} > 2$ 1:1 was also detected. The $Z_{fr} = 1$ fragments were separated visually from the $Z_{fr} = 2$ fragments, because their ionization was four times smaller. Over the viewed length of 167.1 m traces one found 1217 interactions mostly produced by C nuclei. Thus, it was obtained that the mean free path was equal to λ_C = 13.7±0.4 cm. This value corresponds to

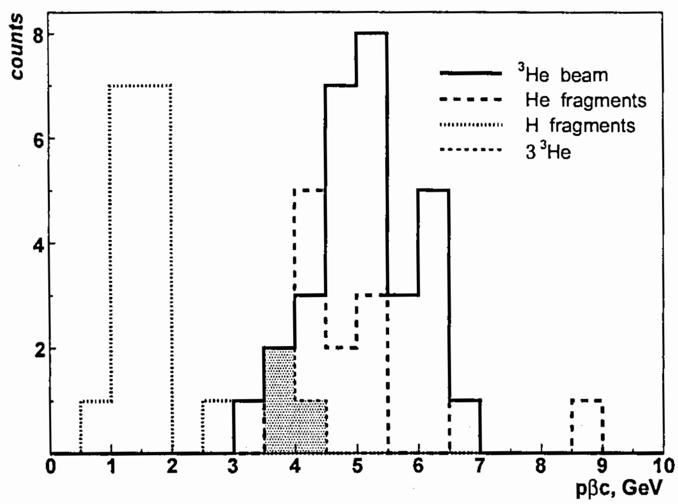

Figure 2: Distribution of the measurements pβc for beam ^{3}He nuclei (30 tracks, solid histogram), singly charged fragments of the "white"stars $\Sigma Z_{fr} = 5 + 1$ and $4 + 1 + 1$ (15 tracks, dot histogram), doubly charged fragments of the "white"stars 3He (14 traces, dotted histogram) and from the 3^{3}He event (shaded histogram)

the estimate based on the data for the neighboring cluster nuclei.

The relativistic fragments H and He can be identified in the cases of small variations in their values pβc, derived from measurements of multiple scattering, where p is the full momentum, and β the speed. It is assumed that the projectile fragments conserve their momentum per nucleon, i. e., pβc$\approx A_{fr} p_0 \beta_0$c, where A_{fr} the fragment atomic number. To achieve the required precision one needs to measure the deflection of the track coordinates in more than 100 points. Despite the workload, this method provides a unique completeness of the information on the composition of the systems of few lightest nuclei.

The presence of ^{3}He nuclei in the beam composition was found to be helpful to calibrate the identification conditions for secondary fragments. The distribution of the pβc measurements for 30 nuclei ^{3}He from the beam is presented in Fig. 2 (solid histogram). The average value of the distribution is $< p\beta c >= 5.1 \pm 0.2$ GeV in the mean scattering $\sigma = 0.8$ GeV. The absolute value is somewhat different from the expected value of 5.4 GeV for ^{3}He nuclei (for ^{4}He - 7.2 GeV) and is defined by the traditionally used constants. The σ value can be assumed to be satisfactory for the separation of isotopes ^{3}He and ^{4}He, and especially their systems.

The contribution of the C, Be and B isotopes was separated via the charge configurations of secondary fragments ΣZ_{fr} in "white"stars and subsequent measurements of the primary charges Z_{pr}. The charges of the projectile nuclei and fragments $Z_{fr} > 2$ were determined by counting of δ-electrons on tracks. The measurement of the charges of the primary nuclei and fragments of the events $\Sigma Z_{fr} = 5 + 1$ and $4 + 1 + 1$, presented in Fig. 3, allows one to conclude that all the events are originated from nuclei $Z_{pr} = 6$. There is an expected shift in the distribution for interaction fragments.

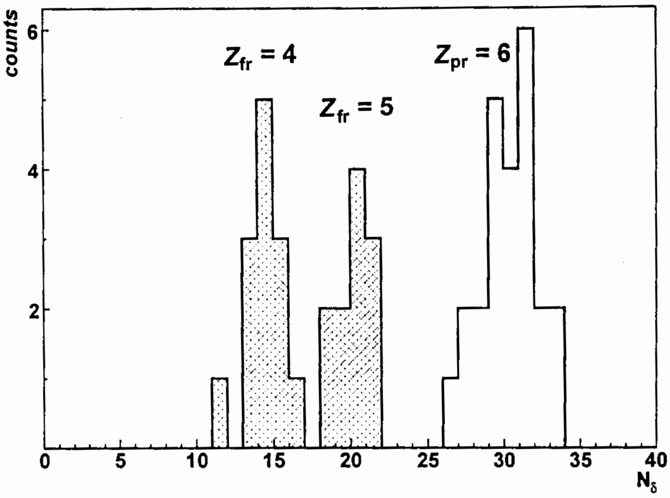

Figure 3: Distributions by the mean number of δ-electrons per 1 mm length for beam particles (solid histogram) and relativistic fragments with charges $Z_{fr} > 2$ (shaded histogram) from "white"stars $\Sigma Z_{fr} = 5 + 1$ and $4 + 1 + 1$

3 Fragment charged configurations

The distribution of 123 "white"stars N_{ws} in the charge configurations ΣZ_{fr} is presented in Table 1. Events with fragments $Z_{fr} = 5$ and 4 and identified charges $Z_{pr} = 6$, accompanied by protons, are interpreted as channels $^9C \to {}^8B + p$ and $^7Be + 2p$, due to the absence of stable isotopes ^9B and ^8Be. These two channels are relative to the most low-threshold dissociation of the nucleus ^9C and constitute about 30% of the events of $\Sigma Z_{fr} = 6$. The ratio of ^8B "white"stars with heavy fragments ($^8B \to {}^7Be + p$) and stars containing only H and He are shown to be approximately equal [9]. Therefore, one can expect that the statistics of the Table 1 contains a large fraction of events produced exactly by the ^9C nuclei.

The result of identification of fragments $Z_{fr} = 1$ in this group of events is presented in Fig. 4 (dotted histogram). The distribution has $< p\beta c > = 1.5\pm0.1$ GeV and $\sigma = 0.4$ GeV. In fact, the identification in these cases is not necessary because of limited options, and protons can serve as a calibration mechanism in more complicated cases.

Table 1 allows one to derive useful indirect conclusions about the composition of the beam. For example, there is only one event $\Sigma Z_{fr} = 4 + 2$, which might arise from the dissociation $^{11}C \to {}^7Be + {}^4He$ having the lowest threshold for the isotope ^{11}C. Thus, a possible presence of ^{11}C in the secondary beam is negligible. Six "white"stars with the total charge $\Sigma Z_{fr} = 7$ are associated with ^{12}N nuclei, captured in the beam. ^{12}N nuclei were produced in charge exchange processes $^{12}C \to {}^{12}N$ in the producing target.

The distribution of "white"stars produced by ^7Be, ^8B and C nuclei of the charge configurations ΣZ_{fr}, which consist only of the nuclei H and He, is presented in the Table 2. One excluded from the sum ΣZ_{fr} one H nucleus for the ^8B cases and 2H for the C cases. There are similar fractions of the channels 2He and He + 2H, which correspond to the appearance of ^7Be as a core of ^9C.

Besides, it is possible to note the production of five "white"stars C$\to$6H (Table 2). Events of this type in the cases of the ^{12}C and ^{11}C isotopes, requiring a simultaneous

Table 1: Distribution of "white" stars N_{ws} in charge configurations ΣZ_{fr}

ΣZ_{fr}	Z_{fr} 6	5	4	3	2	1	N_{ws}
7	-	-	-	-	1	5	2
7	-	-	-	-	2	3	4
6(Z_{pr}=6)	-	1	-	-	-	1	11
6(Z_{pr}=6)	-	-	1	-	-	2	13
6	-	-	-	-	3	-	13
6	-	-	1	-	1	-	1
6	-	-	-	1	1	1	2
6	-	-	-	1	-	3	2
6	-	-	-	-	1	4	22
6	-	-	-	-	2	2	21
6	-	-	-	-	-	6	5
5	-	-	1	-	-	1	2
5	-	-	-	1	-	2	2
5	-	-	-	-	1	3	13
5	-	-	-	-	2	1	7
4	-	-	-	-	1	2	4

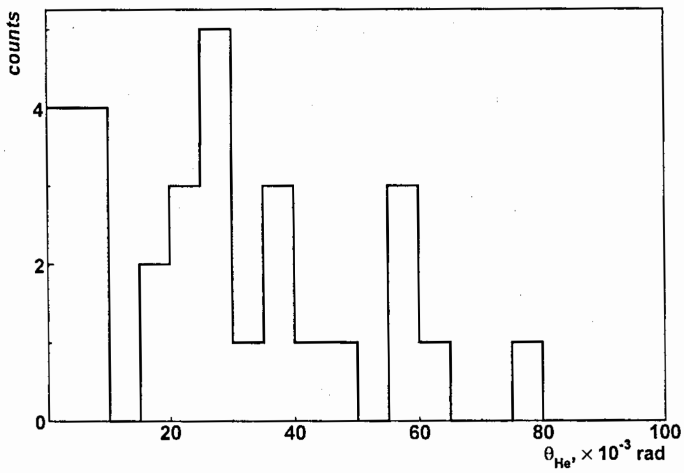

Figure 4: Distribution by polar angles θ for doubly charged fragments in the "white" stars C→3He

Table 2: Distribution of the numbers and fractions of "white" stars of ^{7}Be, ^{8}B and C nuclei, over H and He configurations

Channel	^{7}Be	Fraction, %	^{8}B(+H)	Fraction, %	^{9}C(+2H)	Fraction, %
2He	41	43	12	40	21	42
He+2H	42	45	14	47	22	44
4H	2	2	4	13	5	10
Li+H	9	10	0	0	2	4

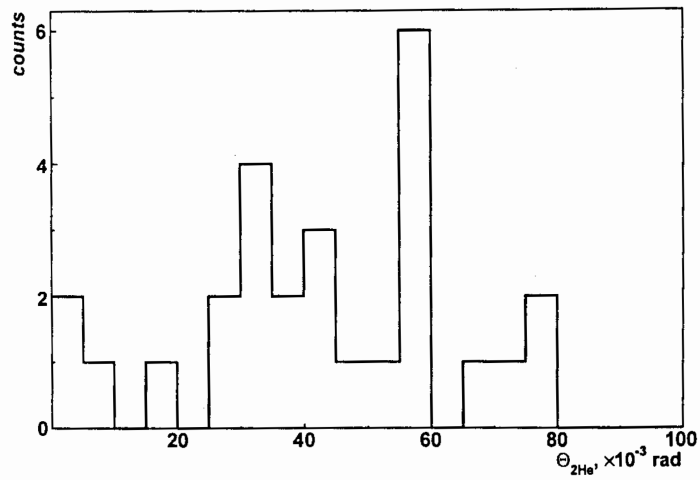

Figure 5: Distribution by opening angles Θ_{2He} between fragments in the "white"stars C→3He.

collapse of three He clusters, could not practically proceed without target fragments due to a very high threshold. Being related to an extremely high threshold, they could not proceed without the production of target fragments. In contrast, similar processes related to the breakups of cluster He pairs, were observed for the "white"stars ^{7}Be→4H [8] and ^{8}B→5H [9]. These events require a full identification of the He and H isotopes and a kinematical analysis to be performed in future. It is quite possible that one will find some cases which would correspond to the cross-border stability in the direction of nuclear resonance states ^{9}C→^{8}C.

The question about the contribution of ^{10}C nuclei to the statistics of the Table 1 which would be characterized by configurations consisting only of the He and H isotopes, remains open. A detailed identification and an angular analysis will be crucial in this regard.

4 Search for 3^{3}He events

Table 1 shows the production of 13 "white"stars with the 3He configuration. The distribution by the polar angles θ for these fragments, which illustrates the degree of collimation, is presented in Fig. 4. Angular measurements allow one to derive the opening angle distribution Θ_{2He} for fragment pairs (Fig. 5). Four narrow He pairs with $\Theta_{2He} < 10^{-2}$ rad are clearly seen due to an excellent spatial resolution. The obtained statistics permits to begin the search for the channel ^{9}C→3^{3}He as the most interesting challenge. The ^{10}C admixture could also lead to the events of a deep nucleonic regrouping ^{10}C→2^{3}He + ^{4}He.

The method of the multiple Coulomb scattering was used to determine pβc values of He fragments. Such measurements were implemented only for 14 tracks because of the characteristics of the stack used and because of the fragment angular dispersions (dashed histogram in Fig. 2). The average value $< p\beta c >$ was found to be equal to 4.6±0.2 GeV, with σ= 0.6 GeV. The fraction of the fragments that could be defined as ^{4}He nuclei is insignificant as compared with ^{3}He. A systematic decrease in the value

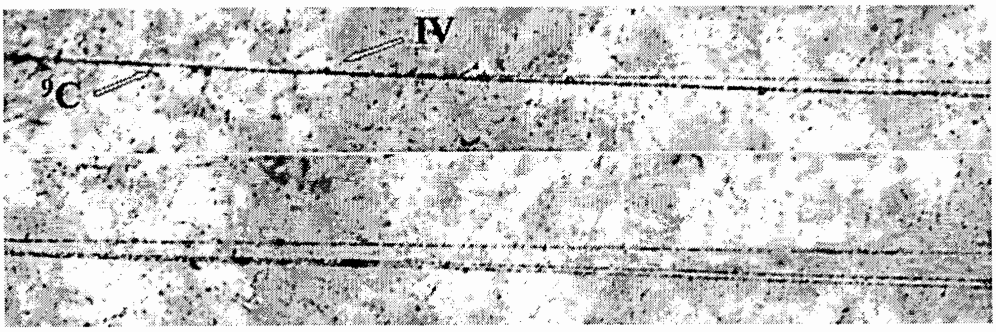

Figure 6: Microphotography of "white"star $^9C \to 3^3He$ at 1.2 A GeV. The upper photo shows the dissociation vertex (indicated as **IV**) and fragments in a narrow cone. Three tracks of relativistic He fragments can clearly be seen in the bottom photo.

$< p\beta c >$ with the respect to the beam calibration is due to energy losses in interactions.

The procedure for determining the pβc values of all three fragments became possible only in a single event C$\to$3He (shaded histogram in Fig. 2). The values allow one to interpret the event as a triple production of ^{3}He nuclei with a total value pβc = 12$\pm$1 GeV. The interpretation of events as $^{10}C \to 3^3He$ + n is unlikely, because in this case one would need to modify not one but a pair of clusters ^{4}He by overcoming a threshold of at least 37 MeV in a peripheral interaction without target fragment production.

This event is a first identified candidate for $^9C \to 3^3He$. Its mosaic microphotography is presented in Figure 6. The values of the 3He transverse momenta P_t, obtained by pβc and angular measurements are equal to 318$\pm$53 MeV/c, 128$\pm$20 MeV/c and 110$\pm$14 MeV/c. Then the total momentum ΣPt transferred to the system 3^3He is equal to 551 60 MeV/c. By introducing the ΣP_t correction, one can get noticeably lower values of P_t^* in the 3^3He center of mass - 138$\pm$23 MeV/c, 66$\pm$10 MeV/c, and 74$\pm$10 MeV/c.

The excitation energy estimated from the difference of the invariant mass M_{eff} of the 3^3He system and the fragment mass is equal E_{3He} = 11.9$\pm$1.4 MeV. The peculiarity of this event is the presence of a 2^3He narrow pair of an energy of E_{2HE} = 46$\pm$8 keV. Such a low E_{2He} value of the relativistic 2^3He pair is close to the decay energy from the ground state of $^8Be \to 2^4He$. In the study of $^7Be \to {}^3He + {}^4He$ [8] so narrow relativistic pairs 2He were not found. The discussed "white"star is one of the four 3He events with such narrow pairs (Fig. 5). This observation can motive the study of an intriguing opportunity of the existence of a 2^3He narrow resonant state near the threshold.

5 Conclusions

For the first time nuclear track emulsion is exposed to relativistic ^{9}C nuclei. The picture of the charge configurations of relativistic fragments is obtained for the most peripheral interactions. A dissociation event $^9C \to 3^3He$ accompanied by neither target fragments of the nucleus target nor charged mesons is identified. This paper provides a framework for further accumulation of statistics and for a detailed analysis of ^{9}C interactions.

6 Acknowledgments

We are very grateful to the JINR Nuclotron staff for the enthusiastic work and friendly cooperation in this experiment. The authors express their particular gratitude to the JINR staff member A. M. Sosulnikova for a large and careful work on visual scanning of emulsions. This work was supported by grants – 96-1596423, 02-02-164-12a, 03-02-16134, 03-02-17079, 04-02-17151 and 04-02-16593 of Russian fund for basic researches, grants VEGA #1/2007/05 and #1/0080/08 of Agency Science of Ministry of Education of the Slovak Republic and the Slovak Academy of Sciences, as well as grants of plenipotentiaries of Bulgaria, Slovakia, the Czech Republic and Romania in 2002-8.

References

[1] G. Baroni et al., Nucl. Phys., A **516**, (1990) 673 – 714

[2] G. Baroni et al., Nucl. Phys., A **540**, (1992) 646 – 658

[3] N. P. Andreeva et al., Phys. At. Nucl., **68**, (2005) 455 – 476; arXiv:nucl-ex/0605015

[4] V. V. Belaga et al., Phys. At. Nucl., **58**, (1995) 1905 – 1911

[5] M. I. Adamovich et al., Phys. At. Nucl., **62**, (1999) 1378 – 1388

[6] D. A. Artemenkov et al., Phys. At. Nucl., **70**, (2007) 1261 – 1265; arXiv:nucl-ex/0605018

[7] T. V. Shchedrina et al., Phys. At. Nucl., **70**, (2007) 1230 – 1234; arXiv:nucl-ex/0605022

[8] N. G. Peresadko et al., Phys. At. Nucl., **70**, (2007) 1266 – 1280; arXiv:nucl-ex/0605014

[9] R. Stanoeva et al., Phys. At. Nucl., **70**, (2007) 1216 – 1221; arXiv:nucl-ex/0605013

[10] D. A. Artemenkov et al., AIP Conf. Proc., **912**, (2007) 78 – 87; arXiv:0704.0384

[11] Webs sites of the BECQUEREL Project http://becquerel.jinr.ru and http://becquerel.lhe.jinr.ru

[12] P. A. Rukoyatkin et al., Czech. J. of Phys., Supplement **C56**, (2006) 379 – 384

ISOSPIN DYNAMICS AND PRODUCTION OF EXOTIC NUCLEI UP TO 70 AMEV

M. Veselský[a,1] and G.A. Souliotis[b,c]

a) Institute of Physics, Slovak Academy of Sciences, Dubravska 9, Bratislava, Slovakia
b) Laboratory of Physical Chemistry, Department of Chemistry, National and Kapodistrian University of Athens, Athens, Greece
c) Cyclotron Institute, Texas A&M University, College Station, Texas, USA

Abstract

The available experimental data from nucleus-nucleus collisions at beam energies from the Coulomb barrier up to 70 AMeV and various projectile-target asymmetries are investigated. The scenario involving pre-equilibrium emission in the early stage followed by deep-inelastic transfer or incomplete fusion leads to consistent agreement in most of the cases. At beam energies around and above 50 AMeV there are signals of the mechanism of neutron loss (dynamical emission) preceding the thermal equilibration of the massive projectile-like fragment. At beam energies below 10 AMeV, deep-inelastic transfer appears to be the dominant reaction mechanism, with contribution from the possible extended evolution of nuclear profile in the window (neck) region, mostly in the case of heavy target nuclei.

1 Introduction

During almost a century of nuclear physics studies, only approximately one half was investigated of up to 6000 nuclei stable against nucleon emission. The known β-unstable nuclei consist mostly of proton-rich nuclei, produced in compound nucleus and spallation reactions. Properties of proton-rich nuclei were investigated to the proton dripline from the light nuclei up to the proton-rich fissile nuclei. The situation differs on the neutron-rich side. Only few regions are known, most thoroughly the light nuclei up to the oxygen, produced via fragmentation of heavier nuclei, where the neutron dripline has already been reached. Heavier neutron-rich nuclei are known mostly in the region of light and heavy fission fragments. An extensive area of very neutron-rich nuclei still remains to be investigated.

The main difficulty in the production of neutron-rich nuclei is that, due to the absence of the Coulomb barrier, emission of neutrons is the most effective way of deexcitation. Intense emission of neutrons from the highly excited (hot) nuclei explains the relatively easy production of proton-rich nuclei. In order to produce neutron-rich nuclei, the excitation energy acquired during the nuclear reaction must be low enough and the neutron-rich nuclei should be produced primarily in the so-called cold processes with minimal neutron loss due to emission.

Frequently used for production of exotic nuclei are spallation and fragmentation reactions at relativistic beam energies, which are limited by the fact that projectile nucleons are stripped by the target and the production cross sections are independent of the target neutron-to-proton (N/Z) ratio. Neutron excess is reached by stripping the maximum possible number of protons and lesser number of neutrons. To reach even higher neutron excess it appears necessary to capture additional neutrons from the

[1]E–mail: fyzimarv@savba.sk

target. Such effect is in principle possible in the reactions of nucleon exchange, which dominate at beam energies around the Fermi energy (20 - 50 AMeV). Highly precise experimental data are rather scarce at present, mostly due to the charge distributions of reaction products, leading to a complex procedure of identification and separation.

2 Production of projectile-like fragments

A large variety of reaction mechanisms has been observed in nucleus-nucleus collisions in the Fermi energy domain (20 - 50 AMeV) depending on the impact parameter, projectile-target asymmetry and the projectile energy [1]. The reaction mechanisms typically observed are peripheral elastic and quasi-elastic (QE) scattering/transfer reactions around the grazing impact parameter, deep inelastic transfer (DIT) reactions at semi-peripheral impact parameters, incomplete fusion (ICF) reactions at central impact parameters with a typical participant-spectator scenario and pre-equilibrium emission of direct particles, caused by the onset of two-body nucleon-nucleon collisions at central and mid-peripheral impact parameters. While such a scheme is well established, there are still many open questions related to the development of isospin-asymmetry in nucleus-nucleus collisions in the Fermi energy domain. Studies of isospin degrees of freedom in nucleus-nucleus collisions in the Fermi energy domain reveal many interesting details of the reaction scenario. Recently, an enhancement in the production of neutron-rich nuclei was observed in peripheral nucleus-nucleus collisions [2, 3], which can be related to the effect of neutron-rich surface of the target on the nucleon exchange. Recent experimental observations in the semi-central collisions signal that the neutron-rich mean-field can play a role in the re-separation phase, leading to fast transfer of neutrons in this phase [4] or to dynamical emission [5]. Large uncertainty exists e.g. in the transition from the regime of binary collision (DIT or ICF) to the high-energy participant-spectator scenario.

2.1 Experiment on production of exotic nuclei at 15 AMeV

The reactions induced by beams with energy around 15 AMeV can in principle demonstrate features of both the reaction mechanisms known at energies close to the Coulomb barrier, such as complete fusion, and reaction mechanisms known at higher energies. The production cross sections at these energies are necessary in order to determine the optimum regime for production of exotic species, such as the optimum beam energy and target thickness. Until now, no high resolution heavy residue data exist in this region.

In order to fill this gap, experimental data at the beam energy of 15 AMeV were obtained recently at the Cyclotron Institute of the Texas A&M University using the recoil spectrometer MARS. A beam of 15 AMeV ^{86}Kr from the K500 superconducting cyclotron, with a typical current up to 10 pnA, interacted with ^{27}Al and ^{58,64}Ni targets of typical thickness around 2.0 mg/cm^2. The reaction products were analyzed with the MARS recoil separator [6]. The primary beam struck the target at 4 degrees relative to the optical axis of the spectrometer.

Figure 1 shows the results for the reaction ^{86}Kr+^{64}Ni at 15 AMeV at the 4 degree setting. The products with Z=29-24 seem to be reproduced reasonably well by the PE+DIT/ICF+SMM simulations [1, 4, 7, 8] and from the comparison of both experi-

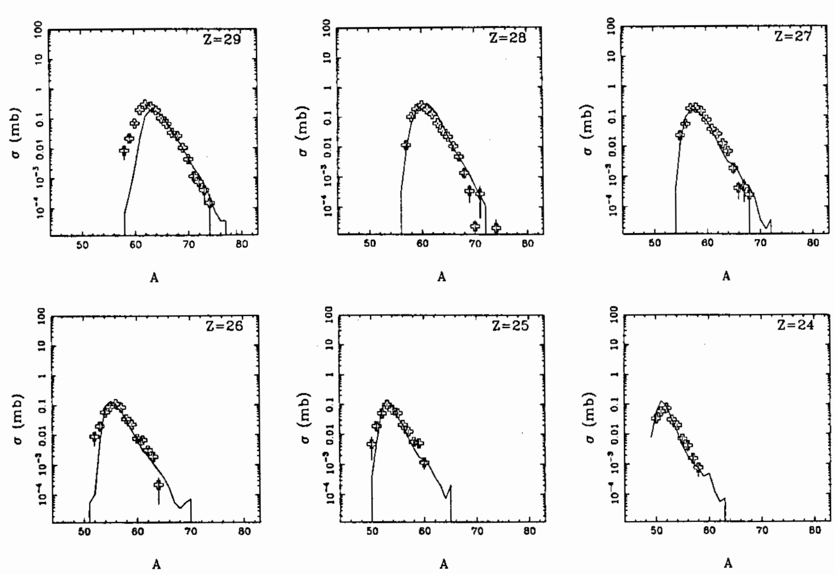

Figure 1: Mass yield curves from the reaction $^{86}Kr+^{64}Ni$ at 15 AMeV at 4 degrees. Symbols - measured data. Lines - result of the PE+DIT/ICF+SMM simulation, filtered by the spectrometer angular and azimuthal acceptance.

mental and calculated total isotopic yields for the reaction $^{86}Kr+^{64}Ni$ at beam energies 15 and 25 AMeV – this work and [2], respectfully – it can be seen that the production cross sections do not drop during the transition from 25 to 15 AMeV, the shapes of mass distributions remain similar, with some possible excess of neutron-rich nuclei appearing at 15 AMeV, representing a component produced mostly at higher angles, which thus needs verification in a corresponding measurement since the measurement at 4 degrees does not provide a decisive answer.

2.2 Systematic analysis of available experimental data

In the framework of the Eurisol Design Study, a project of the future European ISOL facility [9], a representative set of available experimental data was used for model analysis of the production cross sections of exotic nuclei at beam energies 6 – 70 AMeV, with the goal to predict possible exotic beam rates and determine optimum energy for stable and unstable incident beams. Table 1 provides overview of the dominant reaction mechanisms of projectile-like products depending on beam energy and reaction asymmetry. As one could expect, the scenario involving pre-equilibrium emission in the early stage followed by deep-inelastic transfer or incomplete fusion leads to consistent results in most of the cases above 10 AMeV. It nevertheless appears that the participant-spectator scenario starts to play role at energies above 50 AMeV for very asymmetric projectile-target combinations. Also in this domain there are signals of the mechanism of neutron loss (dynamical emission) preceding the thermal equilibration of the massive projectile-like fragment. Such effect seems to be more pronounced in the case of proton-rich projectile-like fragments while in neutron-rich cases it may be overshadowed by intense statistical emission of neutrons. A signal of analogous behavior of the neutrons was observed also in the multifragmentation data in the work [5].

Table 1: Classification of principal reaction mechanisms based on mass asymmetry and beam energy

	Normal kinematics	Nearly symmetric	Inverse kinematics
Low energies $\leq$ 10 AMeV	Deep-inelastic transfer Extended nuclear profile ?		
Transitional energies 10 - 20 AMeV		Pre-equilibrium emission Deep-inelastic transfer + Incomplete fusion	Pre-equilibrium emission Deep-inelastic transfer + Incomplete fusion
Fermi energy domain 20 - 50 AMeV	Pre-equilibrium emission Deep-inelastic transfer + Incomplete fusion	Pre-equilibrium emission Deep-inelastic transfer + Incomplete fusion	Pre-equilibrium emission Deep-inelastic transfer + Incomplete fusion or Participant-Spectator Neutron loss ?
Fragmentation energies $\geq$ 50 AMeV	Pre-equilibrium emission Deep-inelastic transfer + Incomplete fusion	Pre-equilibrium emission Deep-inelastic transfer + Incomplete fusion Neutron loss ?	Pre-equilibrium emission Deep-inelastic transfer + Incomplete fusion or Participant-Spectator Neutron loss ?

Also the behavior in semi-central collisions at lower energies [4], where fast transfer of multiple neutrons can be deduced, points toward non-standard dynamical evolution of neutrons, most probably in the neck region between the projectile and target. At beam energies below 10 AMeV, deep-inelastic transfer appears to be the dominant reaction mechanism, with the possible extended evolution of nuclear profile in the window (neck) region, mostly in the case of heavy target nuclei. It would be desirable to obtain experimental data at normal kinematics between 10-20 AMeV, where one can expect a smooth transition between the behavior at higher and lower energies. However it is interesting to determine the maximum beam energy at which the low energy behavior suggesting an extended nuclear profile survives in the very asymmetric reactions with a heavy target.

2.3 Dynamical neutron emission

The reaction of the massive heavy ions of ^{129}Xe with the light target ^{27}Al was investigated in the work [10] at beam energy 50 AMeV, i.e., around the upper limit of the Fermi energy domain. In this case, as indicated in Fig.3, our filtered PE+DIT/ICF+SMM simulation fails to reproduce the experimental data, both in terms of magnitude and neutron excess (symbols).

A possible explanation for the failure of the PE+DIT/ICF simulation can be a transition from the binary DIT/ICF scenario to ternary participant-spectator scenario. To test this hypothesis the ICF model was modified so that both spectators remain cold, gaining excitation energy and kinematic properties in the same way as the cold

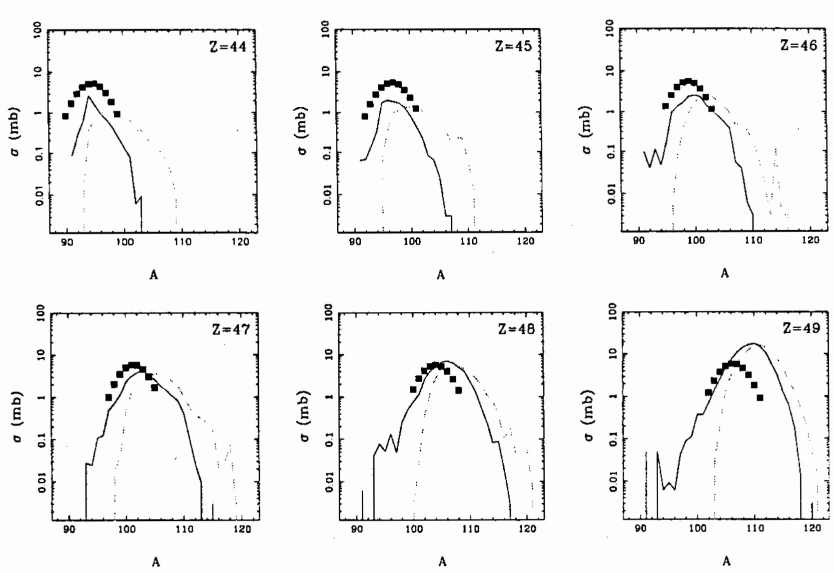

Figure 2: Experimental (symbols) and simulated mass distributions from the reaction $^{129}Xe+^{27}Al$ at 50 AMeV for selected elements. Solid lines represent the PE+participant-spectator+SMM simulation after filtering procedure and subtraction of six neutrons prior to de-excitation. Dashed lines represent simulation without subtraction of neutrons.

fragment in the binary ICF scenario. Simulation using this model was performed and an improvement was achieved in terms of magnitude (dashed line), however the shift in the isospin, with experimental data being less neutron-rich, remained practically unchanged. It is de-facto excluded that the isospin shift could be caused by the de-excitation stage, since in the same reaction at lower beam energy 26 AMeV and in the reactions $^{129}Xe+^{197}Au,^{90}Zr$ at 44 AMeV [11], with similar projectile-like source and excitation energies, no such shift is observed. Thus the shift is caused by the dynamical stage. One possible cause of the shift can be the mechanism of dynamical emission of neutrons, as recently reported in the work [5]. If such emission takes place during the re-separation, a significant shift towards the proton-rich side can be achieved. Such an assumption was tested by a modified participant-spectator simulation (solid line) where six neutrons (with a corresponding decrease of excitation energy) were subtracted from the projectile-like spectator. This simulation leads to a reasonable agreement with experimental data, thus suggesting that mean field effects in the re-separation stage can influence the production cross sections of heavy residues, primarily in proton-rich systems.

A further test of the onset of the participant-spectator scenario can be provided by the reaction of a ^{78}Kr beam with a target of ^{58}Ni which was investigated in the work [12] at beam energy 75 AMeV, i.e., above the Fermi energy domain. In this case, the filtered participant-spectator simulation fails to reproduce the experimental data.

Figure 3 shows that the filtered PE+DIT/ICF+SMM simulation (dashed line) appears to reproduce the magnitude of the cross section in the experimental data (symbols). There still remains a shift in the isospin of the heavy residues, similar to the reaction $^{129}Xe+^{27}Al$ at 50 AMeV. Also in this case improvement was achieved by subtracting neutrons prior to de-excitation, in this case three of them, as it is documented in Figure 3 by the solid lines. Thus again an isospin-dependent mechanism

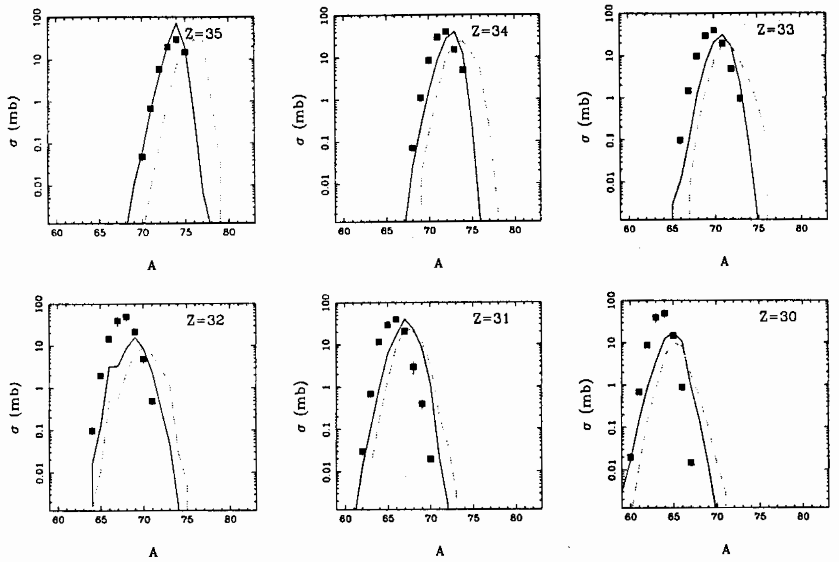

Figure 3: Experimental (symbols) and simulated (lines) mass distributions from the reaction ^{78}Kr+^{58}Ni at 75 AMeV for selected elements. Dashed line - PE+DIT/ICF+SMM simulation after filtering procedure. Solid line - PE+DIT/ICF+SMM simulation after subtraction of three neutrons and filtering procedure.

of dynamical emission of neutrons can play a role.

2.4 Production of exotic nuclei below 10 AMeV

An attempt was undertaken to test the model framework used in the Fermi energy domain at the energies close to Coulomb barrier. It was established that using the original DIT code of Tassan-Got [7] the production cross sections of multi-nucleon transfer could not be reproduced. It was necessary to modify the parametrization of the nucleon density profile to allow opening of the transfer window at larger separation distances. Using the modified parameters of the trapezoidal density profile (maximum full density radius R_0 enlarged by 0.7 fm and the slope increased from 0.65 to 2.2 fm), it was possible to reproduce reasonably well the cross sections of the multinucleon transfer in the reaction ^{58}Ni+^{208}Pb at 5.66 AMeV [13], as documented in Figure 4. The necessary extension of the nuclear density profile can be possibly interpreted as a mean field effect due to evolution of the low density nuclear matter in the window (neck) region in the initial stage of the reaction. This explanation can provide an alternative to the initially suggested enhancement of the di-proton transfer [13]. An analogous behavior was observed also for the collisions of ^{64}Ni+^{208}Pb at 5.47 AMeV [14] and ^{64}Ni+^{238}U at 6.09 AMeV [15], which can be reproduced by the DIT code with the same modified parameters of the nuclear density profile.

In the context of a possible mean field effect such as the above mentioned extension of the nuclear profile and specifically the assumption that it can be related to the initial energy of the beam, it is of interest to investigate data also at somewhat higher initial beam energy. In [16], projectile-like nuclei were observed in the reaction ^{22}Ne+^{232}Th at beam energy 7.9 AMeV, using two detectors positioned at 12 and 40 degrees.

The comparison of the observed isotopic yields (symbols) at 40 degrees with the

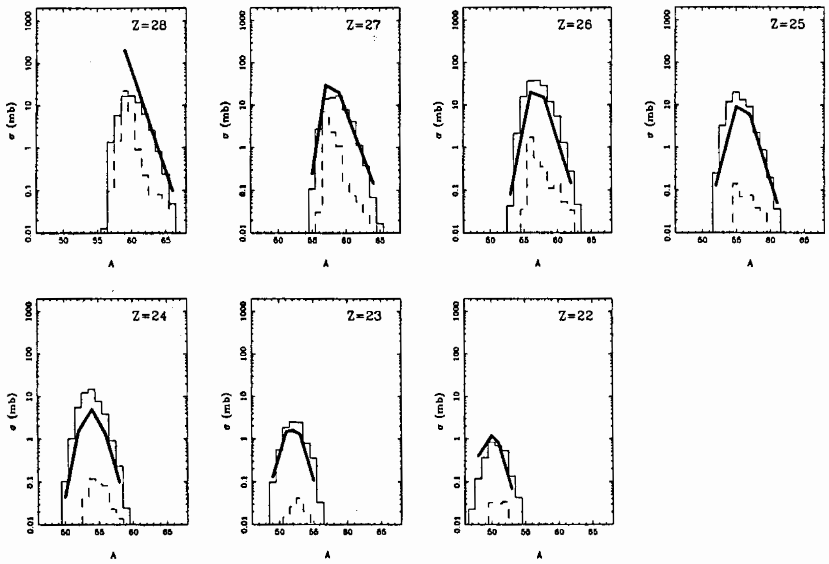

Figure 4: Experimental [13] (thick lines) and simulated mass distributions from the reaction ^{58}Ni+^{208}Pb at 5.66 AMeV for selected elements. Thin solid and dashed lines - simulation with and without extended nuclear profile.

results of a standard PE+DIT/ICF+SMM simulation (dashed lines) and of the version using the DIT code with the extension of the nuclear profile (solid lines) is shown in Figure 5. The extension of the nuclear profile amounted to approximately 75% compared to the three reactions at beam energy 5.5 – 6.0 AMeV. Again the standard PE+DIT/ICF+SMM simulation underpredicts the magnitude of the observed cross sections and an improvement is achieved when using the extended nuclear profile, with the necessary extension weaker by 25% than in reactions at lower beam energy. Thus, it appears that there exists a trend where the magnitude of the extension decreases with beam energy, possibly due to a shorter collision time.

2.5 Technical aspects of secondary beams in the Fermi energy domain

The analysis presented in the previous sections allows to consider the reactions in the Fermi energy domain as a possible source of neutron-rich nuclei for secondary beam formation. A logical continuation of the present study is the investigation of the practical aspects and specifically the possibilities to produce reaction products with optimum mixture and properties for subsequent formation of the secondary beams using the ISOL (IGISOL) method. The kinetic energy of the products will limit the possible target thickness and, due to the wide angular and charge distributions, the in-flight method for the formation of secondary beams would not lead to high quality beams. As relatively suitable appears the possibility to use a version of the ISOL method, where the products will be stopped in a gas volume (gas cell) and subsequently extracted, charge-bred and formed into a beam. Such a solution is in principle verified and practically used to form secondary beams of the fission products or products of fragmentation reactions [17, 18].

For the separation of exotic products we can assume a system consisting of a large-

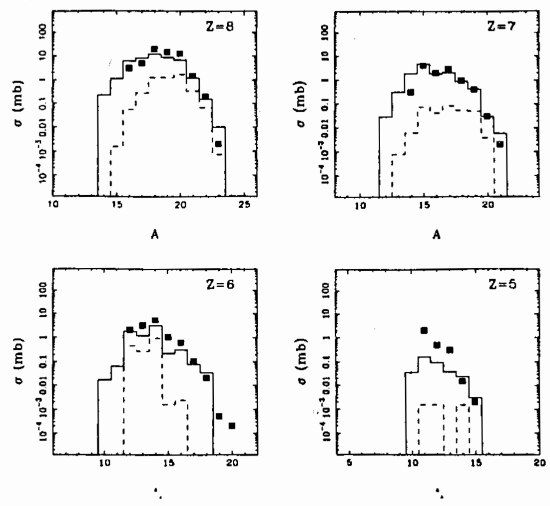

Figure 5: Experimental [16] (symbols) and simulated (lines) mass distributions from the reaction ^{22}Ne+^{232}Th at 7.9 AMeV for selected elements at 40 degrees. Dashed lines - standard PE+DIT/ICF+SMM simulation, solid lines - PE+DIT/ICF+SMM using the DIT code with the extension of the nuclear profile.

bore superconducting solenoid (of typical magnetic field of 5-7 Tesla) along the lines described in [19]. The primary beam will be collected with an on-axis blocker covering the angular range 0 to 2 degrees. The deep inelastic products, along with the elastically scattered beam will pass the solenoid and will be focused into a gas cell after traversing appropriate diagnostic detectors (e.g. PPAC, ionization chamber etc.) and a degrader of appropriate thickness. After that point, the techniques developed in [17, 18] can be applied to extract and form the rare isotope beam (RIB). Depending on the reaction of choice, the angular range up to 10 degrees should be adequate to collect the products of interest from heavy-ion reactions in the Fermi energy regime.

3 Summary and conclusions

The available experimental data from nucleus-nucleus collisions at beam energies from the Coulomb barrier up to 70 AMeV and various projectile-target asymmetries were investigated. The scenario involving pre-equilibrium emission in the early stage of the collision followed by deep-inelastic transfer or incomplete fusion leads to consistent agreement in most of the cases. It nevertheless appears that the participant-spectator scenario starts to play role at energies around 50 AMeV for very asymmetric projectile-target combinations in inverse kinematics. At beam energies around and above 50 AMeV there are signals of the mechanism of neutron loss (dynamical emission) preceding the thermal equilibration of the massive projectile-like fragment. Such effect seems to be clearly pronounced in the case of proton-rich projectile-like fragments while in neutron-rich cases it may be overshadowed by intense statistical emission of neutrons. A signal of analogous behavior of neutrons was observed also in the multifragmentation data of [5]. Also at beam energies below 10 AMeV, deep-inelastic transfer appears to be the dominant reaction mechanism, with contribution from the possible extended nuclear profile in the window (neck) region, mostly in the case of heavy target nuclei.

The production of secondary beams in the Fermi energy domain requires specific technical solutions, including ion-optical devices with angular acceptance up to 10 degrees, such as superconducting solenoids, and effective event-by-event tagging procedure for an in-flight scenario or a highly effective gass cell for production of high-purity secondary beams. A considerable advantage is offered by the possibility that the primary beam can be easily eliminated, since the majority of exotic products is emitted at angles away from zero degrees.

Acknowledgments

The authors wish to thank the staff of the Texas A&M Cyclotron facility for the excellent beam quality. This work was supported by the US Department of Energy under contract DE-FG03-93ER40773, by the Welch Foundation under contract A-1266, by the Slovak Scientific Grant Agency under contract VEGA-2/0073/08. We acknowledge the financial support of the European Commission under the Sixth Framework Program "Research Infrastucture Action – Structuring the European Research Area" EURISOL DS Project Contract no. 515768 RIDS. The EC is not liable for any use that may be made of the information contained therein.

References

[1] M. Veselsky, Nucl. Phys. A 705 (2002) 193.

[2] G.A. Souliotis et al., Phys. Lett. B 543 (2002) 163.

[3] G.A. Souliotis et al., Phys. Rev. Lett. 91 (2003) 022701.

[4] M. Veselsky, G.A. Souliotis, Nucl. Phys. A781 (2007) 521.

[5] M. Veselsky et al., arXiv:0801.3140 [nucl-ex].

[6] R.E. Tribble, R.H. Burch and C.A. Gagliardi, Nucl. Instr. and Meth. A285 (1989) 441; R.E. Tribble, C.A. Gagliardi and W. Liu, Nucl. Instr. and Meth. B56/57 (1991) 956.

[7] L. Tassan-Got, PhD Thesis, 1988, Orsay, France, IPNO-T-89-02, 1989; L. Tassan-Got and C. Stefan, Nucl. Phys. A 524 (1991) 121.

[8] J.P. Bondorf et al., Phys. Rep. 257 (1995) 133.

[9] Eurisol Design Study, *http://www.eurisol.org/*.

[10] K.A. Hanold et al., Phys. Rev. C 52 (1995) 1462.

[11] j. Feng et al., Phys. Rev. C 50 (1994) 2420.

[12] R. Pfaff et al., Phys. Rev. C 53 (1996) 1753.

[13] L. Corradi et al., Nucl. Phys. A 701 (2002) 109c.

[14] W. Krolas et al., Nucl. Phys. A 724 (2003) 289.

[15] L. Corradi et al., Nucl. Phys. A 734 (2004) 237.

[16] A.G. Artukh et al., Nucl. Phys. A 283 (1977) 350.

[17] G. Savard et al., Nucl. Instr. Meth. B 204 (2003) 582.

[18] G. Bollen et al., Nucl. Instr. Meth. A 550 (2005) 27.

[19] G.A. Souliotis et al., Nucl. Instr. Meth. B 266 (2008) 4692.

THE $dp \to (pp)n$ CHARGE EXCHANGE CHANNEL

V.V.Glagolev[a], G.Martinská[b], J.Mušinský[a], N.M.Piskunov[a], J.Urbán[b,1]

a) Joint Institute for Nuclear Research, 141980 Dubna, Russia
b) University of P.J.Šafárik, Jesenná 5, SK-04154 Košice, Slovak Republic

Abstract

An estimate of the spin dependent part of the $np \to pn$ exchange amplitude was made on the basis of the $dp \to (pp)n$ data, taken at 1.67 AGeV/c in a full solid angle geometry. The $np \to pn$ amplitude turned out to be predominantly spin dependent. To extend these studies to higher energies the designed experiment STRELA is well on the way to data taking and processing.

1 Introduction

The elementary $np \to pn$ process can be understood and interpreted from different points of view. Sometimes it is referred to as a backward elastic scattering or charge exchange process. On the quark level it may treated as a u and d quark exchange between the proton and the neutron, respectively. Looking at the reaction with an incoming neutron in the laboratory frame one will have a fast proton and a recoiled neutron in the final state. The deuteron is a fast system of loosely bound proton and neutron, an ideal case for impulse approximation. The pionless deuteron break-up reaction in a few GeV region proceeds predominantly as a quasi free nucleon interaction with participation of a bound nucleon while the second one acts as a passive spectator. Therefore one may expect similar behaviour of the charge exchange processes in the $dp \to (pp)n$ and in the elementary $np \to pn$ reactions. It is worth to underline that the charge exchange in the $dp \to (pp)n$ channel may also proceed via more complicated mechanisms like intermediate inelastic states. But even for the case when the

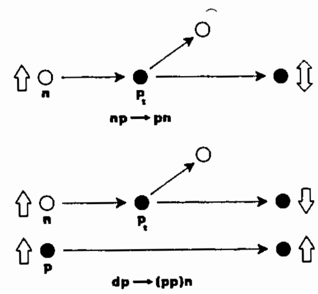

Figure 1: Elementary $np \to pn$ (upper) and $dp \to (pp)n$ (lower) charge exchange reactions. Empty circles stand for the neutron and full circles denote proton. Subscript t means target proton, double arrows show possible spin orientations.

charge exchange is due to a quasi free $np \to pn$ elastic scattering the presence of the

[1]E-mail: jozef.urban@upjs.sk

deuteron itself may call out some distinguishing features of this reaction. The situation is schematically illustrated in figure 1. In the first case both spin orientations are allowed in the final state while in the second one for small angle scattering due to the produced charged symmetry (two protons moving in the very forward direction with small relative momenta) the reaction can proceed only if the scattered proton spin flips as a consequence of the Pauli exclusive principle.

2 Formalism

The original idea to take of use the charge exchange reaction on the unpolarized deuteron for the determination of the spin-dependent part of the $np \to pn$ charge exchange was proposed by Pomeranchuk [1] and Chew [2]. The possibility to use the charge exchange reaction on the unpolarized deuteron for determination of the spin-dependent part of the $np \to pn$ charge exchange was emphasized partly in the series of works [3–8]. The effect can be understood qualitatively in the following way. Two nucleons, bound in the deuteron may be in $^3S_1$ and $^3D_1$ ($T = 0$) spatial and spin symmetric states; their isospin is antisymmetric. In charge exchange at 0°, the transition from $^3S_1$ or $^3D_1$ to a charge symmetric $^1S_0$ or $^1D_2$ state of two protons requires spin flip, in order to satisfy the Pauli principle and ensure an anti-symmetric total wave function. In this way, the spin-dependent part of the elementary charge exchange amplitude will be reflected through the probability of the charge exchange process on the deuteron. Later the mathematical formalism was developed by Dean [6,7]. These formulas were obtained under certain assumptions, namely relying on the validity of the impulse and closure approximations. In the work by Lednicky and Lyuboshitz [9] it was shown that at relativistic energies these two assumptions are also justified.

The differential cross section of the elementary $pn \to np$ charge exchange process may be represented as a sum of the spin-independent (subscript SI) and spin-dependent (subscript SD) parts:

$$(d\sigma/dt)_{np\to pn} = (d\sigma/dt)^{SI}_{np\to pn} + (d\sigma/dt)^{SD}_{np\to pn}. \tag{1}$$

The relation between the cross section of the peripheral charge exchange $dp \to ppn$ reaction of the deuteron and the elementary $pn \to np$ process has been discussed in many works. Mathematical formalism developed in [6–8] allows to connect the differential cross section for the deuteron charge-exchange break-up and the elementary $pn \to np$ reactions, in the frame of the impulse approximation as follows:

$$(d\sigma/dt)_{dp\to(pp)n} = [1 - S(t)](d\sigma/dt)^{SI}_{np\to pn} + [1 - 1/3S(t)](d\sigma/dt)^{SD}_{np\to pn}, \tag{2}$$

where $S(t)$ denotes the deuteron form-factor. This expression implies that at zero transfer from the target proton to the neutron, i.e. at the scattering angle 180° w.r.t. CMS and S(0) = 1, the differential cross section equals to [10]:

$$(d\sigma/dt)_{dp\to(pp)n} = 2/3(d\sigma/dt)^{SD}_{np\to pn}. \tag{3}$$

Thus, the charge-exchange break-up reaction of the unpolarized deuteron on the unpolarized target proton at zero transfer ($t = 0$) is completely determined by the spin-dependent part of the elementary $np \to pn$ backward scattering in CMS (180°), so the deuteron acts as a spin filter. It should be noted that this result also remains valid when the deuteron D-state is taken into account [9]. Thus, studying the process $dp \to (pp)n$, at small transferred momenta, allows for estimation of the spin-dependent part of the elementary $np \to pn$ reaction.

3 The $dp \to (pp)n$ Charge Exchange Channel

3.1 Experimental Results

The experiment was realized at the JINR LHE synchrophasotron by irradiating the one-metre hydrogen bubble chamber with a deuteron beam of 3.35 GeV/c momenta in full solid angle geometry. Applying the standard bubble chamber processing chain: scanning, measuring, geometrical and kinematical reconstruction and visual particle identification, 17 reaction channels have been observed in the final statistics. They all are presented in Table 1. In spite of the fact that only the first reaction is examined in this paper, they may be useful to the interested reader.

	Channel	Number of events
1.	ppn	102778
2.	$ppn\pi^0$	31295
3.	$p\pi^+nn$	65284
4.	dp	16184
5.	$dp\pi^0$	3950
6.	$dp\pi^0\pi^0$	1839
7.	$d\pi^+n$	4963
8.	$d\pi^+n\pi^0$	1843
9.	$\pi^+\pi^+nn$	315
10.	$ppp\pi^-$	5487
11.	$ppp\pi-\pi^0$	167
12.	$ppp\pi^-\pi^0\pi^0$	67
13.	$pp\pi^+\pi^-n$	1163
14.	$pp\pi^+\pi^-n\pi^0$	49
15.	$dp\pi^+\pi^-$	576
16.	$dp\pi^+\pi^-\pi^0$	39
17.	$dp\pi^+\pi^-\pi^0\pi^0$	1414

Table 1: The list of observed channels

The number of events in the studied channel was converted to a cross section using the dp total cross section [11] and the total number of events corrected for losses due to the chamber threshold value. In the case of nuclear beams impinging on a fixed proton target, all the fragments of the incoming nuclei are fast in the laboratory frame and, thus, they can be detected, measured well and identified with minimal losses. The losses were determined under two assumptions: random losses in different reaction channels are proportional to the number of events in a given channel and that the systematical losses are concentrated in the elastic channel at small scattering angles. An exponential function was fitted to the dN/dt, t being the four-momentum transfer squared for $|t| > 0.06(GeV/c)^2$, and extrapolated back for the interval of

$|t| < 0.06(GeV/c)^2$, to estimate the number of events, this gave a systematic error of about 4%. More detailed description of the experimental set-up and data processing can be found in [12]. Approximately half of the observed events corresponds to the deuteron pionless break-up $dp \to ppn$, consisting of charge retention $dp \to (pn)p$ 83 % and charge exchange $dp \to (pp)n$ reactions. In the latter case the neutron is the fastest secondary nucleon in the deuteron frame and with 17 512 events, equivalent to a cross section of 5.85$\pm$ 0.05 mb, forms about 17 % of the break-up. The quoted errors are only statistical.

For the impulse approximation and at higher energies the final state interaction (FSI) may play crucial role. Experimental investigations of final state interactions showed that the backward-forward asymmetries

$$A = \frac{N(\alpha < 90^\circ) - N(\alpha > 90^\circ)}{N(\alpha < 90^\circ) + N(\alpha > 90^\circ)}, \tag{4}$$

of the distribution of the angle α, defined as $cos\alpha = (\vec{p_s}\vec{q})/(|\vec{q}||\vec{p_s}|)$, are very sensitive to FSI, where $\vec{p_s}$ - is the momentum of the spectator with respect to the deuteron frame, and $\vec{q}$ - is the three-dimensional momentum transfer from the incident nucleon to the scattered one. In the works [14, 15] it has been shown that for the values of

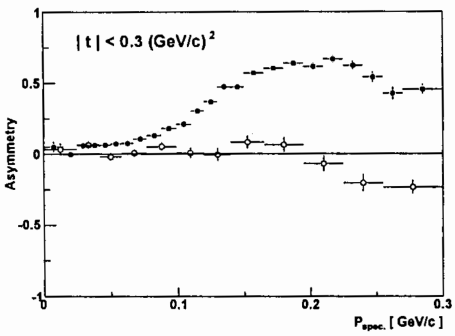

Figure 2: Asymmetry of the angle α as a function of the spectator momenta $|\vec{p_s}|$.All the quantities are to be understood in the deuteron frame. The empty circles correspond to charge exchange $dp \to (pp)n$ and full ones stand for the charge retention $dp \to (pn)p$ break-up data.

$|t| < 0.1(GeV/c)^2$ and spectator momenta $|\vec{p_s}| < 0.1$ GeV/c the asymmetries caused by FSI are practically absent, this is well demonstrated for both charge retention and charge exchange deuteron break-up channels in Fig. 2. It is important to stress the above mentioned absence of FSI when moving to higher energies where experimental data on np-scattering is scarce. In the region above 1 GeV only the preliminary results of the Delta-Sigma group [13] are known. In connection with the achievements of the polarisation research methods at Dubna (Nuclotron) and Juelich (COSY), the chance of restoring the amplitudes and phases of the nucleon-nucleon scattering in the region of energies below and above 1 GeV has significantly enhanced.

In connection with the appreciable contribution of events with intermediate Δ-isobar [15, 16], the main part of which comes from quasi-pp collisions (proceeding mainly via Δ^{++} and Δ^{+}-isobars) see diagrams a) and b) in the Fig. 3, it would be necessary to introduce corrections for this effect.

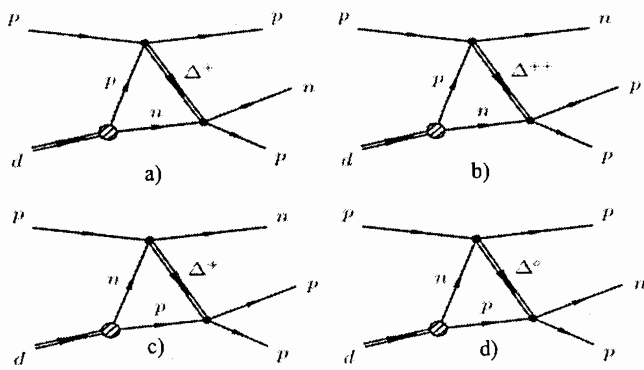

Figure 3: The Feynman diagrams for $dp \to ppn$ reactions with intermediate Δ-isobar.

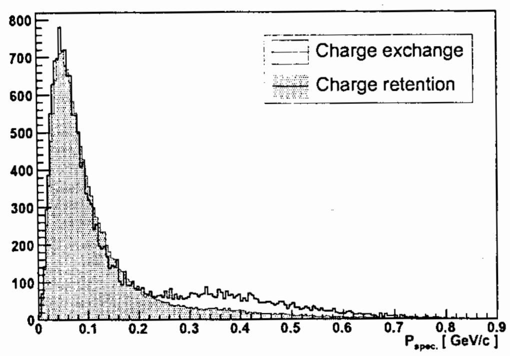

Figure 4: Spectator momentum (deuteron frame) distributions from the charge retention $dp \to (pn)p$ and charge exchange channels $dp \to (pp)n$ normalized to the maxima.

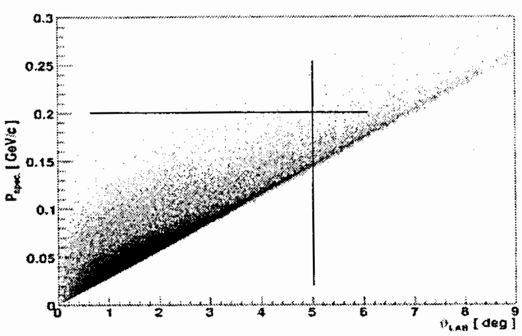

Figure 5: Spectator nucleon momentum (deuteron frame) dependence on its polar angle (target proton frame) for the $dp \to ppn$ events.

In the Fig. 4 the comparison of the spectator momenta distributions from the charge retention and charge exchange break-ups is shown. The relative enhancement in the spectrum of the proton spectators from the charge exchange, connected with the contribution of intermediate isobaric states, is clearly visible. Comparing the two-dimensional plot in Fig. 5 with the histogram in the Fig. 4 one can see that this enhancement is concentrated in the region of momenta above 0.2 GeV/c, i.e. outside the cone of 5° and does not influence the differential cross section at $t = 0$.

The charge exchange differential cross section on the deuteron at $t = 0$ will be estimated from our data and compared with the available data for the $np \to pn$ reaction at the same energy. The closest energy data comes from measurements made at the SATURN accelerator [17, 18]. Fig. 6 shows the values of $d\sigma/dt|_{t=0}$ of the $np \to pn$ reaction as a function of the incident momenta. The individual differential cross sections $d\sigma/dt$, from Bizard et al. [17] in the region of momenta $(1.4 - 1.95)$ GeV/c, at each momentum were extrapolated to $t = 0$ by the expression

$$d\sigma/dt = a\exp(bt + ct^2). \tag{5}$$

To determine the $d\sigma/dt|_{t=0}$ of the $np \to pn$ reaction, at our incident momentum of 1.675 GeV/c/nucleon, an exponential fit was made to the results of Fig. 6, which gave

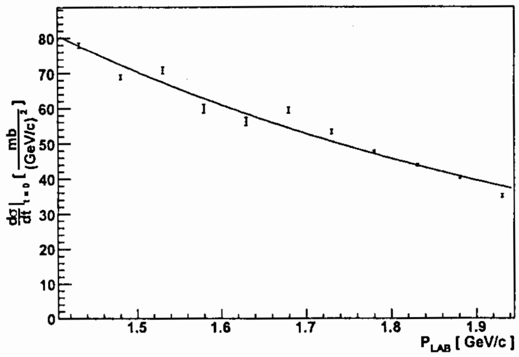

Figure 6: Dependence of the $d\sigma/dt|_{t=0}$ for the $np \to pn$ reaction on the beam momentum. The data points $d\sigma/dt|_{t=0}$ were computed from a fit (5) to the $np \to pn$ experimental results [17]. The solid curve is a simple exponential fit to the data points.

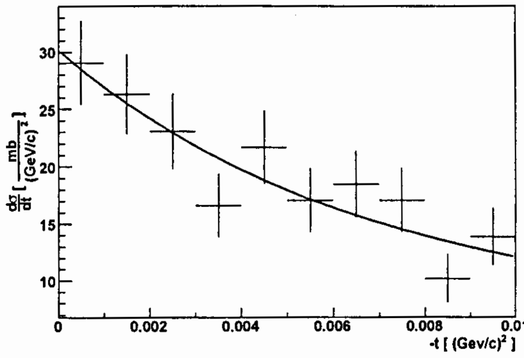

Figure 7: Differential cross section of the $dp \to (pp)n$ charge reaction at small $|t|$. The solid curve is a fit (5) to the data.

the following value of $d\sigma/dt|_{t=0} = 54.7 \pm 0.2$ mb $/(\mathrm{GeV/c})^2$. The obtained value will be related to the estimated differential cross section of the quasi-elastic $dp \to (pp)n$ charge-exchange at $t = 0$ from our experiment. One would like to stress that the systematic error in data by Bizard et al. [17] makes 5%.

The result of a fit (5) to the differential cross section of the $dp \to ppn$ reaction is shown in the Fig. 7. The extrapolation to $t = 0$ has given a value of $d\sigma/dt|_{t=0} = 30.2 \pm 4.1$ mb$/(GeV/c)^2$.

One can introduce the ratio of the differential cross sections at $t = 0$ for the forward scattering (charge exchange) on the deuteron and proton

$$R = \frac{(d\sigma/dt)_{dp}}{(d\sigma/dt)_{np}} = 0.55 \pm 0.08. \tag{6}$$

Under the assumptions stated above it can be related to

$$\frac{2}{3} \times \frac{(d\sigma/dt)^{SD}_{np}}{(d\sigma/dt)_{dp}} \tag{7}$$

and accordingly the value of the spin-independent part of the elastic $np \to pn$ charge exchange cross section

$$R^{ID}_{np} = \frac{(d\sigma/dt)^{SI}_{np}}{(d\sigma/dt)^{SD}_{np}} = \frac{2}{3 \times R} - 1 = 0.21 \pm 0.17 \tag{8}$$

has been obtained.

3.2 Experiment STRELA

Based on the ideas and experimental results presented in the previous subsection the experiment STRELA was designed and constructed in the LHEP, JINR Dubna [19] with the aim to select and detect charge exchange events in deuteron proton collisions.

STRELA is a typical one-arm spectrometer composed of scintillator detectors($S1, S2, S3$), drift chambers($D1-D7$) and analyzing magnet. The recent version of the experimental set-up is shown in figure 8. The sensitive areas of the drift chambers are the following: 125x125 mm^2 for D1-D5 and 250x250 mm^2 for D6-D7. Z axis is chosen in the beam direction. Chambers D1, D2, D4, D5, D6 are equiped with xy wires, the uv planes of D3 and D7 are inclined with an angle of 22.5°, D1 and D6 are composed of 8 sensitive planes while the others contain 4. Each chamber contains equal number of x/u and y/v planes. Two intensities of the magnetic field $B = 1.7T$ and $B = 0.85T$ are used to select deuterons and two protons, respectively. The drift length for all chambers is $r_{max} = 21mm$, more technical details can be found in [20].

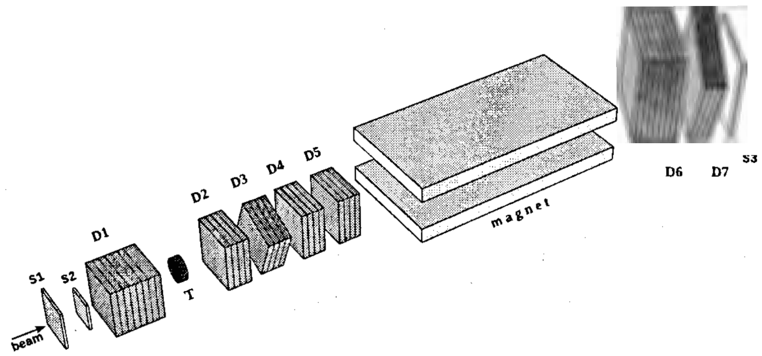

Figure 8: Experimental arragement of the STRELA drift chambers.

The control and read-out electronics were upgraded with new VME crates and all the modules were tested. The basic characteristics of the drift chambers were established from irradiation of a polyethylen target with a deuteron beam of 3.5 GeV/c momentum. For each wire the minimal (t_{min}) and maximal (t_{max}) drift times were determined. The average total drift time was found to be $t_{max} - t_{min} \approx 450ns$. In the track finding procedure the relation between the measured drift time and the minimal distance/radius (r) from the anode wire to the track plays an important role. To find the function, transforming the drift time (t) to radius, also referred to as $r(t)$ relation, is the central task. This tranformation function may depend on many parameters like: the electric field intensity, gas mixture, pressure, temperature and the chamber geometry. For determination of the tranformation function two methods were applied: the linear one, mainly used for on-line and the cumulative or integral one suitable for off-line purposes. It is worth to underline that this process is carried out iteratively and $r(t)$ is corrected in every iteration step.

Track finding and track projection reconstruction takes place for each block of unanimous planes. Blocks are defined dynamically and should involve at least 3 sensitive planes for unambigous track determination. The simplified algorithm can be summarized as follows:

1. Fired wires of different planes with maximal z distance are combined into doublets. For each pair 4 tangentials are computed.

2. For each tangential the distances d_i to all the fired wires are evaluated. If $d_i > d_{min}$ the hit is refused. The cut d_{min} is usually very loose about an order bigger than the chamber spatial resolution ($\approx 90 - 120\mu m$).

3. If the number of hits, found in the previous step, $N_{hits} \geq N_{min}$ the tangential becomes a track candidate. In our case $N_{min} = 4$ was used. If more candidates survive then that with minimal Σd_i is selected.

4. Track candidate is input to the track reconstruction. The projection of a straight track is parametrized in the plane perpendicular to the wires as e.g. for xz plane

$$z = ax + b, \tag{9}$$

where a and b are free parameters. The distance D between the track candidate and each fired wire is computed for all accepted hits. The straight line parameters are determined from χ^2 fit, so that the residual

$$\Delta r = r - |D| \tag{10}$$

is minimized [20]. Then the algorithm is repeated again from the track finding. Usually 2 - 3 iteration steps are sufficient.

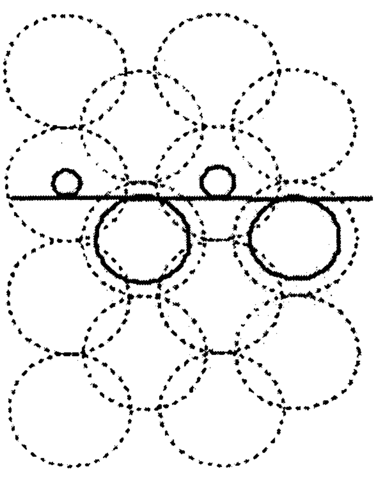

Figure 9: Example of a reconstructed one track event from four hits.

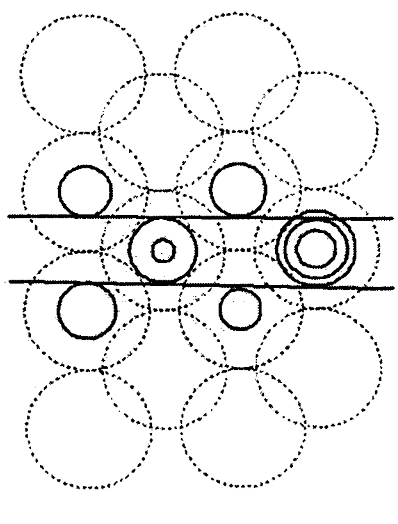

Figure 10: Example of a reconstructed two track event from nine hits.

An examples of one reconstructed track from 4 hits figure 9 and two reconstructed tracks from nine hits are shown in figures figure 9 and figure 10, respectively. The zoom

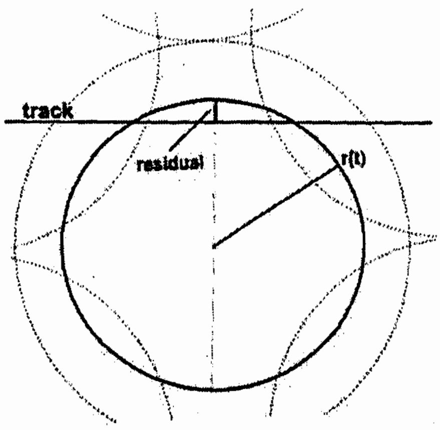

Figure 11: Zoom of a reconstructed one track event from four hits with basic quantities.

in Fig. 11 explains the basic quantities used in the track finding and reconstruction algorithm.

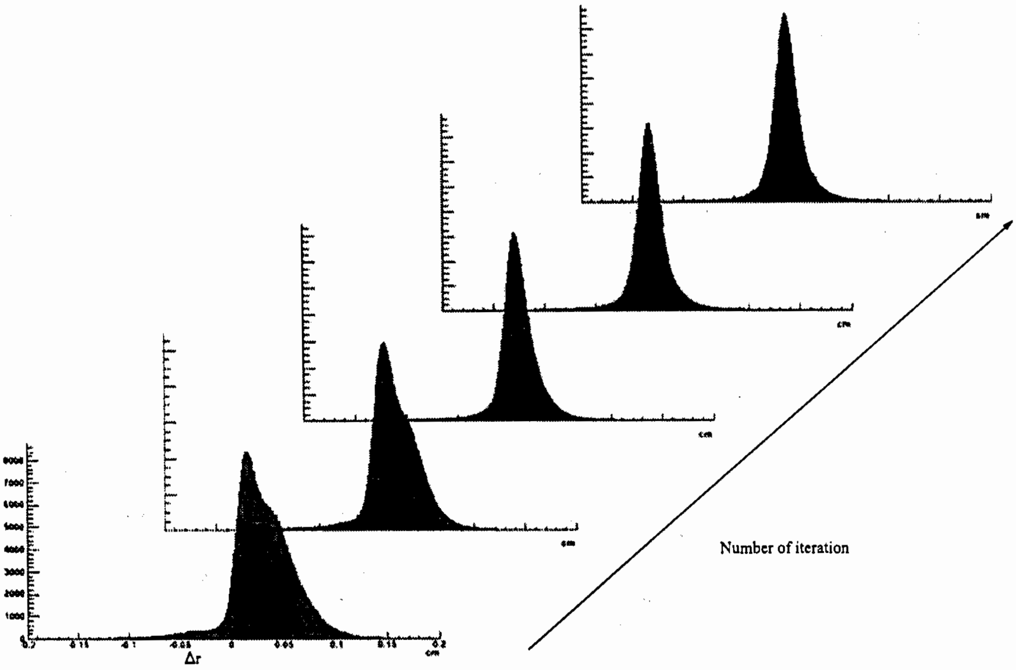

Figure 12: Residual dependence on the number of iteration.

As stated before the transformation function $r(t)$ plays a crucial role in the track reconstruction procedure, therefore during the iteration it also corrected. The criterion for the iterative correction is that the residuals of the reconstructred tracks should have a Gaussian distribution with a zero mean. For that reason the Δr *vs* t dependence of the reconstructed tracks are divided into small Δt intervals, projected to Δr axis, the mean values are computed and the transformation $r(t)$ is corrected for this value. Fig. 12 illustrates the track residual dependendence on the iteration number. As it can be seen four iteration steps give a acceptable mean value. This way of iterative correction to the transformation function $r(t)$ is referred to as autocalibration.

Summary and Conclusion

- The obtained ratio of the charge exchange differential cross sections at $t = 0$ for $dp \to (pp)n$ and $np \to pn$ reactions $R = 0.55 \pm 0.08$ testifies the prevailing contribution of the spin-dependent part to the $np \to pn$ cross section scattering.
- Continuation of researches at higher energies on STRELA set-up is important.
- STRELA electronics (VME + modules) was successfully tested.
- Track reconstruction for STRELA drift chambers was tested on exprimental samples.
- Autocalibration improves the reconstruction quality.
- STRELA is ready for data taking and processing.

Acknowledgement

This work was supported under Slovak Grant Agency VEGA 1/4010/07.

References

[1] I. Pomeranchuk, Sov. JETF 21, 1113 (1951).

[2] G.F.Chew,Phys.Rev. 84, 710 (1951)

[3] A.B. Migdal, J. Exp. Theor. Phys. (in Russian) **28**, 3 (1955)

[4] I. Pomeranchuk, Dokl. Akad. Nauk (in Russian) **LXXVIII**, 249 (1951)

[5] L.I. Lapidus, J. Exp. Theor. Phys.(in Russian) **32**,1437 (1957)

[6] N.W. Dean, Phys. Rev. **D5**, 1661 (1972)

[7] N.W. Dean, Phys. Rev. **D5**, 2832 (1972)

[8] D.V. Bugg, C. Wilkin, Nucl. Phys. **A167**, 575 (1987)

[9] R.Lednicky,V.L.Lyuboshitz, V.V.Lyuboshitz, Proc. XVI ISHEPP, Dubna 2004, 199.

[10] V.V.Glagolev et al., Eur.Phys.J A15, 471 (2002)

[11] D.V.Bugg et al., Phys.Rev. 146, 980 (1966)

[12] B.S.Aladashvili et al., NIM, 129, 109 (1975);
JINR Commun. 1-7645, Dubna, 1973

[13] V.I.Sharov et al., Czech.J.Phys. 55, A283 (2005)

[14] B.S.Aladashvili et al., J.Phys.G: Nucl.Phys. 3, 7 (1977)

[15] B.S.Aladashvili et al., J.Phys.G: Nucl.Phys. 3, 1225 (1977)

[16] B.S.Aladashvili et.al., Nucl.Phys. A274, 486 (1976)

[17] G.Bizard et al., Nuclear Physics B85, 14 (1975)

[18] J.Bystricky,F.Lehar, Nucleon-Nucleon Scattering data,editors H.Behrens and G.Ebel, Fachinformationszentrum Karlsruhe,1978 Edition,N 11-1, p.521

[19] http://strela.jinr.ru

[20] V.V.Glagolev et al., Preprint JINR P13-2008-165, Dubna, 2008

DATA SORTING IN γ-RAY SPECTROSCOPY

M. Morháč[1] and V. Matoušek

Institute of Physics, Slovak Academy of Sciences,
Dúbravska cesta 9, 845 11 Bratislava, Slovakia

Abstract

The paper presents several sorting methods of γ-ray events which were implemented in the data acquisition, processing and visualization system, developed at the Institute of Physics of the Slovak Academy of Sciences. The sorting methods using various shapes of gates (conditions) are presented, including rectangular windows, polygons, gates defined by arithmetic functions, spherical, ellipsoidal and composed gates. The examples illustrating the use of these methods are presented as well.

1. Introduction

Today's generation of γ-ray spectrometers such as Gammasphere [1] are capable of collecting large quantities of high-fold data in which many γ-rays are detected in coincidence in the same event. To utilize the optimum resolving power of the instruments, it is necessary to analyze the data with the optimum gating fold. The optimum gating fold depends on experimental factors such as the average multiplicity of γ-ray cascades and the amount of data collected. Typical high-fold analysis requires gating folds between 2 – 5, but high-fold events of over 10 energies per event occur in the experiments. The question is how to sort such high-fold coincidence data in order to produce spectra of various fixed dimensions under various selection criteria.

The operation of the sorting is based on "gates" or "conditions". When storing the events in "list mode", the sorting operation can substantially reduce storage volume necessary. Very frequently, the gates are used to create slices of the integral spectra of lower dimensionality also. If high-fold coincidence events are unfolded into a lower dimensional histograms, the statistics can become artificially high so that peak positions and statistics may be wrong, [2]. Properly proposed gating methods lead to an improvement in spectral quality, in particular, the peak-to-background ratio, and to a decrease of uncorrelated events in the resulting spectrum.

2. Sorting of high-fold data from γ-ray detector arrays

Sorting methods involve combinatorially decomposing each n-fold event into a number of lower m-fold subevents ($m \leq n$) [2].
Each n-fold event generates

$$\binom{n}{m} = \frac{n!}{m!(n-m)!} = \frac{n(n-1)\cdots(n-m+1)}{1\cdot 2\cdot 3\cdots m}$$

m-fold subevents where each subevent contains m energies from the original event.
Common difficulties using the sorting methods of analysis are in that:

[1] E-mail:Miroslav.Morhac@savba.sk

- if unfolded m-fold subevents are assumed to be independent and can be further decomposed into lower fold events – this is not correct, it can introduce spikes appearing in the spectra, [2]
- if high-fold coincidence events are unfolded into a lower histogram dimension, the statistics can become artificially high so that peak positions and statistics may be wrong.

To avoid these spikes appearing in the spectra each m-fold correlation can only be used once in a spectrum incrementation. Properly proposed gating methods lead to an improvement in spectral quality in particular the peak-to-background ratio, and to a decrease of uncorrelated events in the resulting spectrum.

3. Sorting methods implemented in DaqProVis

Several sorting methods we have implemented in our data data acquisition, processing and visualization software package, DaqProVis, which is developed at the Institute of Physics, SAS [3]. The basic element for data sorting is gate (condition). To satisfy typical experimental needs we have implemented various types of gates / conditions in DaqProVis:

- Rectangular window,
- polygon,
- arithmetic function,
- spherical gates,
- ellipsoids,
- composed gate.

A. Rectangular window

It specifies a set of event variables with lower and upper channels determining the region of event acceptance. This is a classical gating method commonly used. Let us take the simplest two-fold events and let us assume we desire to analyze variable , but only those events that satisfy the condition

$$g_{l1} \le x_1 \le g_{u1},$$

where g_{l1}, g_{u1} are lower and upper limits of the gate, respectively. Analogously for three and more fold events, two-dimensional region can be set e.g.

$$g_{l1} \le x_1 \le g_{u1} \quad \text{AND} \quad g_{l2} \le x_2 \le g_{u2}$$

In general, for n-fold rectangular window gate one can write

$$g_{l1} \le x_1 \le g_{u1} \quad \text{AND} \quad g_{l2} \le x_2 \le g_{u2} \quad \text{AND} \quad \cdots$$
$$\text{AND} \quad g_{\text{ln}} \le x_n \le g_{un}$$

where $x_1, x_2, \ldots, x_n$ are event variables. An example of rectangular gate applied to two-parameter spectrum is shown in Fig. 1. The gate is located to the peak area.

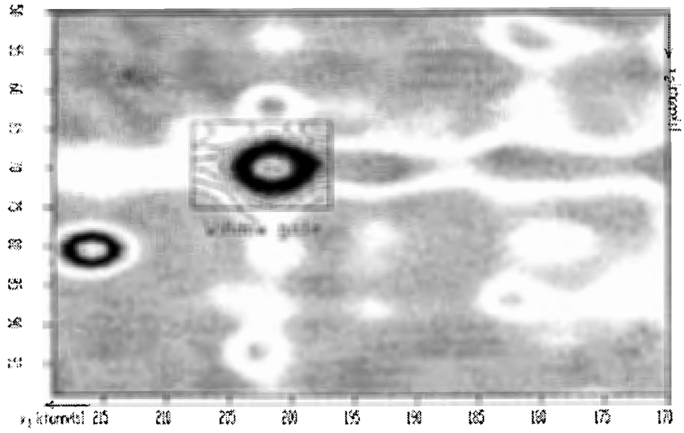

Fig. 1. An example of rectangular gate applied to two-parameter spectrum.

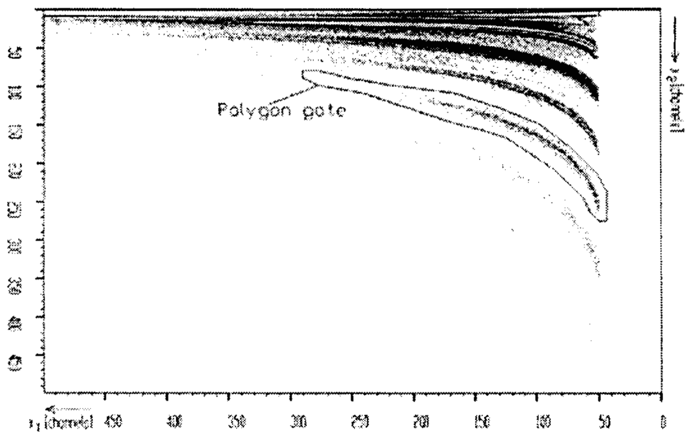

Fig. 2. An example of polygon gate applied to two-parameter spectrum.

B. Polygon

An efficient and simple way to choose the region of event acceptance in two-dimensional space of event variables is interactive setting of appropriate closed polygon. The polygon gate consists of sequence of coordinates of two event variables. It allows one to separate various parts of the spectrum. The advantage of this kind of gate is that one can design easily irregular shape. Its disadvantage is that it cannot be extended to higher dimensions and that it must be set manually. An example of polygon gate applied to two-parameter spectrum is shown in Fig. 2. The gate in the figure is defined by a set of segments which form the closed polygon around the irregular shape.

C. Arithmetic function

This type of gate is represented by mathematical function of event variables (detection lines) $x_1, x_2, \ldots, x_n$

$$f(x_1, x_2, \ldots, x_n) \leq 0$$

The allowed operators are: +, -, *, /, ^, sqr, log, exp, cos, sin. The built-in syntax analyzer is able to recognize the expressions written in Fortran-like style using names of event variables for operands, above-given operators and parentheses. During the sorting, for each event, the value of the function is calculated. If the value is less or equal to zero the event is accepted, i.e., the logical value of the condition is "true".

By employing a suitable analytical function, one can specify more exactly the region of interesting parts in the spectrum.

4. Spherical gates

Photopeak events are distributed approximately with Gaussian distribution. It means that in the hyperspace they have a spherical symmetry. When choosing the function with elliptic base for two variables one can reduce the uncorrelated background

$$\left(\frac{x_1 - c_1}{r_1}\right)^2 + \left(\frac{x_2 - c_2}{r_2}\right)^2 - 1 \le 0,$$

where c_1, c_2 determine the position of the photopeak, r_1, r_2 are proportional to σ_1 ,σ_2 (see Fig. 3).

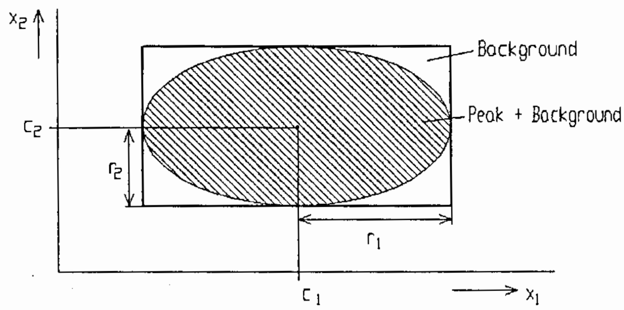

Fig. 3. Elliptical gate.

The extension of this function to n-dimensional case is straightforward. In general, one can define free any arithmetic function using the above-given set of operators.

When sorting events with Gaussian or quasi Gaussian distribution the gates with elliptic base are of special interest. The radii of ellipses are proportional to standard deviations σ_i or to the $\mathrm{FWHM}_i = \sqrt{2\log 2}\sigma_i$ (full width at half maximum) of the photopeak distribution. Then for symmetrical n-dimensional spherical gates one can write

$$\sum_{i=1}^{n}\left(\frac{x_i - c_i}{0.5FWHM_i}\right)^2 - R^2 \le 0$$

However, due to various effects in detectors the peaks exhibit left-hand tailing. It is needed to propose the special gates reflecting the tails in spectrum peaks. In [4] special gates reflecting the tails in spectrum peaks were proposed. The problem is to extend the gate shape in the tail direction. To explain it, we resort to two-dimensional asymmetrical spherical gate by introducing the tailing coefficient T in the variable x_2

$$\left(\frac{x_1 - c_1}{0.5 \cdot FWHM_1}\right)^2 + \left(\frac{x_2 - c_2}{0.5 \cdot FWHM_2 \cdot T}\right)^2 - R^2 \leq 0$$

where $T \geq 1$. To introduce tailings to both directions it turns out that we have to employ logical OR function so that the gate is intersection between two-tailed spherical gates

$$\left(\frac{x_1 - c_1}{0.5 \cdot FWHM_1}\right)^2 + \left(\frac{x_2 - c_2}{0.5 \cdot FWHM_2 \cdot T}\right)^2 - R^2 \leq 0 \quad \text{OR}$$

$$\left(\frac{x_1 - c_1}{0.5 \cdot FWHM_1 \cdot T}\right)^2 + \left(\frac{x_2 - c_2}{0.5 \cdot FWHM_2}\right)^2 - R^2 \leq 0.$$

It is straightforward to extend this idea to n-dimensional spherical gate [4]

$$\left(\frac{x_1 - c_1}{0.5 \cdot FWHM_1 \cdot T}\right)^2 + \left(\frac{x_2 - c_2}{0.5 \cdot FWHM_2}\right)^2 + \ldots + \left(\frac{x_n - c_n}{0.5 \cdot FWHM_n}\right)^2 - R^2 \leq 0 \quad \text{OR}$$

$$\left(\frac{x_1 - c_1}{0.5 \cdot FWHM_1}\right)^2 + \left(\frac{x_2 - c_2}{0.5 \cdot FWHM_2 \cdot T}\right)^2 + \ldots + \left(\frac{x_n - c_n}{0.5 \cdot FWHM_n}\right)^2 - R^2 \leq 0 \quad \text{OR}$$

$$\left(\frac{x_1 - c_1}{0.5 \cdot FWHM_1}\right)^2 + \left(\frac{x_2 - c_2}{0.5 \cdot FWHM_2}\right)^2 + \ldots + \left(\frac{x_n - c_n}{0.5 \cdot FWHM_n \cdot T}\right)^2 - R^2 \leq 0$$

By using the spherical gates the significant volume reductions over the cuboidal gates can be achieved as shown Tab. 1.

Tab. 1. The ratios of volume reduction achieved when using the spherical gates over the cuboidal gates.

DIMENSION	VOLUME OF HYPERSPHERE	VOLUME OF HYPERCUBE	RATIO
1	$2R$	$2R$	1.00
2	πR^2	$4R^2$	1.27
3	$^4/_3\,\pi R^3$	$8R^3$	1.91
4	$^1/_2\,\pi^2 R^4$	$16R^4$	3.04
5	$^8/_{15}\,\pi^2 R^5$	$32R^5$	8.11
10	$^1/_{120}\,\pi^5 R^{10}$	$1024R^{10}$	401.54

From the table we can see that the volume of processed (and consequently stored) events can be significantly decreased if an ellipsoidal gate is used instead of cuboidal gate.

By application of suitable spherical gate the experimenter can separate the events contributing to the background from the spectrum, [5] [6]. This can be achieved if we design the shape of the gate in coincidence with the shape created by distribution of events of our interest in the spectrum.

In the next few examples we present the examples of applying the gates to two- and three-dimesional data. An example of two-dimensional spherical gate is shown in Fig. 4. An example of another two-dimensional γ-ray spectrum with spherical balls gate is shown in Fig. 5. (Asi by sme mali jeden z predchdzajucich obrazkov vyhodit, ukazuju podobne veci.) To illustrate the use of three-dimensional spherical gate, let us have the three-dimensional γ-ray spectrum as shown in Fig. 6. We have chosen the spherical gate similar to that shown in Fig. 7. By applying of this gate to the spectrum from Fig. 6, we get the three-dimensional spectrum shown in Fig. 8. The gate is shown as shaded balls inside of the spectrum, i.e., the shaded channels satisfy the condition connected with the gate. An example of three-dimensional γ-γ-γ-ray spectrum with spherical gate with different widths of Gaussians in different directions is shown in Fig. 9.

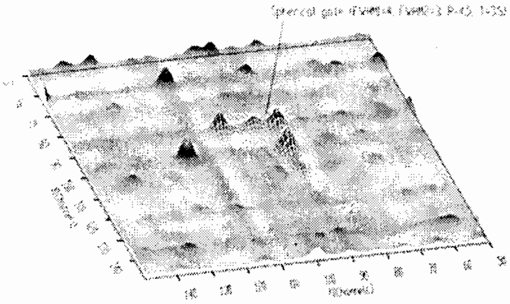

Fig. 4. An example of two-dimensional spherical gate.

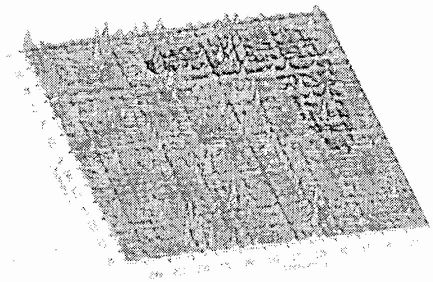

Fig. 5. Two-dimensional γ-ray spectrum with spherical balls gate.

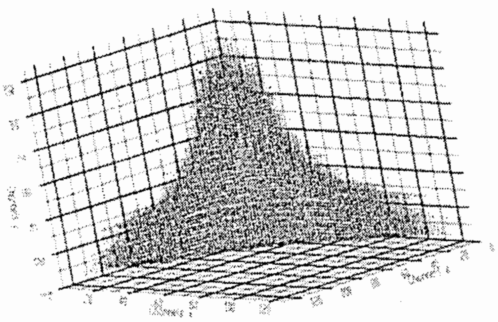

Fig. 6. Three-dimensional γ-ray spectrum.

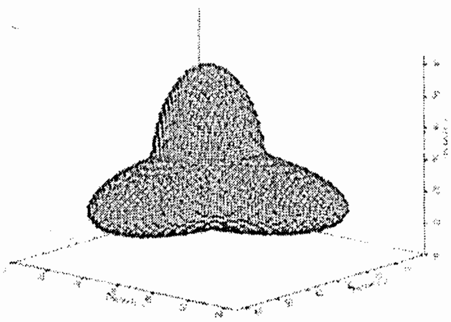

Fig. 7. Spherical gate shown as surface.

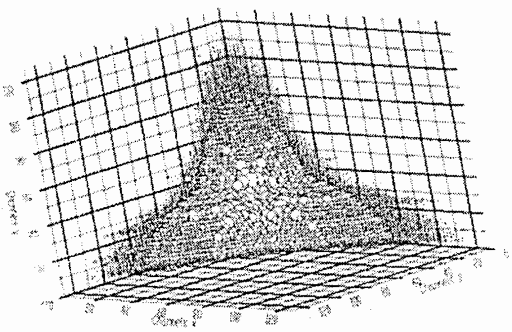

Fig. 8. An example of the application of three-dimensional spherical gate to three-dimensional spectrum. The gate is shown as shaded balls inside of the spectrum.

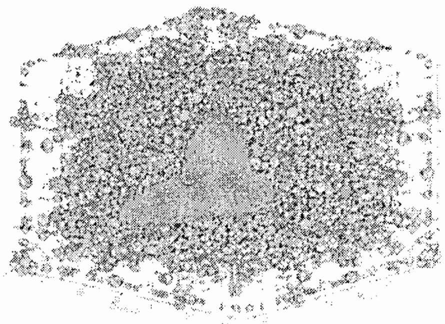

Fig. 9. An example of three-dimensional γ-γ-γ-ray spectrum with spherical gate with different widths of Gaussians in different directions.

The proposed model of this type of gates allows us to change the width of spherical Gaussians. By changing parameters, we can select any part of the spectrum. However, according to this model, one cannot change independently tailings for individual dimensions and angles between the Gaussians.

D. Ellipsoids

To change independently the tailings for individual dimensions and angles between the Gaussians and to make the design of the shape of the gates more flexible we proposed ellipsoid gates. In parametric form the ellipse can be expressed

$$x_1 = r_1 \cos(t) + c_1,$$
$$x_2 = r_2 \sin(t) + c_2,$$

where c_1, c_2 determine the position of the ellipse, r_1, r_2 are radii and are independent of t.

One can change freely the lengths of half-axes, the widths of ellipsoids as well as the angle between them. Let us express n-dimensional k-th ellipsoid E_k with center positioned at $c_1, c_2, ..., c_n$ and lengths of half-axes $a_1, b_1, a_2, b_2, ..., a_n, b_n$,

$$\begin{aligned}
x_1 &= b_1 \cos(t_{n-1})\cos(t_{n-2})....\cos(t_1) + c_1 \\
&\vdots \\
x_{k-1} &= b_k \cos(t_{n-1})\cos(t_{n-2})....\cos(t_{k-3})\sin(t_{k-2}) + c_{k-1} \\
x_k &= A_k(t_{k-1})\cos(t_{n-1})\cos(t_{n-2})....\cos(t_{k-2})\sin(t_{k-1}) + c_k \\
x_{k+1} &= b_{k+1} \cos(t_{n-1})\cos(t_{n-2})....\cos(t_{k-1})\sin(t_k) + c_{k+1} \\
&\vdots \\
x_n &= b_n \sin(t_{n-1}) + c_n
\end{aligned}$$

In order to describe tailings in the gate let us propose the change of radii in dependence on the parameters t_i

for $i = 1$

$$A_1(t_1) = \frac{a_1 + b_1}{2} + \frac{a_1 - b_1}{2}\cos(2t_1) \quad \text{for} \quad t_1 \in \langle 0, \frac{\pi}{2}\rangle \text{ AND } \langle \frac{3\pi}{2}, 2\pi\rangle$$
$$A_1(t_1) = b_1 \qquad \text{otherwise}$$

for $i > 1$

$$A_i(t_{i-1}) = \frac{a_i + b_i}{2} + \frac{a_i - b_i}{2}\sin(2t_{i-1}) \quad \text{for} \quad t_{i-1} \in \langle 0, \pi\rangle$$
$$A_i(t_{i-1}) = b_i \qquad \text{otherwise}$$

where $t_i = u_i + s_i$, $u_i \in \langle 0, 2\pi\rangle$ and s_i is angle shift of the axis. Finally, the n-dimensional gate can be expressed as logical OR of the individual ellipsoids

$$E_1 \text{ OR } E_2 \text{ OR} \ldots \text{OR } E_n .$$

Using this gate, one can define in more flexible way the region of interest.

An example of two-dimensional ellipsoid gate applied to the spectrum of nuclear multifragmentation is shown in Fig. 10, [7]. The ellipsoid gates have been positioned to the areas of our interest, i.e. during the sorting process the events which form the ridges are excluded. An example of three-dimensional ellipsoid gate is shown in Fig. 11. The figure demonstrates that one can change freely the lengths of half-axes, the widths of ellipsoids as well as the angle between them.

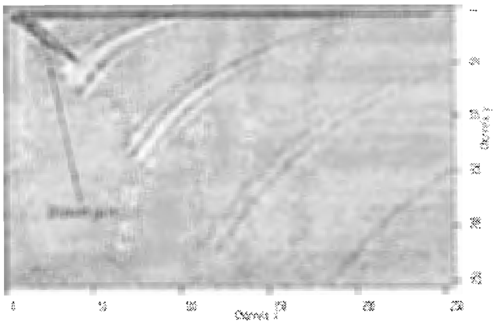

Fig. 10. Two-dimensional ellipsoid gate applied to the spectrum of nuclear multifragmentation.

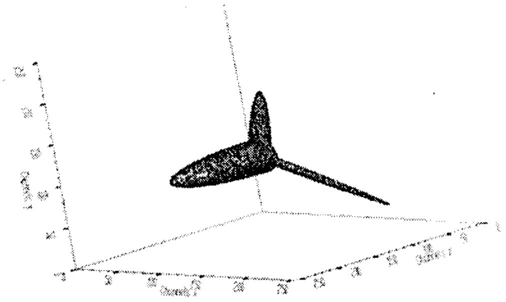

Fig. 11. An example of three-dimensional ellipsoid gate.

E. Composed gates

The result of application of any of the above-defined gates (conditions) is either the value „true", i.e., the event is accepted for further processing or the value „false" (event is ignored). By applying logical operators (AND, OR, NOT) to operands (previously defined gates) and using parentheses one can write very complex logical expressions defining the shape of the composed gate. The shape can be very complicated and can define even the composition of disjoint subsets.

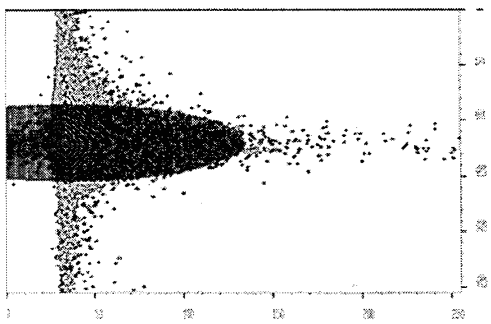

Fig. 12.: Two-dimensional gate *A*.

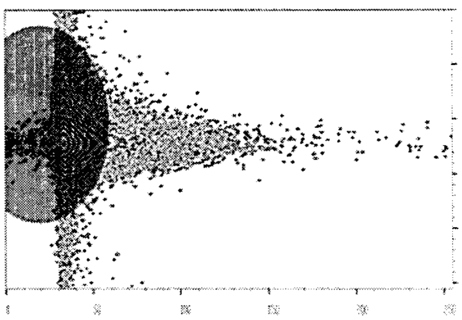

Fig. 13. Two-dimensional gate *B*.

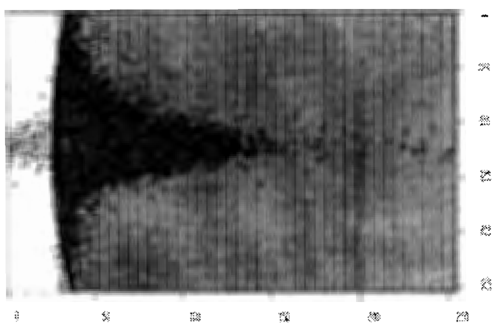

Fig. 14. Two-dimensional gate *C*.

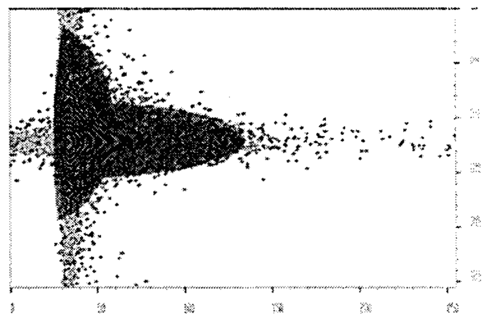

Fig. 15. Resulting composed condition (*A* OR *B*) AND *C*.

Let us denote the gates shown in Figs. 12, 13, 14 as *A*, *B* and *C*, respectively. Then the resulting composed gate defined by logical function (*A* OR *B*) AND *C* is shown in Fig. 15.

5. Conclusions

In the paper we have presented the conventional as well as new developed algorithms of experimental data sorting. An attention must be paid when unfolded events are further decomposed into lower fold events. By using the unsuitable methods, the statistics can become artificially high so that peak positions and statistics may be wrong. The sorting methods presented can decrease the required storage space and improve the resolution of the analyzed γ-ray spectra.

The algorithms of various types of gates/conditions, including rectangular windows, polygons, entered by arithmetic function, spherical and ellipsoidal gates, and composed gates were implemented in DaqProVis system, which is being developed at the Institute of Physics, Slovak Academy of Sciences since early 90-ties. [8, 9]. Thanks to its modular structure and object oriented approach it has evolved to a very efficient tool for the analysis of multidimensional events and spectra [3].

Acknowledgement

This work was supported by Scientific Grant Agency through Project 2/0029/09 from Ministry of Education of Slovak Republic and the Slovak Academy of Sciences.

References

[1] M.A.Delaplanque, R.M.Diamond (Eds.), *GAMMASPHERE, A National Gamma-Ray Facility, A proposal*, March 1988.

[2] C.W.Beausang, et al., *Using high-fold data from the new generation of γ-ray detector arrays*, Nucl. Instr. and Meth., A364, p.560, 1995.

[3] M.Morháč, et al., *DaqProVis, a toolkit for acquisition, interactive analysis, processing and visualization of multidimensional data*, Nucl. Instr. and Meth., A559, pp.76–80, 2006.

[4] Ch.Theisen, et al., *Improvement of high-fold γ-ray data processing: the spherical gate method*, Nucl. Instr. and Meth., A432, p.264, 1999.

[5] J.N.Wilson, et al., *Determination of optimum gating fold, shape and width for analysis of high-fold γ-ray coincidence data*, Nucl. Instr. and Meth., A399, p.147, 1997.

[6] B.Crowell, et al., *Background subtraction for high-fold gamma-ray coincidence data*, Nucl. Instr. and Meth., A355, p.575, 1995.

[7] M.Veselský, et al., *Progress in Research, 2000-2001*, Cyclotron Institute, Texas A&M University College Station, p.13, 2001.

[8] M.Morháč, I. Turzo, and J. Krištiak, *PC-CAMAC based data acquisition system for multiparameter measurements*, IEEE Trans. Nuclear Science, 42, p.1, 1995.

[9] M.Morháč, V.Matoušek and I. Turzo, *Multiparameter data acquisition and analysis system with on-line compression*, IEEE Trans. Nuclear Science, 43, p.140, 1996.

PROCESSING OF MULTIDIMENSIONAL EXPERIMENTAL DATA IN NUCLEAR PHYSICS

M. Morháč[1], V. Matoušek and I. Turzo

Institute of Physics, Slovak Academy of Sciences,
Dúbravska cesta 9, 845 11 Bratislava, Slovakia

Abstract

The paper presents several sophisticated algorithms for the processing of spectroscopic data. These include algorithms for background elimination, for separation of peak containing regions from peak-free regions, deconvolution and identification of information carrier objects.

1. Introduction

One of the basic problems in the analysis of the spectra is the separation of useful information contained in peaks from the useless information (background, noise). In order to process data from numerous analyses efficiently and reproducibly, the background approximation must be, as much as possible, free of user-adjustable parameters. Baseline removal, as the first preprocessing step of spectrometric data, critically influences subsequent analysis steps. The more accurately the background is estimated the more precisely we can estimate the existence of peaks. In the contribution we present an algorithm to determine peak regions and separate them from peak-free regions. Subsequently it allows to propose a new baseline estimation method based on sensitive non-linear iterative peak clipping with automatic local adjusting of width of clipping window. One of the most delicate problems of any spectrometric method is that related to the extraction of the correct information out of the spectra sections, where due to the limited resolution of the equipment, the peaks as the main carrier of spectrometric information are overlapping. Conventional methods of peak searching based usually on spectrum convolution are inefficient and fail to separate overlapping peaks. The deconvolution methods can be successfully applied for the determination of positions and intensities of peaks and for the decomposition of multiplets.

2. Background estimation

Very efficient method of background estimation, based on Statistics-sensitive Non-linear Iterative Peak-clipping algorithm (SNIP), has been developed in [1]. In [2] we extended the SNIP method for multidimensional spectra. In multidimensional spectra, the algorithm must be able to recognize not only continuous background but also to include all the combinations of coincidences of the background in some dimensions and the peaks in the other ones. In [3] we proposed several improvements of the SNIP algorithm. Further we have derived a set of modifications of the algorithm that allow estimation of specific shapes of background and ridges as well. Examples of one-, two-, and three-dimensional spectra before and after background elimination are given in Figs. 1-3.

---

[1] E-mail:Miroslav.Morhac@savba.sk

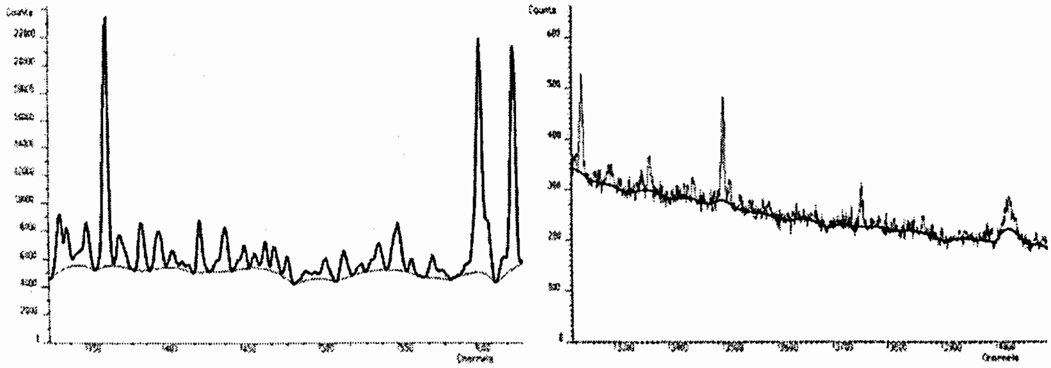

(a) (b)

Fig. 1 An example of γ-ray spectrum with estimated background using decreasing clipping window (a) and background estimated using SNIP algorithm with simultaneous smoothing (b).

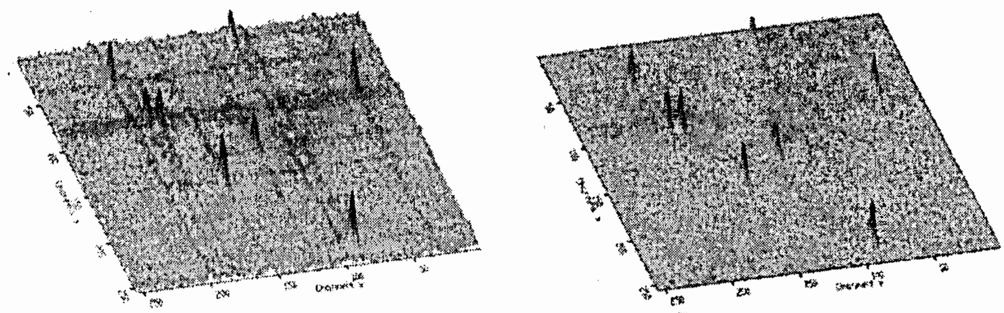

(a) (b)

Fig. 2 An example of two-dimensional γ-γ-ray spectrum before (a) and after background elimination using the algorithm with simultaneous smoothing (b).

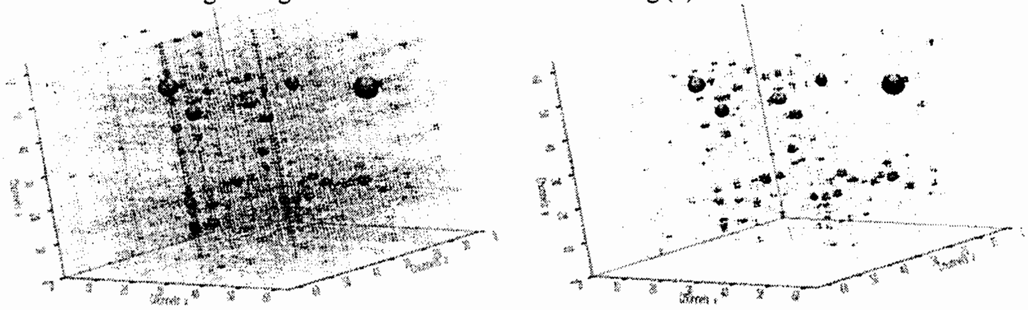

(a) (b)

Fig. 3 An example of three-dimensional γ-γ-γ-ray spectrum before (a), and after background elimination using the algorithm with simultaneous smoothing (b).

3. Estimation of peak regions

In [4-5] the authors propose a peak-search method based on two-pass convolution of the spectrum with the first derivative of the Gaussian. Besides of the identification of peaks the method can be utilized for the determination of peaks intervals [6]. Based on this approach we proposed an improved background estimation algorithm with clipping window adaptive to peak regions widths. The comparison of both methods is presented in Fig. 4.

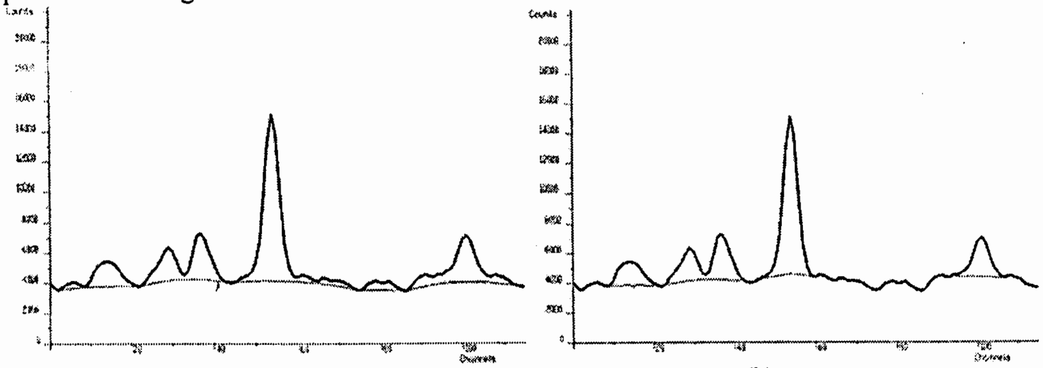

(a) (b)

Fig. 4 Experimental γ-ray spectrum with estimated background using fixed width of clipping window (a), and width automatically adjustable to the widths of peak regions (b).

4. Deconvolution

The peaks as the main carrier of spectrometric information are very frequently positioned close to each other. The extraction of the correct information out of the spectra sections, where due to the limited resolution of the equipment and overlapping of the signals coming from various sources, is a very complicated problem. Deconvolution and restoration are the names given to the endeavor to improve the resolution of an experimental measurement by mathematically removing the smearing effects of an imperfect instrument, using its resolution function. As a rule deconvolution problems are very ill-conditioned, i.e., very small errors or noise in the deconvolved spectrum cause enormous oscillations in the resulting data. In the contribution we have studied only positive definite deconvolution algorithms (Gold [7], Richardson-Lucy [8], [9] and Maximum a posteriori [10]). In [11] we proposed boosted positive definite deconvolution algorithm. In [12] we developed deconvolution algorithm based on Tikhonov regularization of squares of negative values. Both allow to improve the resolution up to delta functions. Examples of one-, and two-dimensional spectra before and after deconvolution are given in Figs. 5 and 6, respectively.

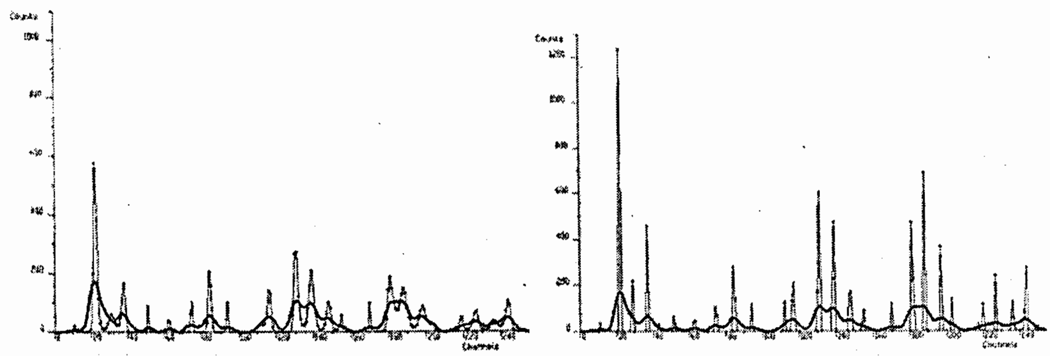

(a) (b)

Fig. 5 Original and deconvolved γ-ray spectrum using classic (a), and boosted (b) Gold algorithm.

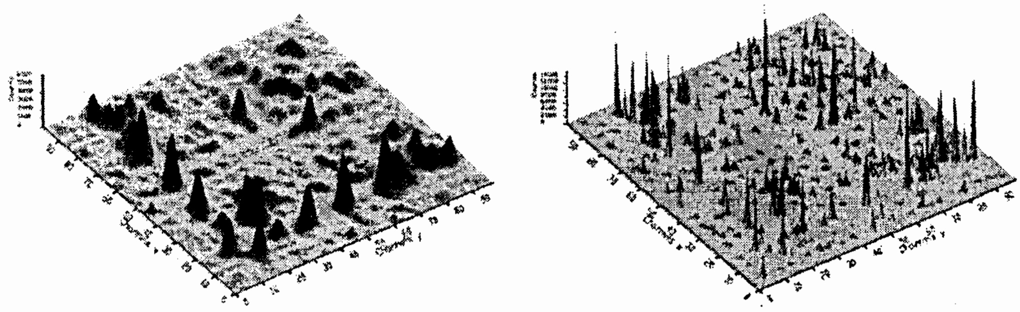

(a) (b)

Fig. 6 Original (a), and deconvolved γ-γ-ray spectrum using boosted Gold algorithm (b).

5. Identification of spectroscopic information carrier objects

In [13] we proposed a peak searching algorithm based on convolution with the second derivative of Gaussian for multidimensional spectra. The algorithm is able to recognize crossing points of ridges of lower-fold coincidences from n-fold coincidence peaks (Fig. 7).

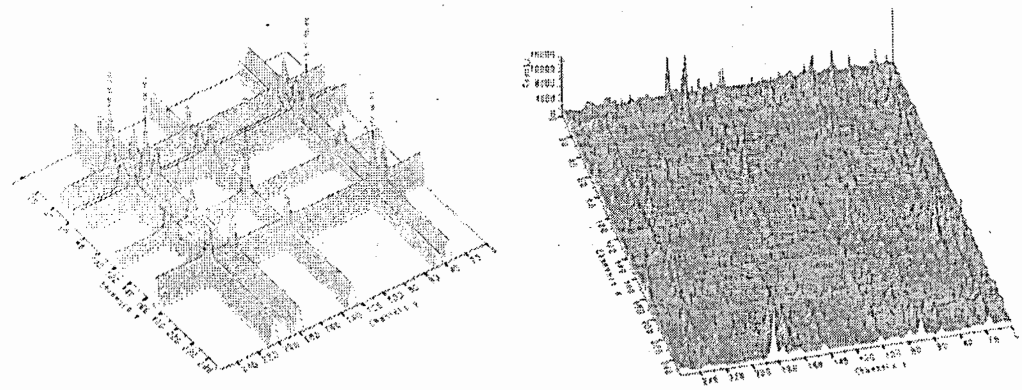

(a) (b)

Fig. 7 Synthetic (a), and experimental (b) two-dimensional spectra with found peaks denoted by marks.

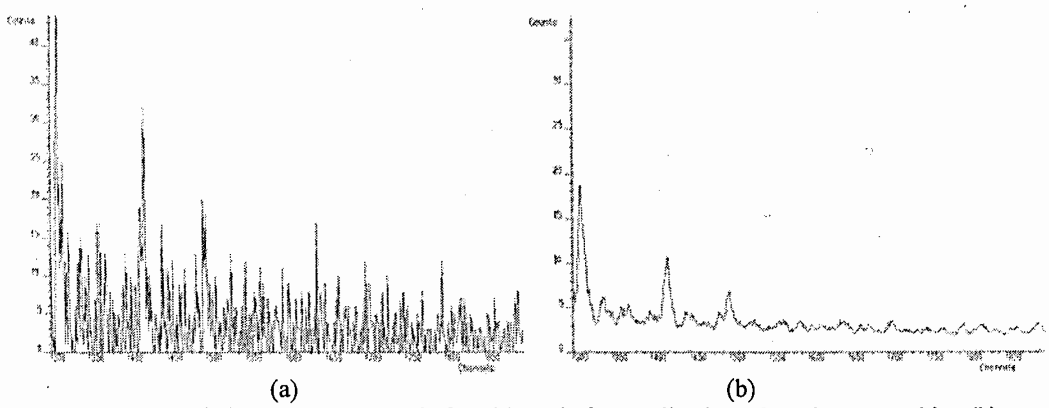

(a) (b)

Fig. 8 Low-statistics γ-ray spectrum before (a), and after application of Markov smoothing (b).

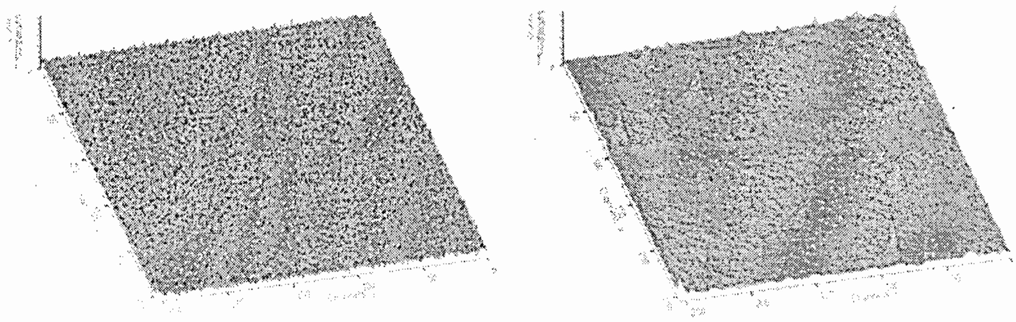

(a) (b)

Fig. 9 Low-statistics γ-γ-ray spectrum before (a), and after application of Markov smoothing (b).

In many cases in low-statistics spectra we need to smooth data before application of peak searching algorithm. In [14] we proposed a smoothing and peak enhancement method based on Markov chains. Again we generalized the method for multidimensional data. In Figs. 8 and 9 we illustrate the smoothing and peak enhancement properties of the method.

In the spectra of nuclear multifragmentation one needs to determine ridges of corresponding points from very sparsely distributed two-dimensional experimental data. In [15] we proposed an algorithm based on linearization and smoothing using inverted positive second derivative of Gaussian. Application of Gold deconvolution allows decomposition of identified ridges to subridges. An illustrative example is presented in Figs. 10 and 11.

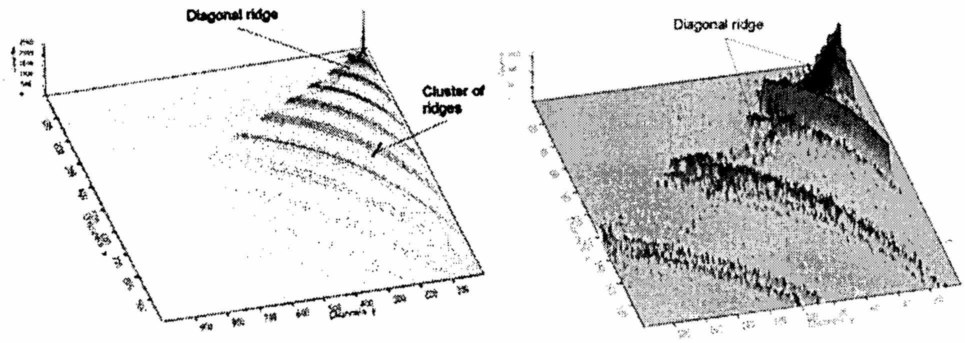

(a) (b)

Fig. 10 Original Si-Si spectrum (a), and its detail (b).

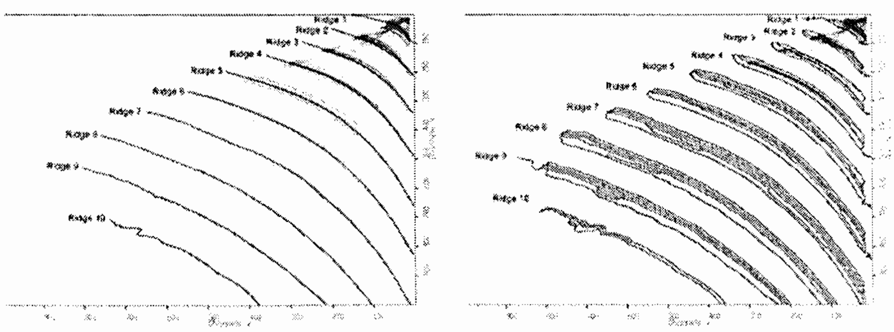

(a) (b)

Fig. 11 Spectrum from Fig. 10 with determined ridges (a), and decomposed to subridges (b).

Identification of rings in two-dimensional spectra from RICH (Ring Imaging Cherenkov) detectors was another problem where our advanced techniques were used.

The goal was to determine the rings of corresponding points from very sparsely distributed two-dimensional experimental data. The algorithm is based on two-dimensional Gold deconvolution. In Fig. 12 we illustrate the results obtained by using the deconvolution algorithm to identify the rings in the synthetic spectrum. The synthetic spectrum was composed of 200 events randomly positioned in 6 circles and another 200 (Fig. 12(a)) or 500 (Fig. 12(b)) random noise events added to these spectra. The identified circles are shown in Fig. 12.

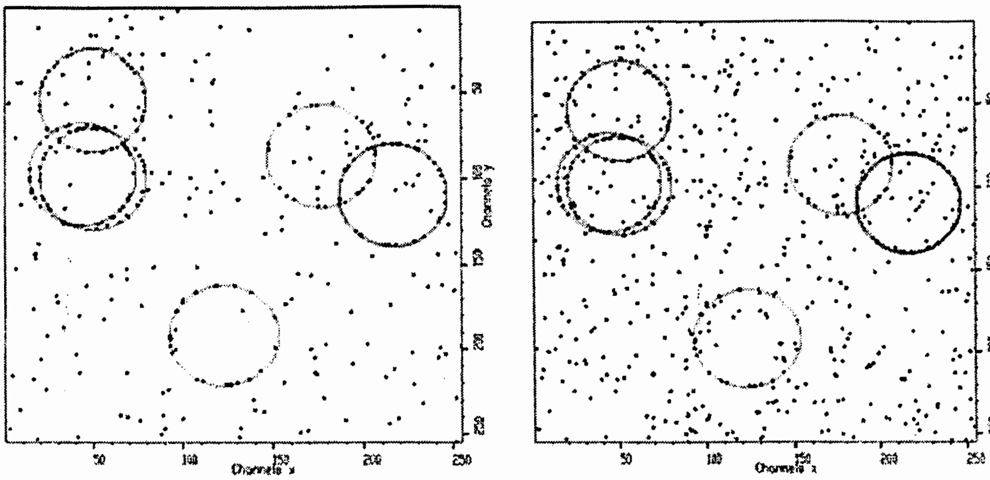

(a) (b)

Fig. 12 Synthetic spectrum composed of 200 randomly distributed events arranged in 6 randomly positioned circles with added 200 (a), and 500 (b) randomly distributed noise events. The circles represent the identified ones.

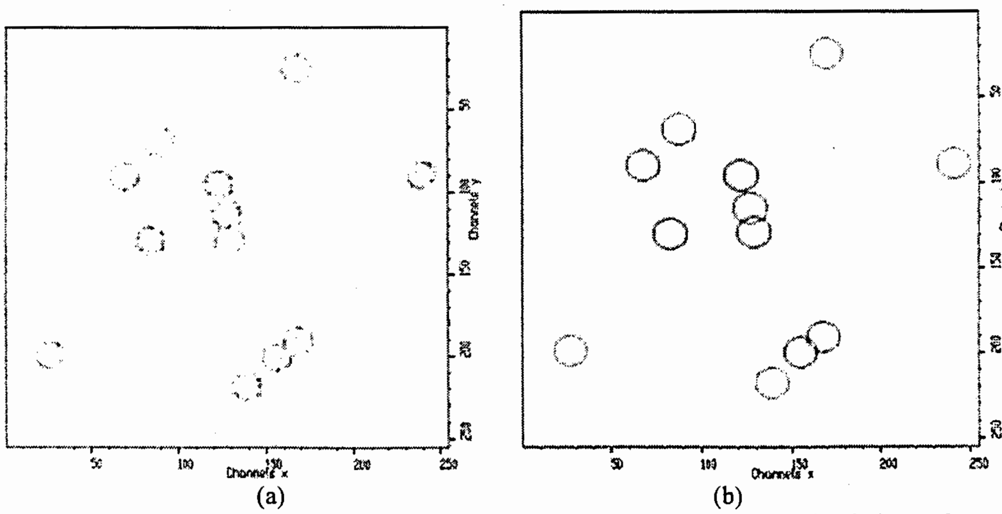

(a) (b)

Fig. 13 An example of simulated spectrum from GEANT (a)., and identified rings after convolution with the response (b).

An example of the result achieved by applying the algorithm to the simulated spectrum obtained from GEANT program is given in Fig. 13. In Fig. 13(a) the simulated spectrum consisting of events randomly distributed in 12 rings and in Fig. 13(b) the identified rings after convolution with the response are presented.

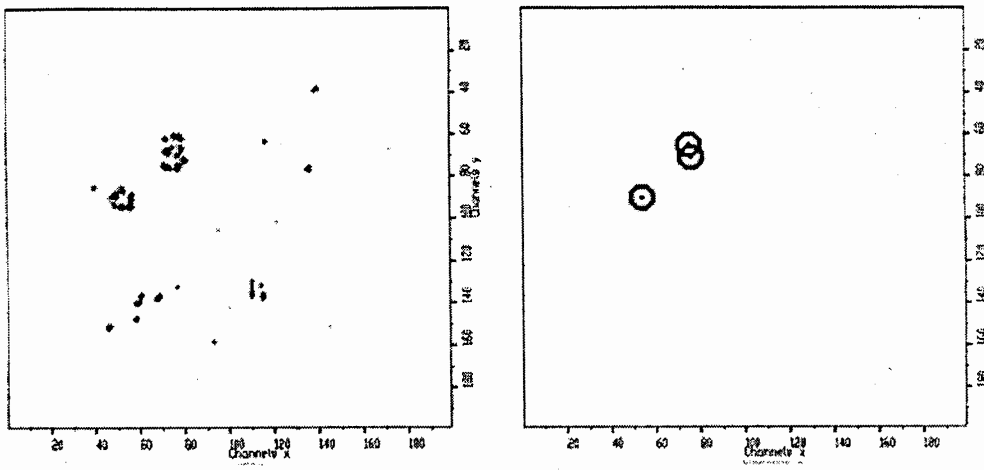

(a) (b)

Fig. 14 An example of experimental RICH spectrum (a), and three identified centers after deconvolution with three rings after convolution with the response (b).

As a final example we present the results obtained from identification of the rings in experimental data from HADES RICH detectors. In Fig. 14(a) the original spectrum containing the events from 3 rings and noise is presented. Spectrum after deconvolution, showing the identified centers of the rings and its convolution is shown in Fig. 14(b). It can be seen, that the algorithm identifies correctly the ring and suppresses the noise in the experimental spectrum.

6. Conclusions

We have generalized and extended the existing basic SNIP algorithm for additional parameters and possibilities that make it possible to improve substantially the quality of the background estimation. We have included these modifications and derived the algorithms for two-, three-, up to n-dimensional spectra.

We proposed an algorithm for the determination of the peak regions. In the contribution we suggested an algorithm of background estimation with the clipping window adaptable to the widths of peak regions as well. Moreover the algorithm for separation of peaks containing regions from peak-free regions can be utilized for fitting purposes to confine the fitting regions.

To improve resolution in spectra we analyzed a series of deconvolution methods. We proposed boosted deconvolution algorithms and the algorithm based on Tikhonov regularization of squares of negative values. Both algorithms are able to decompose the overlapped peaks practically to δ functions while concentrating the peak areas to one channel.

Further in the contribution we present peak searching algorithm based on the second derivatives of Gaussian and peak searching algorithm for low-statistic spectra based on Markov chain method. The presented algorithms were implemented in

DaqProVis system [16] and partially in ROOT system in form of TSpectrum classes[17].

Acknowledgement

This work was supported by Scientific Grant Agency through Project 2/0029/09 from Ministry of Education of Slovak Republic and the Slovak Academy of Sciences.

References

[1] C.G.Ryan, E.Clayton, W.L.Griffin, S.H.Sie and D.R.Cousens, *A statistics-sensitive background treatment for the quantitative analysis of PIXE spectra in geoscience applications*, Nucl. Instr. Meth., **B34**, p.396, 1988.

[2] M.Morháč, J.Kliman, V.Matoušek, M.Veselský and I.Turzo, *Background elimination methods for multidimensional γ-ray spectra*, Nucl. Instr. Meth., A401, p.113, 1997.

[3] M.Morháč and V.Matoušek, *Peak clipping algorithms of background estimation in spectroscopic data*, Applied Spectroscopy, 62, p.91, 2008.

[4] A.Likar and T.Vidmar, *A peak-search method based on spectrum convolution*, Journal of Physics D: Applied Physics, 36, p.1903, 2003.

[5] A.Likar, T.Vidmar and M.Lipoglavšek, *Resolving double peaks in high-resolution spectra by spectrum convolution*, Journal of Physics. D: Applied Physics, 37, p.932, 2004.

[6] M.Morháč, *An algorithm for determination of peak regions and baseline elimination in spectroscopic data*, Nucl. Instr. Meth., A600, pp.478-487, 2009.

[7] M.Morháč, J.Kliman, V.Matoušek, M.Veselský and I.Turzo, *Efficient one and two dimensional Gold deconvolution and its application to gamma-ray spectra decomposition*, Nucl. Instr. Meth., A401, p. 385, 1997.

[8] W.H.Richardson, *Bayesian-based iterative method of image restoration*, Journal of Optical Society of America, 62, p.55, 1972.

[9] L.B.Lucy, *An iterative technique for the rectification of observed images*, Astronomical Journal, 79, p.745, 1974.

[10] B.Hunt, *Prospects for image restoration*, Int. Jour. of Modern Physics, C5, p.151, 1994.

[11] M.Morháč, *Deconvolution methods and their applications in the analysis of γ-ray spectra*, Nucl. Instr. Meth., A559, p.119, 2006.

[12] M.Morháč and V.Matoušek, *Complete positive deconvolution of spectrometric data*, Digital Signal Processing, 19, pp.372–392, 2009.

[13] M.Morháč, J.Kliman, V.Matoušek, M.Veselský and I.Turzo, *Identification of peaks in multidimensional coincidence γ-ray spectra*, Nucl. Instr. Meth., A443, p108, 2000.

[14] M.Morháč, *Multidimensional peak searching algorithm for low-statistics nuclear spectra*, Nucl. Instr. Meth., A581, p.821, 2007.

[15] M.Morháč and M.Veselský, *Identification of isotope lines in two-dimensional spectra of nuclear multifragmentation*, Nucl. Instr. Meth., A592, p.434, 2008.

[16] M.Morháč, V.Matoušek, I.Turzo, and J.Kliman, *DaqProVis, a toolkit for acquisition, interactive analysis, processing and visualization of multidimensional data*, Nucl. Instr. Meth., A559, p.76, 2006.

[17] R.Brun, F.Rademakers, S.Panacek, D.Buskulic, J.Adamczewski and M.Hemberger, *ROOT, An Object-Oriented Data Analysis Framework*, Users Guide 3.02c, CERN, 2002.


LECTURE HALL

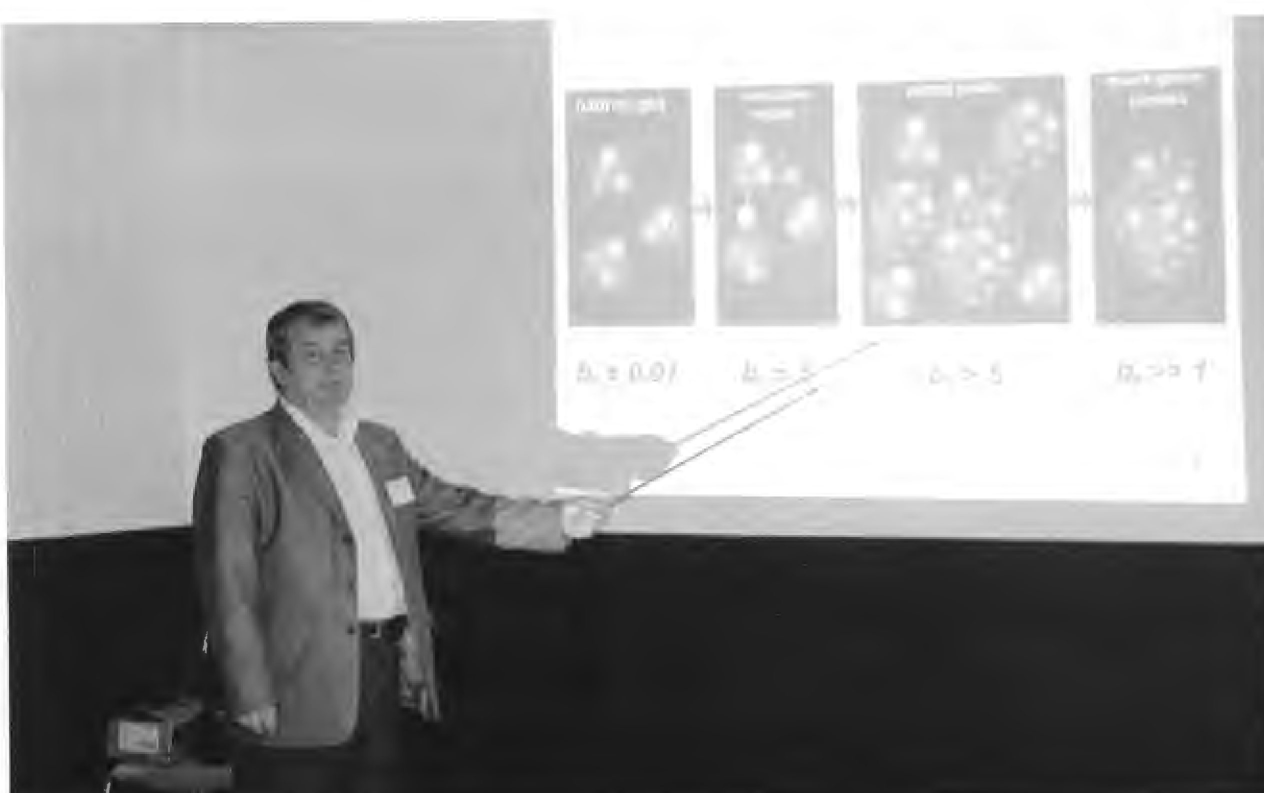


Chairman
Time over!


RNP'09
SOLÁRIUM
CHRBTICE
CELKOVÁ

Научное издание

Relativistic Nuclear Physics: from Hundreds of MeV to TeV

Proceedings of the 10th International Workshop

Релятивистская ядерная физика: от сотен МэВ до ТэВ

Труды 10-го международного совещания

E1,2-2010-17

Ответственная за подготовку сборника к печати *И. И. Мигулина.*

Сборник отпечатан методом прямого репродуцирования
с оригиналов, предоставленных оргкомитетом.

Подписано в печать 16.03.2010.
Формат 60 × 84/8. Бумага офсетная. Печать офсетная.
Усл. печ. л. 22,32. Уч.-изд. л. 18,58. Тираж 110 экз. Заказ № 56892.

Издательский отдел Объединенного института ядерных исследований
141980, г. Дубна, Московская обл., ул. Жолио-Кюри, 6.
E-mail: publish@jinr.ru
www.jinr.ru/publish/